Interactions of low momentum kaons in hydrogen

Bedford, Nigel Hugh

INTERACTIONS OF LOW MOMENTUM KAONS IN HYDROGEN

by

NIGEL HUGH BEDFORD

A thesis submitted to the University of Durham
in candidature for the degree of
Doctor of Philosophy

June 1979

Tc My Parents

ABSTRACT

This experimental study of low energy K^-p interactions was carried out using the British National Hydrogen Bubble Chamber which incorporated a Track Sensitive Target (T.S.T.) to enhance the conversion of γ-rays into $e^+ e^-$ pairs.

The results presented in this work are the channel cross-sections for K^-p interactions below $\sim$ 300 MeV/c, a determination of the ratio (γ), at zero kaon momentum, of the rates of production of charged hyperons and finally an analysis of the data in terms of the K-matrix parametrisation.

Also included is a discussion of errors of measurement which are important in this low momentum region and details of the limitations and problems associated with the T.S.T. type of experiment.

The cross-sections are found to confirm the only other precise data in this region (Kim) with the exception of the $\overline{K^0}n$ channel which is higher in this TST work. The K-matrix parametrisation is able to describe adequately the combined data of the TST work and that of Kim and gives a consistent determination of the mass of the bound state below threshold (1405 MeV). The value of γ was found by two methods and gave the results 2.38 ± 0.04 and 2.35 ± 0.07. This resolves the discrepancy between the two previous determinations of this ratio using different experimental techniques. This part of the work resulted in a publication in Nuclear Physics (reference 25).

CONTENTS

Page No.

CHAPTER ONE

Low Energy K^-p Interactions

1.1 Introduction 1

1.2 Motivation For The Study Of Low Energy K^-p Interactions 3

1.3 Aims Of The Present Experiment 5

1.4 Bubble Chambers And K^-p Interactions 5

1.5 Review Of Experimental Data 6

1.6 Theoretical Review 7

1.7 K-Matrix Analysis 10

1.7.1 Relation Between K-Matrix and T-Matrix 10

1.7.2 Application Of K-Matrix To The $\overline{K}N$ System 12

1.7.3 Corrections For Charge Dependent Effects 17

1.8 Outline Of Thesis 19

CHAPTER TWO

Experimental Details I

2.1 Bubble Chamber 21

2.2 The Beamline And Beam Entry Into The Chamber 24

2.3 Limitations Of The T.S.T. Chamber 28

2.4 Precision Of Measurement 29

2.5 The Exposure 32

2.6 Scanning 32

2.7 Event Recognition 37

2.7.1 $K^-p \longrightarrow \Sigma^+\pi^-$, $\Sigma^+ \longrightarrow p\pi^0$ or $\Sigma^+ \longrightarrow n\pi^+$ 37

2.7.2 $K^-p \longrightarrow \Sigma^-\pi^+$, $\Sigma^- \longrightarrow n\pi^-$ 39

2.7.3 $K^-p \longrightarrow \Sigma^-\pi^+$, $\Sigma^-p \longrightarrow$ neutrals 39

2.7.4 $K^-p \longrightarrow K^-p$ 39

2.7.5 Two Prong Events 39

2.7.6 Zero Prongs With A Neutral Vee 40

2.7.7 One Prong Events 40

2.7.8 Three Prong Events 41

2.8 Data Recording And Scanning Codes 41

2.9 Preselection Of Data Before Measurement 42

2.9.1 Neutral Hyperon Production 42

2.9.2 Collinear Sigma Production 44

CHAPTER THREE

Experimental Details II

3.1 Measuring Technique 45

3.2 Measuring Accuracy Checks 46

3.2.1 Measurement Of Track Curvatures 46

3.2.2 Fiducial Measurement 46

3.2.3 Optical Calibration 46

3.3 Event Processing 47

3.3.1 REAP 47

3.3.2 TRANS 47

3.3.3 Geometrical Reconstruction 47

3.3.4 Kinematic Fitting 48

3.3.5 Event Judging 51

3.3.6 MASTERLIST - Processing Control Programme 52

3.3.7 DATA SUMMARY TAPE (D.S.T.) 53

3.4 Classifications Of Unmeasurable Events 53

3.4.1 Σ Hyperon Production Events 55

3.4.2 Elastic Scattering Events 56

3.4.3 Charge Exchange 56

3.4.4 Σ^0/Λ^0 Hyperon Production 56

3.4.5 Random Losses 57

CHAPTER FOUR

Channel Cross-Sections I

4.1 The Determination Of The Hydrogen Density 58

4.2 Calibration Of The Magnetic Field 61

4.3 Distributions Of Stretch Functions 62

4.4 The Use Of One Prong Decays To Determine The Path Length Distribution 65

4.5 Distribution Of Primary Path Length 71

4.6 The Effect Of Errors Of Measurement On The Primary Momentum 81

4.6.1 Illustration Of The Error Problem 83

4.6.2 Outline Of Error Analysis 85

4.6.3 Reciprocal Momentum Distributions At The Track Centre 86

4.6.4 Parametrisation Of The Errors In $1/p_c$ 90

4.6.5 Theoretical Reciprocal Momentum Distribution 93

4.6.6 Determination Of The Non-Gaussian Error Distributions 98

4.6.7 Estimation Of The Effect Of Errors Of Measurement 101

4.6.8 Conclusions 104

CHAPTER FIVE

Channel Cross-Sections II

5.1 Charged Hyperon Production 106

5.1.1 Geometrical Losses At The Decay Vertex 107

5.1.2 Geometrical Losses At The Production Vertex 111

5.1.3 Correction For Short Lived Sigma Hyperons 112

5.1.4 Effect Of Shallow Chamber 117

5.1.5 Correction For Unmeasurable Events 117

5.1.6 Correction For Scanning Efficiencies 118

5.1.7 Charged Hyperon Cross-Sections 119

5.2 Elastic Scattering 123

5.2.1 Distributions Of Production Angles 125

5.2.2 Events With Short Tracks 128

5.2.3 Elastic Scattering Cross-Section 132

5.3 Neutral Hyperon Production 132

5.3.1 Selection Of Kaon Momenta 135

5.3.2 Geometrical Losses At The Decay Vertex 135

5.3.3 Geometrical Losses At The Production Vertex 137

5.3.4 Minimum Observable Length Of Hyperon 141

5.3.5 Neutral Hyperon Cross-Section 141

5.4 Charge Exchange Channel 144

CHAPTER SIX

Gamma Ratio - Data Aquisition

6.1 Detection Of Charged Hyperons In The Chamber 152

6.2 Previous Determinations Of The Gamma Ratio 153

6.3 Present Experiment 154

6.4 Gamma Ratio Model 156

6.5 Method I - Branching Ratio Method 159

6.6 Method II - Minimum Effective Range (M.E.R.) 161

6.7 Track Ionisation 162

6.8 Scanning 163

6.9 Measuring 164

6.10 Processing 167

CHAPTER SEVEN

Gamma Ratio - Data Analysis

7.1 Selection Of Data For Analysis 168

7.2 Correction For Ambiguous Collinear And Non-Collinear Events 171

7.3 Correction For Scanning Efficiencies 171

7.4 Template Measurement Of The Primary Kaons For $\pi^+\pi^-$ And π^-p Events 171

7.5 Separation Of The Λ^0 Hyperon Events From The $\pi^- p$ Sample 176

7.6 In-Flight Contamination Of Σ Hyperon Events 181

7.7 Correction For $\Sigma^+ p$ And $\pi^- p$ Losses 181

7.8 Final Data 183

7.9 Determination Of The Gamma Ratio (Method I) 183

7.10 Determination Of The Gamma Ratio (Method II) 184

7.11 Conclusions 189

CHAPTER EIGHT

Discussion Of Results And K-Matrix Analysis

8.1 Channel Cross-Sections 191

8.2 Data Analysis 195

8.2.1 Constant Scattering Length Analysis 195

8.2.2 K-Matrix Parametrisations 200

8.2.3 Scattering Parameters 204

8.3 The $\Lambda(1405)$ Resonance 209

8.4 Summary Of The Results 210

8.5 Conclusion 210

APPENDICES 215

REFERENCES 223

ACKNOWLEDGEMENTS 227

LIST OF FIGURES

		Page No.
1.1	K^+p And K^-p Cross-Sections	2
2.1	Plan View Of B.N.H.B.C.	22
2.2	Schematic Diagram Of The Track Sensitive Target	23
2.3	Bubble Chamber Expansion Cycle	25
2.4	Typical Photograph From The Metal Framed Target	26
2.5	K19 Beamline	27
2.6	Template Used To Define The Scanning Fiducial Volume	34
2.7	Event Topologies	38
3.1	Flow Diagram Of The Event Processing Chain	54
4.1	Distribution Of Ranges For Sigmas With Unique Momentum	59
4.2	Distribution Of Stretch Functions Of Primary Kaons (Σ^-_π, Σ^+_p)	63
4.3	Distribution Of Stretch Functions Of Primary Kaons (Σ^+_π, Decays)	64
4.4	K^- Meson Decays; Secondary Particle Momentum Dependence On Kaon Momentum And Centre Of Mass Scattering Angle θ^*	66
4.5	χ^2 Probability Distributions For Charged Hyperon Production	67
4.6	χ^2 Proability Distributions For Unambiguous Kinematic Fits To Kaon Decays	68
4.7	Distribution Of Vertex Momenta For The Primaries Of One Prong Decays	74
4.8	Centre Of Mass Production And ϕ Angle Distributions For Decays	75
4.9	Kaon Decays: Two Dimensional Diagram Of Production Angles	77
4.10	Primary Path Length Distribution	79
4.11	Diagram Defining Variables Used To Study Errors Of Measurement	84
4.12	Difference Between Measured And Adjusted Momenta	87
4.13	Comparison Of Measured And Modified Reciprocal Momenta For K^- Decays	88

4.14	Modified Reciprocal Momentum Distributions	89
4.15	Reciprocal Momentum Errors	92
4.16	Schematic Representation Of The Relation Between Vertex And Centre Of Track Quantities	94
4.17	Theoretical And Observed r_c Distributions For K^- Decays	96
5.1	Production And Decay Angle Distributions ($\Sigma^-\pi$)	108
5.2	Production And Decay Angle Distributions ($\Sigma^+\pi$)	109
5.3	Production And Decay Angle Distributions (Σ^+p)	110
5.4	Distributions Of Proper Lifetime For Σ^- Hyperons	114
5.5	Distributions Of Proper Lifetime For Σ^+ Hyperons	115
5.6	Channel Cross-Section For Σ^- Production	121
5.7	Channel Cross-Section For Σ^+ Production	122
5.8	Kinematics Of Elastic Scattering	124
5.9	Production Angle Distributions For Elastic Scattering	126
5.10	Distribution Of Primary Momenta For Elastic Scatter Events With Short Tracks	129
5.11	Distribution Of ϕ_p Angles For Elastic Scattering Events With Short Secondary Tracks	130
5.12	Cross-Section For Elastic Scattering	133
5.13	Production And Decay Angle Distributions ($\Sigma^0\pi^0 + \Lambda^0\pi^0$)	136
5.14	Division Of Chamber To Investigate Losses Of Neutral Hyperons	138
5.15	Kinematics Of Neutral Hyperon Production	139
5.16	Distribution Of Proper Lifetimes For Λ^0 Hyperons	142
5.17	Cross-Section For Neutral Hyperon Production	145
5.18	Distribution Of Proper Lifetimes For Charge Exchange	147
5.19	Production And Decay Angle Distributions ($\overline{K}^0n$)	148
5.20	Cross-Section For Charge Exchange	151
6.1	Schematic Representation Of The Classification Of Hyperon Events Into Scanning Categories	158

6.2 Ionisation Energy Loss For Kaons In Liquid Hydrogen 165

7.1 Distributions Of K^- Momenta For $\pi^- p$ And $\pi^+ \pi^-$ Events 174
7.2 Distributions Of Primary Momenta For Collinear $\Sigma^{\pm}$ And Non-Collinear $\Sigma^{\pm}$ Events 175
7.3 Invariant Mass Squared vs Pion Momentum 179
7.4 Distributions Of Opening Angles And Pion Momenta For $\pi^- p$ Events 180
7.5 Triangular Plot Of The Fractions Of $\pi^+ \pi^-$, Σ^-_{π}, Σ^+_{π} Events 187

8.1 Summary Of Channel Cross-Sections Determined In The Present Work 192
8.2 Comparison Of The Channel Cross-Sections With The Results Of Martin 194
8.3 Kinematic Behaviour Of Channel Cross-Sections 196
8.4 Dynamic Behaviour Of Charged Hyperon Cross-Sections 197
8.5 Dynamic Behaviour Of Elastic Scattering Cross-Sections 198
8.6 Dynamic Behaviour Of Charged Exchange And Neutral Hyperon Cross-Sections 199
8.7 Results Of K-Matrix Parametrisation 206
8.8 Energy Dependence Of Scattering Parameters 207
8.9 Energy Dependence Of ϕ And γ 208

LIST OF TABLES

		Page No.
1.1	Summary Of Experimental Data	8
1.2	Summary Of K-Matrix Analyses	20
2.1	Properties Of The Materials Inside The Chamber	29
2.2	Critical Length Values In Hydrogen	31
2.3	Summary Of The Exposure Using The Metal Target	33
2.4	Scanning Summary	36
2.5	Scan Code	43
3.1	Summary Of Common Hypotheses Used In KINEMATICS	49
4.1	Range Determinations Of The μ^- And Σ^- Particles	60
4.2	Density Of Saturated Liquid Ne/H_2 Mixture	60
4.3	Stretch Distributions; Mean Values; Variances And Kurtoses	62
4.4	Results Of Scanning For Kaon Decays	72
4.5	Scanning Efficiencies For Kaon Decays	72
4.6	Summary Of Correction Factors Applied To The Measured Number Of One Prong Decays	76
4.7	Typical Values Of $\lambda(p)$ And $\Delta x(p)$	78
4.8	Path Length Distributions	80
4.9	Mean Co-ordinates Of Σ^-_π Events In Four Rolls Of Film	81
4.10	Path Length Normalisations For Each Channel	82
4.11	Relation Between p_v and $1/p_c$	86
4.12	Matrix For Converting 20 MeV/c p_v Intervals Into 0.1 $(GeV/c)^{-1}$ Intervals Of $1/p_c$	91
4.13	The Error Conversion Matrix, A_{err}	102
4.14	Estimation Of The Broadening Effect Of Measurement Errors	103
4.15	Summary Of Correction Factors To Allow For Errors Of Measurement And Their Effect On The Channel Cross-Sections	105

5.1 Summary Of Correction Factors For Charged Σ Production 116

5.2 Scanning Efficiencies For Charged Σ Production 119

5.3 Event Selection Summary (Charged Σ Production) 116

5.4 Charged Hyperon Production Cross-Sections 120

5.5 Loss Free Regions Of The Production Angle Distributions (Elastic Scattering) 125

5.6 Summary Of Correction Factors 128

5.7 Elastic Scattering Cross-Sections 131

5.8 Event Selection For Elastic Scatters

5.9 Division Of Neutral Hyperon Events Into Lifetime, Dip Angle And Chamber Depth Intervals 140

5.10 Summary Of Correction Factors And Event Selection For Neutral Hyperons 143

5.11 Neutral Hyperon Cross-Section 146

5.12 Summary Of Event Selection And Correction For The Charge Exchange Channel 149

5.13 $\overline{K^o}n$ Cross-Sections 150

6.1 Gamma Rato Determinations 154

6.2 Comparison Of The Nuclear Emulsion And Bubble Chamber Techniques 155

6.3 Topological Classifications Of Charged Σ Hyperon Production Reactions 157

6.4 Effect Of Range Cuts On $\pi^+ \pi^-$ Separation 161

6.5 Track Ionisations 162

6.6 Summary Of Scanning Categories 163

7.1 Scanning Results For The Gamma Ratio 169

7.2 Summary Of Corrections Applied To The Scanning Data 170

7.3 Compatibility Of Scan Code And Fitted Hypotheses 172

7.4 Scanning Efficiencies 171

7.5 Separation Of The In-Flight Event From The $\pi^- p$ And $\pi^+ \pi^-$ Categories 177

7.6 Comparison Of Template And Statistical Measurements For Separating In-Flight Events 176

7.7 Estimation Of Loss Due To Short Protons 182

7.8 Data For γ Ratio Determination: Number Of Corrected Events In Each Category 183

7.9 Fraction Of Proton Type Events 184

7.10 Minimum Observable Hyperon Length 185

7.11 Fractions Of $\Sigma^+\pi$, $\Sigma^-\pi$, And $\pi^+ \pi^-$ Events 186

7.12 Dependence Of γ And B As A Function Of The Number Of $\pi^+\pi^-$ Events 188

7.13 Summary Of The Determinations Of B 189

8.1 Scattering Length Solutions 201

8.2 Correlations Coefficients For CSL Fits 202

8.3 Number Of Data Points Used In Analyses 203

8.4 Contributions To The χ^2 203

8.5 Results Of Zero Range K-Matrix Parametrisation 205

8.6 Correlation Coefficients For ZER Fit To All The K + TST Data (I) 205

8.7 Mass And Widths Of Bound State Below Threshold 209

CHAPTER ONE

LOW ENERGY K^-p INTERACTIONS

1.1 Introduction

With the production of beams of kaons and pions in the early 1950's the studies of their interactions began in hydrogen, deuterium and heavier target nuclei. Since then a large number of experiments have been carried out and a vast amount of data has been analysed on meson interactions. Despite this in the low energy region, which is the subject of this thesis, the understanding of the K-meson interaction is less precise than that of the pion interaction for several reasons.

Firstly the endothermic interactions of pions are relatively simple there being only a pion and nucleon present in the secondary particles, whereas the exothermic kaon interaction is more complex and involves pions, nucleons, kaons and hyperons in the final states. Secondly, the experimental data for the pion interactions were acquired before those of the kaons because high intensity beams of pions were easier to produce (since in nuclear interactions pions and kaons are produced in the ratio of ~ 1000:1). Finally the rapid shift in research interest towards higher energies over the last decade has left a paucity of data in the low energy region of kaon nucleon interactions.

The complexity of the kaon interaction relative to that of the pion arises largely from the conservation of strangeness and the larger mass of kaons. These properties are instrumental in determining the final states available. In particular the former is responsible for the considerable difference between the interactions of the K^+ and the K^- mesons themselves (fig. 1.1).

The K^+ meson carries a positive strangeness and can interact only via its elastic scattering channel until sufficient primary

FIG. 1.1: K^+p and K^-p Cross-sections.

(Ref. 1)

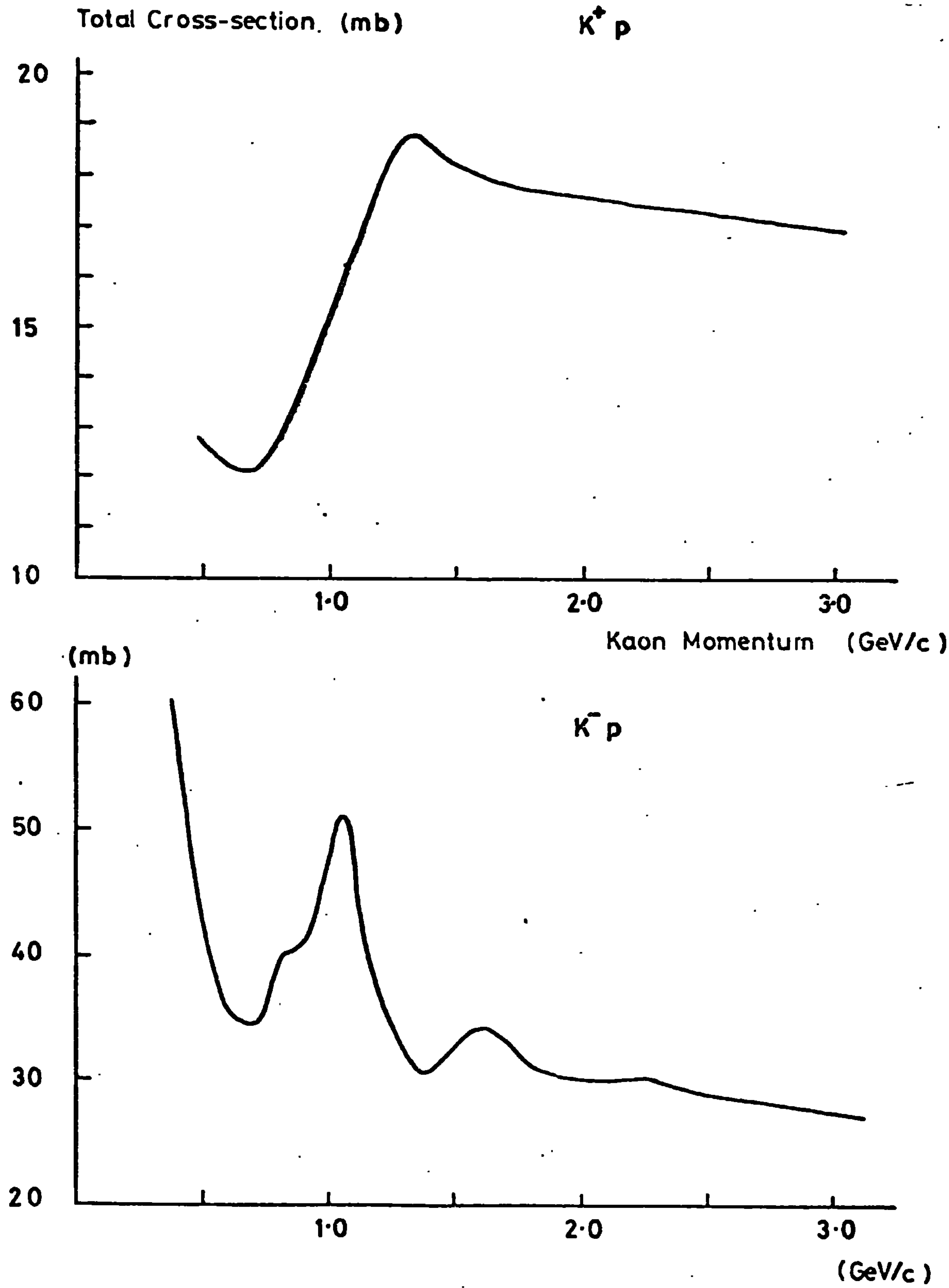

energies are reached for the production of other secondary particles.

The K^- meson has negative strangeness and there are several final states available at low momenta:

$K^- + p \longrightarrow K^- + p$		elastic scattering	(i)
$K^- + p \longrightarrow \overline{K^o} + n$		charge exchange	(ii)
$K^- + p \longrightarrow \Sigma^+ + \pi^-$	)	absorption	(iii)
$K^- + p \longrightarrow \Sigma^- + \pi^+$	)	reactions	(iv)
$K^- + p \longrightarrow \Sigma^o + \pi^o$	)	involving	(v)
$K^- + p \longrightarrow \Lambda^o + \pi^o$	)	charged hyperon	(vi)
$K^- + p \longrightarrow \Lambda^o + \pi^o + \pi^o$	)	production	(vii)

The mass difference between the K^-p and $\overline{K^o}n$ combinations give a threshold momentum of 90 MeV/c for channel (ii). In the remaining channels the final state mass is lower than that of the initial state allowing all to occur at zero kaon momentum.

The conservation of isospin limits the isospin of the final state to that of the initial state. The isospin of the combined K^-p system is 0 or 1 and channels (i) to (iv) are mixtures of these two states whereas the final states of channels (v,vii) and (vi) are pure isospin 0 and 1 respectively.

1.2 Motivation For The Study Of Low Energy K^-p Interactions

The reasons for examining the low energy K^-p interactions are several. Firstly there is a general lack of precise data in this region and with the current research interest lying in multi GeV interactions it seems unlikely that there will be a return to low energies. Furthermore, the data that does exist has been severely criticised; Martin (2) has used forward dispersion relations to link the kaon data from all energies and discrepancies clearly exist in the low momentum region. Also, the ratio, γ , of the production transition rates for Σ^- and Σ^+ at zero primary energy found by the bubble chamber technique (3) is significantly different from that found using nuclear emulsions (4). Any theoretical modelling below threshold (e.g. kaon interactions in nuclei leading to hyperfragments) has to rely mainly on one set of experimental data (3).

Secondly, the $\Sigma^0\pi^0$ and $\Lambda^0\pi^0$ production channels allow the pure isospin states 0 and 1 to be examined. An isospin 0 resonance e.g. the $\Lambda(1520)$, will be manifest only in the $\Sigma^0\pi^0$ production cross-section; correspondingly an isospin 1 resonance will be seen only in the $\Lambda^0\pi^0$ channel. In a bubble chamber these two channels are topologically identical and their separation relies upon using the missing mass squared of the events. In principle a good separation is possible but errors of measurement and background events such as $\Lambda^0\pi^0\pi^0$ introduce uncertainties to this method. Unambiguous separations of the two channels can be made if the γ-ray (originating from the π^0 or Σ^0 decays) conversions into e^+e^- pairs are detected and measured.

Thirdly, there are resonances in kaon interactions (5). Low energy experiments were responsible for the discovery of the well established $\Lambda(1520)$ and the deduction of the $\Lambda(1405)$. The latter lies below the K^-p threshold and its presence is inferred from the extrapolation of the low energy K^-p scattering parameters into the non-physical region. In the higher energy regions the $\Sigma(1480)$ resonance is doubtful (6) and the P_{01} (1570) resonance suggested by Kim (7) also needs confirmation. Recently Bowen et al (8) have reported a structure in the I = 1 total cross-section at $\sim$ 580 MeV/c kaon momentum and Carroll et al (9) have reported a possible $\Sigma(1580)$ resonance.

A final point of interest is the onset of P wave interference in the angular distributions. The D wave is dominant at 390 MeV/c (10) and is the result of the $\Lambda(1520)$, the P wave is believed to have little effect below approximately 280 MeV/c. The onset of this interference is important in determining the validity of the S wave K-matrix analyses.

1.3 Aims Of The Present Experiment

The experiment was designed to examine the K^-p interaction in the 0 - 600 MeV/c momentum region using a neon filled main chamber with a smaller hydrogen filled track sensitive target (T.S.T.) placed inside the main chmaber. The experiment may be divided into three phases. Firstly, the T.S.T. technique has to be shown to work and this is done by analysing the data in the region of the $\Lambda(1520)$ and calibrating the experiment by checking the results with those of Mast et al (10). This involved identifying and correcting losses and biases generated by the geometry of the T.S.T. system. The use of the γ -ray conversions to separate the pure isospin channels $\Sigma^0\ \pi^0$ and $\Lambda^0\ \pi^0$ was also studied. This stage of the work is now complete (11, 12).

The second phase is the examination of interactions at rest and below 300 MeV/c. This is the region of the S wave interaction covered by the data of Kim. The aims are to resolve the discrepancy between the two most precise determinations of the γ ratio, to measure the interaction cross-sections for all channels and perform a K-matrix analysis. This second phase is the subject of the present thesis.

The final phase is a detailed study of the interactions between 410 and 600 MeV/c where there is a lack of data and a need to check the existence of possible resonances in this region. When this data is obtained it will be possible to complete a global phase shift analysis from $\sim$350 MeV/c upwards on statistics of $\sim$1500 events /mb/ 25 MeV/c.

In particular the existence of the Σ resonances can be checked by examining the I = 1 cross-sections and they will also be evident in the phase shift amplitudes. This part of the work is currently in progress.

1.4 Bubble Chambers And K^-p Interactions

At low momenta the secondaries produced by K^-p interactions travel only a few centimeters ($\lesssim 5$ cm) before decaying or coming to rest inside the chamber. The bubble chamber, with a spatial resolution of ~ 1 mm and with good visibility over the full 4π solid angle, is the only adequate means of detecting such interactions at low momentum. However, the bubble chamber is not without its difficulties. At low momenta the main problem is the accuracy with which the kaon momentum may be measured; this accuracy is limited severely by coulomb scattering (see §2.4).

The low cycling rate for bubble chambers (~ 1 cycle/sec) together with the small number of beam tracks per picture (usually 5 - 15) makes the data collection rate extremely low for events with small cross-sections. Assuming 10 m of track length per picture, a 10 μb cross-section will produce only 400 events in 10^6 pictures! This is not a problem for K^-p interactions with 10 - 80 mb cross-sections but serves to illustrate the usefulness of counter experiments which are faster and more selective in their data aquisition.

The conventional hydrogen bubble chamber is also a poor detector of γ-rays and the long conversion length (~ 10 m in H_2) makes it unlikely that more than a few events will exhibit $e^+ e^-$ pairs arising from γ-ray conversion. Ideally a liquid with a short conversion length e.g. xenon should be used, however the target is no longer a free proton but a mixture of neutrons and protons. In this situation background events become a severe problem and the coulomb scattering is very much worse than for hydrogen. The poor γ-ray conversion makes certain channels difficult to resolve (e.g. $K^-p \longrightarrow \Lambda^0 \pi^0$ and $K^-p \longrightarrow \Sigma^0 \pi^0$) although this can be partially overcome with the T.S.T. type of chamber.

1.5 Review Of The Experimental Data

In the momentum region below ~ 300 MeV/c there are three main experiments. Humphrey and Ross (13) and Kim (3) have examined all the reaction channels while Sakitt et al (14) present data on elastic scattering and charged hyperon production only. All three experiments use an S wave K-matrix analysis to fit to their data.

Humphrey and Ross found that the reaction channels are strongly coupled and the behaviour in a single channel affects the other channels via the constraint of unitarity. The elastic nuclear scattering amplitude is almost entirely imaginary and interferes little with the real coulomb amplitude. The simple S wave zero-effective range parametrisation (i.e. energy independent K-matrix elements) was sufficient to describe the data.

Sakitt concluded that the angular distributions were essentially isotropic and predicted an S wave bound state of the $\overline{K}N$ system at 1405 MeV based on the K-matrix analysis: these results agree with those of Kim. The experimental review is best summarised in tabular form and the major experiments since 1958 are shown in Table 1.1. together with the number of events used in each analysis. The results of the K-matrix analyses are presented in Table 1.2. at the end of section 1.7.

1.6 Theoretical Review

The first description of the K^-p system used the S wave effective range expansion which can be written as follows:

$$k \cot \delta = \frac{1}{A} + \frac{1}{2} Rk^2$$

where δ is the phase shift, A the scattering length, R the effective range of the nuclear potential and k is the centre of mass momentum of the incident channel. Both A and R are complex parameters and are different for each partial wave and for each isospin state. The zero effective range approximation removes the energy dependence of the

TABLE 1.1

Summary of Experimental Data

First Author	ref	Date	Exp't	Momentum MeV/c	Number of Events Analysed						K-matrix	Comments
					K^-p	$\overline{K^o}n$	$\Sigma^+\pi^-$	$\Sigma^-\pi^+$	$\Sigma^o\pi^o$	$\Lambda^o\pi^o$		
Ascoli	15	1958	Em	70 - 272	51	-	-	-	-	-	No	
Nordin	16	1961	HBC	300 & 400	117	6	28	10	18		No	K^- lifetime determined $= 1.31\times10^{-8}$ secs.
Humphrey	13	1962	HBC	75 - 275	419	24	101	111	327		Yes	Also presented are: Ratios of charged and neutral hyperon product-ion rates at zero momentum; Σ^+, Σ^- and Λ^o lifetimes; differential cross-section for elastic scattering; nuclear elastic scattering amplitude.
Watson	17	1963	HBC	250 - 513	~5000	~5000					Yes	Identification of the Λ(1520).
Sakitt	14	1965	HBC	60 - 300	1496	-	328	460	-	-	Yes	Also presented:elastic scattering angular distributions.
Abrams	18	1965	HBC	90 - 250	-	80	-	-	-	-	No	$\overline{K^o}n$ data are consistent with bound state below threshold.
Csejthey-Barth	19	1965	Em	50 - 200	129	-	-	-	-	-	No	γ ratio= 2.6 at ~ 90 MeV/c and 1.2 at ~ 160 MeV/c
Kim	3	1965	HBC	80 - 300	4141	233	964	1647	1600		Yes	γ ratio= 2.06 at zero momentum, also presented are elastic scattering differential cross-sections. Bound state is predicted below threshold.
Schlosser	20	1965	HBC	100 - 360	2549	-	-	-	-	-	No	Also gives elastic scattering differential cross-section
Kittel	21	1966	HBC	100 - 300	-	191	-	-	-	-	No	

Table 1.1 Continued

First Author	ref	Date	Exp't	Momentum MeV/c	Number of Events Analysed K^-p	$\overline{K^0}n$	$\Sigma^+\pi^-$	$\Sigma^-\pi^+$	$\Sigma^0\pi^0$	$\Lambda^0\pi^0$	K-matrix	Comments
Thomas	22	1969	Em	0 - 250	45	-	-	-	-	-	Yes	
Berley	23	1970	HBC	350 - 430	-	?	-	-	?	?	Yes	Approx. 60,000 events analysed.
Tovee	4	1971	Em	0	-	-	-	-	-	-	No	γ ratio determination at zero momentum. γ = 2.34.
Mast	10	1975	HBC	220 - 450	-	-	-	-	57,000		No	Legendre polynomial fits to differential cross-section.
Mast	24	1976	HBC	220 - 470	64,600	22,800	-	-	-	-	NO	Partial wave fits to differential cross-sections.
Nowak	25	1978	HBC	0	-	-	-	-	-	-		γ ratio determination, γ = 2.38.

scattering length by putting R = 0. For K^-p interactions only four parameters (two for isospin 0 and two for isospin 1) are required to describe the data in the S wave case.

Dalitz and Tuan (26) formulated a K-matrix parametrisation of the $\bar{K}N$ system which automatically satisfies the conditions of unitarity and time reversal invariance. Suitable approximations to this theory yield the zero effective range theory formulated by Jackson et al (27). All low energy K^-p cross-sections and branching ratios may be expressed in terms of only two complex parameters A_0 and A_1 (the scattering length for the isospin 0 and 1 states respectively) and two real parameters ϕ, a phase, and ϵ a cross-section ratio. (See §1.7 for precise definitions).

Shaw and Ross (28) also developed a multi-channel theory using an M-matrix which is essentially the inverse of the K-matrix developed by Dalitz and Tuan.

More recently Martin (2) has carried out a dispersion relation analysis of the $\bar{K}N$ system. Data on K^+p and K^-p forward elastic scattering (29) allows the real parts of the nuclear scattering amplitudes to be calculated. This may be done using coulomb nuclear interference to calculate the ratio of the real and imaginary parts of the nuclear amplitude and the total cross-section to find the imaginary part using the optical theorem. The high energy dispersion relations were extrapolated to the K^-p threshold where it was found that the real part of the scattering amplitude (from the high energy dispersion relations) did not agree with the real part as calculated using the low energy K-matrix parameters.

It is clear that K-matrix theory is important in the study of low energy K^-p interactions and it is described in detail below.

1.7 K-Matrix Analysis

1.7.1 Relation Between K-Matrix and T-Matrix

The low energy K^-p cross-sections are significant fractions of the geometrical cross-section which is given by $\pi ƛ^2$ where $ƛ$ is the De Broglie wavelength of the incident kaon. In this situation the requirements imposed by the conservation of probability (unitarity) become restrictive and give rise to complicated relationships between the characteristics of the reaction processes and scattering processes in all of the initial and final states connected by these reactions.

The amplitudes for the various reaction and scattering processes may be conveniently parametrised by the elements of a K-matrix; these elements represent the dynamics involved in these processes. The amplitudes obtained from the K-matrix automatically satisfy the unitarity constraints. Time reversal invariance requires that the matrix is symmetric which when combined with the hermitian property implies that all the K-matrix elements are real. This halves the number of parameters and makes this approach an economical method of parametrisation.

Scattering is usually defined in terms of the T-matrix; the scattering is considered as an incoming plane wave in the incident channel i and outgoing spherical waves in each production channel j. The asymptotic form of the wave function is

$$\phi^T_{ij} = \delta_{ji} \frac{\sin k_j r}{k_j r} + T_{ij} \frac{e^{ik_j r}}{r} \qquad 1.1$$

where T_{ij} are the T-matrix elements and k_j are the centre of mass momenta of the outgoing channels. Equation 1.1 applies to the S wave incident and outgoing channels only.

The diagonal elements of the T-matrix are related to the phase shift (δ) and absorption parameter (η) in the following way

$$T_{ii} = \frac{1}{2i}(\exp\,(2i\delta_i)\eta_i - 1) \qquad 1.2$$

The reaction cross-section is related to the T-matrix elements by

$$\sigma(i \longrightarrow j) = 4\pi \frac{k_j}{k_i} (J + \tfrac{1}{2}) \left| T_{ij} \right|^2 \qquad 1.3$$

where J is the total angular momentum of the final state.

The K-matrix differs from the T-matrix by the nature of its boundary conditions. The scattering may be regarded as a plane wave in the incident channel and standing spherical waves in each production channel. The asymptotic form is now

$$\phi^K_{ij} = \delta_{ij} \frac{\sin k_j r}{k_j r} + K_{ij} \frac{\cos k_j r}{r} \qquad 1.4$$

Using these different asymptotic forms the relationship between the T and K-matrix is found to be

$$T = (1 - ikK)^{-1}K \qquad 1.5$$

Equation 1.5 (derived in appendix A) may be used to calculatc the T-matrix elements in terms of the K-matrix elements, then knowing the relationship between T and the measurable cross-sections (equation 1.3) the K-matrix elements can be used to describe the experimental results.

1.7.2 Application Of K-Matrix To The $\overline{K}N$ System

The K-matrix formalism will be developed initially by assuming charge independence and by neglecting coulomb effects. The corrections introduced by these effects will be discussed separately.

The low energy $\overline{K}N$ system may be regarded as a three channel system, $\overline{K}N$, $\Sigma\pi$ and $\Lambda\pi$ where

$\overline{K}N = K^-p, \overline{K^o}n$	denoted by K in the following formalism
$\Sigma\pi = \Sigma^+\pi^-, \Sigma^o\pi^o, \Sigma^-\pi^-$	denoted by Σ " " "
$\Lambda\pi = \Lambda^o\ \pi^o$	" " Λ " " " "

These channels are mixtures of isospin states 1 and 0 and there are two real symmetric K-matrices thus:

$$K^1 = \begin{pmatrix} \beta_K & \beta_{K\Sigma} & \beta_{K\Lambda} \\ \beta_{K\Sigma} & \beta_\Sigma & \beta_{\Sigma\Lambda} \\ \beta_{K\Lambda} & \beta_{\Sigma\Lambda} & \beta_\Lambda \end{pmatrix} \qquad K^0 = \begin{pmatrix} \alpha_K & \alpha_{K\Sigma} \\ \alpha_{K\Sigma} & \alpha_\Sigma \end{pmatrix} \tag{1.6}$$

where α_K is the K-matrix element for the isospin zero transition $\bar{K}N \longrightarrow \bar{K}N$; the other elements are given in obvious notation. Three body channels (e.g. $\Lambda\,\pi\,\pi$) are neglected, their available phase space being small.

The isospin 1 matrix may be partitioned as follows:

$$K^1 = \left(\begin{array}{c|cc} \beta_K & \beta_{K\Sigma} & \beta_{K\Lambda} \\ \hline \beta_{K\Sigma} & \beta_\Sigma & \beta_{\Sigma\Lambda} \\ \beta_{K\Lambda} & \beta_{\Sigma\Lambda} & \beta_\Lambda \end{array}\right) = \begin{pmatrix} \alpha & \beta \\ \beta^\dagger & \gamma \end{pmatrix} \tag{1.7}$$

β, $\beta^\dagger$ and γ are themselves matrices. This partitioning allows both isospin states to be treated as a two channel system.

The T-matrix may be written in the same form as the K-matrix using:

$$T^1 = \begin{pmatrix} T^1_K & T^1_{K\Sigma} & T^1_{K\Lambda} \\ T^1_{K\Sigma} & T^1_\Sigma & T^1_{\Sigma\Lambda} \\ T^1_{K\Lambda} & T^1_{\Sigma\Lambda} & T^1_\Lambda \end{pmatrix} \qquad T^0 = \begin{pmatrix} T^0_K & T^0_{K\Sigma} \\ T^0_{K\Sigma} & T^0_\Sigma \end{pmatrix} \tag{1.8}$$

Equation 1.5 can be used to find the relation between the T and K-matrix elements; (see appendix B) which, for the physically accessible reactions, leads to:

$$T^0_K = \frac{A_0}{1 - ik_K A_0} \qquad T^0_{K\Sigma} = \frac{M_0}{1 - ik_K A_0}$$

$$T_K^1 = \frac{A_1}{1 - ik_K A_1} \qquad\qquad T_{K\Sigma}^1 = \frac{M_1}{1 - ik_K A_1} \qquad 1.9$$

and $$T_{K\Lambda}^1 = \frac{N_1}{1 - ik_K A_1}$$

where k_K is the centre of mass momentum of the incident kaon, A_0 and A_1 are the complex scattering lengths and M_0 M_1 and N_1 are complex constants. All of these may be expressed in terms of the K-matrix elements (see appendix B).

In practice M_0 M_1 and N_1 are not used but two ratios are defined as follows:

(i) $$\epsilon = \frac{\sigma(\bar{K}N \longrightarrow \Lambda\pi)}{\sigma_1} = \frac{k_\Lambda |N_1|^2}{k_\Sigma |M_1|^2 + k_\Lambda |N_1|^2} \qquad 1.10$$

ϵ is the ratio of the cross-section for $\Lambda^0\pi^0$ production to the total isospin 1 hyperon production cross-section σ_1, k_Σ and k_Λ are the centre of mass momenta of the Σ and Λ hyperons respectively.

(ii) $$\phi = \arg\left(T_{K\Sigma}^0 / T_{K\Sigma}^1\right) \qquad 1.11$$

This is the relative phase of the S wave $\Sigma\pi$ production amplitudes for the I = 0 and I = 1 states.

The final stage in this formalism is to relate A_0, A_1, ε and ϕ to the observable cross-sections. This is done by decomposing each $\overline{K}N$ state into its isospin 0 and 1 parts using the Clebsh-Gordon coefficients.

$$
\begin{aligned}
|K^-p\rangle &= \frac{1}{\sqrt{2}}\left(|\phi_K^1\rangle + |\phi_K^0\rangle\right) \\
|\overline{K^o}n\rangle &= \frac{1}{\sqrt{2}}\left(|\phi_K^1\rangle - |\phi_K^0\rangle\right) \\
|\Sigma^+\pi^-\rangle &= \frac{1}{\sqrt{6}}\left(|\phi_\Sigma^2\rangle + \sqrt{3}|\phi_\Sigma^1\rangle + \sqrt{2}|\phi_\Sigma^0\rangle\right) \\
|\Sigma^-\pi^+\rangle &= \frac{1}{\sqrt{6}}\left(|\phi_\Sigma^2\rangle - \sqrt{3}|\phi_\Sigma^1\rangle + \sqrt{2}|\phi_\Sigma^0\rangle\right) \\
|\Sigma^o\pi^o\rangle &= \frac{\sqrt{2}}{\sqrt{3}}\left(|\phi_\Sigma^2\rangle - \frac{1}{\sqrt{2}}|\phi_\Sigma^0\rangle\right) \\
|\Lambda^o\pi^o\rangle &= |\phi_\Lambda^1\rangle
\end{aligned}
\qquad 1.12
$$

where $|\phi_K^I\rangle$ is the wave function of the $\overline{K}N$ system with isospin I (similarly for the $\Sigma\pi$ and $\Lambda\pi$ systems) and $|K^-p\rangle$ etc. are the wave functions of the final states available in K^-p interactions.

The transition matrix elements are then:

$$
\begin{aligned}
\langle K^-p|T|K^-p\rangle &= \frac{1}{2}(T_K^1 + T_K^0) \\
\langle K^-p|T|\overline{K^o}n\rangle &= \frac{1}{2}(T_K^1 - T_K^0) \\
\langle K^-p|T|\Sigma^+\pi^-\rangle &= \frac{1}{2}T_{K\Sigma}^1 + \frac{1}{\sqrt{6}}T_{K\Sigma}^0 \\
\langle K^-p|T|\Sigma^o\pi^o\rangle &= \frac{-1}{\sqrt{6}}T_{K\Sigma}^0 \\
\langle K^-p|T|\Sigma^-\pi^+\rangle &= \frac{-1}{2}T_{K\Sigma}^1 + \frac{1}{\sqrt{6}}T_{K\Sigma}^0 \\
\langle K^-p|T|\Lambda^o\pi^o\rangle &= \frac{1}{\sqrt{2}}T_{K\Lambda}^1
\end{aligned}
\qquad 1.13
$$

The use of equation 1.3 allows the matrix elements to be related directly to the observable cross-sections to give the following results (see appendix C for details).

$$\sigma(K^-p) = \pi\left|\frac{A_1 + A_0 - 2ik_K A_1 A_0}{(1 - ik_K A_1)(1 - ik_K A_0)}\right|^2$$

$$\sigma(\overline{K^o}n) = \pi\left|\frac{A_1 - A_0}{(1 - ik_K A_1)(1 - ik_K A_0)}\right|^2$$

$$\sigma(\Sigma^{\pm}\pi^{\mp}) = \frac{1}{6}\sigma_0 + \frac{1}{4}\sigma_1(1 - \varepsilon) \pm \sqrt{\frac{1}{6}\sigma_0\,\sigma_1(1 - \varepsilon)}\cos\phi$$

$$\sigma(\Sigma^o\pi^o) = \frac{1}{6}\sigma_0$$

$$\sigma(\Lambda^o\pi^o) = \frac{1}{2}\varepsilon\,\sigma_1$$

where

$$\sigma_1 = \frac{4\pi k_\Sigma |M_1|^2}{k_K|1 - ik_K A_1|^2} + \frac{4\pi k_\Lambda |N_1|^2}{k_K|1 - ik_K A_1|^2}$$

$$\sigma_0 = \frac{4\pi k_\Sigma |M_0|^2}{k_K|1 - ik_K A_0|^2}$$

$$\varepsilon = \frac{k_\Lambda|N_1|^2}{k_\Sigma|M_1|^2 + k_\Lambda|N_1|^2}$$

$$\phi = \arg\left(\frac{A_0}{1 - ik_K A_0}\Big/\frac{A_1}{1 - ik_K A_1}\right)$$

The complex constants A_0 A_1 etc. are related to the K-matrx elements (see appendix B) in the following way:

$$A_0 = \alpha_K + \frac{ik_\Sigma\alpha_{K\Sigma}^2}{1 - ik_\Sigma\alpha_\Sigma} \qquad M_0 = \frac{\alpha_{K\Sigma}}{1 - i\alpha_\Sigma k_\Sigma}$$

$$A_1 = \beta_K + \frac{1}{W_1}(\beta_{K\Sigma}W_2 + \beta_{K\Lambda}W_3)$$

$$M_1 = \frac{1}{W_1} \left(\beta_{K\Sigma} + ik_\Lambda(\beta_{\Sigma\Lambda}\beta_{K\Lambda} - \beta_{K\Sigma}\beta_\Lambda) \right)$$

$$N_1 = \frac{1}{W_1} \left(\beta_{K\Lambda} + ik_\Sigma(\beta_{K\Sigma}\beta_{\Sigma\Lambda} - \beta_{K\Lambda}\beta_\Sigma) \right) \qquad 1.14$$

where $W_1 = (1 - ik_\Sigma\beta_\Sigma)(1 - ik_\Lambda\beta_\Lambda) + k_\Lambda k_\Sigma \beta_{\Sigma\Lambda}^2$

$$W_2 = k_\Sigma k_\Lambda(\beta_{K\Sigma}\beta_\Lambda - \beta_{\Sigma\Lambda}\beta_{K\Lambda}) + ik_\Sigma\beta_{K\Sigma}$$

$$W_3 = k_\Sigma k_\Lambda(\beta_{K\Lambda}\beta_\Sigma - \beta_{\Sigma\Lambda}\beta_{K\Sigma}) + ik_\Lambda\beta_{K\Lambda}$$

The above results refer to the charge independent treatment of the $\overline{K}N$ system. The corrections introduced by taking into account charge dependence and the mass difference between the final state particles are discussed below.

1.7.3 Corrections for Charge Dependent Effects

These effects are the K^-p coulomb interaction and the mass differences within the multiplets; the corrections are complex and a detailed description of the theory is given by Dalitz and Tuan (26). Only the effect of these corrections on the results quoted in 1.7.2 will be presented here.

Every occurance of the factor $\dfrac{1}{1 - ik_K A_{0,1}}$ is replaced by another factor $\dfrac{1 - ik_K A_{0,1}}{D}$, and each cross-section is multiplied by an s wave coulomb penetration factor $C^2 = \dfrac{2\pi}{k_K B}\left(1 - \exp\left(-\dfrac{2\pi}{k_K B}\right)\right)^{-1}$

where B = the Bohr radius of the K^-p system (84 fm.).

k_K = the K^-p centre of mass momentum.

$$D = 1 - \frac{1}{2} i(A_0 + A_1)[k_U + kC^2(1 - i\lambda)] - k_0 kC^2(1 - i\lambda)A_0 A_1$$

k_0 = the $\overline{K^o}$ centre of mass momentum; taken as $i\,|k_0|$ below threshold.

$$\lambda = \frac{2}{kBC^2}\left[\log_e(2kR) + \mathcal{R}e\left(\psi\left(\frac{i}{kB}\right)\right) + 2\gamma\right]$$

γ = Euler constant (0.5772).

and $\psi(Z) = \Gamma'(Z) / \Gamma(Z)$ where Γ is a gamma function.

R is the matching radius (taken as 0.4 fm) where the coulomb and nuclear interactions are comparable. Incorporating these alterations into the cross-section for elastic scattering gives:

$$\frac{d\sigma}{d}(K^-p) = \left| \left[2k^2B \sin^2\left(\frac{\theta}{2}\right)\right]^{-1} \exp\left(\frac{2i}{KB} \log_e \sin\left(\frac{\theta}{2}\right)\right) + \frac{C^2}{2D}(A_0 + A_1 - 2ik_0A_0A_1) \right|^2$$

The first term is the coulomb scattering and is dominant in the forward scattering region, the second term represents the nuclear scattering amplitude and is independent of the scattering angle. The remaining results are as follows:

$$\sigma(\overline{K^o}n) = \frac{\pi k_0 C^2}{k_K} \left| \frac{A_1 - A_0}{D} \right|^2$$

$$\sigma_I = \frac{4\pi\, b_I\, C^2}{k_K} \left| \frac{1 - ik_0\, A_I}{D} \right|^2$$

where b_I is the imaginary part of the scattering length A_I. The phase angle ϕ becomes

$$\phi = \phi_{th} + \arg\left(\frac{1 - ik_0A_1}{1 - ik_0A_0}\right)$$

ϕ_{th} is the phase angle at the $\overline{K^o}n$ threshold (= arg (M_0/M_1)).

In practice, the important corrections are for the $\overline{K^o}n$ and K^-p mass differences, which ensures the correct threshold behaviour for $\sigma(\overline{K^o}n)$, and the coulomb penetration factor C. The parameter λ, derived from the overlap of the wave functions, is small and makes little difference to the K-matrix analysis. In the present work D was simplified to neglect λ as shown below:

$$D = 1 - \frac{1}{2} i(A_0 + A_1)\,[k_0 + kC^2] - k_0kC^2 A_0 A_1$$

A summary of the results of the main K-matrix analyses is given in Table 1.2 where the symbols are as defined in the above text.

1.8 Outline of Thesis

The present work is a study of the low energy data from ~ 15 rolls of film and the following results are presented.

(i) Interaction cross-sections for K^-p, $\overline{K^o}n$, $\Sigma^+\pi^-$, $\Sigma^-\pi^+$ and ($\Sigma^o\pi^o$ + $\Lambda^o\pi^o$) channels in the momentum range $\sim$ 100-300 MeV/c.

(ii) K-matrix parameters for the present data.

(iii) A determination of the ratio (γ) of the production rates of charged hyperons at zero kaon momentum.

During the presentation of the results, problems peculiar to low energy interactions are also discussed.

Chapters two and three are devoted to the description of the Bubble Chamber and the subsequent data collection and processing. The next two chapters present the calibration and the analysis procedure used to obtain the results for the channel cross-sections. This is followed in Chapters six and seven by the discussion and results of the γ ratio determination which was carried out as a separate experiment.

The final chapter presents the results of the K-matrix analysis and conclusions.

Table 1.2 : Summary of K-Matrix Analyses

Author	ref	reference symbol	$A_0 = a_0+ib_0$ a_0	b_0	$A_1 = a_1+ib_1$ a_1	b_1	ε	γ	ϕ_{th}°
Humphrey, Ross	13	HR I	-0.22	2.74	0.02	0.32	0.40	2.15	94
		HR II	-0.59	0.96	1.2	0.56	0.39	2.04	-50
Dalitz, Tuan	26	DT (a+)*	0.2	0.8	1.6	0.4			
		DT (a-)	-0.3	1.6	-1.0	0.18			
		DT (b+)*	1.6	1.6	0.7	0.22			
		DT (b-)	-1.8	0.6	-0.33	0.5			
Watson	17	W I	-0.08	3.13	0.02	0.46	0.29		-104
Sakitt	14	S I	0.75	1.13	-0.85	0.15	0.48	2.19	74
		S II	-1.63	0.51	-0.19	0.44	0.31	2.11	-57
Kim	3	K I	-1.67	0.72	-0.00	0.68	0.32	2.09	-53.8
		K II	-0.65	1.54	-0.85	0.16	0.49	2.46	70.5
Thomas	22	TJ I	-1.10	0.55	-0.2	0.44			
		TJ II	-1.10	0.55	-0.5	0.44			
Martin, Ross	30	MR	-1.74	0.70	0.07	0.62	0.34		-52.9

* correspond to constructive coulomb nuclear interference

CHAPTER TWO

Experimental Details I

The following two chapters describe the parts of the experiment and the subsequent data processing that are relevant to the current work; more detailed descriptions of the experiment are given in earlier work (11, 12, 31).

2.1 The Bubble Chamber

The experiment was carried out using the British National Hydrogen Bubble Chamber (fig. 2.1) having dimensions of 1.50 x 0.45 x 0.50 metres. This chamber was modified with a view to detecting the conversions of gamma rays into the electron - positron ($e^+ e^-$) pairs in order to make an improved separation of the $\Lambda^o\pi^o$ and $\Sigma^o\pi^o$ production channels.

A track sensitive target (T.S.T.) of size 1.35 x 0.33 x 0.075 metres was placed inside the main chamber (fig. 2.2). This small chamber contained liquid hydrogen at a temperature of 29.5°K and acted as a target for the K^- mesons. The outer chamber contained a mixture of neon and hydrogen (78% of neon by number) at a temperature of 29.8°K. This Ne/H_2 mixture provided a gamma ray conversion length of ~40cm. The side walls of the T.S.T. were made from 1.0 cm thick perspex which was transparent and allowed both chambers to be photographed. The perspex also allowed the gamma rays and secondary particles to pass from the inner to the outer chamber.

The operating conditions were chosen to ensure that the liquid hydrogen in the target and the Ne/H_2 mixture in the outer chamber were sensitive to charged particles simultaneously. This placed severe restrictions on the composition of the Ne/H_2 mixture and the conversion length, which depends on this composition, was about 45 cm compared to a theoretical minimum of ~25 cm.

The temperature difference between the chamber and target was maintained by separate cooling loops, however only a single expansion

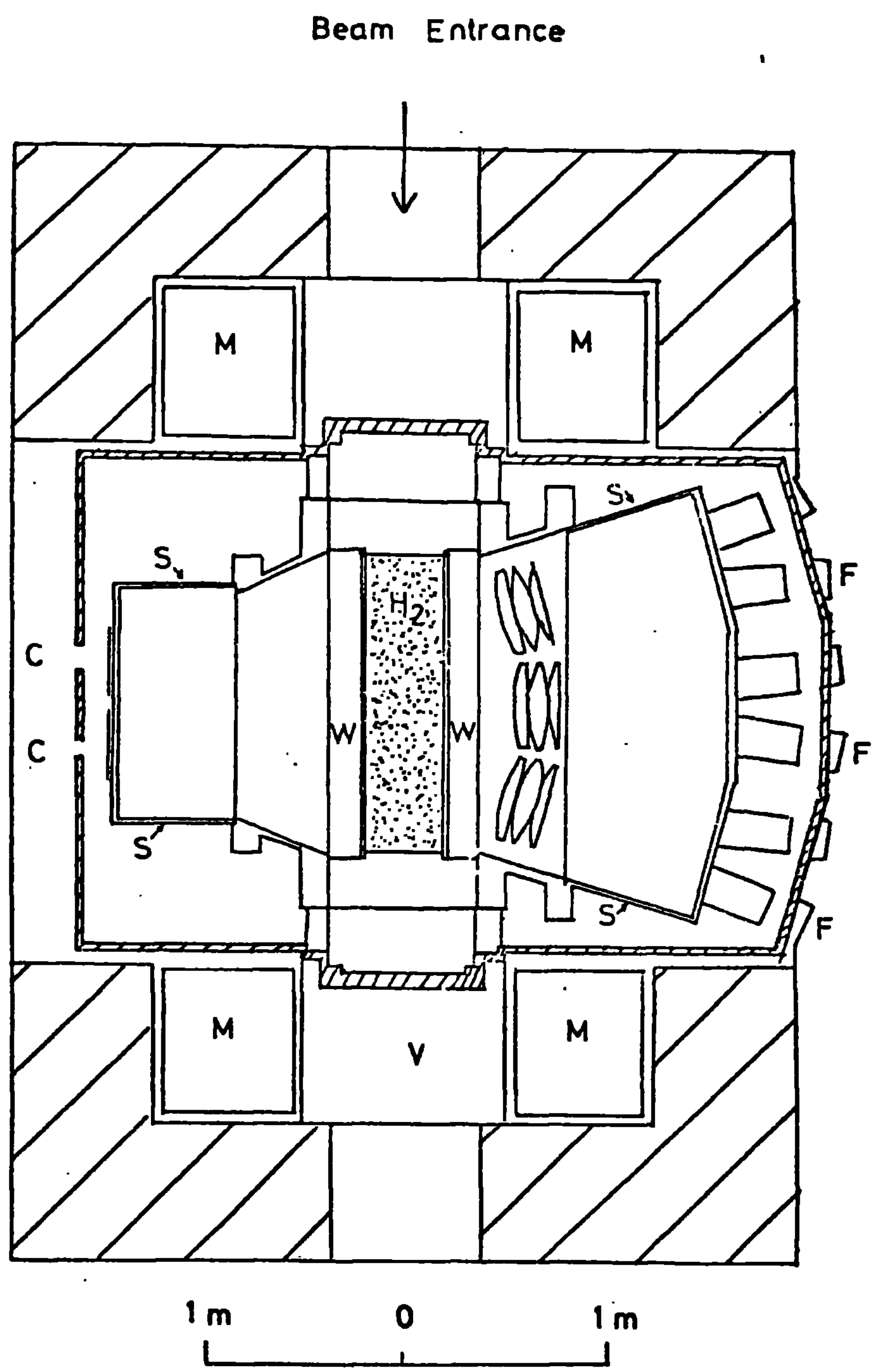

C = Camera
F = Flash
M = Magnet

S = Shield of Hydrogen
V = Vacuum
W = Window

FIG 2.1: PLAN VIEW OF B.N.H.B.C.

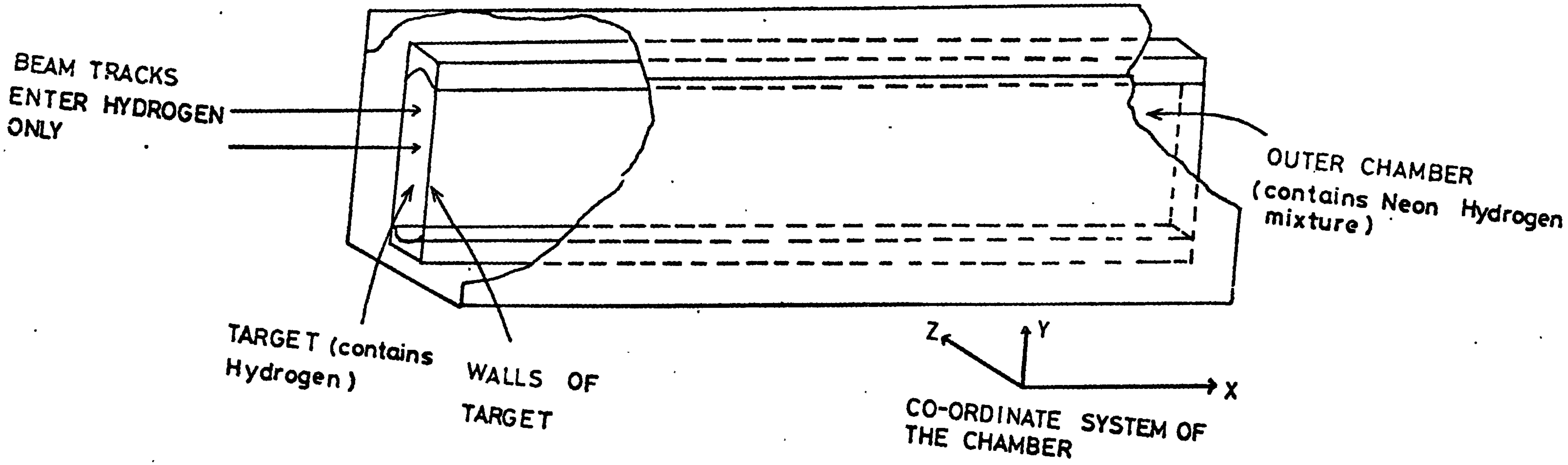

FIG 2.2: SCHEMATIC DIAGRAM OF THE TRACK SENSITIVE TARGET

mechanism was required. The perspex interface was sufficiently flexible to transmit the pressure variations from the outer chamber to the target; the displacement was $\sim 500\mu m$ and this ensured that the liquids were track sensitive simultaneously.

The expansion cycle is shown schematically in fig. 2.3. A timing pulse arrived $\sim$ 30 ms before the entry of the beam into the chamber in order to allow apparatus to be triggered. The actual expansion started 15 ms before the beam arrival and the chamber became sensitive to charged particles when the static pressure of the liquid was lower than the liquid vapour pressure. The bubbles produced by the charged particles were allowed to grow for ~ 1.5 ms before being photographed using electronic flash tubes for illumination. The static pressure was then reapplied to collapse the bubbles and prepare for the next cycle. Bubbles were typically $250\mu m$ in diameter as deduced from the film. This large size was produced by the diffraction pattern around the bubble caused by the small camera aperture used; this small aperture was necessary to ensure an adequate depth of focus over the whole chamber.

Two types of T.S.T. were used in the experiment. The first consisted of two flexible perspex walls sealed to a steel frame which in turn was connected to the main chamber. This metal frame being opaque reduced the observable volume of the chamber and also the γ-ray detection efficiency. The second T.S.T. was constructed entirely out of perspex and hence removed these problems. A typical photograph from the metal framed target is shown in fig. 2.4. The crosses are fiducial reference points engraved onto the Ne/H_2 side of the perspex walls and onto the inside of the chamber windows. These fiducials were used to produce a three dimensional reconstruction of each event.

2.2 The Beamline And Beam Entry Into The Chamber

The K19 beamline at the Rutherford Laboratory was used for this experiment (fig. 2.5). The 7 GeV/c protons produced by NIMROD struck a

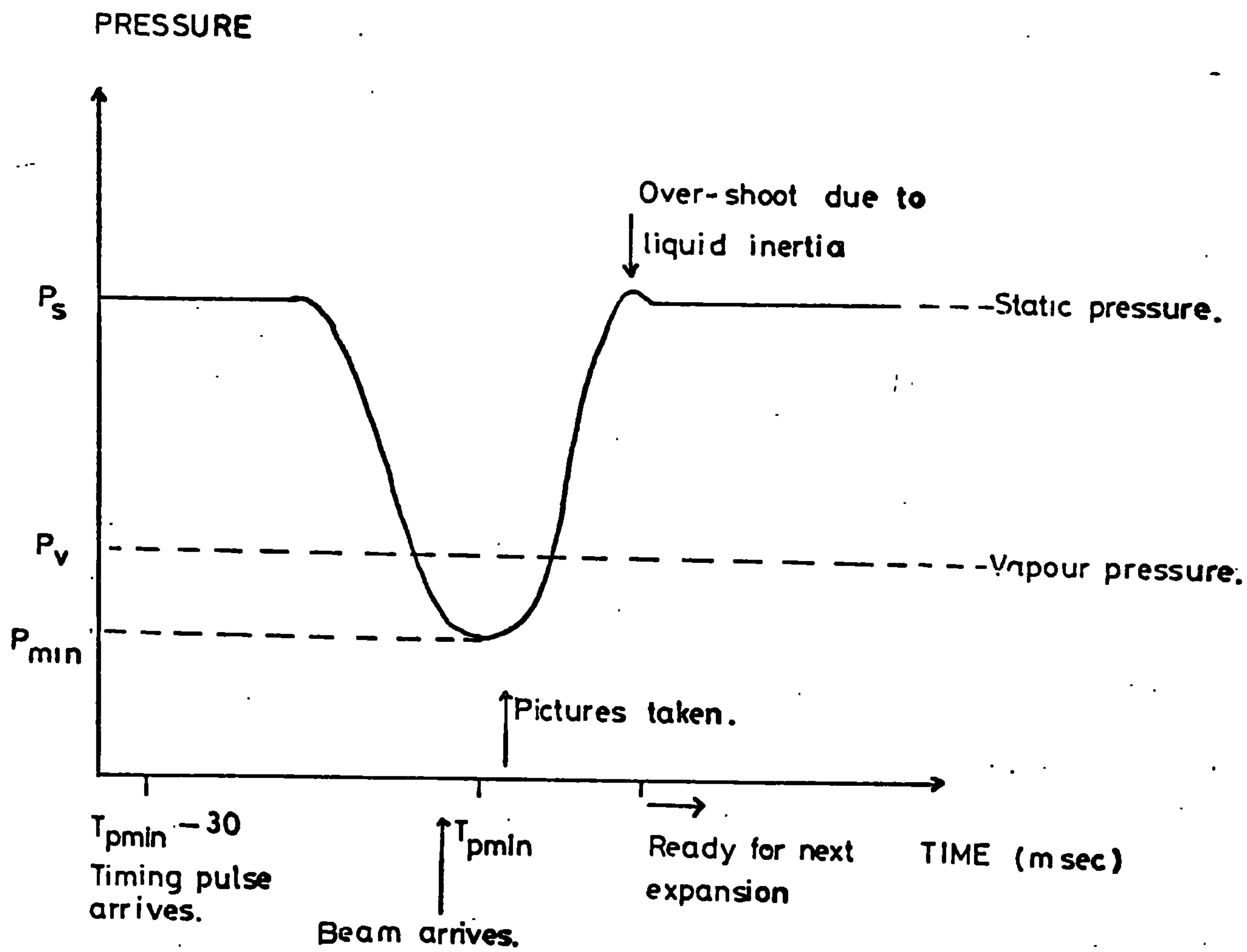

FIG 2.3: BUBBLE CHAMBER EXPANSION CYCLE.

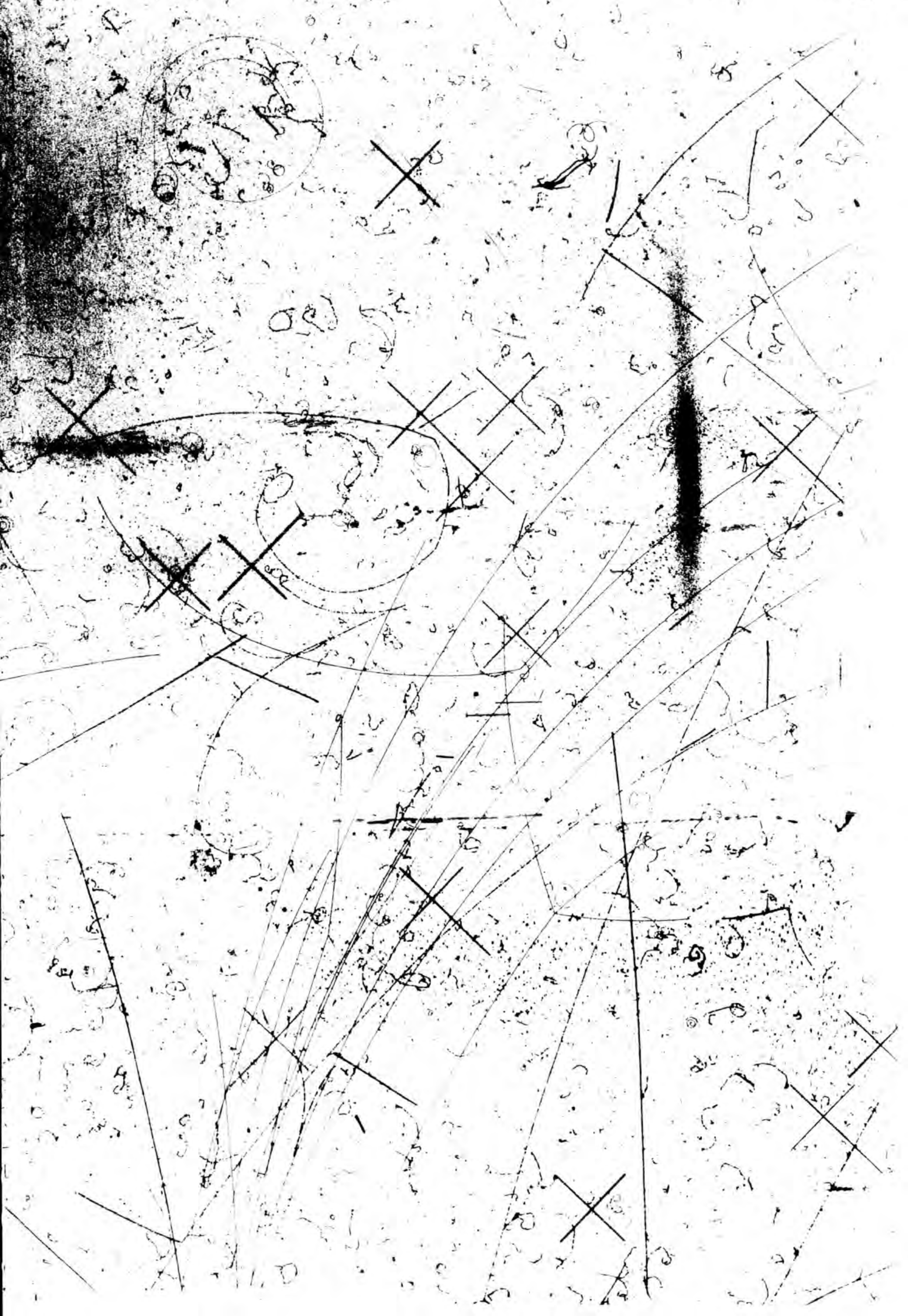

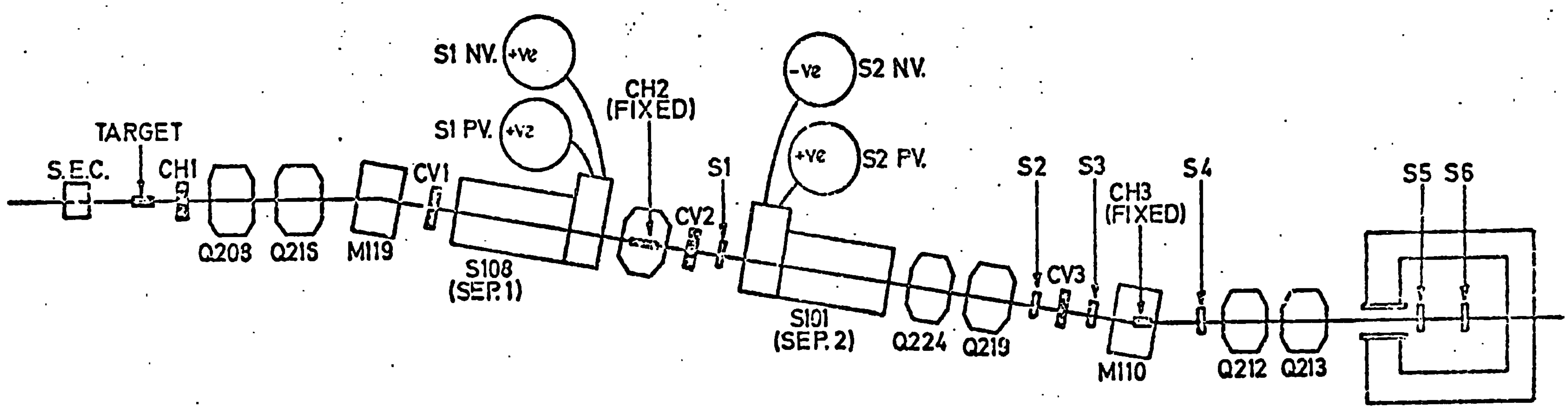

FIG 2.5: K19 BEAM LINE.

copper target to produce mainly protons, and kaons. An initial flux of 6 x 10" protons / pulse produced about 30 kaons at the entry port of the chamber. The separation of the kaons from the particle beam was effected by a momentum selection using a bending magnet (M119) and by mass selection using electrostatic separation (S108, S101). The beam was focussed at various points along its path by pairs of quadrupole magnets; one pair horizontally and the other vertically (Q208, Q216, Q224, Q219).

For this experiment the incident momentum of the beam should lie between the 0 and 600 MeV/c. At these momenta time dilation is insufficient to prevent the kaons decaying before arriving at the chamber. The beam was actually transported at 700 MeV/c and slowed down by ionisation energy loss in an aluminium degrader placed at the chamber entrance. The thickness of the degrader was varied to produce the correct beam momentum in the centre of the chamber. The entire chamber was placed in a magnetic field of 12.2 Kgauss having a direction approximately along the camera line of sight. An extra bending magnet was placed at the entry port to compensate for the fringe field.

The degrader spreads the beam both in space and in momentum. It added to the background of muons and pions entering the chamber. The background without the presence of the degrader would be due only to kaons decaying after the final mass separation stage. The background with the degrader was typically 25%. however at low momenta there is a sufficiently large difference in the track ionisations of the various particles to enable unambiguous selection of kaon beam tracks.

2.3 Limitations Of The T.S.T. Chamber

The introduction of T.S.T. into the bubble chamber introduced several problems associated with the physical size of the target.

(i) The depth ($\sim$ 8 cm) introduces detection biases for certain classes of event. For example the visibility of the Λ^0 hyperon in a conventional bubble chamber is limited mainly by the ability to separate the decay vee of the Λ^0 from the primary vertex. At low momenta the decay length of the hyperon is typically 2-3 cm and this is commensurate with the chamber depth. Many hyperons will decay outside the hydrogen target and the decay vees will appear in the Ne/H_2 mixture where the measuring precision is considerably poorer. Corrections for events lost in this manner must be carefully evaluated.

(ii) The classification of charged hyperon events usually require a secondary decay process to be observed. Hyperons striking the perspex walls before decaying will appear topologically different and events of this type will be classified differently. This problem may have to be corrected for by making fiducial volume adjustments to ensure that the decay products are visible.

(iii) The perspex walls of the T.S.T. offer a considerable stopping power and interaction cross-section to kaons (Table 2.1). At low momenta, beams entering the perspex will either stop or interact in flight. This is not serious for events with charged secondaries; however for the neutral channels (zero prong events) with an associated vee there will be ~ 50% contamination from interactions in perspex. These events are impossible to distinguish from genuine hydrogen interactions on the basis of topology alone and they need to be measured before they can be identified and rejected from the sample of events used in the analysis.

Table 2.1 : Properties Of The Materials Inside The Chamber

Medium	Density gm cm^{-3}	Interaction Length (cm)	Radiation Length (cm)	Stopping Power Relative to H_2	Thickness (cm)
Hydrogen	0.063	~ 450	~ 990	~ 1	8
Perspex	1.2	~ 50	~ 35	~ 9	2
Ne/H_2 Mixture	0.635	~ 110	~ 45	~ 4.5	37

2.4 Precision Of Measurement

There are two main factors which limit the measuring precision;

the first is the reduced track length imposed by the dimensions of the T.S.T. and the second is multiple coulomb scattering which is particularly important at these low momenta. It is extremely important to know when the errors are dominated by coulomb scattering particularly as it is likely to impose a limit on the measurable momenta.

A particle track is measured at several points along its curved path on each of three views. These measurements are reconstructed in three dimensions to give values for the radius of curvature, the angle of dip relative to the plane normal to the line of sight and the azimuthal angle relative to the forward direction. All of these values are calculated at the track centre and it is the measurement of the radius of curvature which determines the particle momentum.

The effect of random measuring errors on the value of momentum is

$$\left(\frac{\Delta p}{p}\right)_m \sim \frac{7.8 f_o p}{0.3\ HL^2}$$

and the effect of coulomb scattering is given by

$$\left(\frac{\Delta p}{p}\right)_c \sim \frac{45}{\beta H \sqrt{\mathcal{X}_o L}}$$

where f_o = accuracy of the measuring system transformed into chamber space ($\sim$ 0.01 cm).

H = magnetic field (Kgauss).

L = track length (cm).

p = particle momentum (MeV/c).

β = particle velocity /c.

$\mathcal{X}_o$ = radiation length of medium (990 cm for hydrogen).

The factor 7.8 in the first expression arises from the three dimensional track reconstruction and the 45 in the second equation is the multiple coulomb scattering constant for hydrogen.

These errors become comparable when

$$\frac{7.8 f_o p}{0.3\ HL^2} \sim \frac{45}{\beta H \sqrt{\mathcal{X}_o L}}$$

$$\text{i.e. } L_p \sim 0.315(p\beta)^{2/3} \text{ cm}$$

This gives the critical length above which coulomb scattering dominates. Typical values of L_p in hydrogen are given in Table 2.2.

Table 2.2 : Critical Length Values In Hydrogen

Momentum (MeV/c)	Kaon Velocity $\beta_K = p/E$	L_p (cm)	$\Delta p/p$ %	Pion Velocity β_π	L_p (cm)	$\Delta p/p$ %
100	0.198	2.3	40	0.581	4.7	10
150	0.291	3.9	21	0.731	7.2	6
200	0.375	5.6	13	0.819	9.4	5
250	0.451	7.4	9	0.872	11.4	4
300	0.519	9.1	8	0.906	13.2	4
350	0.629	12.6	5	0.944	16.5	3
400	0.772	18.9	2	0.974	22.0	2

In the present momentum region (~300 MeV/c) coulomb errors are clearly dominant. The error on the momentum of the kaon is particularly large below ~150 MeV/c and this shows that there is a basic limitation in the bubble chamber technique. Detailed error analyses are required if cross-sections below ~150 MeV/c are to be obtained.

Coulomb scattering is stronger in the Ne/H_2 mixture, consequently the values of L_p are smaller than those in Table 2.2 and hence the problems in the mixture are even more severe than for the hydrogen. Measurements in the Ne/H_2 mixture were made when there was only a short track length available in the hydrogen. Many baryon tracks came to rest in the Ne/H_2 mixture and the particle ranges could be used to give precise momentum determinations.

The remaining measured quantities dip angle (λ) and azimuthal angle (ϕ) are also affected by coulomb errors and their critical lengths are

$$L_\lambda = 0.584\ (p\beta)^{2/3}$$

and

$$L_\phi = 0.467\ (p\beta)^{2/3}$$

The values of L_λ and L_ϕ are similar to those obtained for L_p.

2.5 The Exposure

This took place at the Rutherford Laboratory during August and November 1973. 433,000 photographs were taken in the first run using the metal framed target with beam momenta in the range 0 - 445 MeV/c. The second run with an all perspex target produced 47,000 pictures with beam momenta 240 - 580 MeV/c.

A summary of the first run is given in Table 2.3. The entire data were divided between four collaborating laboratories; University College, London; Birmingham University; Université Libre du Bruxelles and Durham University. During the course of the experiment Warsaw University joined the collaboration. The data were divided so that each laboratory possessed a sample from the entire momentum range.

2.6 Scanning

The film was projected onto a table top to produce an approximately lifesize image of the event. A fiducial volume, fixed relative to the chamber walls, was defined on the second view by a gridded template (fig. 2.6). Each beam track entering the volume was examined and followed until it

(i) left the fiducial volume

(ii) left the T.S.T. through the perspex walls, giving a clear continuation track in the Ne/H_2 mixture

(iii) interacted inside the volume

(iv) decayed inside the volume

The primary interaction was required to lie within the volume but the secondary processes such as vees and γ-ray conversions were allowed to lie in any visible region.

Table 2.3 : Summary Of The Exposure Using The Metal Target

Block No.	Roll No's.	Frames	No. Of K^-/Frame	Entry Momentum (MeV/c)	Exit Momentum (MeV/c)
1	1 - 105	229,000	5	260	0
2	106 - 126	54,000	8.4	315	235
3	127 - 147	45,000	10.1	370	320
4	148 - 168	54,000	12.3	405	370
5	169 - 188	51,000	8.8	445	410

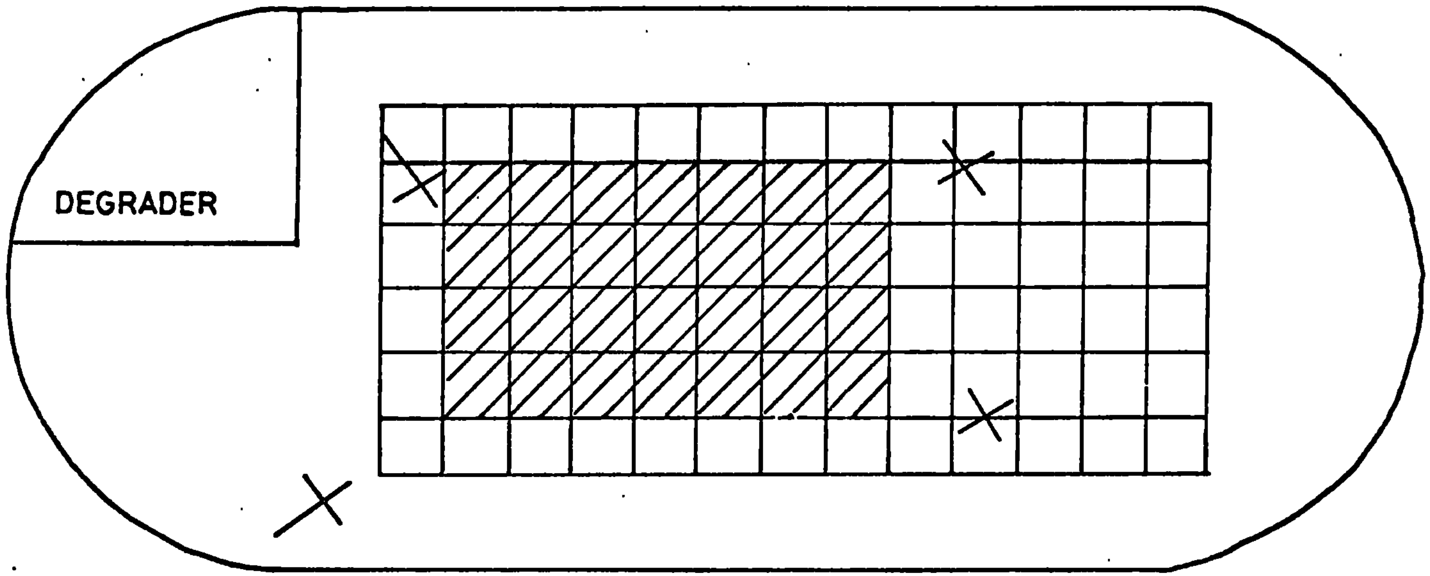

Shaded area defines the fiducial volume used in the present work.

FIG 2.6: TEMPLATE USED TO DEFINE THE SCANNING FIDUCIAL VOLUME.

The scanning for the current work was carried out on four separate occasions. The first occasion was to obtain the data for the γ ratio determination, this scan was the Durham/Warsaw contribution to the data used in the γ ratio determination (see § 6.3). The remaining scanning was carried out in different laboratories on different occasions; this merely reflects the fact that the data were collected so as to provide a complete coverage of all the low energy K^-p interaction channels for the cross-section determinations. All the scanning was repeated to enable the double scan efficiencies to be calculated. The four scans were as follows:

(i) A general scan of 5 rolls of film (1 roll = 2,600 frames) for charged sigma hyperon production and charge exchange channels. This scanning which was carried out in Durham by the Warsaw group comprised ~ 1/3 of the total data used in the γ ratio determination. This data was also used in the channel cross-section determinations.

(ii) A scan for charged hyperon, elastic scattering and charged exchange channels. This covered 8 rolls of film and was scanned entirely by the Warsaw group in Warsaw.

(iii) A separate scan for the neutral hyperon channels was carried out by the Brussels group (2½ rolls of film). The 5 rolls of film scanned in the γ ratio work was partially scanned by the London group for neutral hyperon channels. A few second scans were carried out in Durham.

(iv) A complete scan of 7½ rolls for kaon decays. This was done in Durham for the purposes of path length normalisation. The 8 rolls of film from scan (ii) were normalised using other means (see §4.5).

The summary of the scanning is shown in Table 2.4, the data divide into three groups and will be called the Durham, Warsaw and Brussels data for easy reference.

The scanning for the γ ratio determination was carried out in a reduced fiducial volume in order to remove any biases caused by

Table 2.4 : Scanning Summary

Channel	Durham (5 Rolls)	Warsaw (8 Rolls)	Brussels ($2\frac{1}{2}$ Rolls)
$K^-p \longrightarrow K^-p$	No	Yes	No
$K^-p \longrightarrow \Sigma^+\pi^-$	Yes	Yes	No
$K^-p \longrightarrow \Sigma^-\pi^+$	Yes	Yes	No
$K^-p \longrightarrow \Sigma^0\pi^0$	No	No	Yes
$K^-p \longrightarrow \Lambda^0\pi^0$			
$K^-p \longrightarrow \overline{K^0}n$	Yes	Yes	No
$K^- \longrightarrow \mu^-\bar{\nu}_\mu$	Yes	No	Yes
$K^- \longrightarrow \pi^-\pi^0$	Yes	No	Yes
$K^- \longrightarrow \pi^+\pi^-\pi^-$	Yes	No	Yes

poor visibility near the chamber edges. The other scans were carried out over larger fiducial volumes, however only the reduced fiducial volume was used in this work. The differences in the scanning and processing procedures that were adopted for the γ ratio determination will be mentioned where appropriate in chapters six and seven. A general description of the event recognition is given in the following section.

2.7 Event Recognition

Events are classified according to their topology (i.e. their appearance); in the present work the topologies of different physical channels are often distinct and only a few ambiguities arise.

The topology of an event can be described using a three digit coded thus:

$$\text{Topology} = N_1\ N_2\ N_3$$

where N_1 is the number charged particles produced at the primary vertex,

N_2 is the number of decay kinks in the track of a particle having strangeness,

N_3 is the number of vees associated with the primary vertex.

The precise meaning of this code will become clearer in the following discussion.

2.7.1 $K^-p \longrightarrow \Sigma^+\pi^-$, $\Sigma^+ \longrightarrow p\pi^0$ or $\Sigma^+ \longrightarrow n\pi^+$ Topology = 210

This type of event is shown in fig. 2.7; the Σ^+ hyperon decays by two possible modes and these may distinguished by the difference in ionisation of the decay particle. A dark unbroken track indicates the proton decay mode whilst a light, broken track indicates the pion mode. The ionisation of the Σ^+ hyperon is always high and all hyperon tracks are dark and unbroken. These events may also be divided into "collinear" and "non-collinear" categories; the collinear events which have a 180° opening angle between the secondaries are comprised mainly of kaon interactions at rest where the conservation of momentum forces the secondaries to travel in opposite directions with equal momenta.

FIG 2·7: EVENT TOPOLOGIES.

APPEARANCE	CHANNEL(S)		SCAN CODE	TOPOLOGY
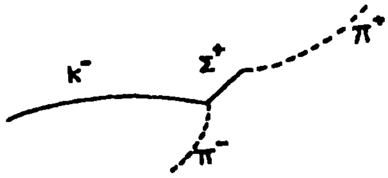	$K^- p \to \Sigma^+ \pi^-$ $\hookrightarrow n\pi^-$	Σ^-_π	221200 222200	210
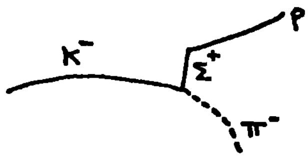	$K^- p \to \Sigma^+ \pi^-$ $\hookrightarrow p\pi^\circ$	Σ^+_p	221100 222100	210
	$K^- p \to \Sigma^- \pi^+$ $\hookrightarrow n\pi^-$	Σ^-_π	211200 212200	210
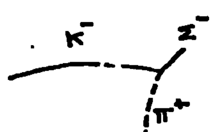	$K^- p \to \Sigma^- \pi^+$ $\downarrow$ $\Sigma p \to$ neutrals	Σ^-_σ	211300 212300	200
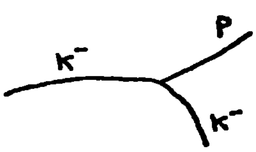	$K^- p \to K^- p$	KS	1000000	200
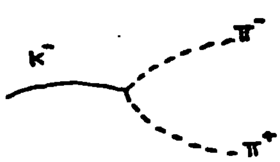	$K^- p \to \Sigma^{+} \pi^-$, $\Sigma^+ \to n\pi^+$ $K^- p \to \Sigma^- \pi^-$, $\Sigma^- \to n\pi^-$ $K^- p \to \overline{K^\circ} n$, $\overline{K^\circ} \to \pi^+\pi^-$	$\pi^+\pi^-$	200010	200
	$K^- p \to \Sigma^+\pi^-$, $\Sigma^+ \to p\pi^\circ$ $K^- p \to \Lambda^\circ\pi^\circ$, $\Lambda^\circ \to p\pi^-$ $K^- p \to \Sigma^\circ\pi^\circ$, $\Sigma^\circ \to \Lambda\gamma$, $\Lambda \to p\pi^-$	$\pi^- p$	200020	200
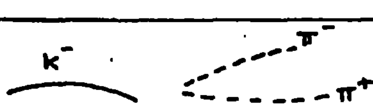	$K^- p \to \overline{K^\circ} n$, $\overline{K^\circ} \to \pi^+\pi^-$	$\overline{K^\circ}$	000002	001
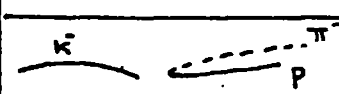	$K^- p \to \Lambda^\circ \pi^\circ$, $\hookrightarrow p\pi^-$ $K^- p \to \Sigma^\circ \pi^\circ$ $\hookrightarrow \Lambda^\circ \gamma$ $\hookrightarrow p\pi^-$	Λ°	000001	001
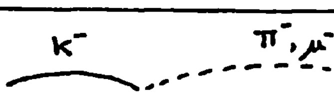	$K^- \to \pi^\circ \pi^-$ $K^- \to \bar{\nu}_\mu \mu^-$	1 prong decay.	100000	100
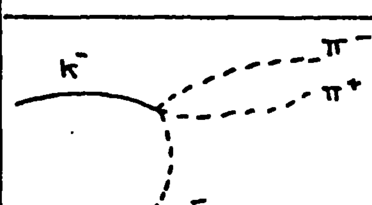	$K^- \to \pi^+\pi^-\pi^-$	tau decay.	300000	300

2.7.2 $K^-p \longrightarrow \Sigma^-\pi^+,\ \Sigma^- \longrightarrow n\pi^-$ Topology = 210

This reaction is similar in appearance to the Σ^+ production reaction (fig. 2.7). The negative hyperon however has only one decay mode. Collinearity is also a feature of this channel.

2.7.3 $K^-p \longrightarrow \Sigma^-\pi^+,\ \Sigma^-p \longrightarrow$ neutrals Topology = 200

The Σ^- hyperon may interact in flight, enter the perspex wall of the T.S.T. or be captured by a proton on coming to rest in the hydrogen (fig. 2.7). No decay products are seen and this event is seen as a simple two prong. When a vee is associated with end point of the Σ^- hyperon this is classified as a 201 topology.

2.7.4 $K^-p \longrightarrow K^-p$ Topology = 200

These events have the positive tracks travelling in the forward direction; both of the secondary tracks are heavily ionising and will generally appear darker than the beam track (fig. 2.7). The positive track is sometimes difficult to see, its length being ~ 1 mm. Many elastic scatters produce protons of momentum $\lesssim 100$ MeV/c which are difficult to see and often invisible. These events appear as 1 prongs (topology = 100) and are recorded as elastic scatters with an unseen proton. The scattered kaon often interacts for a second time, this was recorded but only the primary interaction was used in the analysis for the total cross-sections.

2.7.5 Two Prong Events Topology = 200

The main types of two prong event (fig. 2.7) may be classified into two groups. The $\pi^+\pi^-$ event has two lightly ionising secondaries and may arise from four reaction channels.

(i) The Σ^+ hyperon channel where the Σ^+ decays into a π^+n close to the primary vertex making the Σ^+ track invisible.

(ii) The Σ^- hyperon channel.

(iii) The $\overline{K^0}n$ production channel, the $\overline{K^0}$ decaying into $\pi^+\pi^-$ close to the vertex leaving no visible gap.

(iv) The production of $\Lambda^0\pi^+\pi^-$; the phase space for this channel is severely limited at low momenta and its contribution to the total $K^- p$ cross-section is negligible.

The $\pi^- p$ event has a heavily ionising positive track and may arise from:

(i) Σ^+ production with Σ^+ decaying into $p\pi^0$ close to the primary vertex

(ii) Σ^+ production when the Σ^+ decays in the forward direction; the invisible decay kink will cause the event to be classified a $\pi^- p$.

(iii) Σ^0 or Λ^0-hyperon production where the associated vee lies close to the vertex.

2.7.6 <u>Zero Prongs With A Neutral Vee</u> <u>Topology = 001</u>

This topology includes the following channels (see fig. 2.7)

$$K^- + p \longrightarrow \Lambda^0 + \pi^0, \quad \Lambda^0 \longrightarrow p + \pi^0$$

$$K^- + p \longrightarrow \Sigma^0 + \pi^0, \quad \Sigma^0 \longrightarrow \Lambda^0 + \gamma,$$

$$\Lambda^0 \longrightarrow p + \pi^-$$

$$K^- + p \longrightarrow \overline{K^0} + n, \quad \overline{K^0} \longrightarrow \pi^+ + \pi^-$$

The decay vee of the neutral particle was required to lie within two grid squares (~ 20 cm) of the primary vertex. This ensured efficient scanning over a small region of space; time dilation of the decay length was insufficient to cause any losses over this distance (at 400 MeV/c the Λ^0 decay length is ~ 2.8 cm).

The vees from the Λ^0 hyperons differ from those of the $\overline{K^0}$ meson by the ionisation of the positive track; the latter having a light and broken appearance indicating a π^+ meson. On finding a Λ^0 type vee, a further search was carried out for γ-ray conversions which could occur anywhere in the chamber volume including the Ne/H_2 mixture.

2.7.7 <u>One Prong Events</u> <u>Topology = 100</u>

The following are the most common decay modes of the K^- meson:

$$K^- \longrightarrow \mu^- + \bar{\nu}_\mu \qquad 63.5\ \%$$

$$K^- \longrightarrow \pi^- + \pi^0 \qquad 21.16\ \%$$

$$K^- \longrightarrow \pi^- + \pi^0 + \pi^0 \qquad 1.73\ \%$$

$$K^- \longrightarrow \mu^- + \bar{\nu}_\mu + \pi^0 \qquad 3.20\%$$

$$K^- \longrightarrow e^- + \bar{\nu}_e + \pi^0 \qquad 4.82\%$$

These are easily detected (see fig. 2.7) as there is always a noticeable ionisation change at the primary vertex.

2.7.8 Three Prong Events — Topology = 300

Tau decay of the K^- meson is extremely distinctive (fig. 2.7) and contributes 5.59% to the total decay rate. The three secondaries are lightly ionising, however care must be taken to eliminate Dalitz pairs from this topology since confusion may arise from the decay

$$K^- \longrightarrow \pi^- + \pi^0$$
$$\hookrightarrow \gamma + \gamma$$
$$\hookrightarrow e^+ + e^-$$

The π^0 has a short lifetime ($\sim 0.8 \times 10^{-16}$ sec) and an immediate conversion of one of the γ-rays into an $e^+ e^-$ pair produces a three prong event. Electrons are usually considerably more lightly ionising than the pions. If the positive pion is seen to decay into $\mu^+ + \nu_\mu$ followed by $\mu^+ \longrightarrow e^+ + \nu_e + \bar{\nu}_\mu$, the tau decay is positively identified.

The slight neon comtamination in the pure hydrogen (due to diffusion through the perspex interface) produces multi-prong events which often simulate a three prong event. Usually the tracks are short ($\sim$ 1 $\rightarrow$ 2 mm) and heavily ionising which makes the identification of these events straight forward.

2.8 Data Recording And Scanning Codes

Each event found inside the fiducial volume was given a scan code which assigned a physical channel to the event where possible.

This scheme was developed for the γ ratio determination and was extended to include all channels for the cross-section work. The seven digit scan code was constructed as shown in Table 2.5. The elastic scatter part of the code was added arithmetically to the remaining six digits to allow the recording of secondary events which occurred after the scatter. This precise coding was used when judging events after measurements and provided a method for automatic judging and remeasuring (see §3.3).

The data for each event were recorded as follows:

(i) Frame Number.

(ii) Event number; usually there was more than one event per frame.

(iii) The zone of the event obtained from the gridded squares on the fiducial volume template.

(iv) Scan code.

(v) The zones of any γ-ray conversions.

These data formed the basis of the book-keeping system called MASTERLIST and this system was used to control all subsequent data processing.

2.9 Preselection Of Data Before Measurement

In order to reduce the total amount of measuring, a preselection was applied to certain types of event which were not of interest.

2.9.1 Neutral Hyperon Production

As mentioned earlier in §2.3 there is a high probability that a zero prong event occurs in the perspex wall of the target. The majority of these were removed by a simple two view comparison test. This involved checking the position of the primary vertex relative to the fiducial crosses marked on the T.S.T. walls. The effect of perspective causes the vertices inside the chamber to shift this relative position when the view point is altered; for vertices inside the perspex walls this position remains unaltered by changing the view. This effect was easily seen using a simple template and ~ 40% of all recorded zero prongs were removed by this test which was applied to the Durham film sample (5 rolls).

Table 2.5 : Scan Code

Digit Number	Name	Values	Meaning
1	Elastic Scatter Code	1	If 1st interaction $K^-p \longrightarrow K^-p$
		2	If 1st and 2nd interactions were $K^-p \longrightarrow K^-p$.
			If no elastic scatter this digit was omitted.
2	Prong Code	n	n is the number of charged secondaries (does not apply to elastic scatters).
3	Sigma Hyperon Code	0	If no Σ is seen.
		1	If a Σ^- is seen.
		2	If a Σ^+ is seen.
4	Collinearity Code	0	For non $\Sigma^{\pm}$ events.
		1	If event is collinear.
		2	If event is non-collinear.
5	Sigma Decay Code	0	For non $\Sigma^{\pm}$ events.
		1	For proton Decay.
		2	For pion decay.
		3	For no seen decay.
6	Two Prong Identification Code	0	For non $\pi^+\pi^-$, π^-p events.
		1	For $\pi^+\pi^-$ events.
		2	For π^+p events.
7	Vee Identification Code	0	If no vee is seen.
		1	If vee is a Λ^o decay.
		2	If vee is a $\overline{K^o}$ decay.

For the Brussels sample of film (2½ rolls) this was not carried out, however a momentum selection was made using a beam profile template. (The construction of a template is described later in § 6.9). This template selected events having a residual range of $\gtrsim 3$ cm corresponding to a kaon momentum of ~ 120 MeV/c and was imposed to remove the large number of interactions occurring at zero kaon momnentum. These events were about five times more numerous than the in-flight interactions and not of interest in the cross-section calculations.

2.9.2 Collinear Sigma Production

In-flight Σ hyperon production events generally appear non-collinear in configuration, however for forward and backward Σ production all events are collinear irrespective of the incident kaon momentum. In order to ensure that in-flight events were not lost, a template selection was made on all collinear events where the hyperon was produced within 45° of the kaon direction. Of these events, those having a residual range $\gtrsim 3$ cm were included for measurement. A template selection was also made for events where the hyperon track was short and collinearity was difficult to assess accurately. These selections were included for measurement to ensure that a complete sample of in-flight events was available for analysis if required.

CHAPTER THREE

Experimental Details II

3.1 Measuring Technique

The table top image was measured using an image plane digitiser, where a single fringe of the Moire fringe system used for digitising corresponded to $\sim 25\mu m$ on the table top which transformed to $\sim 2\,\mu m$ on the film plane. Normal setting errors corresponded to about 8 - 10 μm on the film (see § 3.2.3).

Events were measured on three views where possible. A three-dimensional reconstruction requires only two views, however the extra measured view increased the probability that two would be consistent within the errors of measurement. For each event the primary vertex was measured together with four fiducial crosses and the beam track. All secondary tracks and vertices were also measured including any vees or γ-ray conversions. This was repeated for each view. Where possible nine points were measured on each track; shorter tracks could be accepted with fewer points. Neutral and short tracks were measured by two points, one at each end of the track. Tracks recognised as stopping inside the chamber could be measured up to their full length to enable the GEOMETRY reconstruction programme to calculate the particle momentum from its range. The system also allowed particle tracks which passed through the persepx wall into the Ne/H_2 mixture to be measured.

The transformation from the x,y coordinates of the image plane to those of the film plane is complex and must account not only for the straight forward linear translations and rotations introduced by the projection system but also for the distortions of the optical system, magnification effects (usually dependent on the chamber depth) and projector tilt. The transformation equations for x and y are derived empirically by measuring locations of 20 fiducial crosses with known locations on the film plane.

The transformation may be represented by polynomial expansion of the form

$$x' = A + Bx + Cy + Dx^2 + Ey^2 + Fxy + \ldots\ldots\ldots\ldots\ldots\ldots$$

where A to F are constants and x' is the film plane co-ordinate. A similar expansion describes the y co-ordinate with different coefficients. After fitting, the calculated positions of the fiducials are found to lie within $\sim 5 \mu m$ of their known positions on the film plane.

3.2 Measuring Accuracy Checks

In order to ensure that a high precision of measurement was obtained various checks were carried out during the entire measurement of the data.

3.2.1 Measurement Of Track Curvatures

A two dimensional circle fit was carried out on-line. If the resulting root mean square deviation of the measured points was greater than the expected value (which was momentum dependent to account for coulomb scattering) then the measurement was rejected and the track remeasured until it was acceptable.

3.2.2 Fiducial Measurement

The on-line system calculated the distances between pairs of fiducial crosses measured on each view and compared these with standard values Deviations of more than 0.5 mm caused the measurements to be rejected. Repeated failures indicated a disturbance in the projection system and measurements ceased until the cause of the failure had been rectified.

3.2.3 Optical Calibration

Any systematic shift in the optical system required the constants A to F in the transformation equations to be re-determined. These shifts manifest themselves in the error distributions of the measured fiducial crosses about their known values which should centre on zero.

These checks ensured a high precision of measurement, the overall errors on vertices and tracks were $\sim 8 \mu m$ and $10 \mu m$ respectively, which led to a high pass rate through the three-dimensional reconstruction programme of 85 - 90%.

3.3 Event Processing

This was carried out using a series of computer programmes which are outlined below.

3.3.1 REAP

The data from the measuring tables was fed onto a disk in an IBM 1130 computer. This disk was transferred to an IBM 360/195 at the Rutherford Laboratory using REAP which translates the IBM 1130 coding and stores the data on a disk in the larger machine.

3.3.2 TRANS

The three-dimensional reconstruction programme (see§3.3.3 below) required the measured data to be in a standard format. TRANS performed this conversion and also corrected for distortions in the optical system of the projectors. It also determined the sense of curvature of the tracks and added vertices at the end of possible stopped tracks.

3.3.3 Geometrical Reconstruction

A standard programme called HGEOM (32) was used to reconstruct the events in three-dimensions. The programme was written origonally for processing events in a conventional bubble chamber and was modified for use with the T.S.T. and renamed BAGEOM.

The modifications included energy loss calculations for hydrogen, perspex and Ne/H_2 mixture; bremstrahlung radiation energy loss for electrons was also added.

Tracks passing through the perspex wall of the T.S.T. were divided into two parts and the mass dependent helix fit carried out using the energy loss appropriate to the medium. The fits were done separately as the errors of measurement are different for the two media and there was also a possibility that a small angle elastic scatter occurred inside the perspex. Each fit produced its own values for the track parameters. Another mass dependent helix fit was made to the two tracks; the parameters of the track in the Ne/H_2 mixture were converted to the centre of the hydrogen track using the range-energy tables. A weighted average of the track variables in hydrogen and the Ne/H_2 mixture was used to determine the final track parameters.

The e^+e^- pairs arising from the γ-ray conversion were rejected if the vector addition of the e^+ and e^- momenta showed that they were not associated with the primary vertex.

The programme BAGEOM passed the mass dependent helix fit data onto the next processing programme called KINEMATICS.

3.3.4 Kinematic Fitting

The standard programme KINEMATICS (33) tested each of the reconstructed events against various hypotheses. These hypotheses assigned particular masses to the particle tracks depending upon the event topology. The hypotheses used in the present work are summarised in Table 3.1. Having assigned the particle masses, KINEMATICS proceeds to apply the conservation of energy and momentum to each vertex of the event. For each vertex there are four constraint equations:

$$\sum p_x = \sum_i p_i \cos\lambda_i \cos\phi_i - p\cos\lambda\cos\phi = 0$$

$$\sum p_y = \sum_i p_i \cos\lambda_i \sin\phi_i - p\cos\lambda\sin\phi = 0$$

$$\sum p_z = \sum_i p_i \sin\lambda_i - p\sin\lambda = 0$$

$$E = \sum_i (p_i^2 + m_i^2)^{\frac{1}{2}}$$

where p_i, λ_i and ϕ_i are the momentum, angle of dip and azimuthal angle for the outgoing tracks, and p, λ and ϕ are the incident particle parameters. E is the total energy of the system in its initial state. For the primary vertex the total energy is

$$E = (p^2 + m^2)^{\frac{1}{2}} + M$$ where m and M are the masses of the kaon and proton respectively.

At any vertex if all the parameters are known the above equations

Table 3.1 : Summary Of Common Hypotheses Used In KINEMATICS

Topology	Reaction
Zero Prong + vee [001]	$K^-p \rightarrow \overline{K^0}n$, $\overline{K^0} \rightarrow \pi^+\pi^-$ $K^-p \rightarrow \Lambda^0\pi^0$, $\Lambda^0 \rightarrow \pi^-p$
Zero Prong + vee + γ [002]	$K^-p \rightarrow \Lambda^0\pi^0$, $\Lambda^0 \rightarrow p\pi^-$, $\pi^0 \rightarrow \gamma\gamma$, $\gamma \rightarrow e^+e^-$ $K^-p \rightarrow \Sigma^0\pi^0$, $\Sigma^0 \rightarrow \Lambda\gamma$, $\Lambda^0 \rightarrow p\pi^-$, $\gamma \rightarrow e^+e^-$
Two Prong [200]	$K^-p \rightarrow K^-p$ $K^-p \rightarrow \pi^-\pi^+n$ (unseen $\Sigma^{\pm}$ or $\overline{K^0}$) $K^-p \rightarrow \pi^-p\pi^0$ (unseen Σ^+) $K^-p \rightarrow \Sigma^-\pi^+$ (no decay seen) $K^-p \rightarrow \Sigma^+\pi^-$ (no decay seen)
Two Prong [210]	$K^-p \rightarrow \Sigma^+\pi^-$, $\Sigma^+ \rightarrow p\pi^0$ $K^-p \rightarrow \Sigma^+\pi^-$, $\Sigma^+ \rightarrow n\pi^+$ $K^-p \rightarrow \Sigma^-\pi^+$, $\Sigma^- \rightarrow n\pi^-$
One Prong [100]	$K^- \rightarrow \mu^-\bar{\nu}_\mu$ $K^- \rightarrow \pi^0\pi^-$
Three Prong [300]	$K^- \rightarrow \pi^+\pi^-\pi^-$

act as constraints on the fitting of the vertex [4C fit]. If one quantity is missing e.g. when a track is short and there is no curvature measurement, one of the equations is used to determine the missing quantity leaving three equations to be used as constraints (3C fit). In complex events there are two or more vertices, each one contributing four equations similar to these above. In general the number of constraints, n_c, on an event of n_v vertices and n_p particles having n_u unmeasured quantities is given by

$$n_c = 4n_v - n_u$$

Generally the higher the value of n_c the smaller the errors on the fitted quantities become.

The KINEMATICS programme was modified to process events having a primary kaon of zero momentum. The original version gave a low fitting efficiency for these events. The programme carries out its fitting using the parameters at the centre of the track; however the constraint equations apply to the parameters at the vertex. These equations are transformed using the energy loss tables for charged particles and this gives rise to the quantity $\frac{dp_v}{dp_c}$ which is the change in the vertex momentum with that at the centre of track. This quantity is well defined at momenta $>$ 50 MeV/c but below this value any change in p_v has little effect on the corresponding value of p_c. As this gradient is poorly determined in this region its importance below 50 MeV/c was diminished on multiplication by the empirical factor

$$\left[1 + \cot \frac{\pi p}{2 \times 0.05}\right]^{-\frac{1}{2}}$$

where p is the primary momentum in GeV/c. This factor has the value 1 at 50 MeV/c and zero at 0 MeV/c. This function progressively decouples the parameters at the track centre from those at the vertex and encourages the minimisation programme to produce an acceptable fit with $p \sim 0$ MeV/c.

This is physically very reasonable because the path length available for interaction below 50 MeV/c is small ($\sim$ 1.3 mm) and is less than 1% of the interaction length making an in-flight interaction extremely unlikely. The factor above is entirely empirical and serves merely to parametrise the true physical situation.

3.3.5 Event Judging

This part of the processing was carried out by a physicist and involved examining on the scanning table every event which failed in the processing chain. The events examined at the judging stage may be summarised as follows:

(i) Events failing geometrical reconstruction.

(ii) Events passing reconstruction but failing the kinematic fitting.

(iii) Events not measured.

(iv) Events having final kinematic fits which were inconsistent with the scan code.

(v) Events with ambiguous track identities.

The track and hypothesis ambiguities often required a proton to be distinguished from a pion and these were usually resolved using the track ionisation (see § 6.7). The most common ambiguities of this type were:

(i) $\Lambda^o/\overline{K^o}$

(ii) $\Sigma^+ \longrightarrow p\pi^o/\Sigma^+ \longrightarrow n\pi^+$

(iii) $\pi^+\pi^-/\pi^-p$

In each case the identification of the positive track resolves the ambiguity.

In practice two judge processes were carried out, usually after the first and second measurements. After preliminary judging it was found unnecessary to examine all of the above events and an element of automation was incorporated.

All events failing geometrical reconstruction and kinematic fitting were automatically remeasured. Only events failing after the remeasure were judged. Failures at the first measure were usually due to errors and these often passed on remeasure.

Events having ambiguous fits could be partially resolved using the scanning code which assigns a physical channel to the event. In cases where the code may be unreliable, for short tracks (< 5 cm) or for steep tracks ($\lambda > 45^{o}$) these were judged in the usual way.

The unmeasured events fall into several groups:

(i) Missed by accident; these were automatically remeasured.

(ii) Deemed as "not measurable" by the measurer; if this was confirmed, the reason was noted (see § 3.4), if not confirmed then the event was remeasured.

(iii) Classified as "not an event"; all of these were judged and were rejected if the classification was confirmed.

These modifications apply to the bulk of the data processed in this work; the zero prong Λ^{o} events in the Brussels sample (§ 2.6) were processed using an automatic first judge controlled by the scan data in the computer. The "auto-judge" accepted all events having unambiguous Λ^{o} fits and pointing Λ^{o} fits where a complete fit failed but the Λ^{o} is found to point to the primary vertex. Λ^{o} events ambiguous with $\overline{K^{o}}$ fits were assumed to be genuine Λ^{o} events. All other events were automatically remeasured and the normal judging carried out after the second measure.

3.3.6 MASTERLIST - Processing Control Programme

After scanning, the details of every event were recorded in a masterlist on a computer disk. Each event was described by a record twenty words long giving basic information about the event such as frame number, event zone etc. A status number was used to define the current status of the event and was updated as necessary during the processing chain. The MASTERLIST programme controlled the output of measuring lists, remeasuring lists and judging lists.

The entire processing sequence is summarised in the flow diagram in fig. 3.1. In general the procedure followed was a double scan, followed by three measures interspersed with two judges.

3.3.7 DATA SUMMARY TAPE. (D.S.T.)

The final data were collected together to form a D.S.T. This tape contained fitted events only and included the following information for each hypothesis fitting the event.

(i) x, y, z co-ordinates of all vertices.

(ii) 1/p, tan λ , ϕ values for all tracks, both fitted and unfitted, together with the errors on these quantities.

(iii) Missing mass quantities and the number of degrees of freedom for the fit.

(iv) Fit probability.

(v) Measured length of each track.

(vi) Chamber magnetic field values.

The analysis used this D.S.T. for the production of angular and momentum distributions used in the cross-section determinations.

3.4 Classification of Unmeasurable Events

Typically 10-15% of the events remain unmeasurable at the end of processing and must be allowed for when calculating the total cross-sections. Simple scaling by 10-15% is likely to be inaccurate since there is a danger of correcting twice. This is illustrated in the case of elastic scattering. K^- mesons which are scattered through large angles are usually too short to be measured and are classified as "unmeasurable". This becomes apparent in the production angular distributions in the centre of mass by a loss of events at cos $\theta^* \sim -1$ producing structure in an otherwise isotropic distribution. The correction for this loss and also for the unseen events is easily made by scaling the isotropic

Flow Diagram Of Processing Sequence

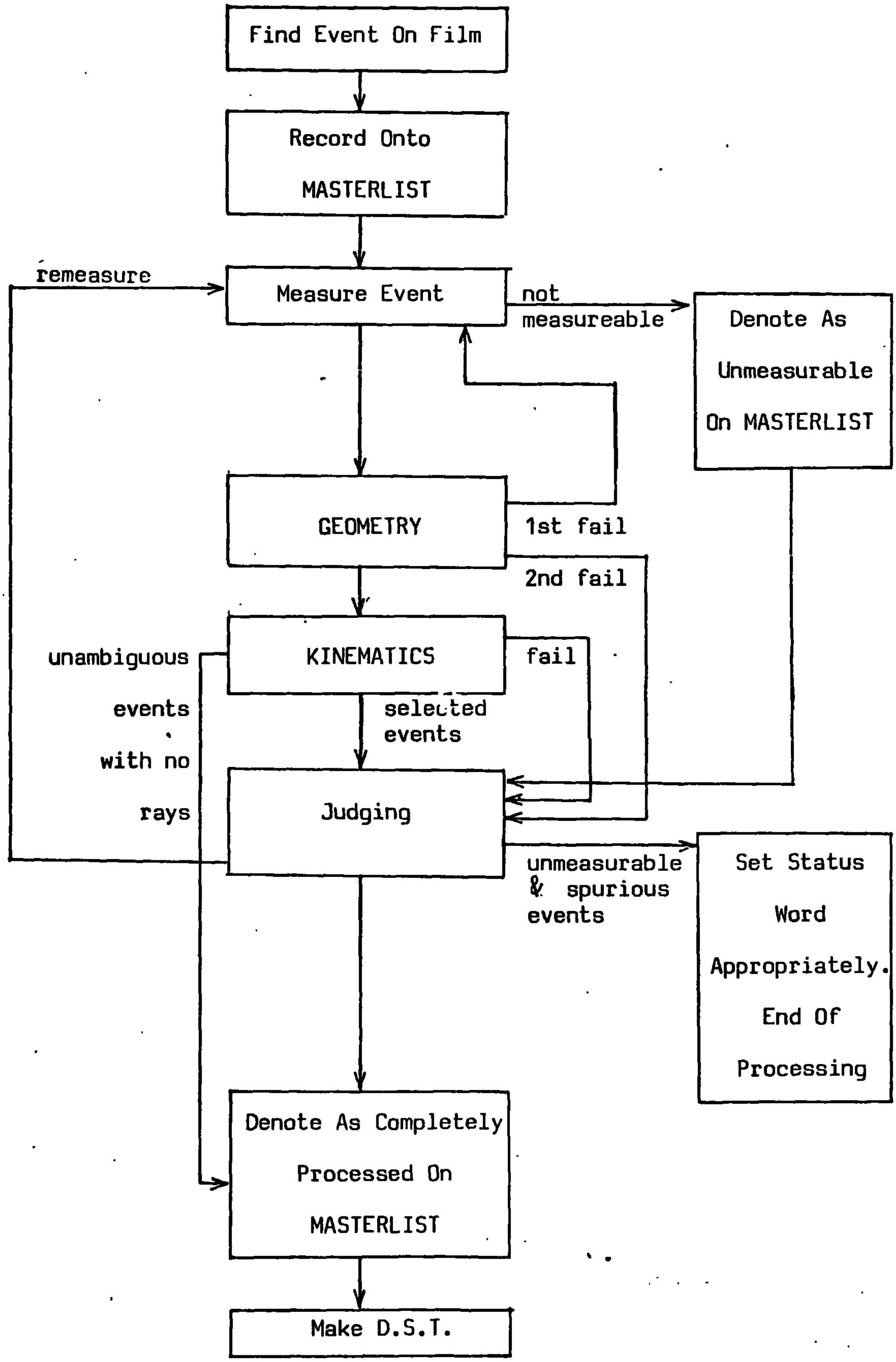

Fig. 3.1 : Flow Diagram Of The Event Processing Chain

part of the cos θ^* distribution. However if the cross-sections are now scaled further by the proportion of all the unmeasured events, this loss has now been doubly corrected. Consequently it is necessary to separate from the unmeasurable events those which are automatically corrected for in the angular distributions ("geometrical loss"). This leaves only a proportion of the unmeasurable events ("random loss") to be corrected for using a scaling factor.

The removal of these geometrical losses from sample of unmeasured events is discussed below for each channel in turn.

3.4.1 Σ Hyperon Production Events

The charged hyperon events where the Σ decays into a charged pion have identical topologies and hence similar losses. The Σ^+ hyperons decaying into protons are less efficiently identified, due to the lack of ionisation change at the decay vertex. The geometrical losses for all the hyperon topologies were anticipated and the following categories were adopted:

(i) Σ hyperon too short to be measured ($\lesssim$ 1 mm).

(ii) Σ hyperon produced in the forward or backward direction relative to the kaon. The production vertex was often difficult to locate for these events.

(iii) Σ hyperon decayed in the forward direction. This usually applied to the proton decay mode only, although steeply dipping decay pions were also difficult to measure.

(iv) Event orientation made measurement impossible. Losses of this type are corrected by using ϕ angle distributions (see chapter five) and arose when the production plane included the line of sight. This category also included steeply dipping tracks.

(v) Decay proton too short to be measured. This arose from low momentum protons with ranges of less than $\sim$ 1 mm.

3.4.2 Elastic Scatter Events

The main losses in these events arose from the invisibility of the secondary products. The scanning included all scattering events and all kinks (or 1 prongs) in primary beams. The kinks were forward elastic scatters with unseen recoil protons. The present work rejects these as being due mainly to coulomb scattering. Most of the kink type events had small scattering angles ($\lesssim 15°$) and this is within the region of coulomb-nuclear interference. The classification for the unmeasurable elastic scatters were:

(i) Proton not seen.

(ii) Proton too short to be measured.

(iii) Secondary kaon not seen.

(iv) Secondary kaon too short to be measured. This often occurred because of a secondary interaction close to the primary vertex.

(v) Short secondary tracks. Events of this type were difficult to resolve, the tracks often possessed similar lengths and ionisations and little or no curvature was evident.

3.4.3 Charge Exchange

The main geometrical losses for this channel arose from a $\overline{K^o}$ decay close to the production vertex simulating a 2 prong $\pi^+\pi^-$ event. This problem becomes serious at low momenta, the decay length of the $\overline{K^o}$ meson being a few millimetres. The detection of the vertex of the vee was also difficult ; at low momenta the decay products are nearly collinear: these were called "wide vee" events.

3.4.4 Λ^o/Σ^o Hyperon Production

These events may simulate a π^-p type of event by decaying close to the production vertex. The opening angle of the vee is usually smaller than for a $\overline{K^o}$ and the decay pion differs in ionisation from the proton; both these properties aid the measurement and detection of Λ^o vees.

3.4.5 Random Losses

Events not belonging to any of the above categories were classified as random losses and these occurred mainly for the following reasons:

(i) Overlapping tracks from other events or beam tracks.

(ii) Unclear images on two views due to poor illumination or film quality.

(iii) Chamber turbulence; this sometimes caused random drifting of the bubbles.

(iv) Clerical errors and book keeping mistakes.

These losses populate all production angle and decay angle distributions uniformly and an overall correction factor is sufficient to include these events in the final results.

CHAPTER FOUR

CHANNEL CROSS-SECTIONS I

This chapter presents the results from which the channel cross-sections are subsequently calculated. It includes the determination of the hydrogen density; the calibration of the magnetic field; the determination of the distribution of primary path length and the distributions of the stretches of the fitted events. Also included in this chapter is a discussion of measurement errors which are particularly important in this low momentum region.

4.1 The Determination Of The Hydrogen Density

The nominal value adopted by the collaboration for the density was 0.0558 gm cm^{-3}; however the T.S.T. is surrounded by a Ne/H_2 mixture and there is a possibility of neon diffusing through the seals of the perspex wall into the pure hydrogen contained inside the target. A small amount of diffusion of the neon will lead to an increase in the stopping power of the hydrogen.

The density was determined from the measured ranges of particles having a unique production momentum. Negative sigma hyperons which are produced by K^-p interactions at zero primary momentum have a unique momentum of 172.9 MeV/c. The majority decay in flight but the few which come to rest before decaying have a unique range. These events with an associated production pion are classified as collinear two prong events and the present data contained a sample of ~ 250 fully measured events of this type.

The range distribution of the hyperons for this sample is shown in fig. 4.1. The background of events having ranges < 0.8 cm is due mainly to the Σ^- hyperons which strike the perspex walls before coming to rest and to in-flight Σ^- interactions with protons. This background is seen to be small and hence was not removed from the region of length

FIG 4.1: Distribution of Ranges for Sigmas With Unique Momentum

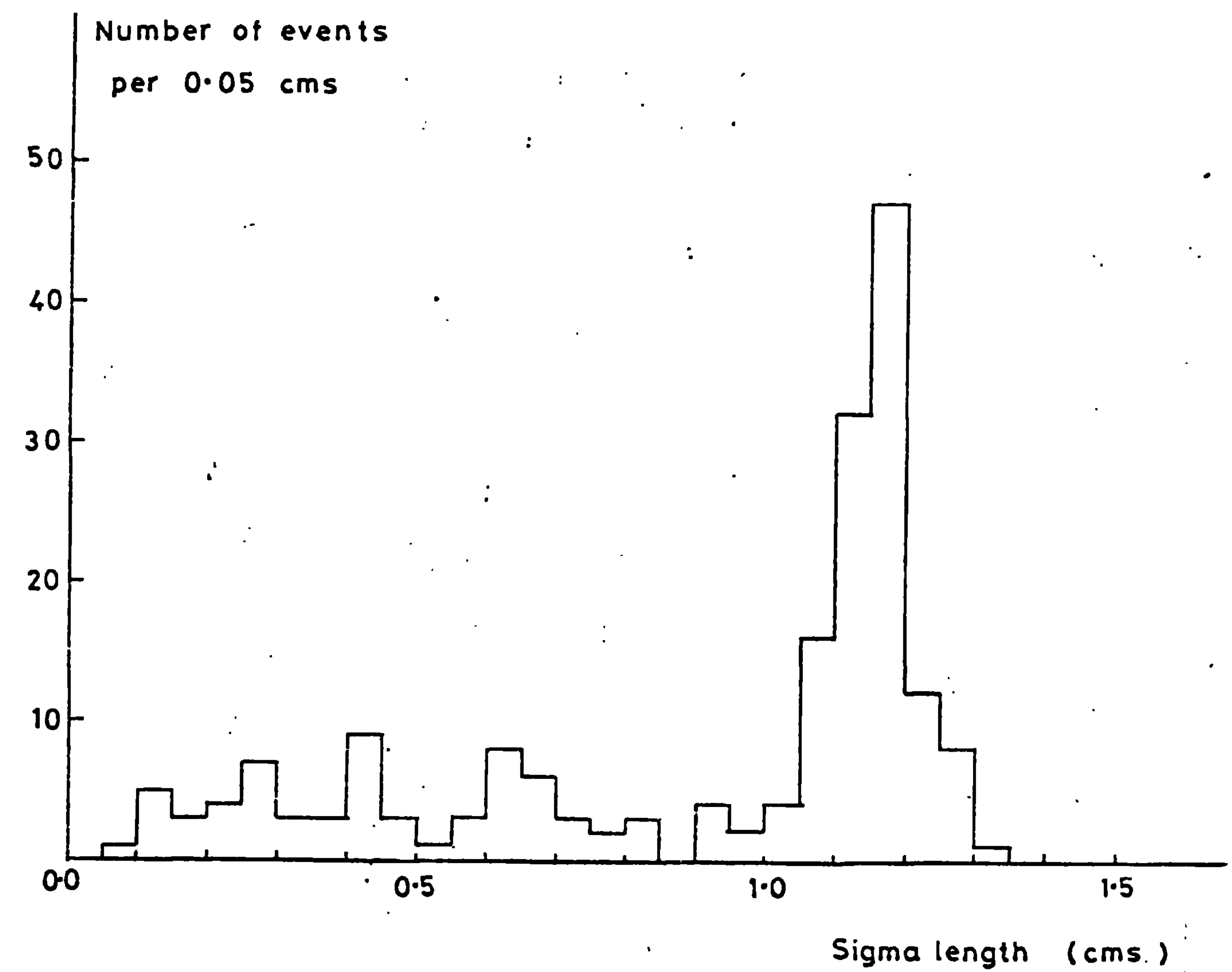

of 0.85 - 1.35 cm which was used in the determination of the mean range of the Σ^- hyperon.

The contamination of this sample with in-flight events, which appear collinear because the hyperon is produced in the forward or backward direction relative to the kaon, is < 2% of the total sample and was neglected. From the unique range of the hyperon the stopping power and hence the density of the hydrogen was determined.

A separate determination of the hydrogen density was carried out within the collaboration by the University College laboratory. The range of the Σ^- hyperon was measured together with the range of the muon produced by pion decays occurring at rest inside the chamber. The unique momentum muon (29.79 MeV/c) has range similar to that of the hyperon. The results of the separate determination are compared with those of the present work in table 4.1.

Table 4.1 Range Determinations Of The Σ^- And μ^+ Particles

Range (cm)	Particle	Correction To Nominal Density Of 0.0558 gm cm^{-3}	
1.134 $\pm$ 0.004	Σ^-	1.020 $\pm$ 0.005	(UCL)
1.136 $\pm$ 0.006	μ^+	1.025 $\pm$ 0.006	(UCL)
1.147 $\pm$ 0.007	Σ^-	1.007 $\pm$ 0.007	(Present Work)

The present result is an agreement with the UCL value and is also consistent with the values of hydrogen density quoted by Leutz et al (34) (see table 4.2). The density applicable to the T.S.T. at 29.6 °K is found by linear interpolation of these values.

Table 4.2 Density Of A Saturated Liquid Ne/H_2 Mixture. (gm cm^{-3})

Mole Fraction Of Neon	Temperature °K			Interpolated Density
	28.0	29.0	30.0	At 29.6 °K
0.00	0.0590	0.0567	0.0539	0.0550
0.01	0.0643	0.0618	0.0588	0.0601

The density of hydrogen is unaffected by pressure at the 1% level because of the incompressibility of the liquid and these results may be regarded as applicable to the T.S.T. The density is strongly dependent on the neon concentration and it is clear that the measured value is consistent with a neon contamination of less than $\sim 0.4\%$.

The nominal value of 0.0558 gm cm^{-3} was accepted as being accurate to $\sim 2\%$ and is sufficiently precise for the present work.

4.2 Calibration Of The Magnetic Field

The magnetic field inside the chamber was nominally 1.23 Tesla. Since the measured values of momenta depend directly on this field it is essential to check its value. This was carried out using events which contain particles of known momentum. For example charged hyperon production by kaons at rest gives secondary particles of momenta 172.9 and 181.3 MeV/c for Σ^- and Σ^+ production respectively. The secondary pion is usually a long track and easily measured. Its radius of curvature can be found and used to calculate the particle momentum from the relation

$$p = \frac{0.3B\rho}{\cos\lambda}$$

where p = particle momentum in MeV/c

B = magnetic field in Kgauss

ρ = radius of curvature of the particle track (cm)

λ = angle of dip of the track

The momentum obtained from this relation is compared with the nominal value. Precise results were obtained within the collaboration by measuring a carefully selected sample of collinear Σ hyperon events. Care was taken to select only events at rest. The measured sample was processed using the field value of 12.3 Kgauss to give pion momenta of:

174.1 ± 0.5 MeV/c for the π^+ meson

and 183.5 ± 1.0 MeV/c for the π^- meson

These are in good agreement with the expected values ($<1\%$ difference) and the field value of 12.3 kgauss was accepted as sufficiently accurate.

4.3 Distribution Of Stretch Functions

The stretch function is designed to show up the existence of fitting biases and is defined as

$$S = \frac{(x_f - x_m)}{\sqrt{(\sigma_m^2 - \sigma_f^2)}}$$

where x_f and x_m are the fitted and measured quantities and σ_m and σ_f are their respective errors. The quantities used in fitting an event are ϕ, tan λ and 1/p as described in §3.3. An unbiased fitting technique will yield gaussion distributions of mean value zero, unit variance and a kurtosis of three. The stretch distributions for the primary kaons of the Σ^-_π, Σ^+_p, Σ^+_π events and also for one prong decays of kaons are shown in figs. 4.2 and 4.3 and their means, variances and kurtoses in table 4.3 below.

Table 4.3 Stretch Distributions: Mean Values, Variances And Kurtoses

Event	ϕ			Tan λ			1/p		
	mean	var.	kurt	mean	var.	kurt	mean	var.	kurt
$\Sigma^-\pi$	-0.02	0.98	3.17	-0.12	1.02	3.19	-0.03	1.02	3.10
Σ^+p	-0.14	1.16	2.89	0.21	1.00	3.01	0.13	1.15	2.72
$\Sigma^+\pi$	0.00	0.94	3.17	-0.08	1.02	2.97	-0.07	0.98	3.11
Decays	0.09	1.35	6.86	0.02	1.26	3.89	-0.09	1.37	7.45
Expected	0	1	3	0	1	3	0	1	3

On the whole these are in reasonable agreement with the expected values which indicates that the errors are correctly estimated. For the decays the hypothesis of the most common decay mode was selected to give an estimate of the stretch distributions.

The stretch distributions of the one prong decays are expected

FIG 4.2: Distributions of Stretch Functions for Primary Kaons.

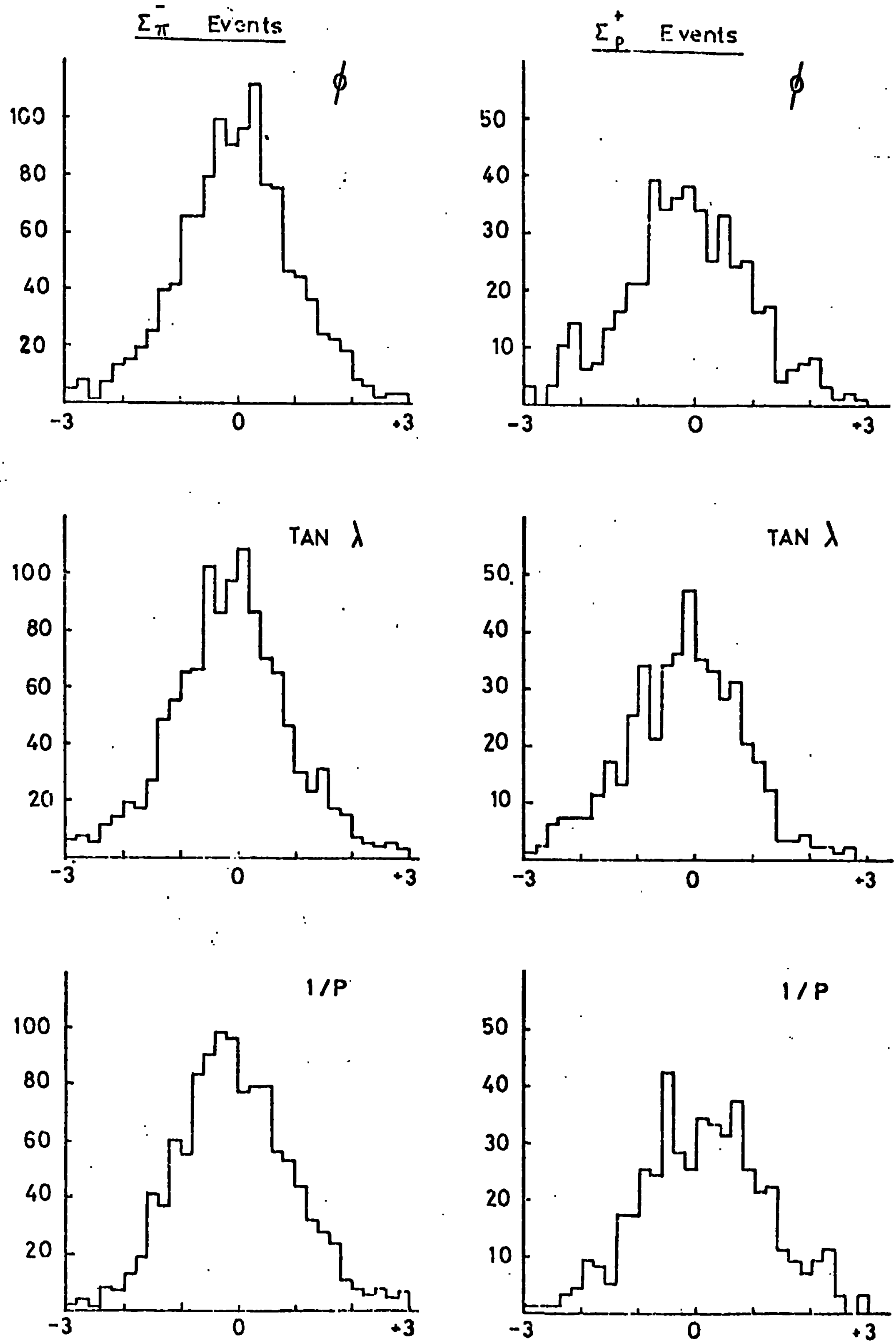

FIG 4·3: Distributions of Stretch Functions for Primary Kaons

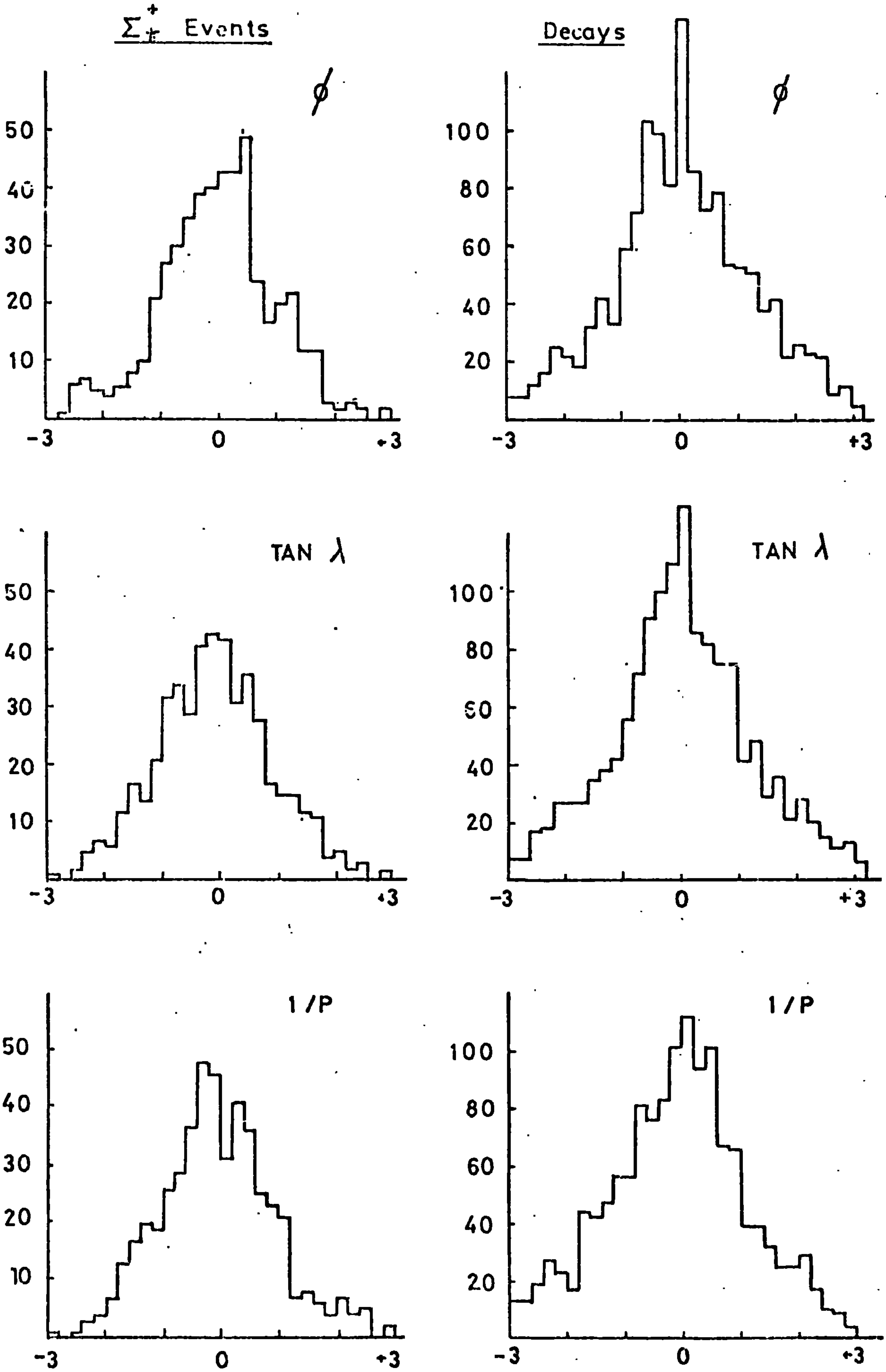

to be non-gaussian in form due to the ambiguity in fitting the decay modes. Fig. 4.4 shows the large overlap in the momenta of the decay secondaries which gives rise to the difficulty of fitting a unique hypothesis to an event. This makes it impossible to use the fitted momentum values for the decays and because these are used for the primary path length normalisation this constrains the entire cross-section analysis to use the measured (unfitted) momentum values of the primary kaons (see § 4.4).

The χ^2 probability of fit is another guide to the proper estimation of errors. Ideally the distribution is uniform if the errors are estimated correctly. An over estimate of the errors will allow the KINEMATICS programme to fit events more easily and will produce an excess of events with high fit probabilities, the reverse is true for under estimated errors. Spuriously fitted events will also cause the distribution to peak at low probability. The χ^2 probabilities for the charged hyperon channels and one prong decays are shown in figs. 4.5 and 4.6. Apart from the excess of low probability events, the stretch distributions and χ^2 probability distributions confirm that the fitting procedure is unbiased. The origin of the low probability events is unlikely to be due to events with spurious fits because at these low energies no alternative channels exist. The high probability of large angle single or plural scatters, particularly at low momenta, is not accounted for in the r.m.s. estimate of the coulomb errors and this will cause an under estimate of the true measurement errors.

4.4 The Use Of One Prong Decays To Determine The Path Length Distribution

The channel cross-sections are calculated from the following expression:

$$\sigma_i(p) = \frac{N_i(p)}{L(p)N_o\,\rho} \qquad 4.1$$

FIG 4·4: K^- Meson Decays; Secondary Particle Momentum Dependence on Kaon Momentum and Centre of Mass Scattering Angle θ^*

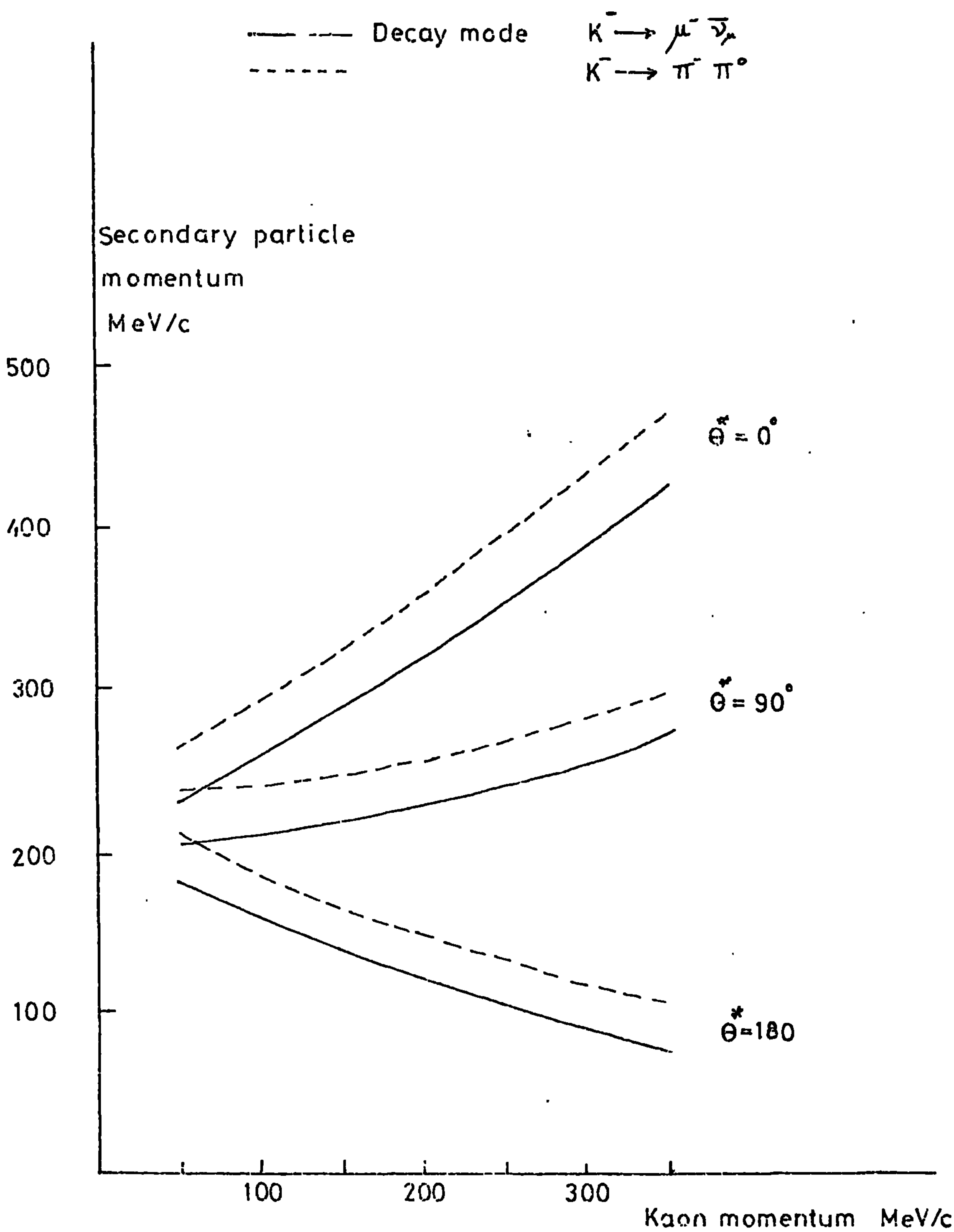

FIG 4·5 χ^2 Probability Distributions for Charged Hyperon Production.

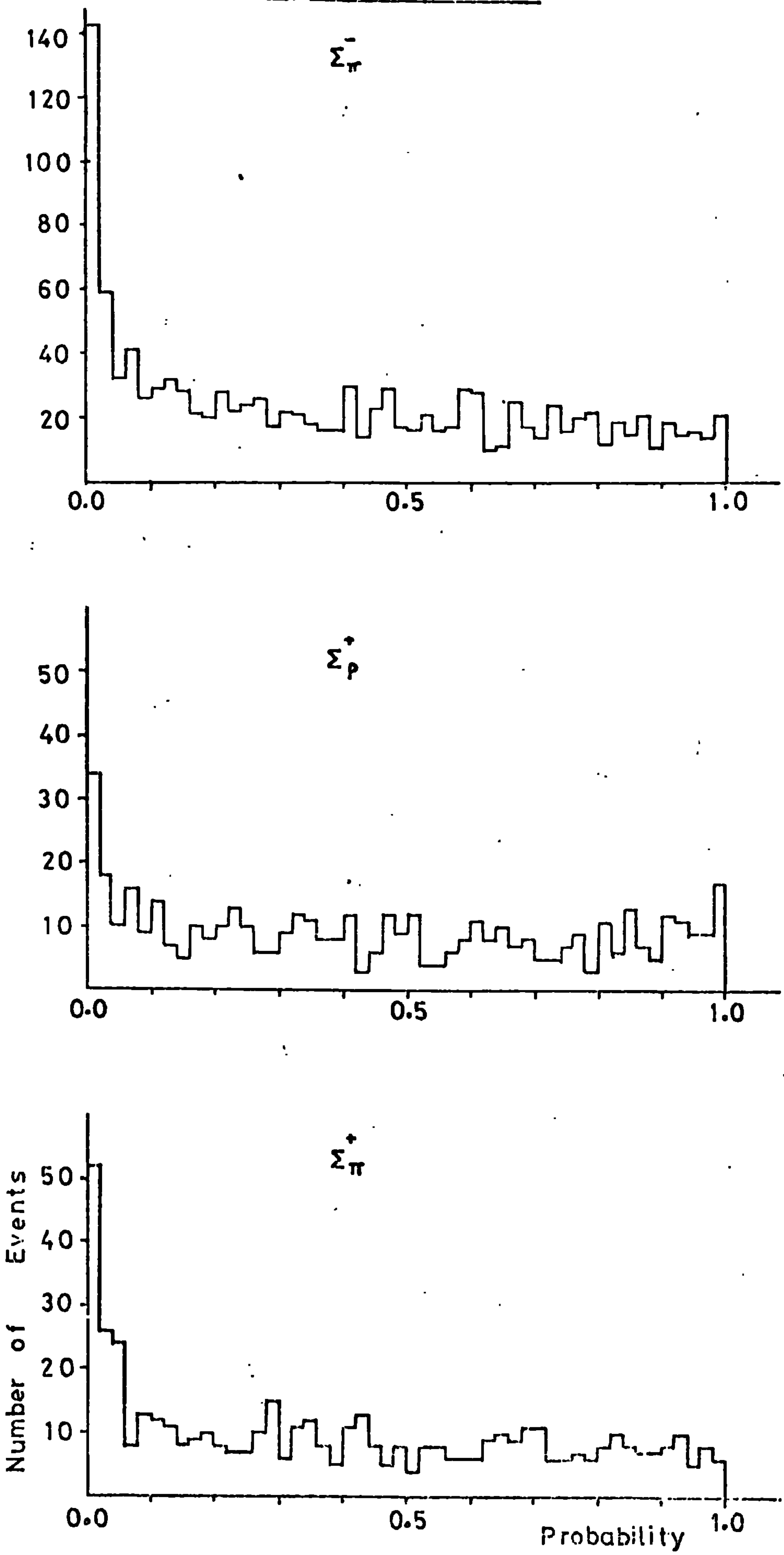

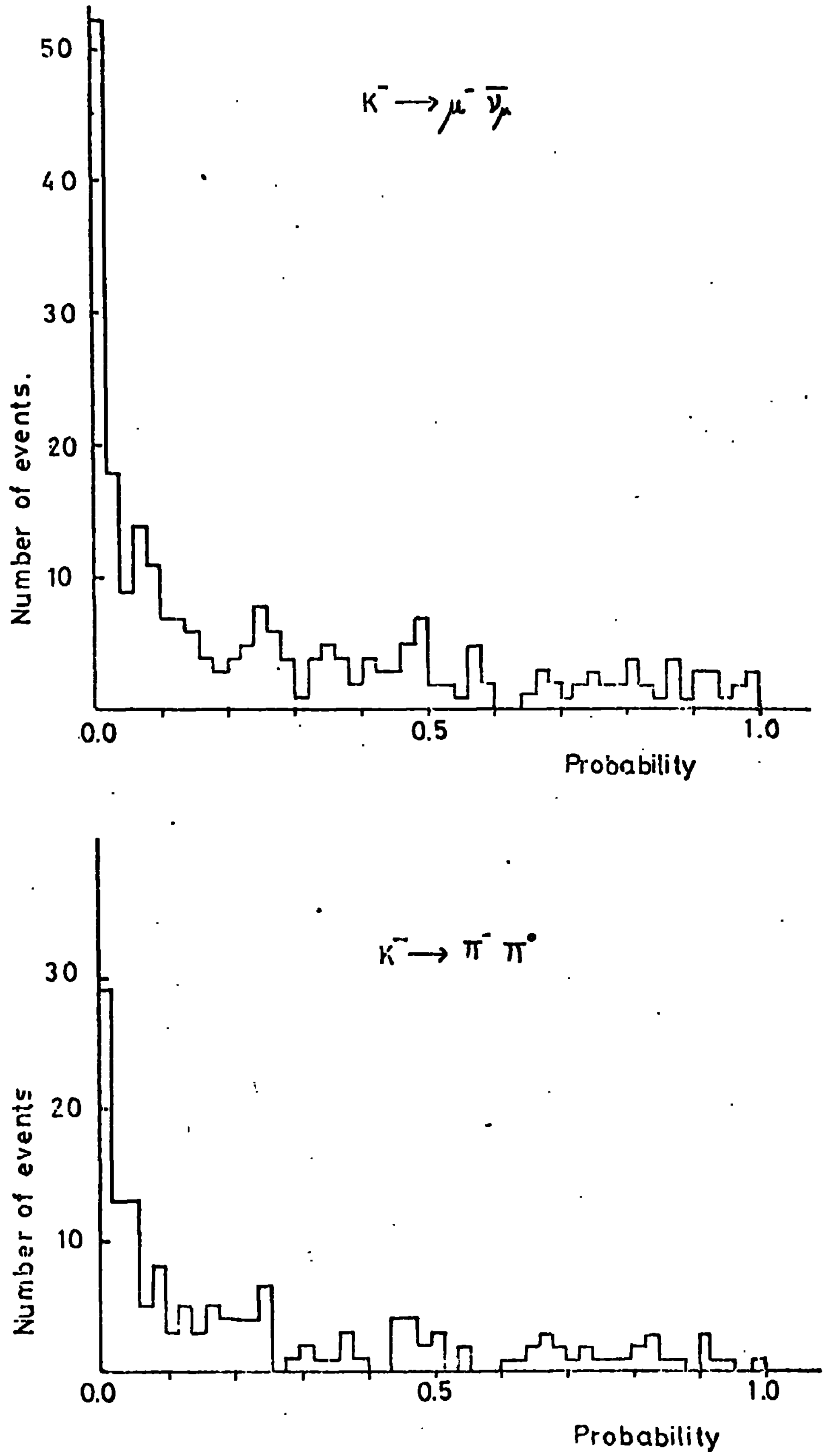

FIG 4.6: χ^2 Probability Distributions for Unambiguous Kinematic Fits to Kaon Decays.

where $N_i(p)$ is the number of strong interactions in channel i in momentum interval p to p + dp; L(p) is the total track length of all the primary kaons in the momentum interval p to p + dp; N_0 is Avogadro's number and ρ is the hydrogen density.

The cross-section is a function of two momentum dependent quantities: firstly, $N_i(p)$ which is calculated from the observed number of interactions after corrections to account for scanning and geometrical losses and secondly L(p) which is found using the total number of kaon decays in each momentum interval.

The determination of L(p) is discussed in this section, chapter five presents the correction factors used to calculate $N_i(p)$.

The negative kaon may decay by the following modes:

$K^- \longrightarrow \mu^- + \bar{\nu}_\mu$	63.5%	
$\longrightarrow \pi^- + \pi^0$	21.16%	
$\longrightarrow \pi^- + \pi^+ + \pi^-$	5.59%	(tau decay)
$\longrightarrow \pi^- + \pi^0 + \pi^0$	1.73%	
$\longrightarrow \mu^- + \bar{\nu}_\mu + \pi^0$	3.26%	
$\longrightarrow e^- + \bar{\nu}_e + \pi^0$	4.82%	

The lifetime of the kaon is 1.23×10^{-8} sec and it is the decay law which allows L(p) to be calculated. If the number of observed decays in a particular momentum interval is known then the total number of kaons having entered the momentum interval can be thus calculated. It is usual to employ the tau decay mode of the kaon since it is easily recognisable and produces a 4 C kinematic fit with a well defined fitted value of primary momentum. However the proper time available at these low momenta is too small to provide a useful number of events (typically 25 tau decays / 1000 frames). Consequently the one prong decays have to be used, these are considerably more numerous (~ 500 events / 1000 frames) but have the disadvantage of a kinematic ambiguity (see § 4.3) which restricts the subsequent analysis to use the measured momenta only.

From the number of one prong decays $N_d(p)$ in the momentum interval p to p + dp the track length which led to their creatinn is

$$L(p) = N_d(p) \times \frac{pc\,\tau_K}{m_K},$$

then the equation 4.1 can be re-written as

$$\sigma(p) = \frac{N_i(p)}{N_d(p)\; N_o \rho \frac{pc}{m_K} \tau_K} \qquad 4.2$$

The experimentally determined quantities in 4.2 are $N_i(p)$ and $N_d(p)$. It is customary to determine these using fitted rather than unfitted values of momentum, however it is essential to be certain that these two distributions are affected by errors in the same way. It is obviously wrong to use fitted values of momentum for one distribution and unfitted values for the other as errors for the fitted values are smaller than those of the unfitted quantities and will cause a distortion in the overall shape of the distribution of $\frac{N_i(p)}{N_d(p)}$. It is also invalid to use two number distributions arising from kinematic fits having different numbers of constraints for the same reason. The result found by Hamam (31) suggests that it is also invalid under certain circumstances to use the results from kinematic fits having the same number of constraints. This result came from a comparison of the pulls (pull = measured quantity - fitted quantity) in the elastic scatters, tau decays and charged hyperon events with a hyperon decay. All these are 4 C hypotheses and it was found that the pulls for the tau decays and elastic scatters were similar, however the pulls for the hyperon events were narrower in width implying a smaller shifting from the measured values. This effect causes a tightening of the decay momentum distribution relative to that of the hyperon channel distribution and this implies that even the conventional approach of using fitted values requires corrections to account for this.

The use of measured momenta largely removes these problems and leaves all the measurements for all channels affected by the same error distribution, i.e. that of measuring a radius of curvature using ~ 9 discrete measurements along the track. The disadvantage of using measured momenta is that below ~140 MeV/c the errors of measurement can seriously affect the momentum distributions and this must be investigated thoroughly.

4.5 Distribution Of Primary Path Length

Five rolls of film were double scanned by the scanning team for one prong and three prong decays using the same fiducial volume as for the strong interactions. A single scan was also made on 2½ rolls of film used for the $\Sigma^0\pi^0/\Lambda^0\pi^0$ channels.

The results of the scanning are presented in tables 4.4 and 4.5 (details of the scanning efficiency calculation are given in § 5.1.6).

The observed number of tau decays, when corrected for the scanning loss and compared with the correspondingly corrected number of one prong events, account for 5.5 ± 0.3 % of the total decay branching fractions. This agrees with the accepted value of 5.59 % (5) and lends confidence to the method of using one prong decays to obtain the track length distribution. This is not an unexpected result as in this low energy region the angles of decay are usually large and there is a distinct ionisation change at the decay vertex which makes these decays easy to detect.

The one prong decay events which were measured were selected from the entire five rolls by sampling alternate events on one of the

Table 4.4: Results Of Scanning For Kaon Decays

	One Prong Decays	Tau Decays
Number Of Events Found On First Scan	4381	230
Number Of Events Found On Second Scan	4330	230
Number Of Events Found In Both Scans	3666	174
Total Number Of Different Events Found After Two Scans	5045	286

Table 4.5: Scanning Efficiencies For Kaon Decays

	One Prong Decays	Tau Decays
First Scan Efficiency	0.847	0.756
Second Scan Efficiency	0.837	0.756
Double Scan Efficiency	0.975	0.942

scanning lists. This resulted in a sample of 2334 measured events of which 1940 produced final kinematic fits. The GEOMETRY and KINEMATICS pass rates were 96% and 86% respectively and produced 1849 events fitting the two body decay modes of the K^- meson:

$$K^- \longrightarrow \mu^- + \bar{\nu}_\mu$$
$$K^- \longrightarrow \pi^- + \pi^0$$

This resulted in a normalisation factor of ~2.72. The failures in KINEMATICS will consist largely of the unfittable three body decay modes with two unseen neutral particles. The momentum distribution of the decays, which contains 1754 events inside the fiducial volume, (see fig. 4.7) was normalised to the corrected total number of events found in the same fiducial volume using the factors in table 4.6. The three body decays were allowed for using the branching ratio.

Apart from these corrections there were also geometrical losses to be considered. These were due to steeply dipping tracks and forward decays. The latter loss was small (see fig. 4.8), the ionisation difference between the primary and secondary tracks was apparent for all events except those with steeply dipping secondaries. The steep track loss is apparent in the ϕ angle distribution defined as follows:

$$\cos \phi = \frac{(\vec{K} \wedge \hat{z}).(\vec{K} \wedge \vec{\mu})}{|\vec{K} \wedge \hat{z}|\,|\vec{K} \wedge \vec{\mu}|}$$

where $\vec{K}$ is the direction of the primary, and $\vec{\mu}$ is the direction of the secondary and $\hat{z}$ is a unit vector along the line of sight (perpendicular to the film plane). If the normal to the decay plane lies in the xy plane of the chamber the event is seen edge on and $\phi = 0^\circ$. If the normal is parallel to the line of sight ($\phi = 90^\circ$) the event is clearly visible, hence losses would be expected for small values of ϕ. The ϕ angle should be isotropic if there are no losses and it can be seen (fig. 4.8) that losses do exist below $\sim 25^\circ$. The overall correction factor for these losses, ϕ and $\cos\theta^*$, was calculated using a two dimensional plot of these

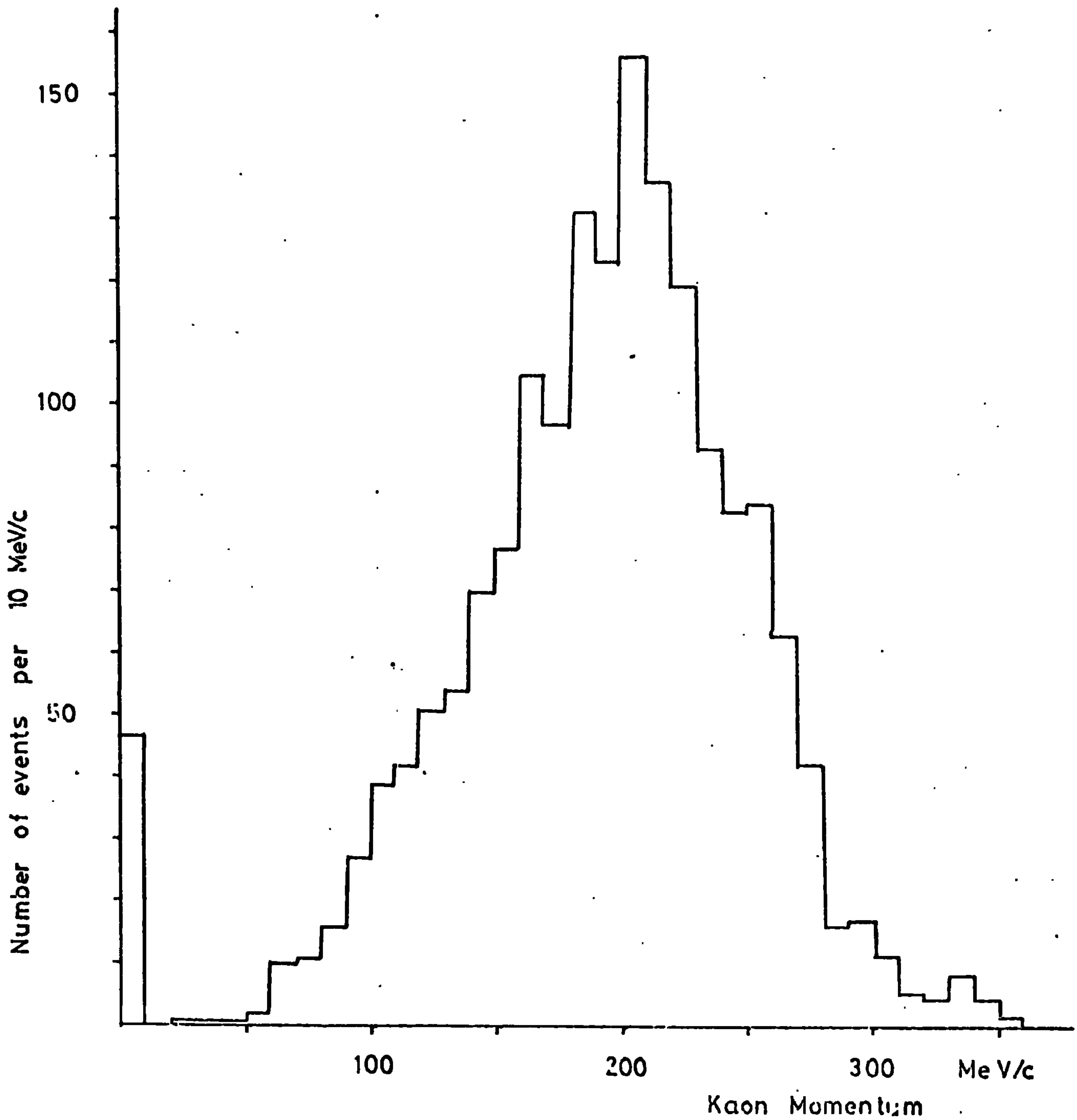

FIG 4.7 Distribution of Vertex Momenta for The Primaries of One prong Decays.

FIG 4·8: Centre of Mass Production & Phi Angle Distributions.

For Decays.

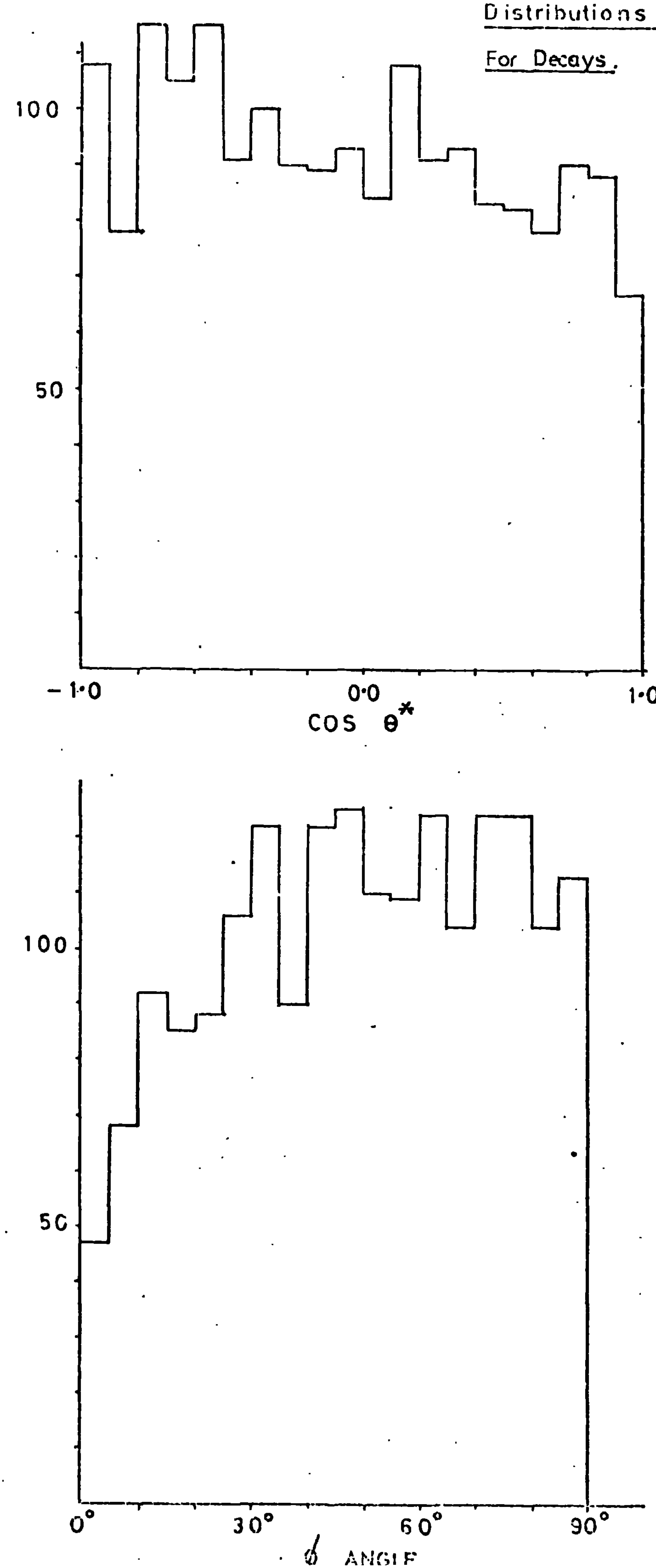

distributions (fig 4.9) as these losses are not mutually exclusive. The central region ($-0.8 < \cos\theta^* < 0.8$ and $25 < \phi < 155$) defined the average number of events per unit area and gave a geometrical correction factor of 1.105. The correction factors applied to the measured momentum distribution in fig 4.7 are summarised below in table 4.6.

Table 4.6:

Summary Of Correction Factors

Applied To The Number Of Measured One Prong Decays

Scanning loss	1.026
Normalisation factor	2.728
Correction for branching ratio into three body final states	1.059
Geometrical loss factor	1.105
Overall correction factor	3.275

The total number of kaons in a momentum interval is deduced from the number of decays in that interval by using the decay law:

$$\frac{dN}{dt} = -\frac{1}{\tau}N_0 \qquad 4.3$$

where N_0 is the original number (at time $t = 0$) and τ is the decay lifetime. The proper time (t) may be converted to laboratory distance using the relation:

$$x = \frac{pct}{m} \qquad 4.4$$

p and m being the particle momentum and mass respectively. Differentiating equation 4.4 with respect to t and substituting into 4.3 gives

$$N_0 dx = \frac{-pc\tau}{m} dN \qquad 4.5$$

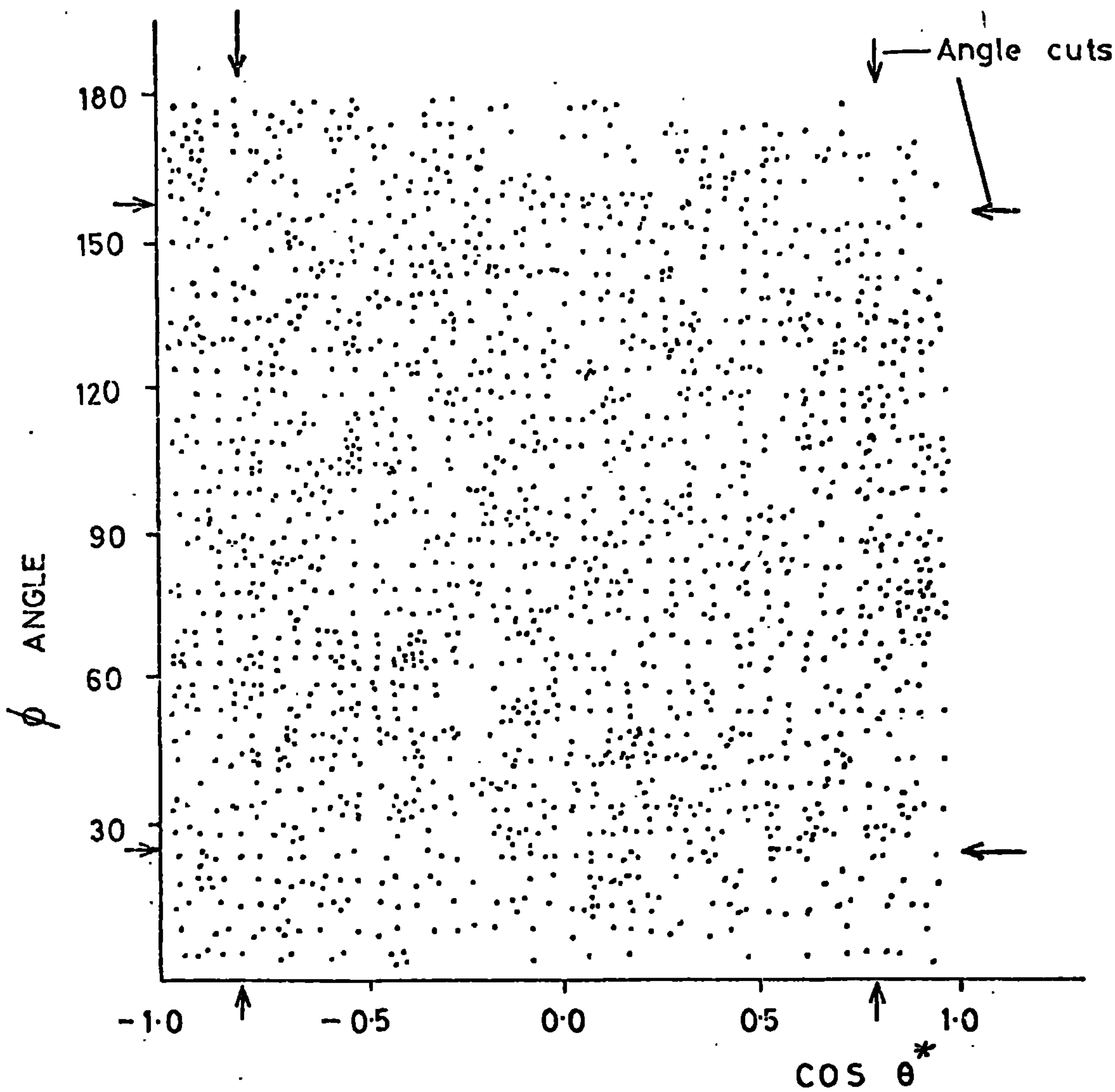

FIG 4·9: Kaon Decays; Two dimensional Diagram of Production Angles.

$$\therefore \quad N_o dx = \lambda \, dN \quad \text{where } \lambda = \text{mean distance to decay.}$$

consequently the path length for the primary kaons per momentum interval is given by

$$L(p) = N_o(p) \times \Delta x(p) \qquad 4.6$$

where $N_o(p)$ is the total number of kaon tracks in momentum interval p to p + dp and $\Delta x(p)$ is the distance a kaon travels for the ionisation energy loss to degrade its momentum by an amount dp. Providing $\Delta x(p)$ is small compared to the mean decay distance, equation 4.5 may be substituted into 4.6 to give

$$L(p) = \lambda(p) \, dN(p) \qquad 4.7$$

This is the expression used to determine L(p); $\lambda(p)$ is the mean decay length at momentum p and dN(p) is the observed number of decays in momentum interval p to p + dp.

Table 4.7 compares the typical values of $\Delta x(p)$ and $\lambda(p)$ and justifies the assumption used to produce equation 4.7.

Table 4.7: Typical Values of $\lambda(p)$ And $\Delta x(p)$

p MeV/c	$\Delta x(p)$ cm	$\lambda(p)$ cm	$\Delta x/\lambda$
95	0.47	71.4	0.007
195	3.03	146.4	0.021
295	8.90	221.6	0.040

The track length distribution for the five rolls of film which were measured is shown in fig. 4.10 and the final results are listed in table 4.8.

The normalisation was extended to the two and a half rolls used in the $\Sigma^o\pi/\Lambda^o\pi^o$ scanning by using the single scan number of one prongs. The eight rolls were normalised using the total number of charged Σ hyperons produced at rest ($\Sigma^-\pi + \Sigma^+\pi + \Sigma^+p + \pi^+\pi^- + \pi^-p$). The number is common to both sets of data and a scaling factor was found. The classification

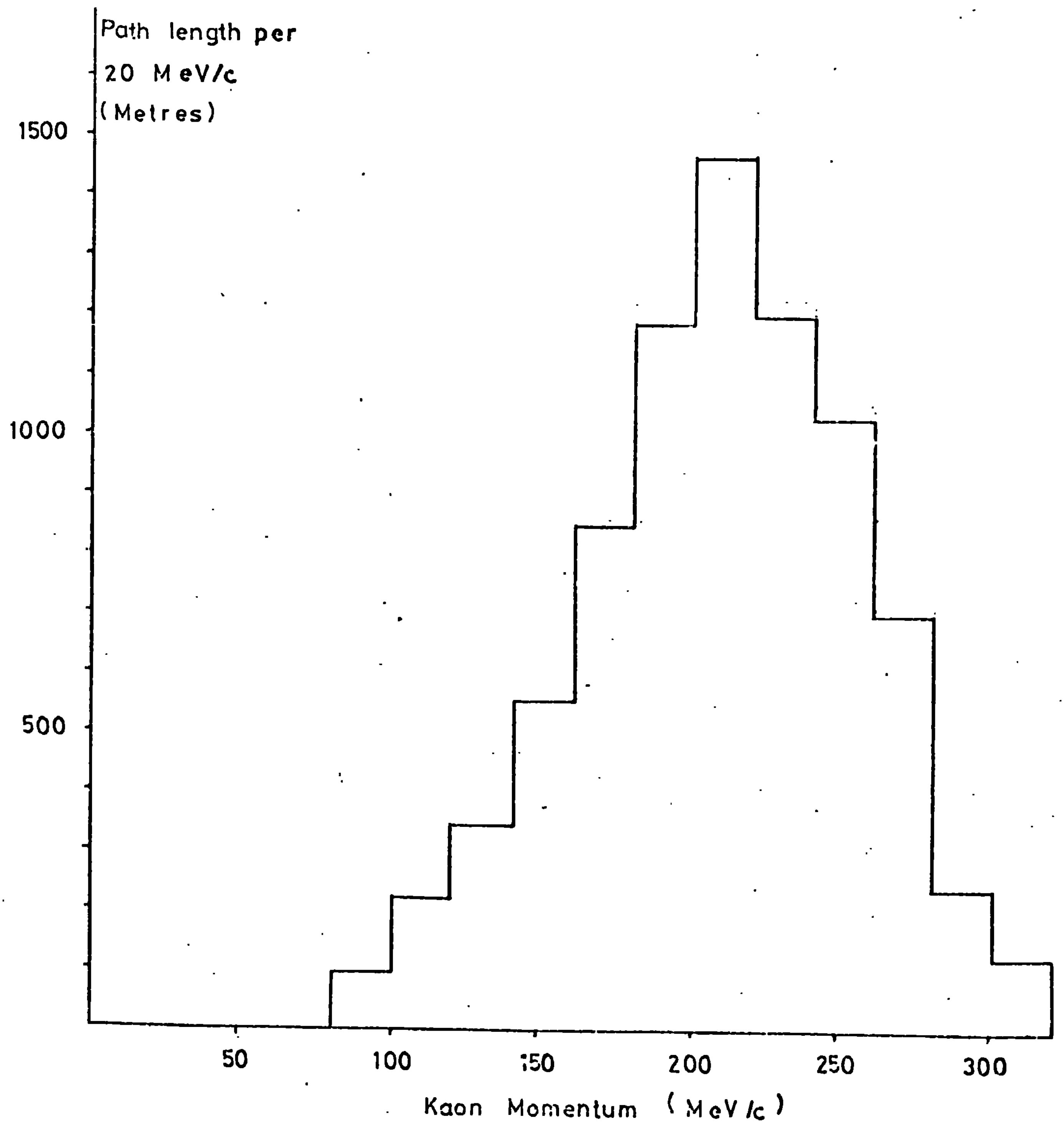

FIG 4.10: Primary Path Length Distribution

Table 4.8: Path Length Distribution

Momentum Interval Central Value MeV/c	Observed Number Of Decays	Corrected Number Of Decays	Decay Length (m)	Path Length (m)	Path Length Per 20 MeV/c (m)
85	16	52.4	0.639	33.5	96.6
95	27	88.4	0.714	63.1	
105	39	127.7	0.789	100.7	219.6
115	42	137.6	0.864	118.8	
125	51	167.0	0.939	156.8	336.2
135	54	176.9	1.014	179.4	
145	70	229.3	1.089	249.7	543.3
155	77	252.2	1.164	293.6	
165	105	343.9	1.239	426.1	843.9
175	97	317.7	1.315	417.8	
185	131	429.0	1.389	595.9	1185.6
195	123	402.8	1.464	589.7	
205	156	510.9	1.540	786.8	1511.5
215	137	448.7	1.615	724.7	
225	119	389.7	1.690	658.6	1196.2
235	93	304.6	1.765	537.6	
245	83	271.8	1.840	500.1	1026.9
255	84	275.1	1.915	526.8	
265	63	206.3	1.991	410.7	695
275	42	137.6	2.066	284.3	
285	16	52.4	2.141	112.2	235.6
295	17	55.7	2.216	123.4	
305	11	36.0	2.291	82.5	121.3
315	5	16.4	2.366	38.8	

of events into $\Sigma^-\pi$, $\Sigma^+\pi$ and $\pi^+\pi^-$ groups is dependent on the ability to distinguish the short hyperon track which in turn is dependent on the magnification of the scanning machine. In order to remove this magnification dependence between events scanned at different laboratories the total number of charged hyperons was used.

One assumption made in this method of extrapolation is that the beam operating conditions remained constant throughout the experiment. The five rolls of film used to determine the shape of the path length distribution sampled the entire exposure and an examination of the distribution of events inside the chamber as a function of roll number showed that there was no systematic, long term change in the beam focussing (see table 4.9). The variance is the mean square of the coordinate from the average value, and shows that the shape of the distribution remained

Table 4.9: Mean Coordinates Of $\Sigma^-\pi$ Events In Four Rolls Of Film

Roll Number	$\langle x \rangle$	Variance	$\langle y \rangle$	Variance	$\langle z \rangle$	Variance
22	-7.78 ± 0.22	59.5	-1.89 ± 0.14	26.8	23.02 ± 0.06	4.48
26	-9.61 ± 0.51	56.9	-0.01 ± 0.35	27.5	23.01 ± 0.14	4.83
78	-8.71 ± 0.61	62.2	$+0.74 \pm 0.43$	30.7	22.97 ± 0.16	4.04
104	-7.15 ± 0.32	62.7	-0.76 ± 0.23	33.5	22.92 ± 0.08	4.28

approximately constant. Each of the six channels studied in this work was scanned over different sections of the total 15½ rolls of film (see table 2.4) hence the path length normalisations will differ; these are summarised in table 4.10.

4.6 The Effect Of Errors Of Measurement On The Primary Momentum

The usual procedure for removing errors of measurement from a series of observations is to convolve the unknown "true" distribution (often parametrised) with a distribution which represents the errors of measurement in order to reproduce the observed results. The "true"

Table 4.10: Path Length Normalisations For Each Channel

20 MeV/c Momentum Intervals Central Value	Path Length (m) For Each Of The Channels Below			Percentage Error In Length
	$K^-p \to K^-p$	$K^-p \to \Sigma^{\pm}\pi^{\mp}$ $K^-p \to \overline{K^0}n$	$K^-p \to \Sigma^0\pi^0$ $K^-p \to \Lambda^0\pi^0$	
90	151	248	145	15.2
110	343	563	329	11.1
130	525	862	504	9.8
150	349	1393	815	8.2
170	1320	2163	1266	7.0
190	1854	3040	1779	6.3
210	2364	3876	2268	5.8
230	1871	3067	1795	6.9
250	1606	2633	1541	7.7
270	1087	1782	1043	9.8
290	368	604	353	17.4
310	190	311	182	25.0

The errors were calculated using poisson errors on the number of decays in each momentum interval. The error in the conversion factor is small (< 2%) and is neglected.

distribution is adjusted until a χ^2 test or a maximum likelihood method indicates that the best estimate has been reached. The procedure is straightforward if the error distribution is well known; this usually takes the form of a gaussian for 1/p quantities. However in the present situation the errors are distinctly non-gaussian and this is illustrated below. It will be seen that the bubble chamber technique is only accurate for momenta $\gtrsim$ 140 MeV/c.

4.6.1 Illustration Of The Error Problem

A typical distribution of vertex momenta is shown in fig. 4.7; this was determined using the measured momentum at the centre of the track and transforming this value to that at the vertex using a range-momentum table. This table may be parametrised as

$$R \propto p^{3.6} \qquad 4.8$$

where p is the particle momentum and R is the range. It is valid between momenta of approximately 30 MeV/c to 500 MeV/c for kaons and is adequate for the ensuing discussion.

Applying equation 4.8 to the vertex and 'centre of track' momenta gives:

$$R_c = Ap_c^{3.6} \quad \text{at the centre} \qquad 4.9$$

$$R_c - \ell_{\frac{1}{2}} = Ap_v^{3.6} \quad \text{at the vertex} \qquad 4.10$$

where $\ell_{\frac{1}{2}}$ is the track length (see fig. 4.11). Eliminating R_c and differentiating gives:

$$\frac{d\left(\frac{1}{p_v}\right)}{\left(\frac{1}{p_v}\right)} = \frac{d\left(\frac{1}{p_c}\right)}{\left(\frac{1}{p_c}\right)} \left(\frac{p_c}{p_v}\right)^{3.6} \qquad 4.11$$

This relation illustrates the important difficulty inherent in low momentum work where the ratio p_c/p_v is usually much greater than unity.

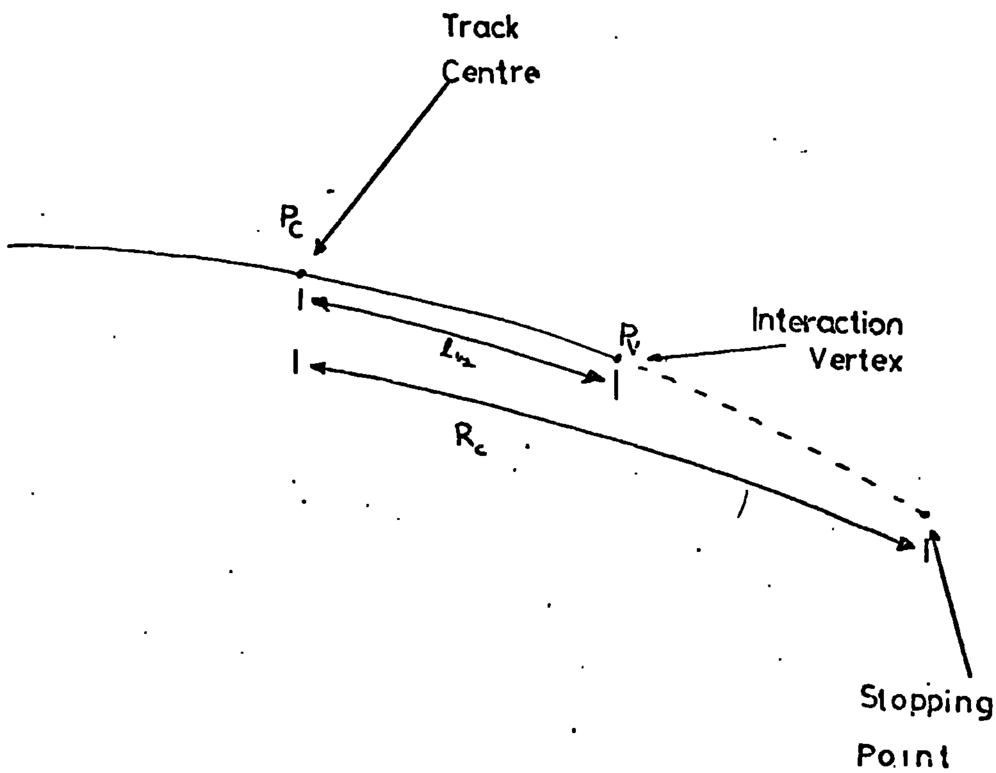

FIG 4.11: Diagram Defining Variables Used to Study Errors of measurement.

Consequently gaussian errors in $1/p_c$ become highly skew in $1/p_v$. High momentum studies will not suffer from this problem as $p_c \sim p_v$ and to first order the vertex quantities have the same error distributions as the quantities at the centre of track. The effect of equation 4.11 may be illustrated with reference to the momentum distribution of collinear (i.e. at rest) Σ hyperon events (fig. 7.2) where the distribution should be a delta function at zero momentum. The values of vertex momenta extrapolated from the measured momenta clearly extend up to 150 MeV/c. The peak at zero momentum is a technical feature and corresponds to all the events whose vertex momenta were required to be negative using the transformation from the track centre. This distribution reflects the effect of measurement errors, clearly there is a highly skew error distribution which needs careful consideration.

4.6.2 Outline Of Error Analysis

The method of calculating the distorted error distributions used the measured quantity which was known to have gaussion errors, namely the track curvature which corresponds to the reciprocal of the particle momentum at the centre of track, $1/p_c$.

The following procedure was adopted:

(i) A relationship was determined between the vertex momenta (p_v) and the corresponding $1/p_c$ values which could be used to transform a p_v distribution into its $1/p_c$ counterpart and vice-versa.

(ii) The widths of the gaussian errors of $1/p_c$ were parametrised

(iii) The gaussian error distributions, whose widths varied with $1/p_c$, were divided into equal vertex momentum intervals using the relationship from (i).

(iv) The non-gaussian error distributions arising from (iii) were convolved directly with the vertex momentum distributions to obtain an estimate of the effects of errors.

4.6.3 Reciprocal Momentum Distributions At The Track Centre

A distribution of $1/p_c$ values for a sample of events is difficult to interpret because of the different track lengths over which the primaries have been measured. It is possible however, to adjust the $1/p_c$ values using the range-momentum relation to correspond to a measurement made at a particular value of track half length, $\ell_{\frac{1}{2}}$. The value chosen for $\ell_{\frac{1}{2}}$ was an average value of 9.2 cm which ensured that most measurements were shifted by $\lesssim$ 20 MeV/c (see fig. 4.12) and this small change left the error distributions relatively unaltered. This adjustment took place in the high momentum region (> 200 MeV/c) which is outside the range of highly distorted errors. The effect of the adjustments is illustrated in fig. 4.13 for a sample of one prong decays, similar results were obtained for the interaction channels (fig. 4.14). A feature of this distribution is a structure at $1/p_c \sim 6.0$.

It is now possible to relate a value of vertex momentum (p_v) to a unique value of reciprocal momentum at the centre of the track ($1/p_c$). This is illustrated in table 4.11 for vertex momentum intervals of 20 MeV/c and is also shown schematically in fig. 4.16 later.

Table 4.11: Relation Between p_v And ($1/p_c$)

p_v (GeV/c)	$1/p_c$ (GeV/c)$^{-1}$	p_v	$1/p_c$
0.0	6.214	0.18	5.127
0.02	6.214	0.20	4.797
0.04	6.213	0.22	4.491
0.06	6.204	0.24	4.172
0.08	6.170	0.26	3.906
0.10	6.088	0.28	3.655
0.12	5.940	0.30	3.426
0.14	5.729	0.32	3.220
0.16	5.440		

FIG 4·12: Difference Between Measured and Adjusted Momenta.

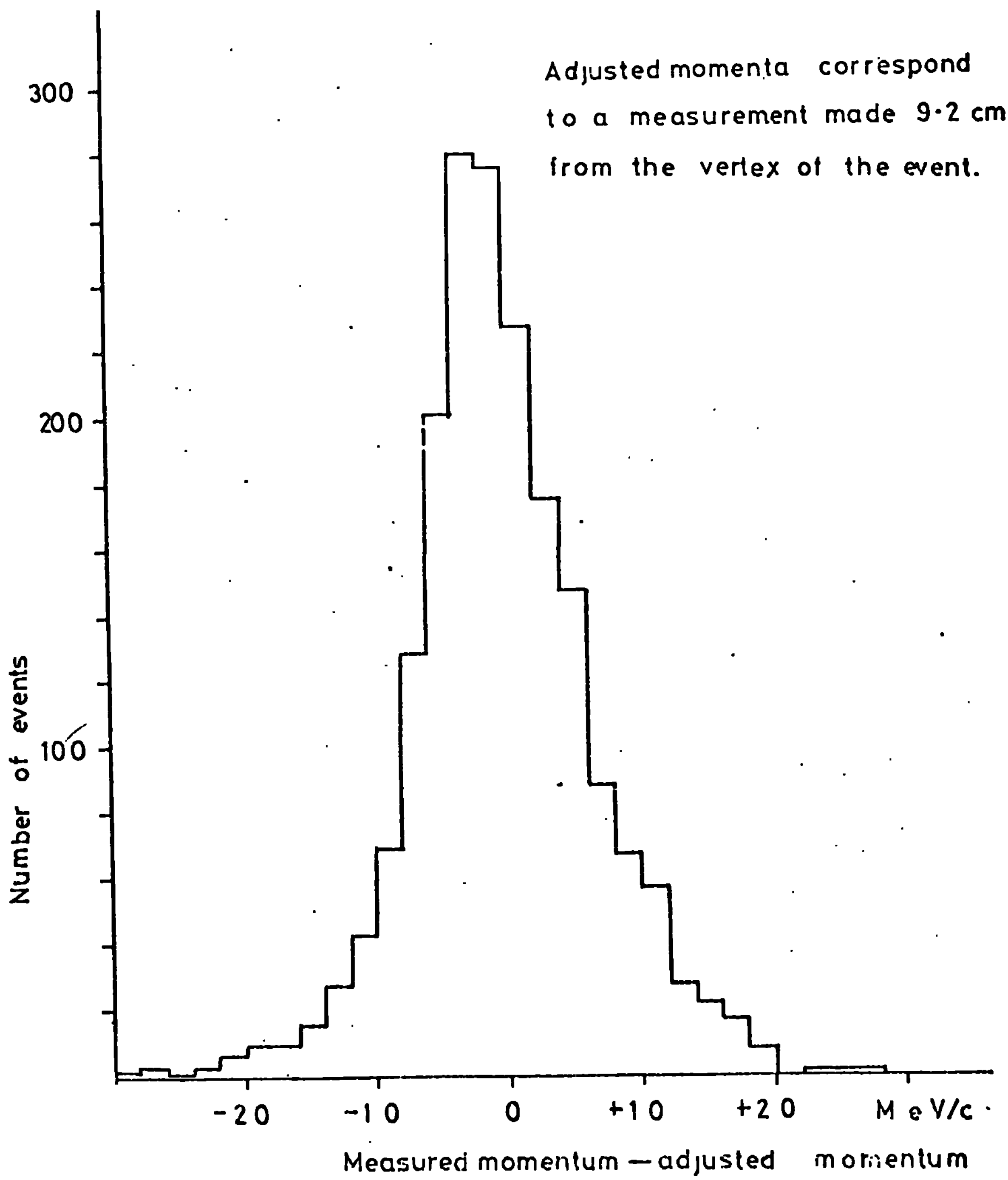

FIG 4·13: Comparison of Measured and Modified Reciprocal Momenta for K^- Decays.

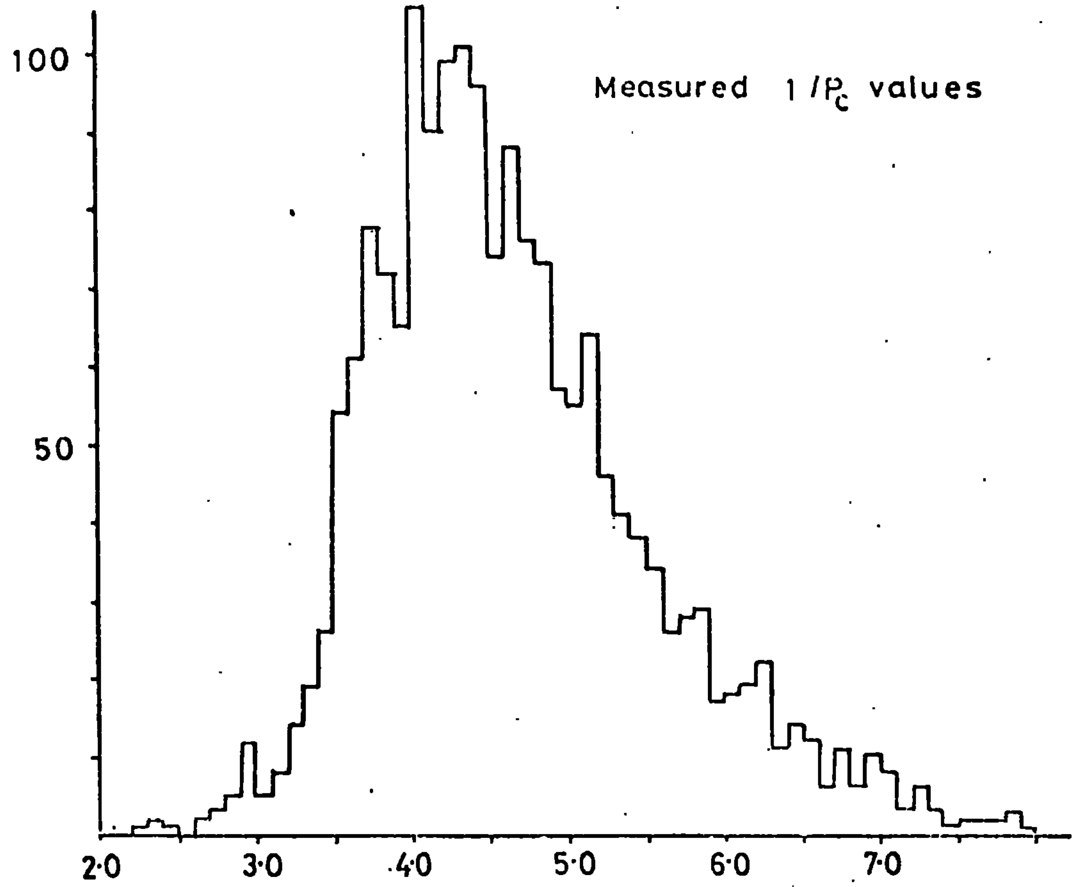

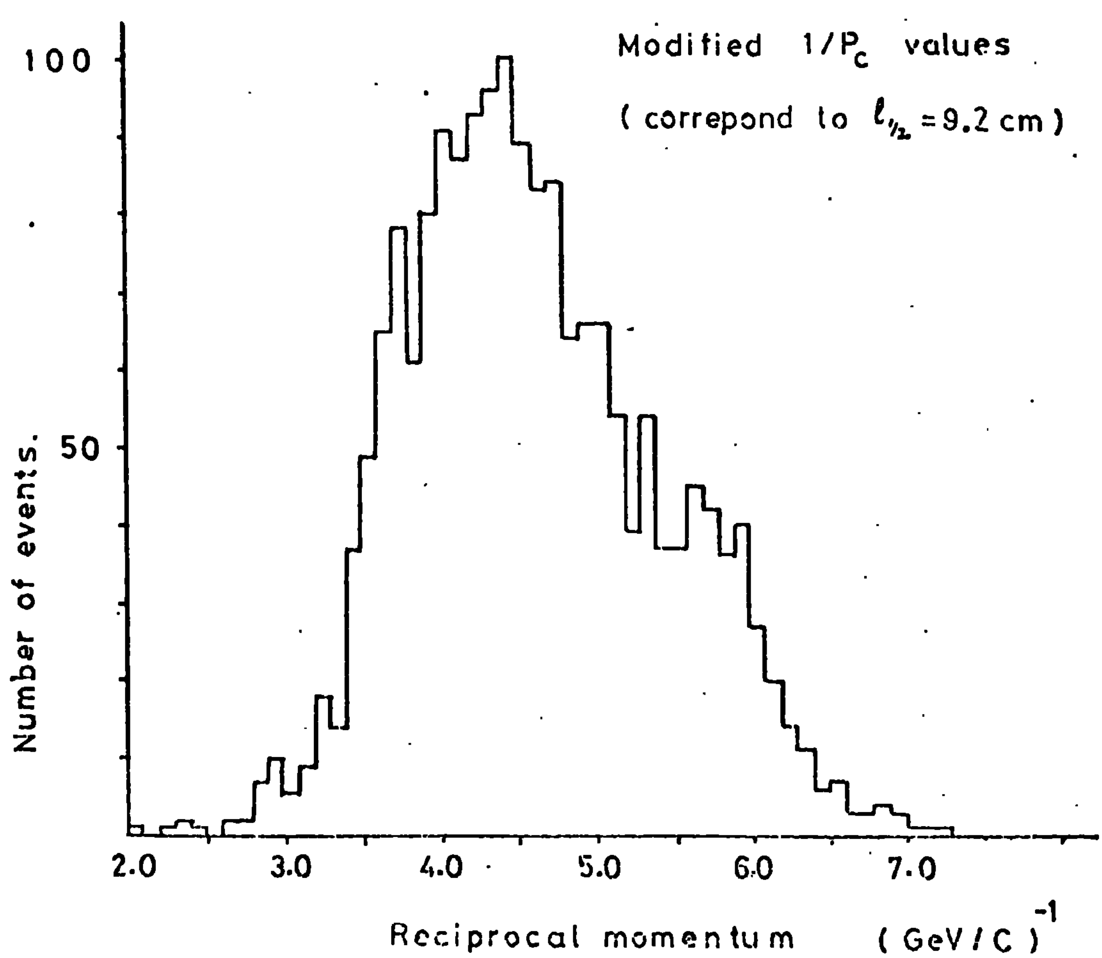

FIG 4·14: MODIFIED RECIPROCAL MOMENTUM DISTRIBUTIONS

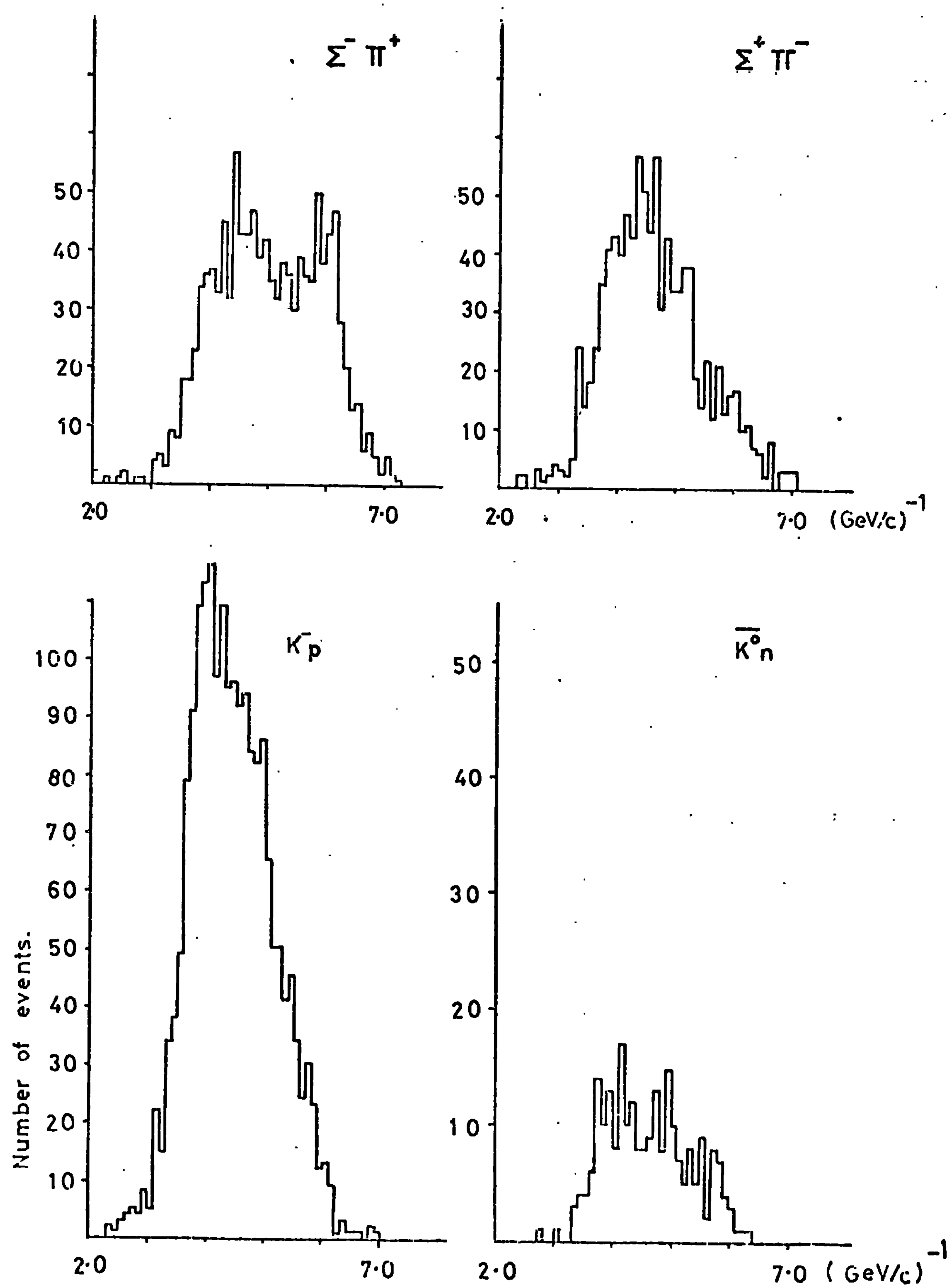

Clearly, equal intervals in the p_v values do not transform into equal $1/p_c$ intervals. In order to transform a p_v distribution of 20 MeV/c intervals into a $1/p_c$ distribution of 0.1 $(GeV/c)^{-1}$ intervals, a redistribution must be carried out. This transformation procedure may be represented in matrix notation by

$$A\,x_v = x_c \qquad 4.12$$

where vectors x_v and x_c represent the contents of the vertex and centre of track distributions respectively and A is the transformation matrix which depends on the interval widths used and the mean length of track between the vertex and track centre (9.2 cm in this work). Table 4.12 shows the form of matrix A and it is able to show where an event, falling in a particular p_v interval, would lie in the corresponding $1/p_c$ intervals. It is clear from this table that by summing the rows of the matrix that the Jacobian relating $1/p_v$ to $1/p_c$ will enhance the population of $1/p_c$ values in the region ~ 6.0 and lead to the structure that is observed.

The functional relationship between p_v and $1/p_c$ has now been found and the next problem to be considered is the error variation of the $1/p_c$ values.

4.6.4 Parametrisation Of The Errors In $1/p_c$

The error of measurement at the track centre $\Delta(1/p_c)$ depends on the values of $1/p_c$ and $\ell_{\frac{1}{2}}$. In fig. 4.15 the values of $\Delta(1/p_c)$ increase approximately linearly with $1/p_c$, the dispersion about this mean increase is caused by the dependence of $\Delta(1/p_c)$ on $\ell_{\frac{1}{2}}$ and is of secondary importance. Hence only the former was used to derive the parametrisation of the $\Delta(1/p_c)$ behaviour:

$$\Delta\left(\frac{1}{p_c}\right) = 0.125\left(\frac{1}{p_c}\right) - 0.29 \qquad 4.13$$

Using the results in these last two sections it is now possible to derive

Table 4.12: Matrix For Converting 20 MeV/c p_v Intervals Into 0.1 $(GeV/c)^{-1}$ Intervals Of $1/p_c$

$p_v \longrightarrow$ MeV/c

$\frac{1}{p_c}$ ↓ GeV/c^{-1}	20–40	40–60	60–80	80–100	100–120	120–140	140–160	160–180	180–200	200–220	220–240	240–260	260–280	280–300	300–320
3.25	–	–	–	–	–	–	–	–	–	–	–	–	–	–	.390
3.35	–	–	–	–	–	–	–	–	–	–	–	–	–	–	.486
3.45	–	–	–	–	–	–	–	–	–	–	–	–	–	.324	.124
3.55	–	–	–	–	–	–	–	–	–	–	–	–	–	.436	–
3.65	–	–	–	–	–	–	–	–	–	–	–	–	.180	.240	–
3.75	–	–	–	–	–	–	–	–	–	–	–	–	.399	–	–
3.85	–	–	–	–	–	–	–	–	–	–	–	–	.399	–	–
3.95	–	–	–	–	–	–	–	–	–	–	–	.354	.023	–	–
4.05	–	–	–	–	–	–	–	–	–	–	–	.376	–	–	–
4.15	–	–	–	–	–	–	–	–	–	–	.088	.270	–	–	–
4.25	–	–	–	–	–	–	–	–	–	–	.314	–	–	–	–
4.35	–	–	–	–	–	–	–	–	–	–	.314	–	–	–	–
4.45	–	–	–	–	–	–	–	–	–	.031	.284	–	–	–	–
4.55	–	–	–	–	–	–	–	–	–	.327	–	–	–	–	–
4.65	–	–	–	–	–	–	–	–	–	.327	–	–	–	–	–
4.75	–	–	–	–	–	–	–	–	.010	.316	–	–	–	–	–
4.85	–	–	–	–	–	–	–	–	.303	–	–	–	–	–	–
4.95	–	–	–	–	–	–	–	–	.303	–	–	–	–	–	–
5.05	–	–	–	–	–	–	–	–	.303	–	–	–	–	–	–
5.15	–	–	–	–	–	–	–	.234	.081	–	–	–	–	–	–
5.25	–	–	–	–	–	–	–	.319	–	–	–	–	–	–	–
5.35	–	–	–	–	–	–	–	.319	–	–	–	–	–	–	–
5.45	–	–	–	–	–	–	.206	.129	–	–	–	–	–	–	–
5.55	–	–	–	–	–	–	.346	–	–	–	–	–	–	–	–
5.65	–	–	–	–	–	–	.346	–	–	–	–	–	–	–	–
5.75	–	–	–	–	–	.336	.102	–	–	–	–	–	–	–	–
5.85	–	–	–	–	–	.476	–	–	–	–	–	–	–	–	–
5.95	–	–	–	–	.407	.188	–	–	–	–	–	–	–	–	–
6.05	–	–	–	.149	.543	–	–	–	–	–	–	–	–	–	–
6.15	–	–	.290	.851	–	–	–	–	–	–	–	–	–	–	–
6.25	1.0	1.0	.110	–	–	–	–	–	–	–	–	–	–	–	–

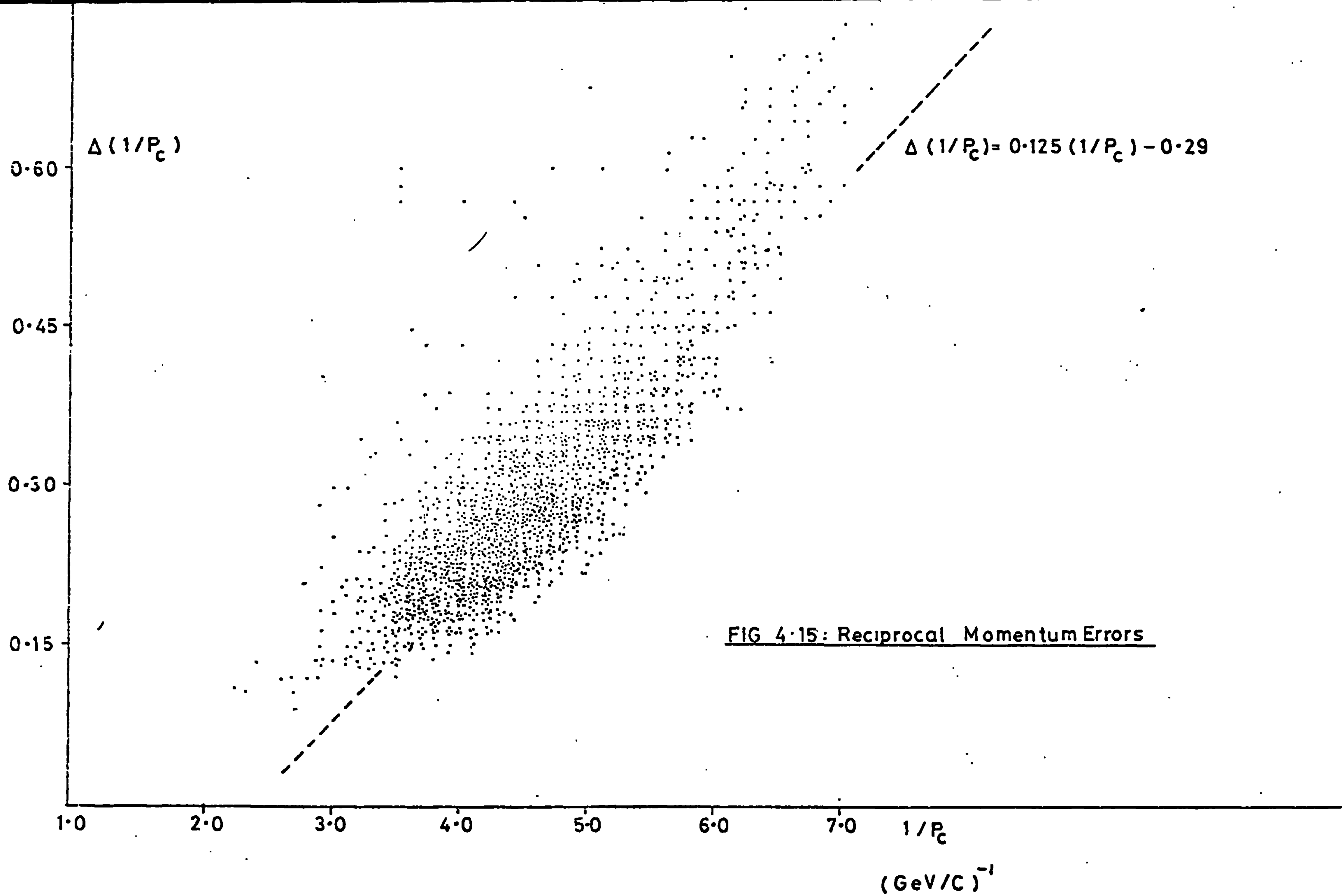

FIG 4·15: Reciprocal Momentum Errors

a theoretical model for the $1/p_c$ distribution, fold in errors of measurement (see fig. 4.16) and compare the results with those actually observed (see fig. 4.14).

4.6.5 Theoretical Reciprocal Momentum Distribution

The probability of an event occuring at a particular value of $1/p_c$ can be calculated using the range-momentum relation

$$R = ap^b$$

Assuming that the cross-section for strong interactions varies with momentum as power law

$$\sigma = kp^{-\alpha} \qquad 4.14$$

then the mean free path λ is

$$\lambda = \frac{p^\alpha}{nk} \qquad 4.15$$

where k, α and a are constants, n is the number of target nuclei per unit volume. For decays 4.15 simplifies to

$$\lambda = \frac{c\tau p}{m} \qquad \text{as} \quad \alpha = 1$$

If a particle travels a distance dx whilst losing momentum dp_v, then the probability of interaction in the vertex momentum interval p_v to $p_v + dp_v$ is given by

$$P(p_v)dp_v = \frac{dx}{\lambda} \qquad \text{providing that } dx \ll \lambda$$

The particle range is $R_v = ap_v{}^b$

hence $dx \equiv dR_v = abp_v{}^{b-1}\, dp_v$

$$\therefore \qquad P(p_v)dp_v = abp_v{}^{b-1} \frac{dp_v}{\lambda}$$

and this leads to $P(p_v)dp_v = \dfrac{nab}{k}\, p_v{}^{b-1-\alpha}\, dp_v$ 4.16

Using equations 4.9 and 4.10 to convert p_v to p_c gives

$$p_v = \left(p_c{}^b - \frac{\ell_{1/2}}{a}\right)^{1/b}$$

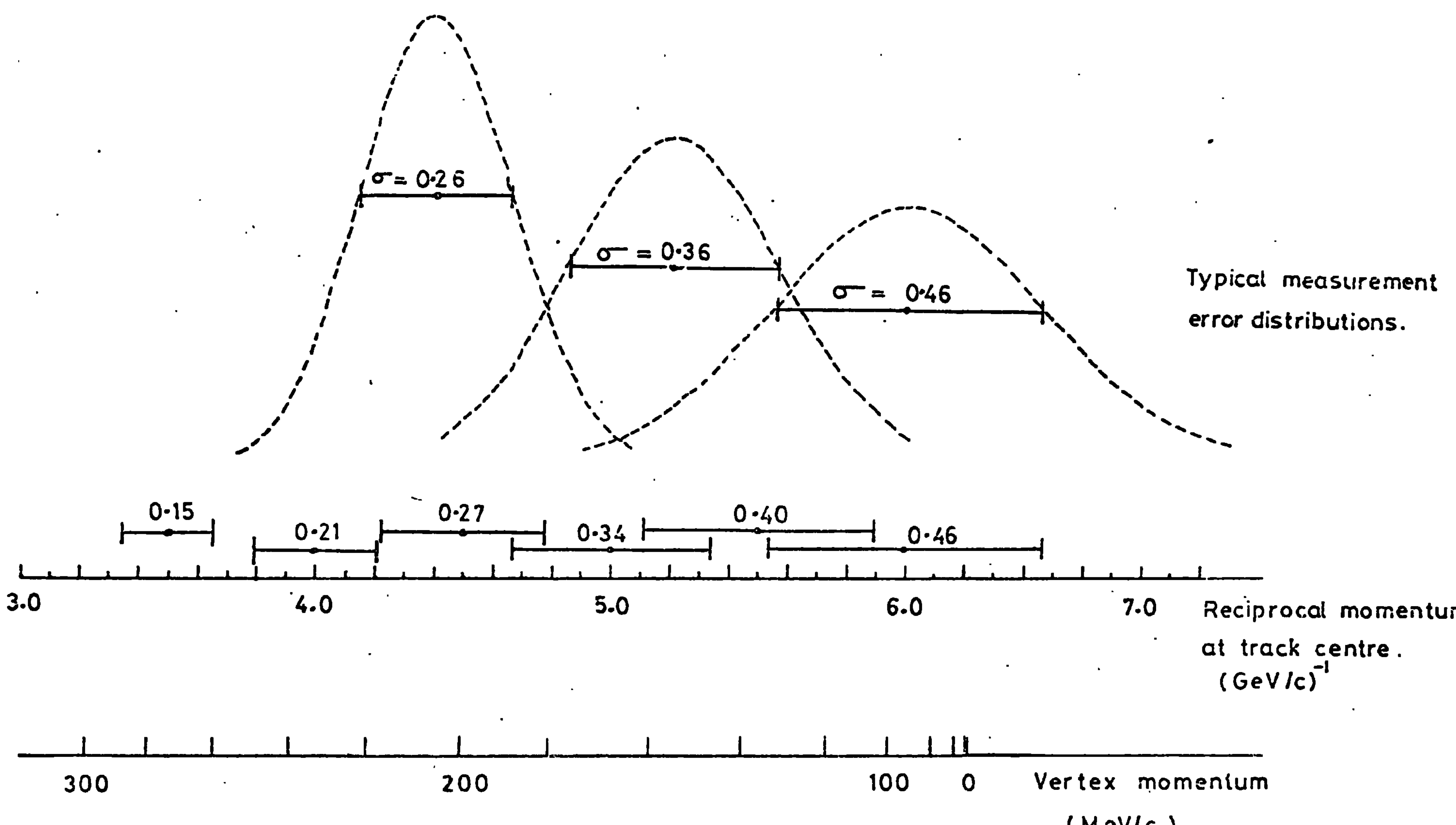

FIG 4·16: Schematic Representation of the Relation Between Vertex and Centre of Track Quantities.

On differentiating this expression to find dp_v/dp_c and substituting for p_v and dp_v in equation 4.16 gives

$$P(p_c)dp_c = \frac{nab}{k}\left(p_c^{\,b} - \frac{\ell_{\frac{1}{2}}}{a}\right)^{-\alpha/b} p_c^{\,b-1}\,dp_c$$

making the substitution $r_c = 1/p_c$ leads to the final result:

$$P(r_c)dr_c = \frac{nab}{k}\left(r_c^{-b} - \frac{\ell_{\frac{1}{2}}}{a}\right)^{-\alpha/b} r_c^{-(b+1)}\,dr_c \qquad 4.17$$

This result gives the probability that an event, in a channel having a mean free path with power law behaviour, occurs in a particular reciprocal momentum interval.

As $\left(r_c^{-b} - \frac{\ell_{\frac{1}{2}}}{a}\right) \longrightarrow 0$ the probability will rise rapidly, and the value of α will affect both the rapidity of the rise and the value r_c at which the rise becomes dominant. The theoretical distributions have been plotted for decays (α = 1 exactly) and for Σ^- hyperon production ($\alpha \sim 2.0$) (see figs, 4.17, and 4.18) for values of $r_c > 4.4$. This limit was imposed because the expression 4.17 does not take into account the a priori probability of an event entering the chamber with momentum p. Below $\sim$ 230 MeV/c the flux of particles is approximately constant, there being only a few interactions in-flight and only a small number of kaons with entrance momenta below this value.

The probability of decay as a function of vertex momentum was evaluated using the decay law and attenuation due to interactions was included. This probability distribution was transformed to the track centre and compared with the results obtained using equation 4.17 (see fig. 4.17). The agreement indicates that the neglect of beam attenuation in equation 4.17 is unimportant.

Finally the errors of measurement were convolved into the

FIG 4·17: Theoretical and Observed r_c Distributions for K^- Decays

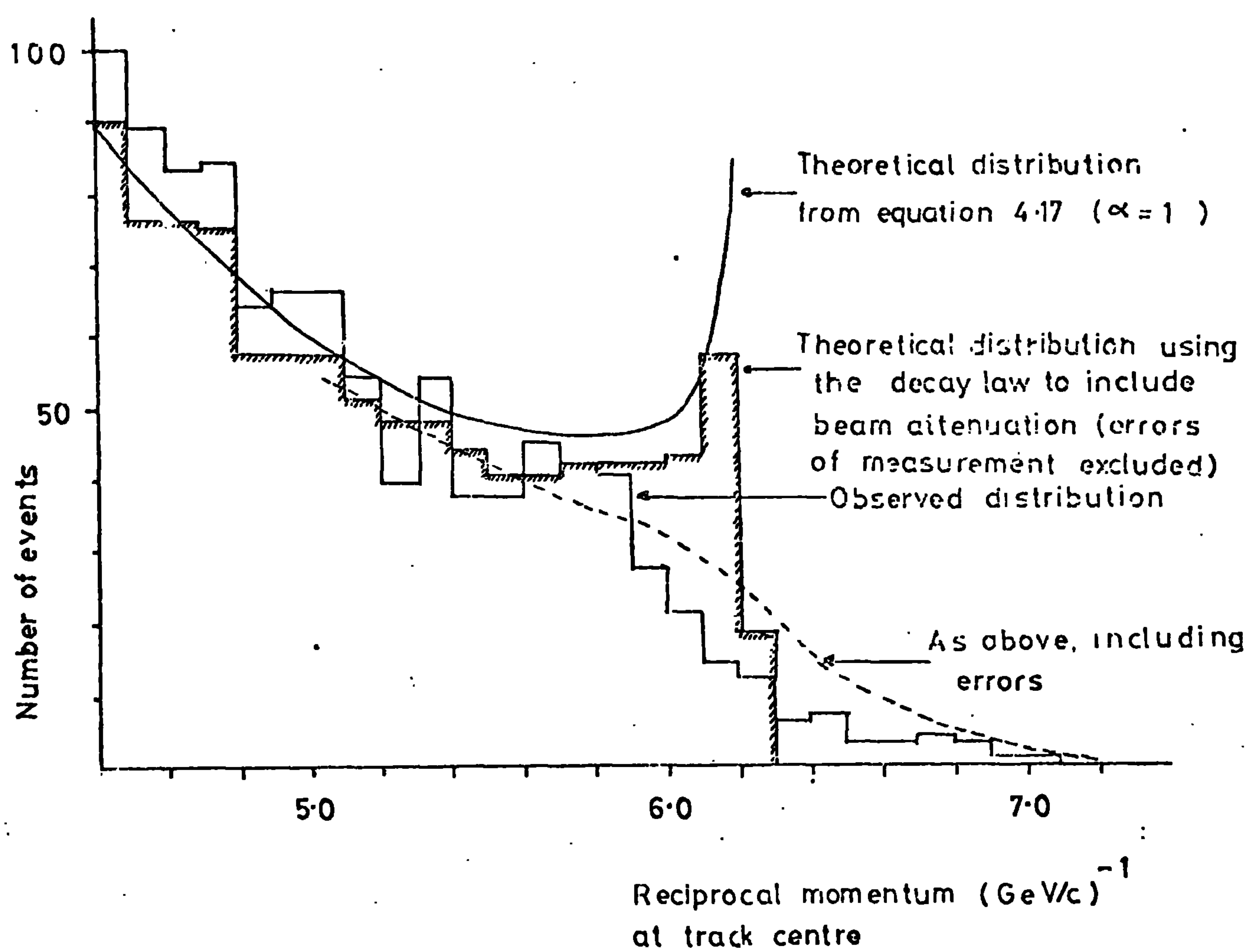

FIG 4·18 : Theoretical and Observed r_c Distributions

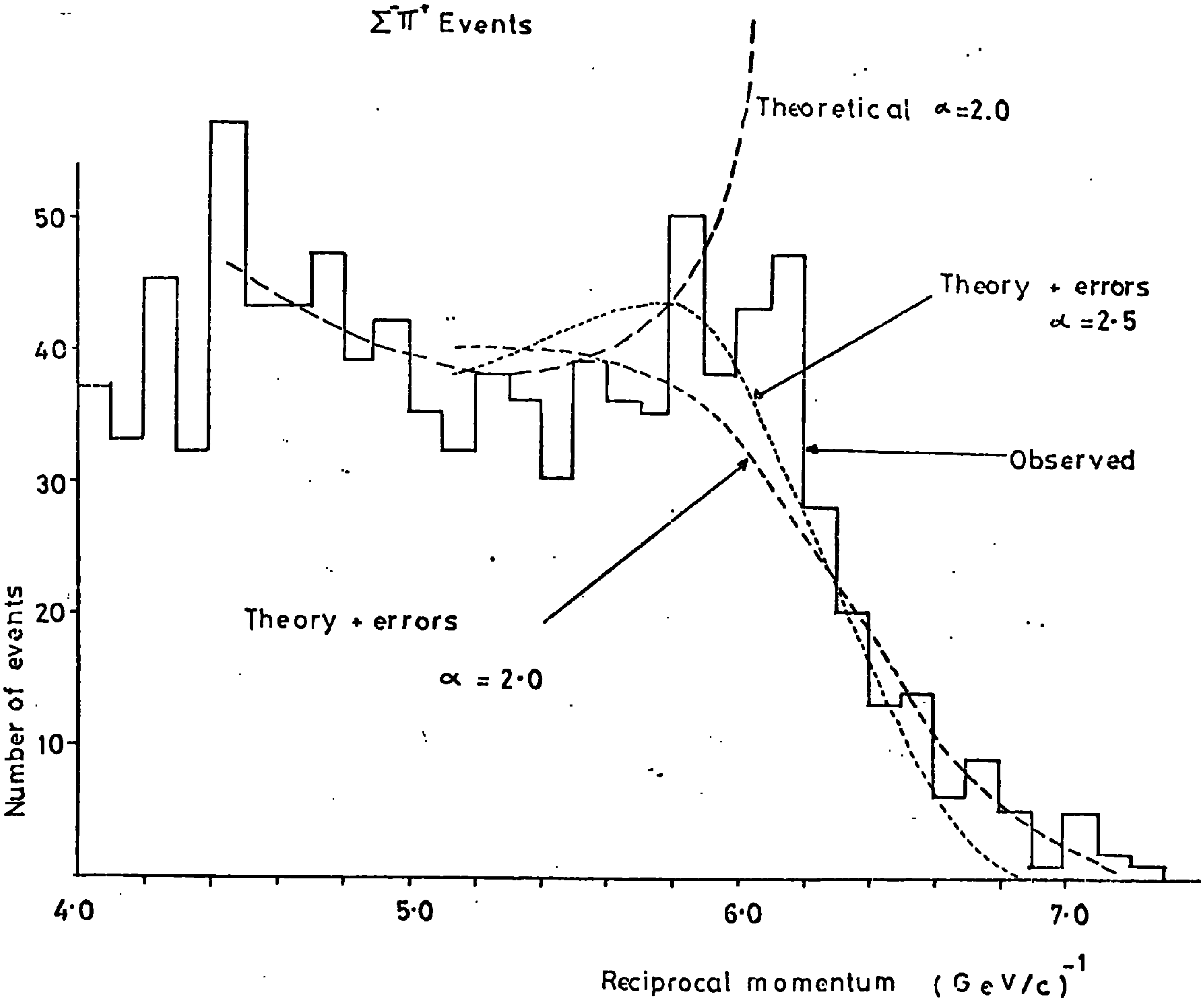

theoretical distribution to produce an expected distribution of r_c. This is consistent with the observed r_c distribution for one prong decays. The observed behaviour of the r_c distribution for Σ^- production is consistent with the power law behaviour of the cross-section given by $\alpha = 2$, although $\alpha = 2.5$ gives an improved description and suggests that the results of Kim (from which the value of α was derived) could be under estimates of the true values. The effect of errors is important for $r_c > 5.8$ which corresponds to vertex momenta below 140 MeV/c.

The r_c distribution for Σ^+ production is consistent with $\alpha \sim 1$ and agrees with the previous results of Kim (3). The r_c distributions for the remaining channels were not studied for various reasons. Firstly, the elastic scatter events which were measured and appeared on the final D.S.T were not a completely unbiased sample of events from the entire momentum range Secondly, the charge exchange channel which has a threshold of 90 MeV/c can not be described by a power law dependent cross-section. Finally the neutral hyperon events were not studied below $\sim$ 140 MeV/c and the poor statistics of in-flight events would yield little information.

Having shown that the r_c distribution is understandable using this simple model, the remainder of the error analysis can be presented with confidence.

4.6.6 Determination Of The Non-gaussian Error Distributions

This determination was carried out using the vertex momentum intervals which had been transformed into r_c space (see fig. 4.19). The central value of the vertex interval was transformed to r_c and equation 4.13 was used to determine the width of the gaussian error distribution. The probability of a measurement lying within a particular vertex momentum interval was found simply by calculating the area under the gaussian in that interval. This was done for each vertex momentum interval, each of which used a slightly different gaussian. The results are shown in fig. 4.20 which gives the probability distribution for each central value

FIG 4·19: Example to Illustrate the Method of Calculating the non gaussian Error Distributions.

Probability of an event with momentum 160–180 being measured as 160–180 MeV/c is $\dfrac{\text{area A} - \text{area B}}{\text{total area under gaussian}}$

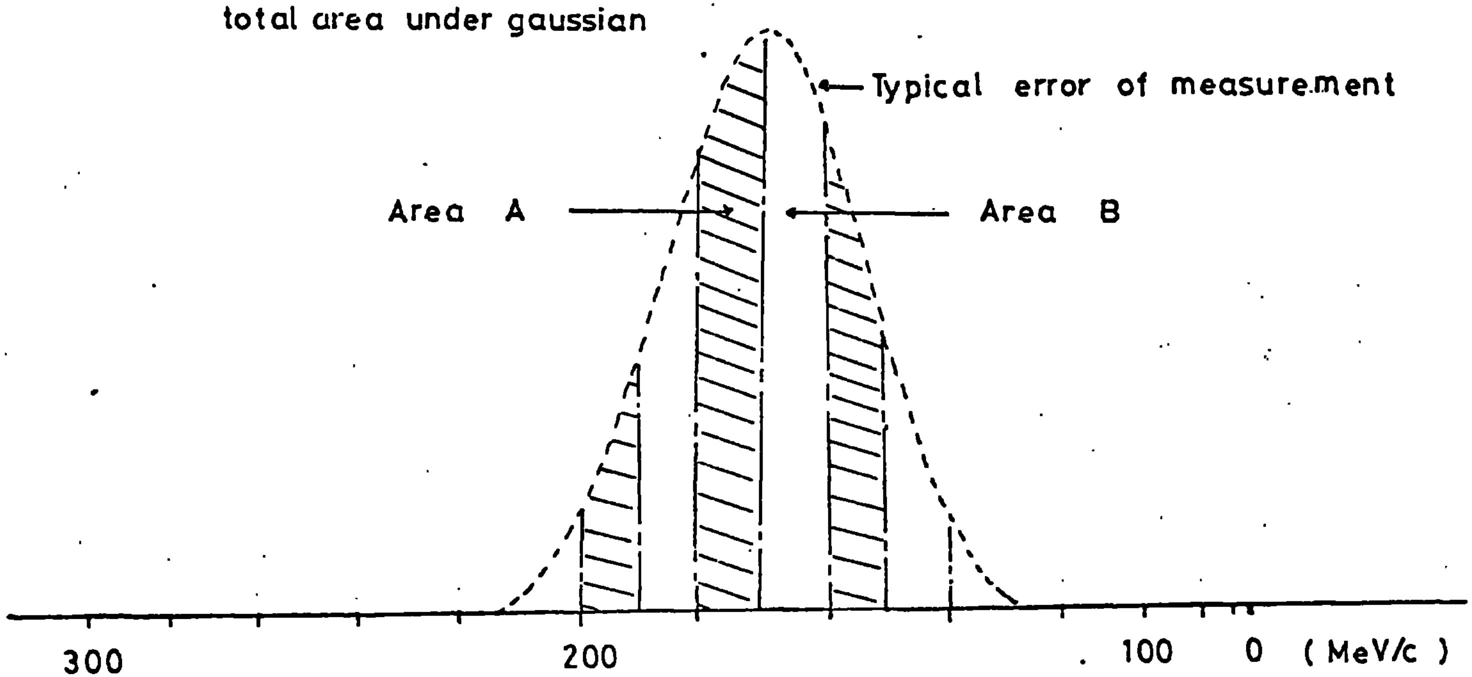

Vertex momentum transformed to r_c space

FIG 4·20: Non-gaussian Error Distribution for Various True Momentum Intervals (denoted by their central values).

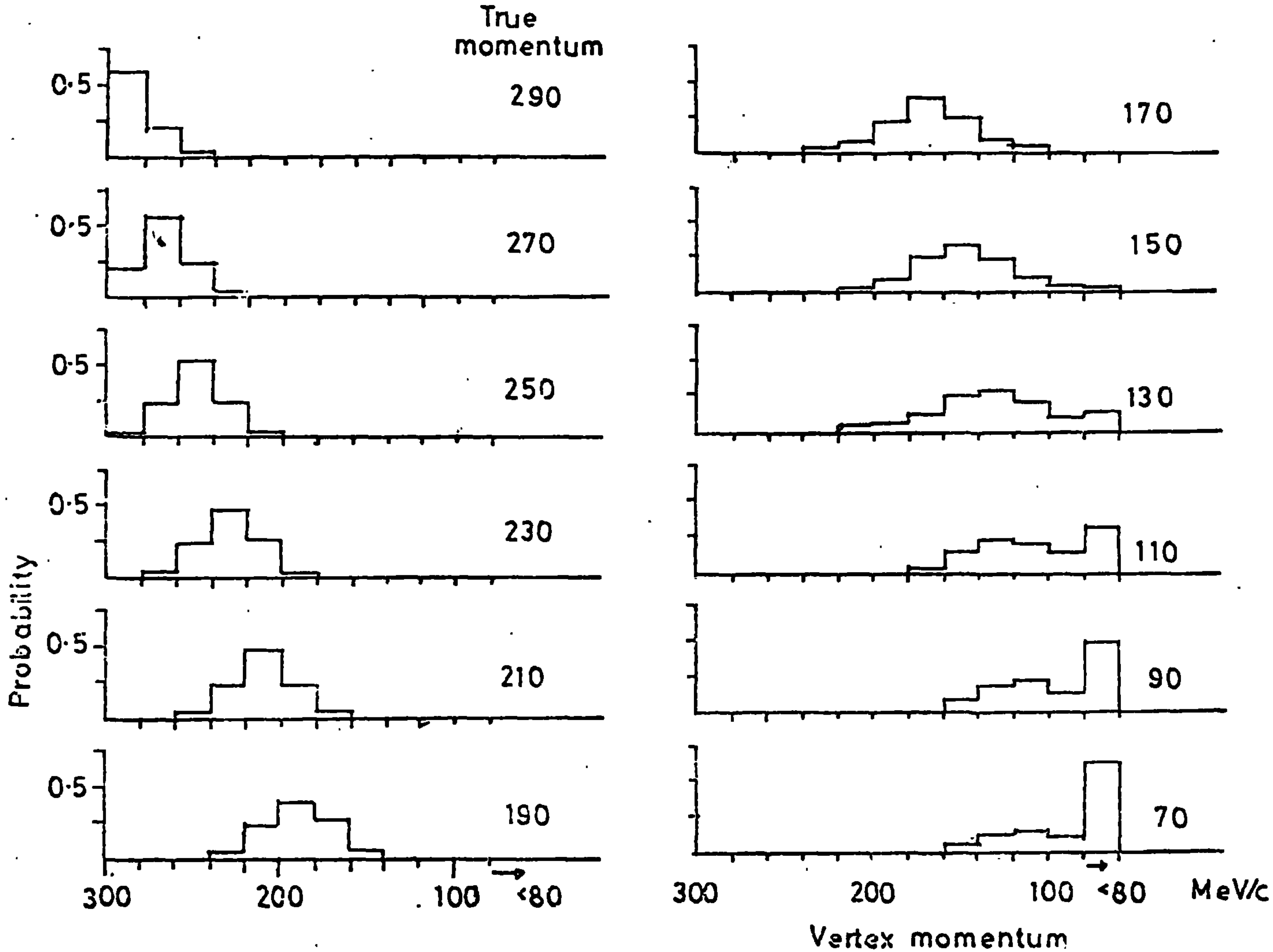

of vertex momentum used.

These distributions may be represented in matrix form thus:

$$x_{obs} = A_{err} x_{true} \qquad 4.18$$

where the column vectors x_{obs} and x_{true} contain the numbers of events in each momentum interval for the observed and "true" distributions respectively. A is the conversion matrix and is shown in table 4.13.

4.6.7 Estimation Of The Effects Of Errors Of Measurement

Because of the complex nature of the momentum distributions (see for example, fig. 4.7) for the interaction channels a simple parametrisation of the true distribution is not possible. The observed distribution was used as an approximation to the "truth" (the spike at 0-20 MeV/c was ignored) and the errors were convolved into this distribution to produce an artificial distribution broader than the original which reflected the effect of errors of measurement on the "true" values. The broadening of the observed distribution by the error conversion matrix was reversed and subtracted from the observed distribution to produce an estimate of the "true" momentum distribution. This is best illustrated by example in the table 4.14.

The observed distribution is presented in the column labelled $N_{obs}(p)$. Each of these numbers is divided into momentum intervals according to the matrix A_{err}. The columns are summed to give the artificially broadened momentum distribution. The row marked "Change" indicates the effect of the broadening, and these numbers are negated and then added to the origonal observed distribution to give the estimate of the true distribution. A correction factor was then determined and was defined as

$$N_t(p) = f(p)\, N_{obs}(p) \qquad 4.19$$

This procedure was carried out for the one prong decays, charged hyperons and neutral kaon production channels.

Table 4.13: The Error Conversion Matrix A_{err}

Observed Momentum Intervals	"True" Momentum Intervals → MeV/c 300 - 280	280 - 260	260 - 240	240 - 220	220 - 200	200 - 180	180 - 160	160 - 140	140 - 120	120 - 100	100 - 80	< 80
300 - 280	0.580	0.197	0.005	—	—	—	—	—	—	—	—	—
280 - 260	0.196	0.554	0.224	0.080	—	—	—	—	—	—	—	—
260 - 240	0.023	0.218	0.527	0.220	0.017	—	—	—	—	—	—	—
240 - 220	—	0.034	0.237	0.456	0.253	0.018	—	—	—	—	—	—
220 - 200	—	—	0.044	0.215	0.477	0.228	0.032	—	—	—	—	—
200 - 180	—	—	—	0.047	0.234	0.395	0.250	0.046	—	—	—	—
180 - 160	—	—	—	0.008	0.069	0.226	0.383	0.241	0.062	0.010	—	—
160 - 140	—	—	—	—	0.015	0.076	0.242	0.335	0.216	0.080	0.020	0.002
140 - 120	—	—	—	—	0.004	0.023	0.105	0.235	0.267	0.176	0.073	0.116
120 - 100	—	—	—	—	—	—	0.005	0.134	0.214	0.197	0.108	0.302
100 - 80	—	—	—	—	—	—	—	0.081	0.157	0.175	0.112	0.475
<80	—	—	—	—	—	—	—	0.047	0.102	0.131	0.096	0.625

Table 4.14: Estimations Of Broadening Effect Of Measurement Errors

(Rounded To Nearest Whole Number)

Momentum		$N_{obs}(p)$	1	2	3	4	5	6	7	8	9	10	11	
300 - 280	1	30	17	6	–	–	–	–	–	–	–	–	–	
280 - 260	2	129	25	71	29	1	–	–	–	–	–	–	–	
260 - 240	3	186	4	41	98	41	3	–	–	–	–	–	–	
240 - 220	4	245	–	8	58	112	62	4	–	–	–	–	–	
220 - 240	5	319	–	–	14	68	152	73	10	–	–	–	–	
200 - 180	6	270	–	–	–	13	63	107	68	12	–	–	–	
180 - 160	7	227	–	–	–	2	20	51	87	55	14	2	–	
160 - 140	8	159	–	–	–	–	2	12	38	53	34	13	3	
140 - 120	9	115	–	–	–	–	–	3	12	27	31	20	8	
120 - 100	10	88	–	–	–	–	–	–	–	12	19	17	9	
100 - 80	11	51	–	–	–	–	–	–	–	4	8	9	6	
			46	126	199	237	302	250	215	163	106	61	26	Artificially Broadened
			16	-3	13	-8	-17	-20	-12	4	-9	-27	-25	Change
			14	132	173	253	376	290	239	155	124	115	76	True Distribution N_t (p)
			0.47	1.02	0.93	1.03	1.05	1.07	1.05	0.97	1.07	1.31	1.49	Correction Factor f (p)

The channel cross-sections depend on the ratio of two number distributions (see Equation 4.2) hence the effect of errors of measurement is only the ratio of the factors f(p) (determined from equation 4.19) for each channel to that for the decays. Table 4.15 summarises the results.

These results clearly indicate that there is no systematic change in the cross-section values for momenta in the range 120 - 260 MeV/c. The large fluctuations of the ratio above ~ 260 MeV/c are due to low statistics, the errors being 30 - 100%. A typical error in the centre of the distribution (~ 200 MeV/c) is ~ 10% for the $\Sigma^{\pm}$ channels and ~ 20% for the $\overline{K^o}$ channel.

4.6.8 Conclusions

Within the present statistical errors (~ 5 - 15%) it is clearly unnecessary to remove the effect of errors of measurement. The r_c distribution approach to this problem gives a clear indication of the magnitude of the difficulties involved in removing the errors. Fig. 4.16 demonstrates that for momenta below 160 MeV/c, r_c errors of $<$ 0.2 (3% errors) are required before the gaussian error distributions cease to spread over several momentum intervals.

Typical errors for the bubble chamber technique are ~ 5% and this indicates that bubble chambers are inadequate for high precision analyses below ~ 160 MeV/c.

Table 4.15: Summary Of Correction Factors To Allow For Errors Of Measurement And Their Effect On The Channel Cross-Sections

Momentum Interval	f(p) Decays	f(p) Σ^-	f(p) Σ^+	f(p) $\overline{K^o}$	$\frac{f(p)\ \Sigma^-}{f(p)\ \text{Decays}}$	$\frac{f(p)\ \Sigma^+}{f(p)\ \text{Decays}}$	$\frac{f(p)\ \overline{K^o}}{f(p)\ \text{Decays}}$
80 - 100	1.49	1.57	1.47	-	1.05	1.47	-
100 - 120	1.31	1.37	1.26	1.54	1.05	0.96	1.17
120 - 140	1.07	0.87	0.94	1.07	0.81	0.94	1.00
140 - 160	0.97	0.99	1.09	1.09	1.02	1.09	1.12
160 - 180	1.05	0.99	1.07	1.14	0.94	1.02	1.09
180 - 200	1.07	1.06	1.06	1.03	0.99	0.99	0.96
200 - 220	1.05	1.07	1.10	1.03	1.02	1.05	0.98
220 - 240	1.03	0.97	1.06	1.09	0.94	1.03	1.06
240 - 260	0.93	0.99	1.01	1.00	1.07	1.08	1.08
260 - 280	1.02	0.85	0.77	1.07	0.83	0.75	1.05
280 - 300	0.47	0.73	1.07	-	1.55	2.27	-

CHAPTER FIVE

CHANNEL CROSS-SECTIONS II

The cross-sections for low energy K^-p interactions are presented in this chapter together with details of the corrections applied to the observed numbers of events in each momentum interval. These corrections account for losses which on the whole are due to special geometrical configurations of the events causing it either to be classified in another category (e.g. 210 as 200 topology) or to be unmeasurable.

Using the known properties of the angular distributions and, where applicable, the particle lifetimes an estimate for some of these losses may be obtained. Other losses such as the scanning efficiency and that due to unmeasurable events are calculated separately. The latter correction applies only to those events which are unmeasurable for entirely random reasons, e.g. poor film illumination or obscuration by fogging on the film. The unmeasurable category of events has been divided into two parts to calculate this (see § 3.4).

The effect, if any, of the narrow chamber must also be considered as a possible source of loss or systematic error in the event detection.

5.1 Charged Hyperon Production

At these low momenta charged Σ hyperons are produced in the following two channels:

$$K^- + p \longrightarrow \Sigma^+ + \pi^-$$

$$K^- + p \longrightarrow \Sigma^- + \pi^+$$

These are followed by decay into

$$\Sigma^+ \longrightarrow n + \pi^+ \qquad (\Sigma^+_\pi \text{ events})$$

$$\Sigma^+ \longrightarrow p + \pi^0 \qquad (\Sigma^+_\pi \text{ events})$$

$$\Sigma^- \longrightarrow n + \pi^- \qquad (\Sigma^-_\pi \text{ events})$$

The probability of the hyperon interacting strongly with a proton is small compared to that of the decay process; however if the Σ^- hyperon loses all its kinetic energy by ionisation before the decay occurs it may be absorbed by a proton to produce neutral particles:

$$\Sigma^- + p \longrightarrow n + \Lambda^o$$

These events will be clasified as two prong, Σ^-_σ , events. The Σ^+_π, Σ^+_p and Σ^-_π events are topologically identical and may be analysed in the same way.

The configuration of the above events may by divided conveniently into two parts; the production vertex and the decay vertex. It is the separate identification of these vertices which determines the event classification and its likelihood of being measurable accurately. In cases where the decay vertex is not seen, the event will be classified as a two prong event ($\pi^+\pi^-$ or π^-p) and will be lost from the Σ^-_π, Σ^+_π and Σ^+_p categories. Similarly if the production vertex is not easily visible it is often unmeasurable and will not appear on the final D.S.T. of fitted events. The losses at each of these vertices are independent of each other and are considered separately.

5.1.1 Geometrical Losses At The Decay Vertex

The decay vertex is detected as a kink in the dark hyperon track and becomes easier to detect as the angle of decay increases. When, in the case of the $\Sigma^+\pi$ and $\Sigma^-\pi$ events, this is accompanied by a change in ionisation even the small angles of decay are easy to see and to measure. The Σ^+p events having a forward decay are likely to be undetected and to be classified as π^-p events as there is no ionisation change at the decay vertex: even if the event is correctly classified it will be difficult to measure the position of the decay vertex accurately and losses must be expected in this region. There are also events whose decay plane (the plane containing the Σ hyperon and the decay particle) contains the line of sight and hence the decay appears 'forward' as seen on the film; they are also difficult to measure. These losses may be demonstrated in figs. 5.1 - 5.3 where the decay angles ϕ_d,θ^*_d are defined as:

FIG 5·1 : Production and Decay Angle Distributions.

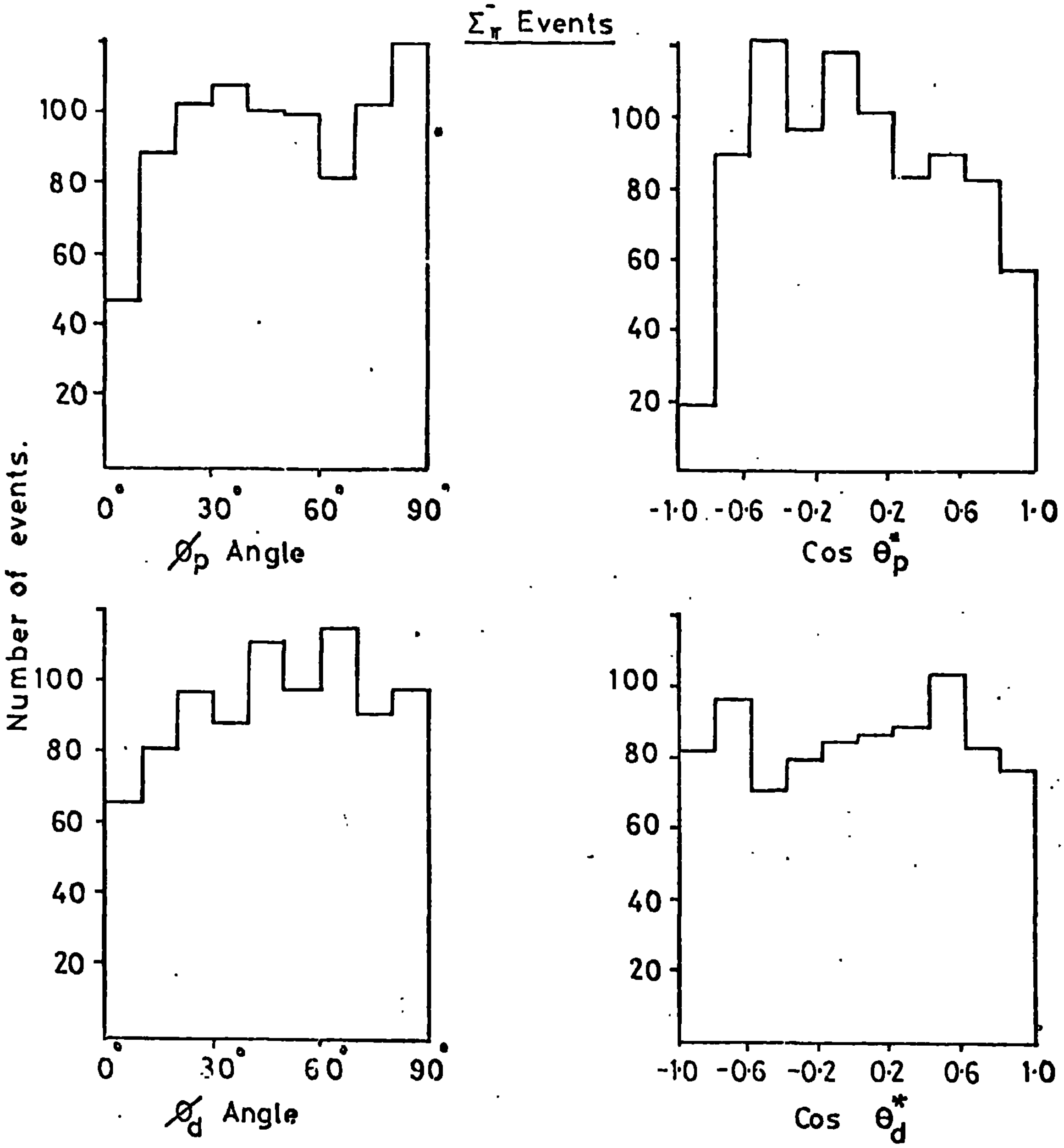

FIG 5.2 Production and Decay Angle Distributions.

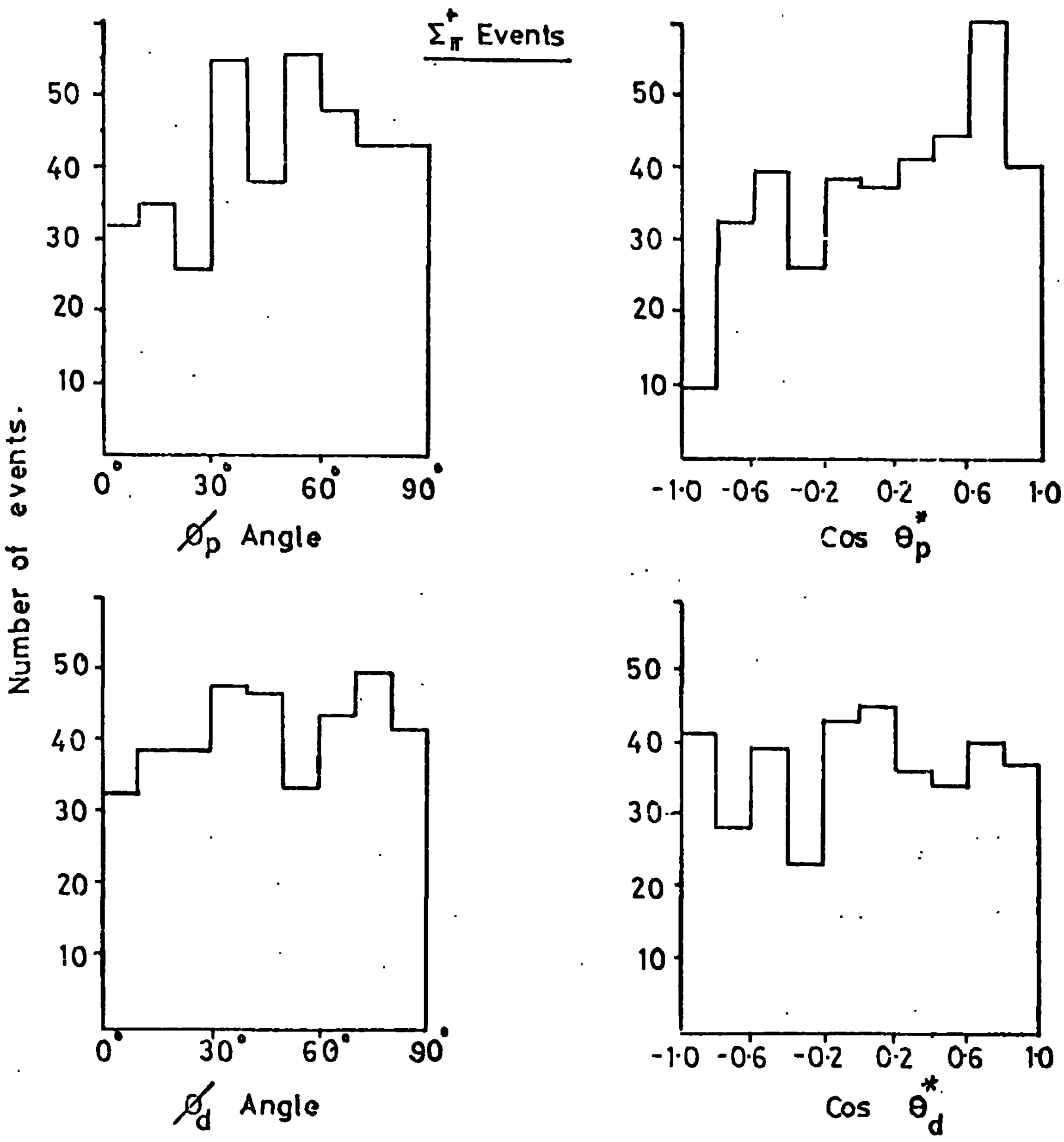

FIG 5·3: Production and Decay Angle Distributions.

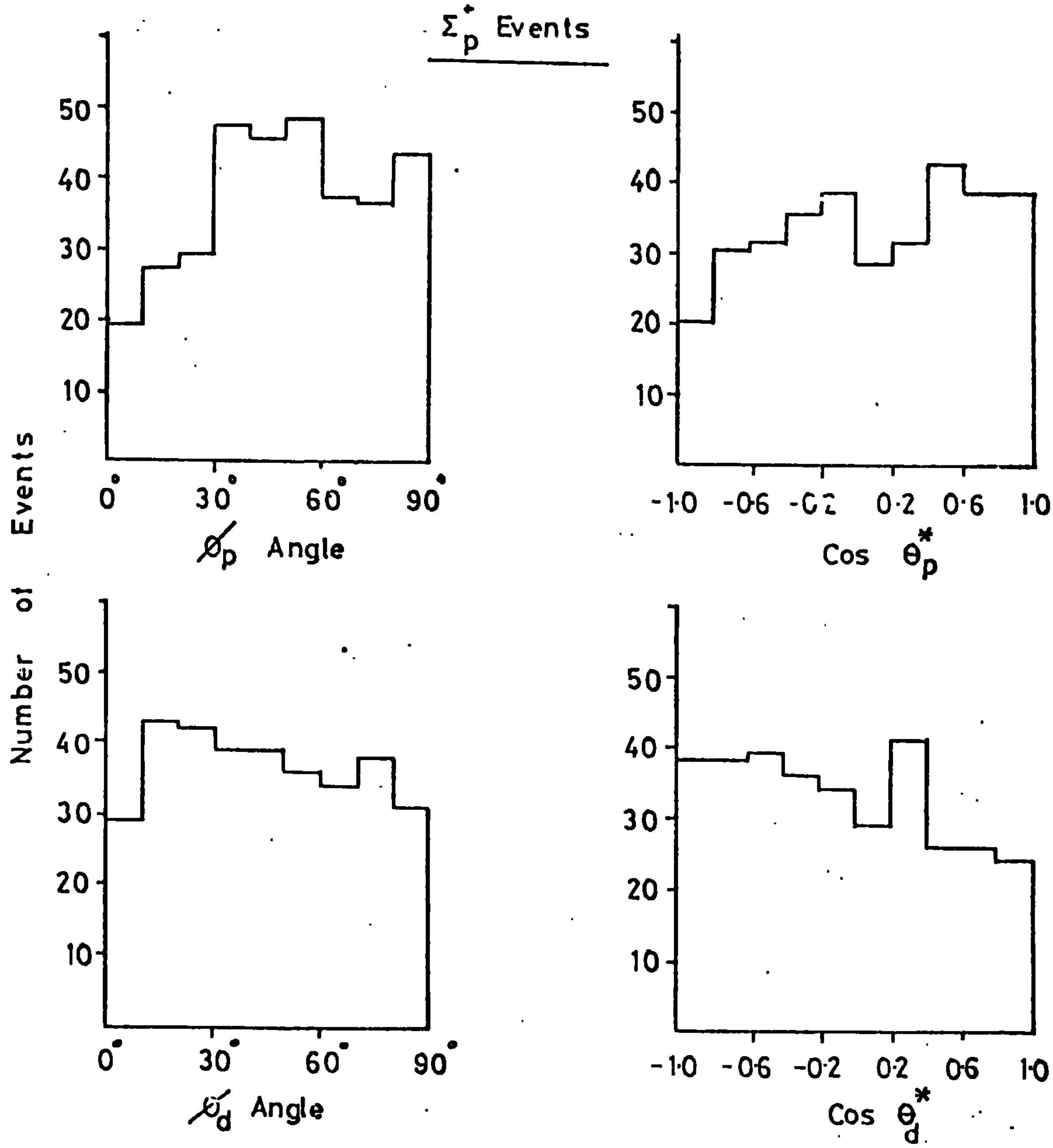

$$\cos\phi_d = \frac{(\vec{\Sigma}\wedge\vec{z}).(\vec{\Sigma}\wedge\vec{D})}{|\vec{\Sigma}\wedge\vec{z}|\,|\vec{\Sigma}\wedge\vec{D}|}$$

and

$$\cos\theta^*_d = \frac{\vec{\Sigma^*}.\vec{D^*}}{|\vec{\Sigma^*}|\,|\vec{D^*}|}$$

$\vec{\Sigma}$ and $\vec{D}$ are the laboratory momenta of the Σ hyperon and decay particle respectively, $\vec{z}$ is a unit vector in the chamber Z direction (line of sight) and the 'starred' quantities refer to the centre of mass system. In an L = 0 decay the secondary particles are uniformly distributed over the whole 4π solid angle hence the cos θ^*_d distribution is expected to be flat. ϕ_d is the angle between the decay plane and the x - y plane and would be a flat distribution if orthogonal views had been available for scanning. As mentioned earlier events lying in the line of sight are difficult to see and losses are expected for values of ϕ_d at 0° and 180°. The ϕ_d distribution is symmetric about 90° and for the present analysis the values of $\phi_d > 90°$ were translated into the first quadrant.

The cos θ^*_d distributions for the $\Sigma^+\pi$ and $\Sigma^-\pi$ show no obvious loss in forward or backward directions whereas that of the Σ^+p events exhibits a clear loss above cos $\theta^*_d = 0.4$ for reasons stated earlier in this section. The expected losses in the ϕ_d angle are small and lie below $\sim 10°$. Because the cos θ^*_d and ϕ_d distributions are not mutually exclusive and correcting for each separately would lead to over-correction a two dimensional plot of cos θ^*_d and ϕ_d was constructed (similar to that of fig. 4.9). The central loss-free region was used to calculate the true number of events and hence the correction factor to be applied to the observed number (see Table 5.1 later).

5.1.2 <u>Geometrical Losses At The Production Vertex</u>

The losses at the production vertex are independent of those at the decay vertex and the correction factors were determined using the production angle distributions cos θ^*_p and ϕ_p (see figs. 5.1 - 5.3) which are defined in obvious notation as

$$\cos \theta^*_p = \frac{\vec{K^*} \cdot \vec{\Sigma^*}}{|\vec{K^*}||\vec{\Sigma^*}|}$$

and

$$\cos \phi_p = \frac{(\vec{K} \wedge \vec{Z}) \cdot (\vec{K} \wedge \vec{\Sigma})}{|\vec{K} \wedge \vec{Z}| \; |\vec{K} \wedge \vec{\Sigma}|}$$

The losses in the forward and backward θ^*_p directions are due to difficulties in measuring events of this type with an ill-defined vertex of production. The ϕ_p angle losses extended up to 30° for the Σ^+ production events and are due to the short sigma track (usually $\lesssim$ 0.5 cm) being difficult to see when the production plane is in the line of sight. The correction factors were found using the two dimensional cos θ^*_p vs ϕ_p distribution and the results are shown in Table 5.1.

The onset of P wave interference in the cos θ^*_p distributions was difficult to determine with the current statistics: they were consistent with an L = 0 interaction up to 320 MeV/c and the results from the entire momentum region were combined.

5.1.3 Correction For Short Lived Sigma Hyperons

Many of the hyperon events are classified as two prong $\pi^+\pi^-$ or π^-p events because the sigma track is too short to be seen ($<$ 1 mm). Some events are unmeasurable for the same reason. This loss may be corrected for by using the known decay rate for Σ hyperons.

If ℓ_{min} is the minimum length of hyperon track that is visible in the x - y plane then this is related to the real space length of the track (ℓ_o) thus

$$\ell_{min} = \ell_o \cos \lambda$$

where λ is the angle of dip. The proper time (i.e. time in the rest frame of the hyperon) taken to travel a distance ℓ_o in the laboratory is

$$t = \frac{m}{pc} \ell_o$$

where p is the particle momentum, m its mass and c is the velocity of light. The time taken to travel the minimum projected length ℓ_{min} is then

$$t_{min} = \frac{m}{pc}\,\frac{\ell_{min}}{\cos\lambda}\ .$$

Events with short Σ tracks will in general have small values of t_{min} and losses are clearly seen in the proper lifetime distributions shown in figs. 5.4 and 5.5. The effect of the dip angle which could introduce losses for values of $t \gtrsim 0.2 \times 10^{-10}$ sec is not apparent and the slopes of the distributions are clearly consistent with the known lifetimes of the hyperons.

The loss of Σ^- hyperons above $\sim 3.2 \times 10^{-10}$ sec is due to the absorption of the hyperon at rest by a proton, these events are classifie as two prong $\Sigma^-\sigma$ events and may be corrected for using a maximum proper time cut.

It is possible to correct the observed number of events between t_{min} and t_{max} using the correction factor f defined as

$$f = \left(e^{-t_{min}/\tau} - e^{-t_{max}/\tau}\right)^{-1}$$

where τ is the hyperon lifetime.

The expected loss of events below $\sim 0.2 \times 10^{-10}$ sec may be compared with the observed number of $\pi^+\pi^-$ events. The minimum observable distance is ~ 0.5 mm, however for some geometrical configurations even 1 mm is difficult to see. Taking a mean of 0.75 mm, this corresponds to a travel time of $\sim 0.16 \times 10^{-10}$ sec for a Σ hyperon of 180 MeV/c momentum (from production by a kaon at rest). Using the decay law the probabilities of a hyperon event being classified as a two prong $\pi^+\pi^-$ event are 19% and 11% for Σ^+ and Σ^- respectively. Using a sample of 1035 collinear Σ^+_π and 4271 Σ^-_π events this gives 666 $\pi^+\pi^-$ events which

FIG 5·4 : Disribution of Proper Lifetime for Σ^- Hyperons

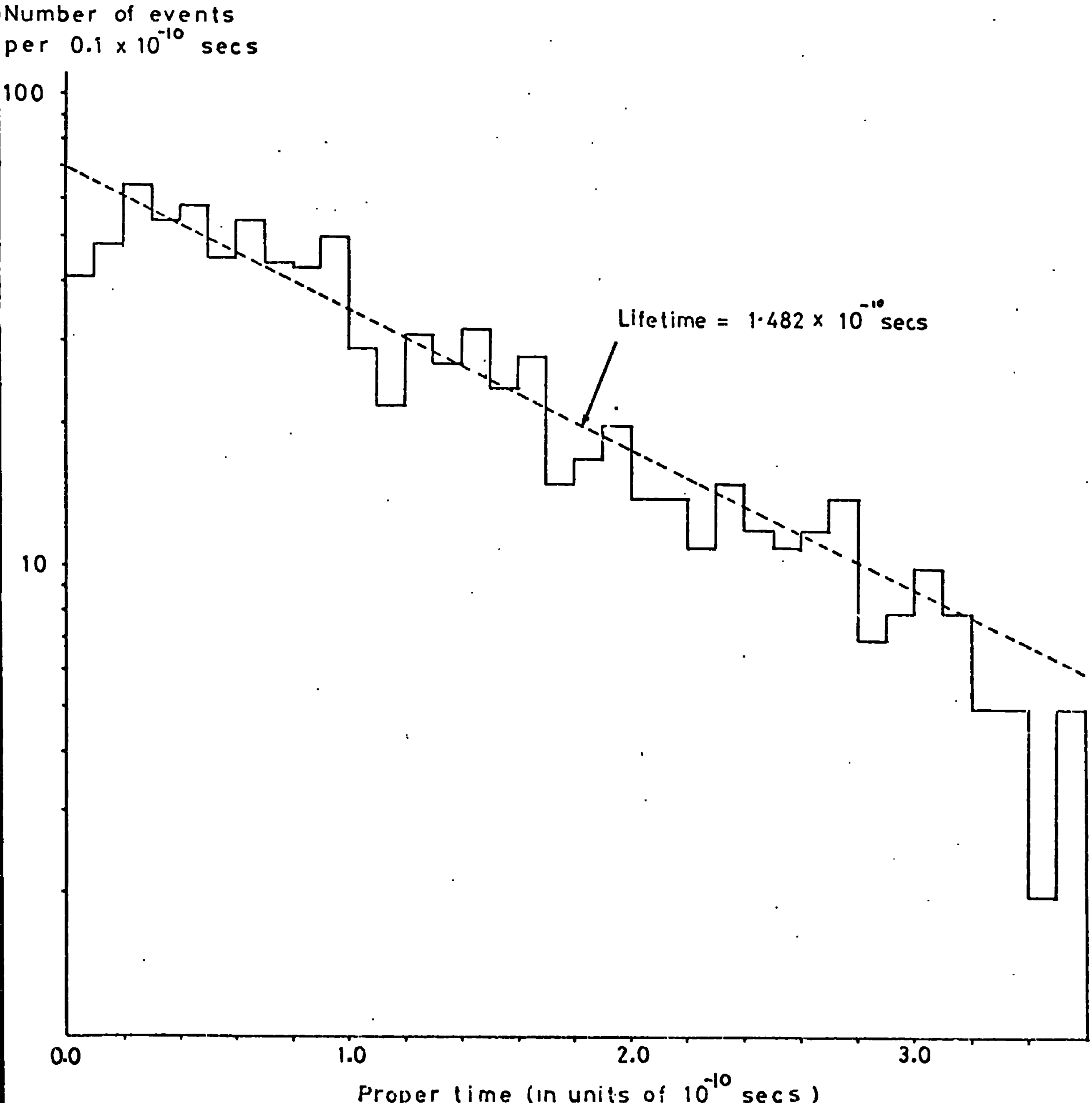

FIG 5·5 : Distribution of Proper Lifetime for Σ^+ Hyperons.

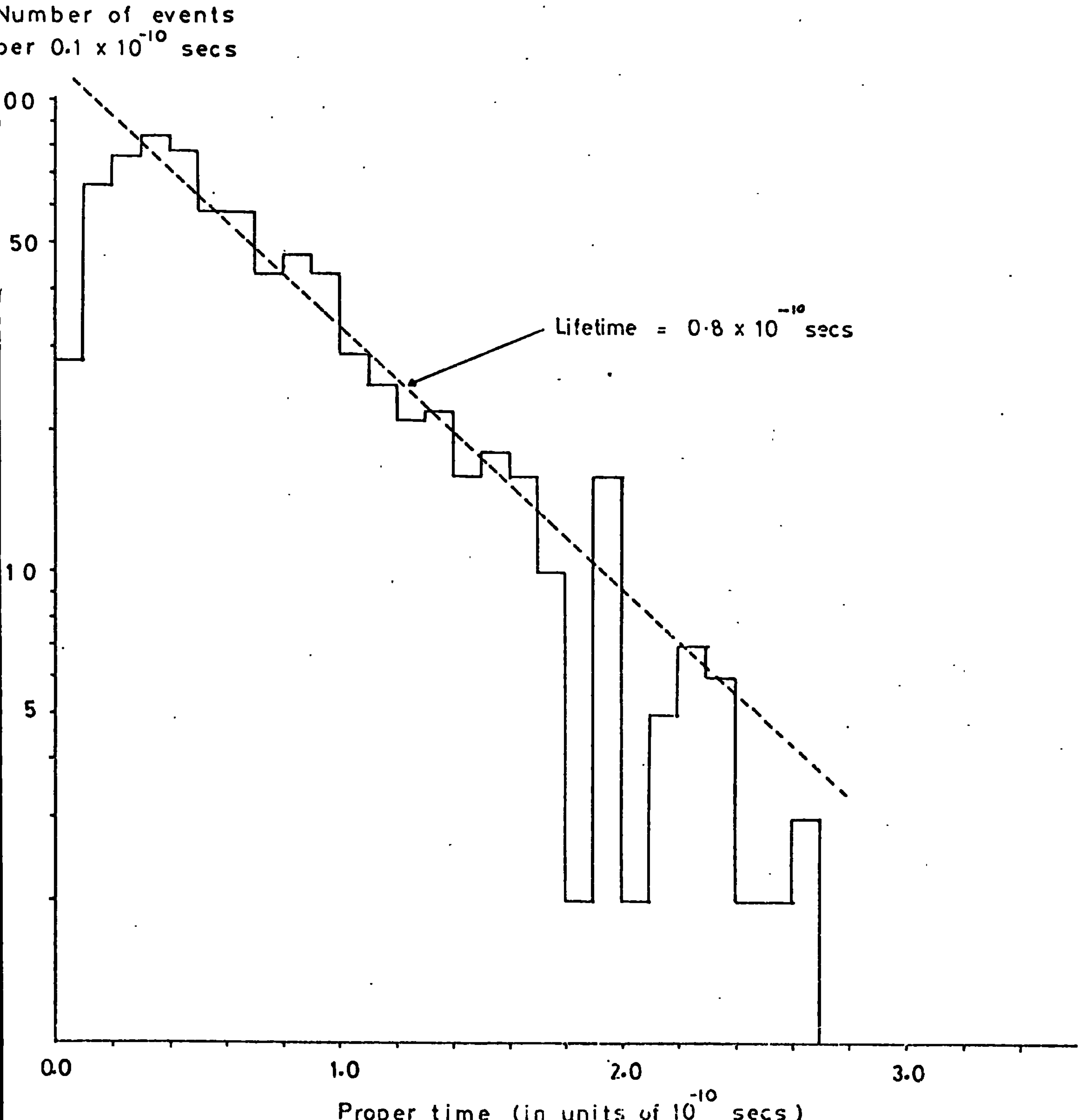

Table 5.1:

Summary Of Correction Factors For Charged Σ Production

(excluding lifetime weighting factors).

	$\Sigma^-\pi$	$\Sigma^+\pi$	Σ^+p
Correction for losses in cos θ^*_d and ϕ_d	1.206	1.218	1.213
Correction for losses in cos θ^*_p and ϕ_p	1.037	1.000	1.131
Correction for spurious measurements	1.007	1.000	1.015
Correction for incompatable fits and scan codes	1.061	1.111	1.108
Correction for randomly unmeasurable events	1.128	1.088	1.069
Correction for scanning efficiency	1.000	1.000	1.000
Overall correction	1.506	1.471	1.649

Table 5.3: Event Selection Summary

	$\Sigma^-\pi$	$\Sigma^+\pi$	Σ^+p
Number of scanned events	1452	638	601
Number of measurable events	1224	552	524
Number of events with compatible scan codes and fitted hypotheses	1154	497	473
Number of events inside reduced fiducial volume	1024	447	415
Number of events after removal of spurious measurements	1017	447	409
Number of events after lifetime cut	902	386	346
Number of events after collinearity angle cut	846	376	331

is in excellent agreement with the observed number of 698.

5.1.4 Effect Of Shallow Chamber

The shallow chamber ($\sim$ 8 cm) could introduce detection biases for events near the chamber walls because hyperons produced within a few millimetres of the perspex wall and which travel towards the wall have only a small proper time available for decay. These are likely to be classified as two prong events and will not appear in the proper lifetime or angular distributions. Hamam (31) found that, by removing events within $\sim$ 4 mm of the target walls and considering only those events well inside the chamber, these losses were negligible. The present study is less likely to be affected because of the generally lower momenta of the hyperons.

A method of lifetime correction was adopted which is independent of the chamber depth. Each event was weighted by the factor

$$w = (e^{-t_{min}/\tau} - e^{-t_{pot}/\tau})^{-1}$$

where t_{pot} is the time taken by the hyperon to reach the chamber boundary or to stop in the hydrogen whichever is the shorter. This factor automatically accounts for the events lost near the chamber edges by giving high weighting factors to those few events which are seen.

The results obtained from this approach agreed with those derived using the overall correction factor f and indicates that there are no detectable losses due to the shallow chamber. Table 5.4 presents the weighted number of events in each momentum interval.

5.1.5 Correction For Un-measurable Events

The classification of un-measurable events was discussed in detail in section 3.4. The results of this are given overleaf as the ratio of the number of random unmeasurable events to the total number of unmeasured events.

	Σ^+_p	Σ^+_π	Σ^-_π
Ratio	0.47	0.56	0.69

The events unmeasured for geometrical reasons are automatically corrected for by the factors from sections 5.1.1 - 5.1.4.

5.1.6. Correction For Scanning Efficiencies

The double scan efficiency was found to be high for the charged hyperon channels, the calculation used information obtained from both scans and proceeds as follows:

Using the following

N_T = unknown total number of events

N_1 = number of events on scan one only

N_2 = number of events on scan two only

N_{12} = number of events common to both scan one and scan two

The first and second scanning efficiencies (e_1 and e_2) may be written as

$$e_1 = \frac{N_1}{N_T}$$

$$e_2 = \frac{N_2}{N_T}$$

likewise $$e_1 e_2 = \frac{N_{12}}{N_T}$$

These give $$e_1 = \frac{N_{12}}{N_2}, \qquad e_2 = \frac{N_{12}}{N_1}$$

and for the double scan efficiency

$$e_{1+2} = e_1 + e_2 - e_1 e_2$$

The scanning efficiencies for the charged hyperon channels are presented in table 5.2

Table 5.2: Scanning Efficiencies For Σ^+ and Σ^- Production

Category	e_1	e_2	e_{1+2}
Σ^-_π	0.970	0.984	1.000
Σ^+_π	0.969	0.984	1.000
Σ^+_p	0.968	0.982	0.999

5.1.7 Charged Hyperon Cross-Sections

A summary of the correction factors applied to the observed numbers of events is shown in Table 5.1, the correction factors not previously discussed are derived from table 5.3 which gives details of the event selection. These corrections are simple scaling factors to account for random losses resulting from the event selection.

Compatibility was required between the fitted hypothesis and scanning code; events rejected on these grounds were assumed to be poorly measured and were corrected for using a scaling factor.

The channel cross-sections were evaluated using equation 4.1 viz.

$$\sigma(p) = \frac{N(p)}{N_o \rho L(p)}$$

where the values of L(p) appropriate to the charged hyperon channels were taken from table 4.10 and the value of 297.6 mb.m for $(N_o \rho)^{-1}$

The $\Sigma^-\pi^+$ and $\Sigma^+\pi^-$ production cross-sections are shown in figs. 5.6 and 5.7 and tabulated in table 5.4.

The errors are calculated using the error in L(p) given in table 4.10; and an error in N(p) of $\sqrt{N(p)}$. The correction factors derived from the angular distributions were calculated from

$$\left(\frac{df}{f}\right)^2 = \left(\frac{1}{N_i} - \frac{1}{N_i + N_o}\right)^2 dN_i^2 + \frac{dN_o^2}{(N_i + N_o)^2}$$

For poisson errors this simplified to

$$\left(\frac{df}{f}\right)^2 = \frac{1}{N_i} - \frac{1}{N_i + N_o}$$

Table 5.4:

Charged Hyperon Production Cross-Sections

Momentum Interval	lifetime weighting $\Sigma^-\pi$	$\Sigma^+\pi$	Σ^+p	corrected number $\Sigma^-\pi$	$\Sigma^+\pi$	Σ^+p	(mb) $\sigma(\Sigma^-\pi^+)$	(mb) $\sigma(\Sigma^+\pi^-)$
80 - 100	45.7	12.2	7.2	68.8	17.9	11.8	82.6 ± 19.6	35.6 ± 10.7
100 - 120	85.2	21.9	14.9	128.3	32.2	24.5	67.8 ± 11.2	30.0 ± 6.9
120 - 140	114.7	25.4	13.2	172.7	37.4	21.7	59.6 ± 9.1	20.4 ± 4.0
140 - 160	117.7	43.7	43.9	177.2	64.3	72.4	37.9 ± 5.1	29.2 ± 4.2
160 - 180	134.4	57.3	59.5	202.4	84.3	98.1	27.8 ± 3.5	25.1 ± 3.2
180 - 200	156.7	68.9	63.5	235.9	101.3	104.7	23.1 ± 2.6	20.2 ± 2.4
200 - 220	157.4	97.8	69.7	237.0	143.8	114.9	18.2 ± 2.0	19.9 ± 2.1
220 - 240	76.1	57.0	51.2	114.6	83.8	84.4	11.1 ± 1.5	16.3 ± 2.1
240 - 260	70.5	52.1	40.9	106.2	76.6	67.4	12.0 ± 1.8	16.3 ± 2.4
260 - 280	32.5	23.0	24.9	48.9	33.8	41.0	8.2 ± 1.8	12.5 ± 2.5

FIG 5·6 : Channel Cross-section for Σ^- Production.

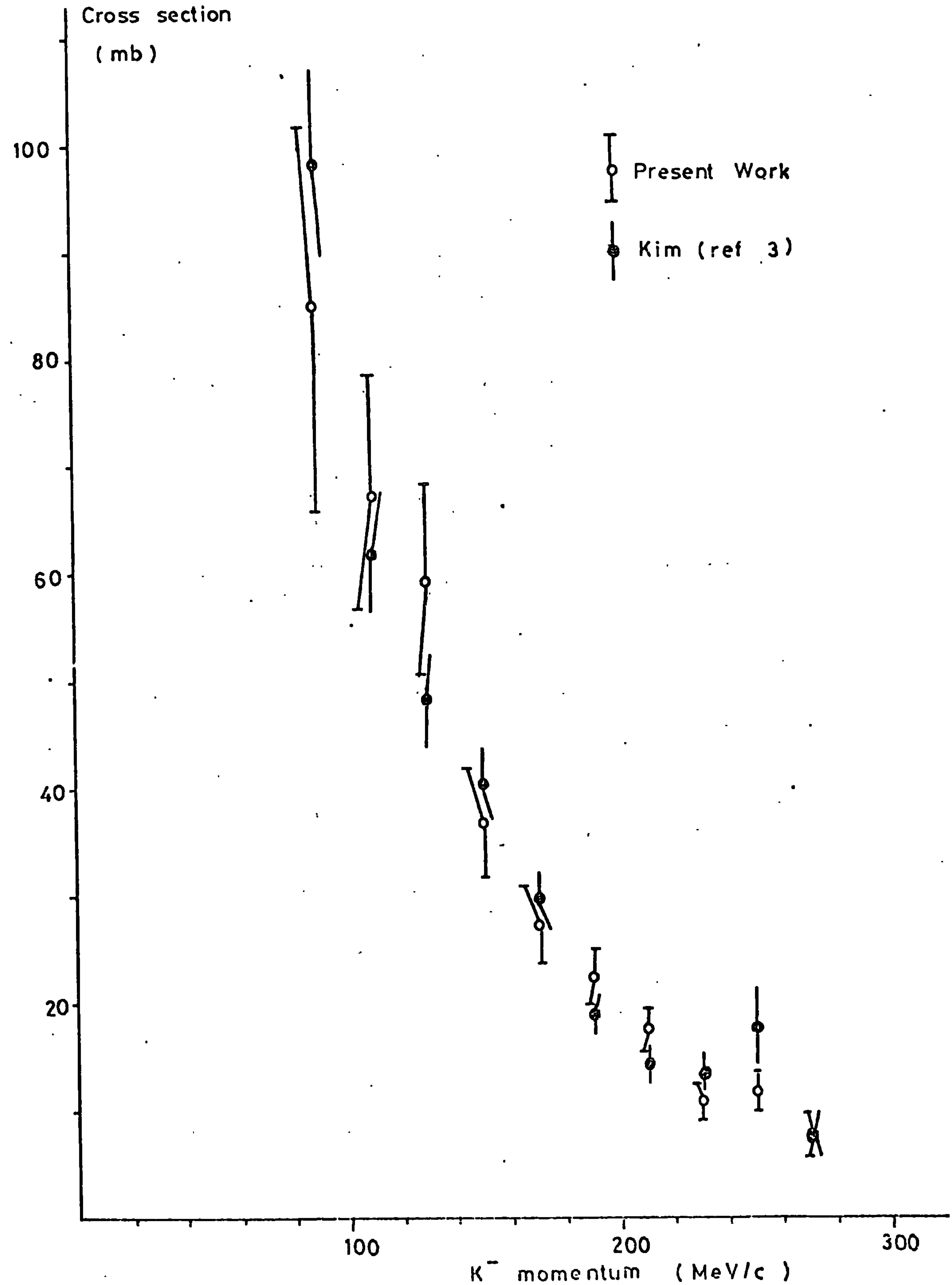

FIG 5·7 : Channel Cross-section for Σ^+ Production.

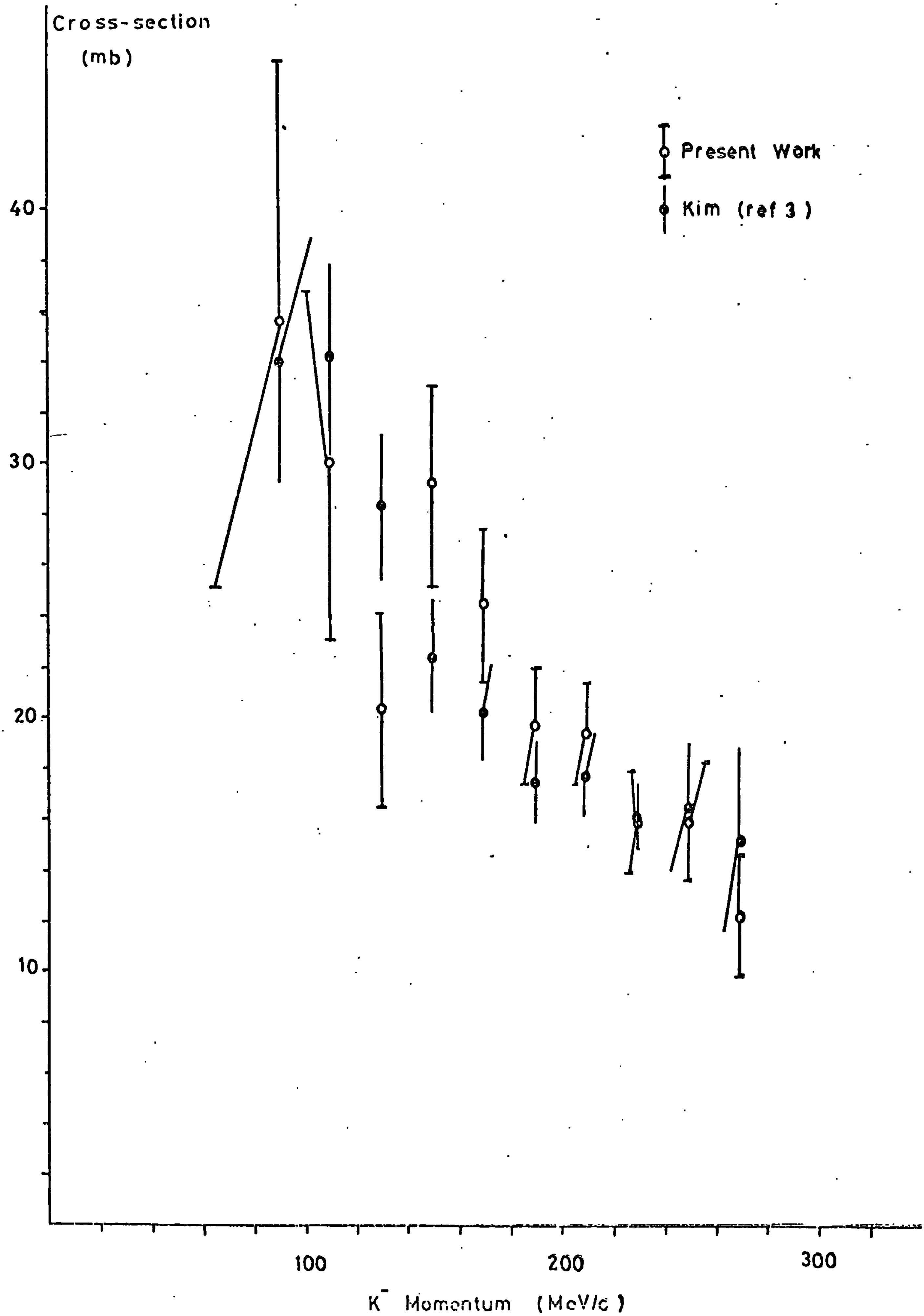

where N_i is the number of events lying inside the region where no angular losses are apparent and N_o is the number lying outside the region. Errors of $\lesssim$ 1% were typical and were neglected in comparison to the statistical errors.

5.2 Elastic Scattering

The elastic scattering channel, whilst being a simple two prong event which should be easy to scan and measure, suffers from severe losses due to tracks of short length. Fig. 5.8 shows the kinematics of the reaction; the secondary particle momenta are plotted as functions of centre of mass scattering angle and primary kaon momentum.

Protons with momenta below ~ 100 MeV/c (corresponding to a range of ~ 3 mm) are difficult to see and to measure hence losses are to be expected in the forward cos θ^*_p direction. Similarly the scattered kaon will be short in the backward direction; events of this type are usually unmeasurable rather than invisible, the range of the kaon being greater than that of the proton (1.5 cm corresponding to 100 MeV/c). As the primary momentum increases the secondary tracks become longer and fewer losses will be apparent.

Another problem at low momenta is that the ionisation difference between the recoil proton and the scattered kaon is insufficient to enable a positive identification for each track to be made when there is no curvature to be measured. Events of this type will often possess ambiguous kinematic fits to the elastic scattering hypothesis.

The present analysis considers the range of primary momenta from 120 - 320 MeV/c, however it is only above ~ 200 MeV/c when the above problems become confined to the extreme forward and backward directions.

Events with an unseen secondary track (usually the proton) are classified as one prong events and because there is little change in the ionisation of the kaon these events appear as 'kinks' in the beam tracks. These are difficult to scan efficiently, especially when the kink is in

FIG 5·8: Kinematics of Elastic Scattering

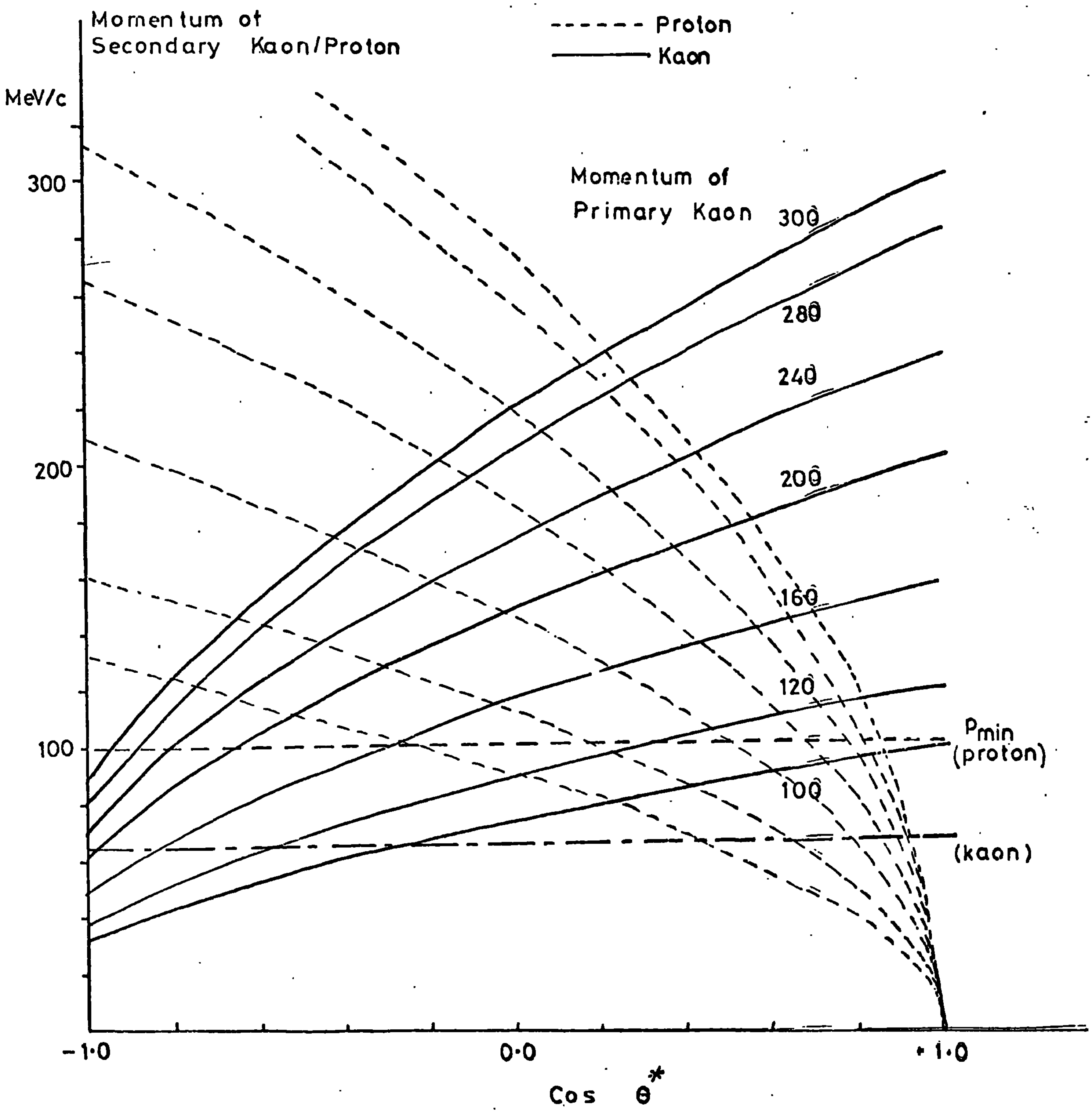

the same direction as the curvature produced by the magnetic field. In view of these difficulties only the two prong elastic scatter events were measured in this work. This selection removes the coulomb nuclear interference region from the angular distributions, however this is unimportant in the derivation of the total cross-sections and gives only a small effect (~ 5%) at 120 MeV/c. This effect decreases rapidly as the primary momentum increases. The cross-sections quoted in this work are the nuclear cross-sections only and do not include any contribution from the coulomb scattering.

5.2.1 Distributions Of Production Angles

For elastic scattering the corrections accounting for losses are momentum dependent and, although the same angular distributions are used for these events as for the charged hyperon production, it is necessary to divide the distributions into 40 MeV/c momentum intervals.

The production angle distributions are shown in Fig. 5.9 after having applied a minimum proton momentum selection of 100 MeV/c. This removes events with low beam momenta and also events in the forward scattering region: as has been discussed earlier these are difficult to scan and measure and it is best to exclude events of this type and use only those events which are clearly visible. In making corrections for angular losses only those regions unaffected by this momentum cut were considered. The regions deemed free of losses were derived with reference to figs. 5.8 and 5.9 and are summarised in Table 5.5

Table 5.5: Loss-Free Regions Of The Production Angle Distributions

Momentum Interval (MeV/c)	ϕ Angle	Cos θ^*
120 - 160	30 → 90	-0.6 → 0.4
160 - 200	30 → 90	-0.9 → 0.4
200 - 240	20 → 90	-0.9 → 0.6
240 - 280	20 → 90	-0.9 → 0.8
280 - 320	0 — 90	-0.9 → 0.8

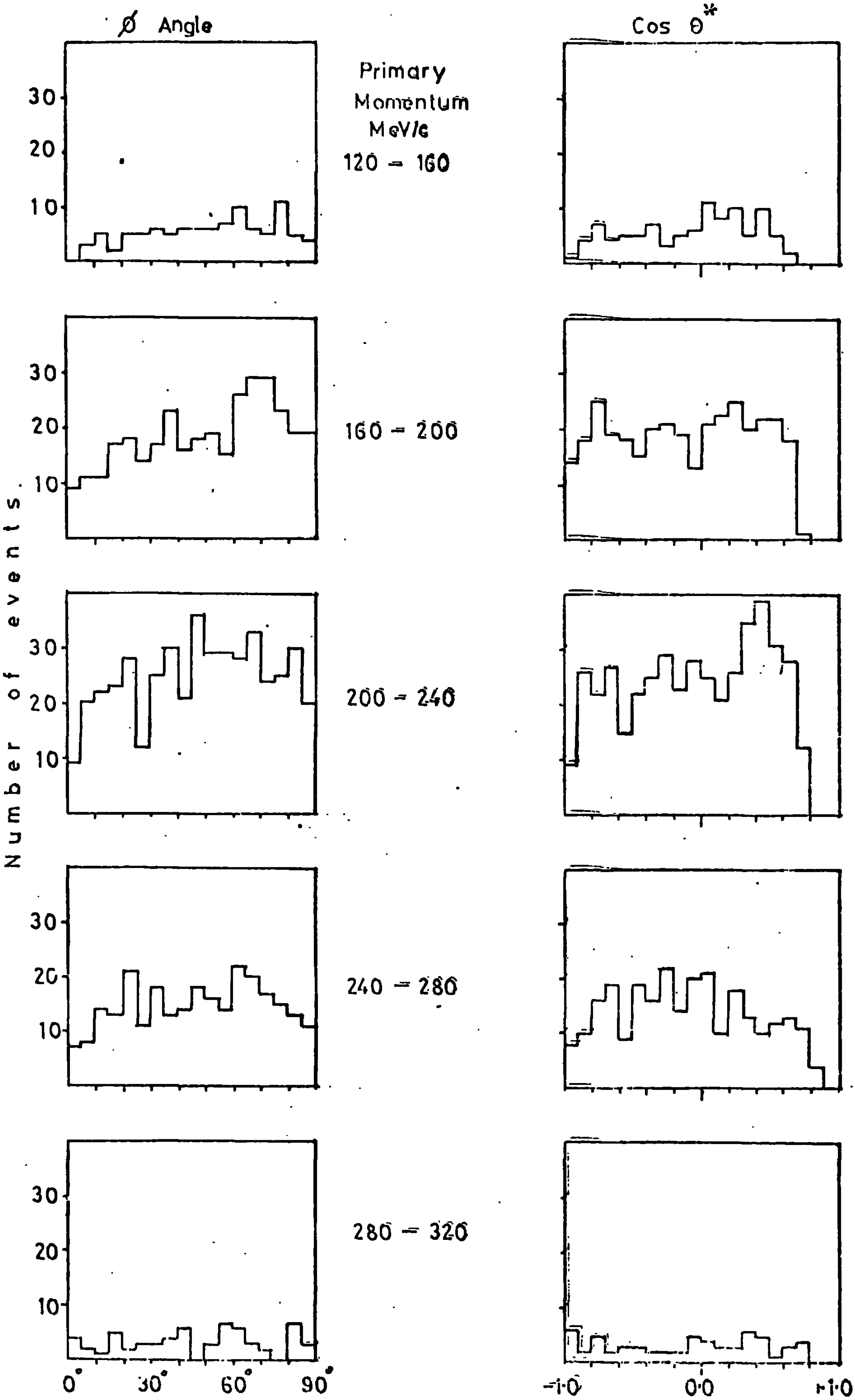

FIG 5·9 : Production Angle Distributions for Elastic Scattering

The losses observed in the cos θ^* distributions are those which would be expected from the kinematics of the scattering channel.

The possible onset of the P wave interference at $\sim$ 280 MeV/c is difficult to establish due to lack of statistics, the evidence from the distributions suggest that the low energy elastic scattering is S wave. The S wave property and the two dimensional cos θ^* versus ϕ angle diagram enable the correction factors to be calculated (see table 5.6) in the same way as for charged hyperon production.

5.2.2 Events With Short Tracks

These events fall into two main categories, firstly those which have tracks too short for even an attempt at measuring to be made; (typically $<$ 2.0 mm) these are classed as unmeasurable. Secondly those with longer tracks ($\lesssim$ 3 cm) where a momentum determination of the proton can be made using its range in hydrogen. In this latter category there are events which having been measured three times, are unable to provide momentum information for the short track either from curvature of from range after geometrical reconstruction. However, for these partially unsuccessful events the measured beam momenta were available and were used to add these events into the main momentum distribution. Furthermore their momentum spectrum (see fig. 5.10) was assumed to be typical of the unmeasurable category above. In this way a momentum dependent correction has been made for the unmeasurable events.

Some of these events with short tracks are being corrected for automatically by the factors in § 5.2.1. The ϕ angle distribution for this sample of events (fig. 5.11) exhibits a similar structure to that of the fully measurable events except for a small excess of events at $\phi < 15^o$ which are the ones that are doubly corrected. However this is a small error leading to an error of $<$ 2% over estimation of the channel cross-section.

The precise details of the method of correction are given in table 5.7.

Table 5.6:

Summary Of Correction Factors

Correction for randomly unmeasurable events		1.072
Correction for spurious losses		1.101
Scanning efficiency		1.000
Production angle corrections	(120 - 160 MeV/c)	1.540
	(160 - 200 MeV/c)	1.305
	(200 - 240 MeV/c)	1.330
	(240 - 280 MeV/c)	1.216
	(280 - 320 MeV/c)	1.202

Table 5.8:

Event Selection For Elastic Scatters

Total number of two prong elastic scatters	2494
Total number of measurable events	2138
Number of events found on the D.S.T.	1942
Events inside reduced fiducial volume	1555
Events fully measured	1235
(Only 155 events were randomly unmeasurable)	

FIG 5·10: Distribution of Primary Momenta for Elastic Scatter Events with Short Tracks.

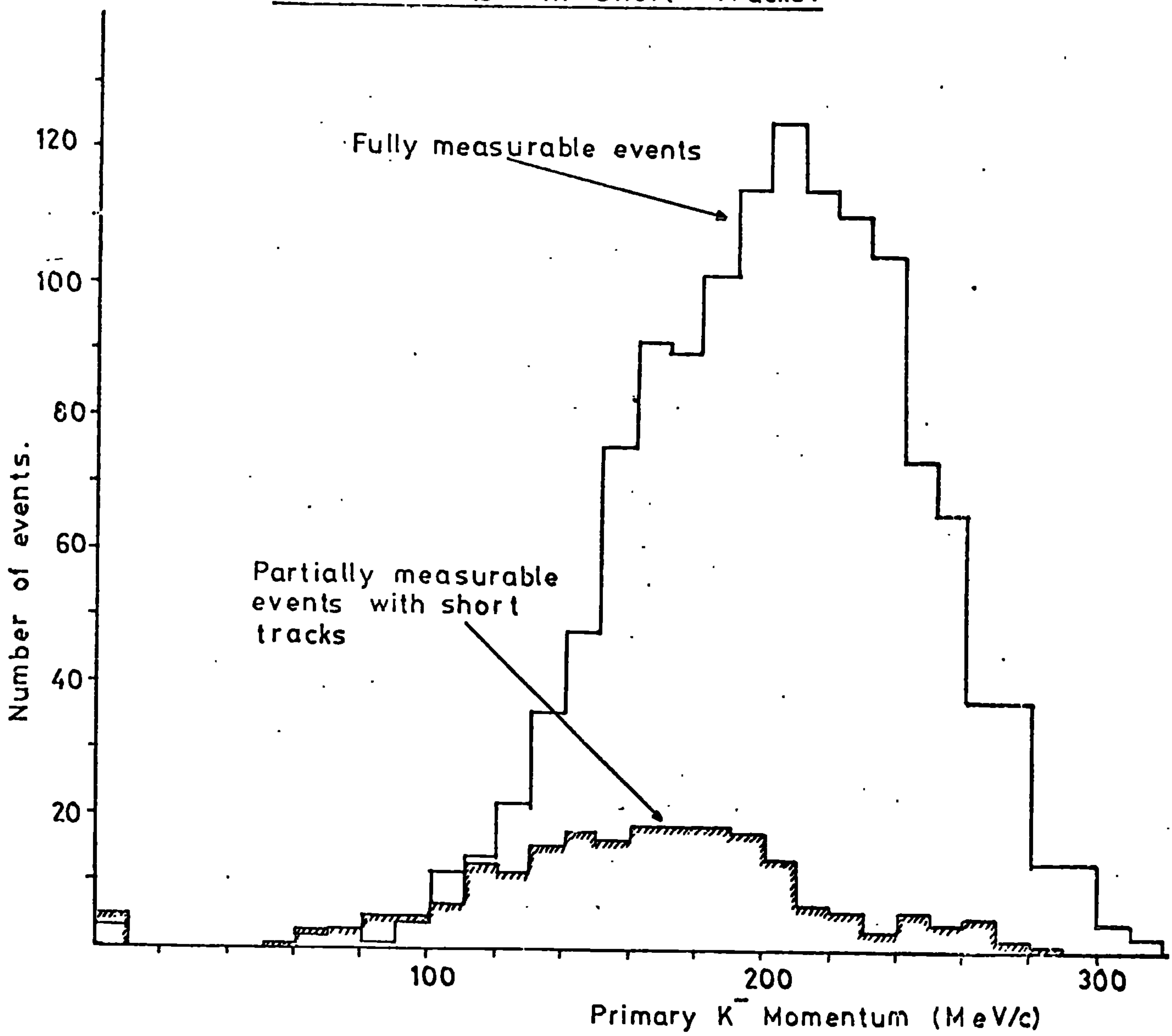

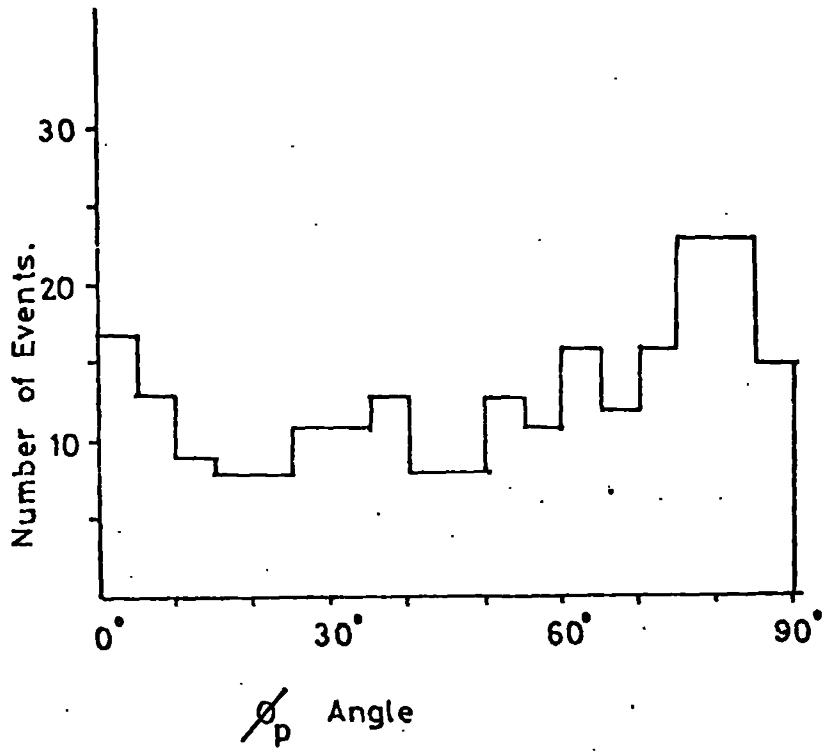

FIG 5·11: Distribution of ϕ_p Angles for Elastic Scattering Events with Short Secondary Tracks.

Table 5.7: Elastic Scattering Cross-Sections

Momentum Interval	(a)	(b)	(c)	(d)	(e)	(f)	Corrected Events	$\sigma(K^-p \rightarrow K^-p)$ mb
120 - 140	33	28	24	25.6	19.2	77.8	141.4	80.2 $\pm$ 12.6
140 - 160	70	35	30	27.9	23.9	121.8	221.4	77.6 $\pm$ 9.9
160 - 180	154	38	32	34.8	26.0	214.8	330.8	74.6 $\pm$ 7.5
180 - 200	183	87	32	35.8	25.3	244.1	376.0	60.4 $\pm$ 5.6
200 - 220	225	21	18	19.7	14.3	259.0	406.6	51.2 $\pm$ 4.4
220 - 240	219	9	8	8.7	6.1	233.8	367.0	58.4 $\pm$ 5.6
240 - 260	173	10	8	9.7	6.8	189.5	272.0	50.4 $\pm$ 5.4
260 - 280	92	7	6	6.8	4.7	103.5	148.5	40.7 $\pm$ 5.7
280 - 300	42	2	2	2.0	1.4	45.4	64.4	52.1 $\pm$ 11.9
300 - 320	19	0	0	0.0	0	19.0	26.9	42.1 $\pm$ 14.3

Column

(a) Observed number of fully measured events after proton momentum cut and fiducial volume cut

(b) Observed number of measurable 'short track' events inside the fiducial volume

(c) Calculated distribution of unmeasurable events with short tracks

(d) Values of column (b) adjusted to account for the proton momentum cut

(e) Values of column (c) adjusted to account for the proton momentum cut and fiducial volume cut

(f) Total number of two prong elastic scatters [(a) + (d) + (e)]

5.2.3 Elastic Scattering Cross-Section

The correction factors applied to the observed number of events due to the data selection (see table 5.8) are summarised in table 5.6. Of the 356 unmeasurable events, 201 were for reasons of short tracks and the remaining 155 were corrected for by renormalisation. The double scanning efficiency for the two prong scatters was ~ 100% and no correction was required.

The final results are shown in fig. 5.12 and listed in table 5.7.

5.3 Neutral Hyperon Production

The only neutral hyperon channels with a significant amount of phase space available at low momenta are

$$K^- + p \longrightarrow \Lambda^0 + \pi^0$$

$$K^- + p \longrightarrow \Sigma^0 + \pi^0$$

The three body channels such as

$$K^- + p \longrightarrow \Lambda^0 + \pi^0 + \pi^0$$

although still open at zero kaon momentum are rare in comparison to the two body channels. These channels were fitted to various hypotheses depending on the number of observed γ-rays.

Events with only one associated vee were tested against the following hypotheses:

$$K^- + p \longrightarrow \Lambda^0 + \pi^0 \qquad \text{(i)}$$
$$\Lambda^0 \longrightarrow p + \pi^-$$

$$K^- + p \longrightarrow \Lambda^0 + \gamma \qquad \text{(ii)}$$
$$\Lambda^0 \longrightarrow p + \pi^-$$

$$\Lambda^0 \longrightarrow p + \pi^- \qquad \text{(iii)}$$

The second hypothesis in reality is a rare process but it provides a mechanism for obtaining more kinematic fits onto the D.S.T. Events which have repeatedly failed hypotheses (i) sometimes fit hypothesis (ii); this artificial fitting introduces no bias into the final results as only the measured beam momentum is used in the cross-section determination.

FIG 5·12: Cross-section for Elastic Scattering

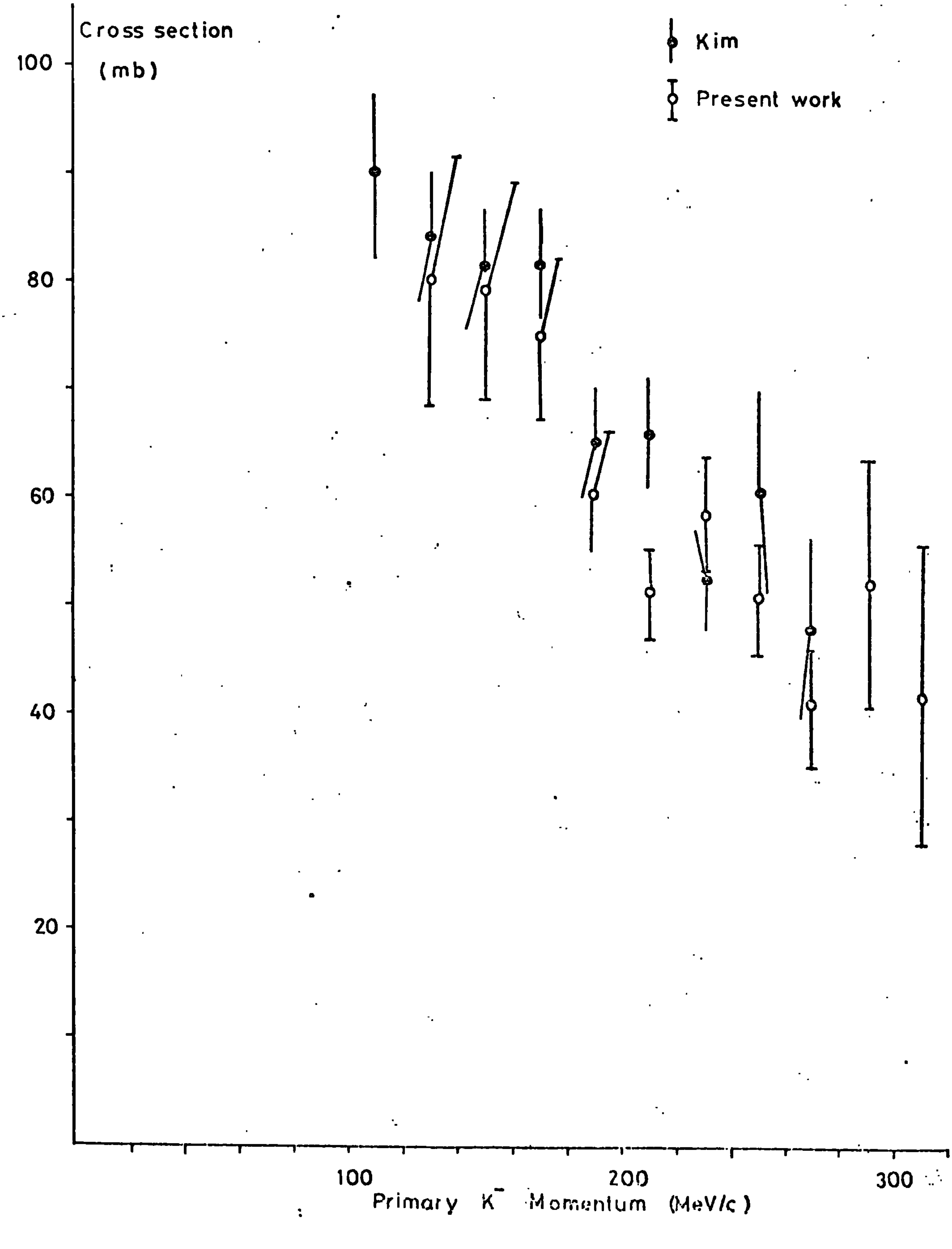

Hypothesis (iii) is the "pointing vee" fit and fits only the decay part of the interaction using the Λ^0 direction and the momenta of the decay particles. This fit is used in the absence of the multivertex hypothesis (i).

Events having a single associated γ-ray conversion are tested against the following hypotheses:

$$K^- + p \longrightarrow \Lambda^0 + \gamma, \quad \gamma \longrightarrow e^+ + e^-, \quad \Lambda^0 \longrightarrow p + \pi^-$$

$$K^- + p \longrightarrow \Lambda^0 + \pi^0, \quad \pi^0 \longrightarrow \gamma + \gamma, \quad \gamma \longrightarrow e^+ + e^-, \quad \Lambda^0 \longrightarrow p + \pi^-$$

$$K^- + p \longrightarrow \Sigma^0 + \pi^0, \quad \Sigma^0 \longrightarrow \Lambda^0 + \gamma, \quad \gamma \longrightarrow e^+ + e^-, \quad \Lambda^0 \longrightarrow p + \pi^-$$

The existence of the γ-ray conversion provides extra constraints on the fitting and allows the Σ^0 production channel to be fitted. If the event failed these hypotheses the γ-ray measurements were ignored and the fitting programme KINEMATICS tested the remaining measurements against hypotheses (i) - (iii) above.

This list of hypotheses gives rise to many fitting ambiguities which can not be resolved by judging; the situation is similar for more complex events with two or three associated γ-rays. The determination of the total neutral hyperon production cross-section requires a knowledge of the primary momentum spectrum and the production and decay angles. Only the 'pointing vee' part of each event was used together with the measured beam momentum which was included on the final D.S.T. of fitted events.

The associated γ-rays were not used in this study although it is possible with higher statistics to use the extra constraints to obtain a separation of the $\Lambda^0\pi^0$ and $\Sigma^0\pi^0$ channels.

The zero prong events may be analysed in a similar fashion to the charged hyperon events, both possess production and decay vertices which will exhibit losses for certain geometrical configurations. The main difference is that the Λ^0 hyperon, being neutral, loses no energy on travelling through the liquid hydrogen and its typical decay length of 2 - 3 cm is commensurate with the chamber depth of 8 cm (cf. $\Sigma^{\pm}$ production, decay length $\sim$ 1 cm). This problem is investigated using a method similar to that used by Fallahi (12) in the higher momentum region where the biasing effects of the wall were clearly noticeable.

5.3.1 Selection Of Kaon Momenta

The following analysis was applied only to events with primary momenta in excess of 160 MeV/c. This limit was imposed to remove the large number of zero prongs with zero kaon momenta which could severely contaminate the in-flight sample. It is known that the effect of errors of measurement is to distribute the at-rest events between momenta of 0 and $\sim$ 150 MeV/c (fig. 7.2).

5.3.2 Geometrical Losses At The Decay Vertex

The major loss arises from events where the decay plane lies in the line of sight and the event is difficult to scan and measure. This loss is apparent in the ϕ_d angle distribution (fig. 5.13) below $-15°$. The ϕ_d angle is defined in the same way as for the charged hyperon analysis.

A small loss is visible in the $\cos \theta^*_d$ (where θ^*_d is the c.m. angle between the proton and the original hyperon direction) distribution for protons which are produced in the backward direction. These usually possess low momenta in the laboratory and are difficult to scan for.

The overall correction factor for the decay angle losses was

FIG 5·13: Production and Decay Angle Distributions.

Neutral Hyperon Production

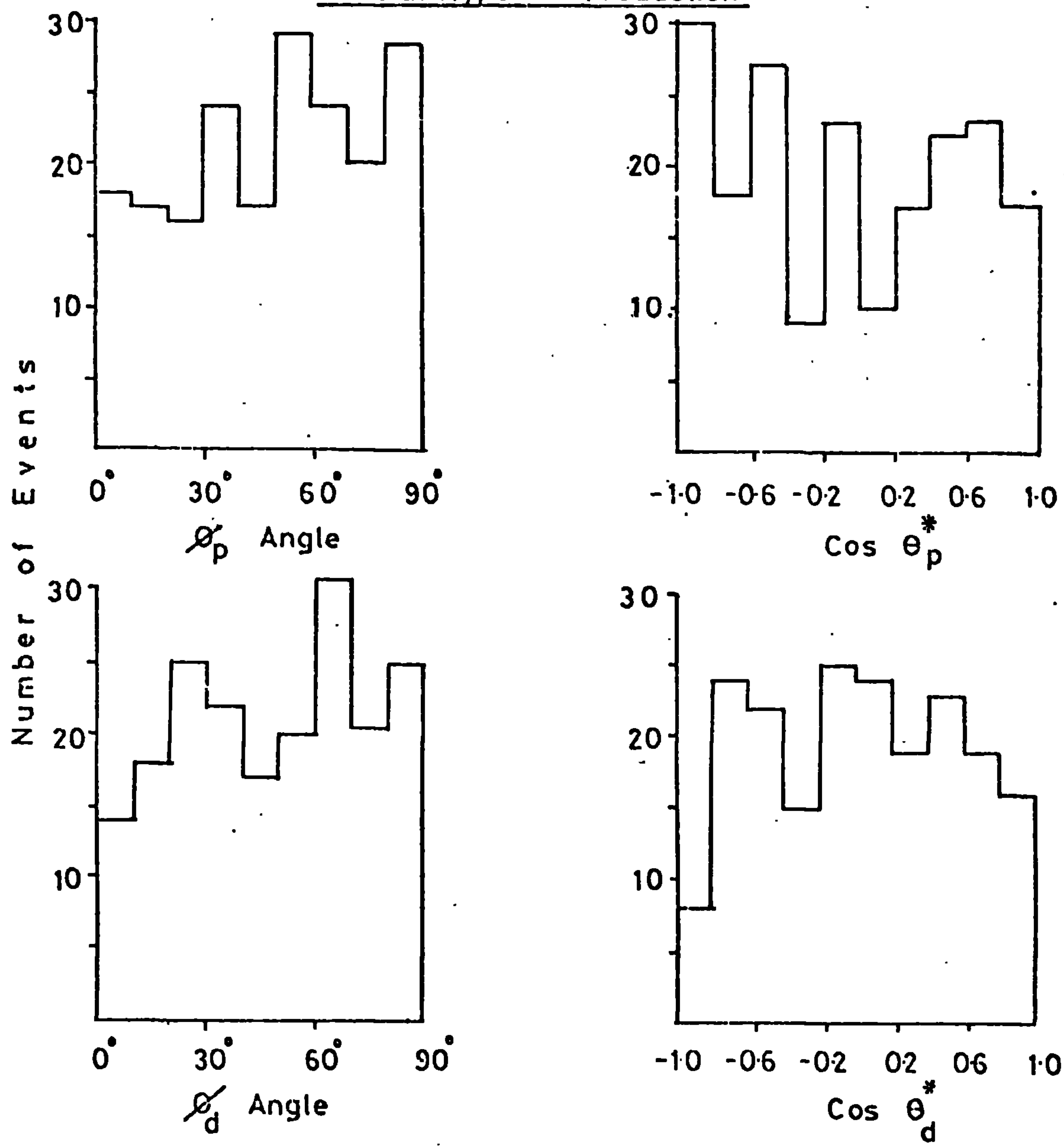

found to be 1.161 using the two-dimensional diagram of ϕ_d versus cos θ^*_d.

5.3.3 Geometrical Losses At The Production Vertex

In the analysis of neutral hyperon events care must be taken to ensure that the narrow chamber does not introduce any bias into the results. The long decay length of the neutral hyperon may lead to losses for certain types of event which are produced near the perspex wall. When the Σ^0 hyperon is produced near the wall and travels towards it, the decay is likely to occur in the H_2/Ne mixture. These events are not recorded and are lost from the D.S.T. used in this analysis. Events travelling into the chamber have a high probability of decaying inside the pure hydrogen liquid.

The effects of this problem were investigated by classifying events in various ways. The chamber was divided into four volumes. (fig. 5.14) two in each half of the chamber depth. The kinematics of the Λ^0 production process was used to determine the depth of the volumes adjacent to the perspex walls. Fig. 5.15 shows the hyperon momentum and mean decay length as a function of primary momentum and centre of mass scattering angle. As the primary kaons are flat (i.e. angle of dip, λ , = 0°) in the chamber, the minimum potential length available to the hyperon occurs when the scattering angle is at 90° to the primary direction and when the scattering plane is perpendicular to the perspex walls. This distance is simply the perpendicular distance from the walls to the interaction vertex. Assuming the worst case of a scattering plane perpendicular to the walls, then the distance between the vertex and the wall is

$$D_v = \ell_\Lambda \sin\theta_p \simeq \frac{pc\tau}{m} \sin\theta^*_p$$

where θ_p is the scattering angle of the hyperon in the laboratory and ℓ_Λ is the decay length of the hyperon. At low momenta there is an approximate equivalence between laboratory and centre of mass angles and

FIG 5·14: Division of Chamber to Investigate Losses of Neutral Hyperons

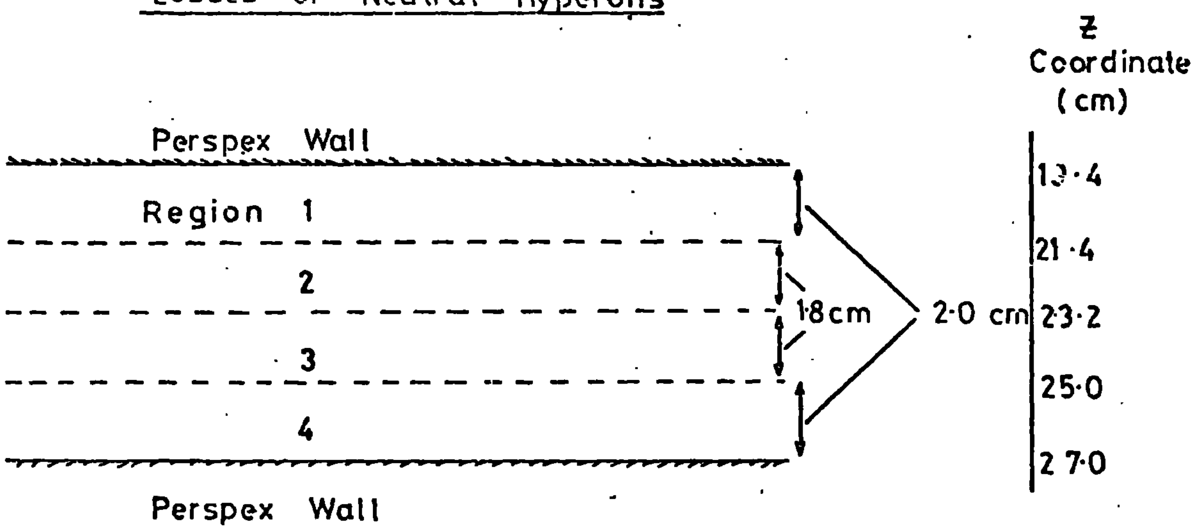

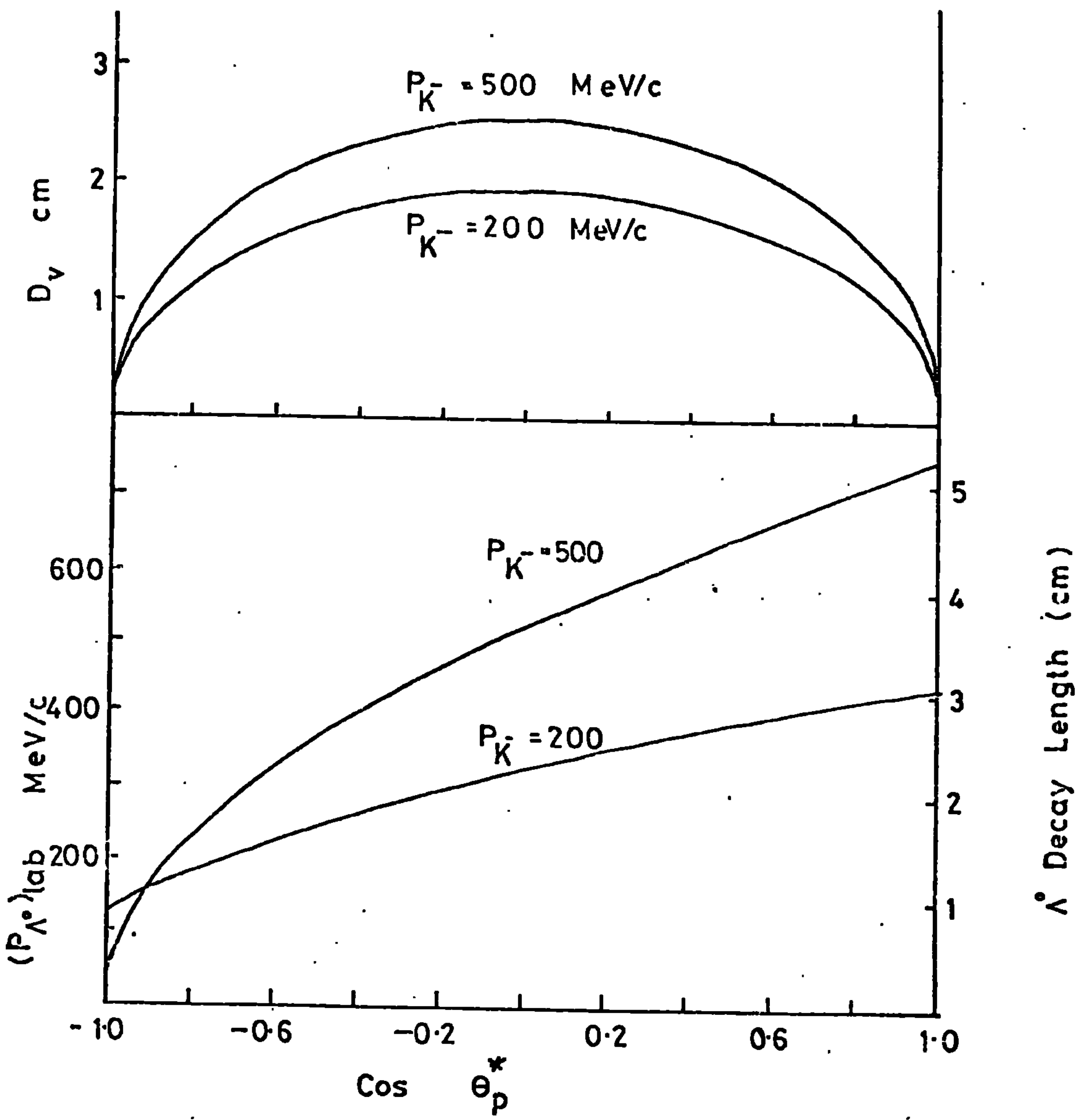

FIG 5·15: Kinematics of Neutral Hyperon Production

θ_p can be replaced by θ_p^*. The values of D_v are shown in fig. 5.15 and clearly indicate that, in the worst possible case, a decay vee is usually seen if the vertex is at least 2 cm from the perspex walls.

The central two regions are, therefore free from biases caused by the narrow chamber.

The events occurring in each of these volumes were further sub-divided depending on the Λ^0 lifetime ($< \tau/2$, $\tau/2 \longrightarrow \tau$, $> \tau$) and on the angle of dip for the hyperon(positive value (down), negative value (up)). The results of this division is shown in table 5.9.

Table 5.9: Division Of Neutral Hyperon Events Into Lifetime, Dip Angle And Chamber Depth Intervals

Region	Z Coordinate (cm)	$< \frac{1}{2}\tau$		$\frac{1}{2}\tau \longrightarrow \tau$		$> \tau$	
		Up	Down	Up	Down	Up	Down
1	19.4 - 21.4	12	6	8	1	13	14
2	21.4 - 23.2	8	10	8	10	13	14
3	23.2 - 25.0	9	14	6	5	9	9
4	25.0 - 27.0	6	4	3	7	4	10

If no biases exist then there will be equal numbers of events travelling up and down irrespective of the location within the chamber. The events most likely to exhibit assymetric behaviour are those near the walls and with long lifetimes; as this is not seen in the present results the production angle losses can be estimated using the ϕ_p and cos θ^*_p distributions (fig. 5.13). The slight backward peak in the cos θ^*_p distribution is consistent with the results obtained by Fallahi (12) who showed that the P wave contribution is significant even at 250 MeV/c. The present statistics are too small to determine the onset of the contribution.

No losses are seen in these distributions and the only remaining correction is that of the hyperon lifetime.

5.3.4 Minimum Observable Length Of Hyperon

A Λ^0 hyperon decaying close to the interaction vertex is classified as a two prong $\pi^- p$ event if no gap between the primary and decay vertices is seen. These events may be corrected in exactly the same way as for charged hyperons. Each event is weighted by the inverse of its probability of decay between ℓ_{min} and ℓ_{pot}. These are the minimum projected length,

$$\ell_{min} = \frac{p}{m} c \, t_{min} \cos \lambda$$

and the potential length of the hyperon. The latter is the distance between the primary vertex and the chamber boundary as measured along the direction of the hyperon and may be converted to a proper time using the above relation with $\lambda = 0°$.

The weighting factor used was

$$W = \left(\exp (- t_{min}/\tau) - \exp (- t_{pot}/\tau) \right)^{-1}$$

events lying outside t_{min} and t_{pot} were rejected from the sample. This method is analogous to using the hyperon lifetime distribution (fig. 5.16) and correcting for the loss of short lived hyperons. The lifetime is in good agreement with the accepted world value of 2.63×10^{-10} sec.

The weighting factor correction automatically corrects for the shallow chamber effects (if any) and as these are neglibible it is not surprising to find that the cross-section results from the lifetime distribution and those from the weighting factor are consistent.

5.3.5 Neutral Hyperon Cross-Section

The remaining corrections applied to the observed number of events are summarised in table 5.10. Events fitting hypotheses with topologies greater than 002 were not used and a small correction factor was introduced. A selection of secondary particle momenta was made to remove spurious measurements, only about 2% of events were rejected by

FIG 5·16: Distribution of Proper Lifetimes for Λ^0 Hyperons.

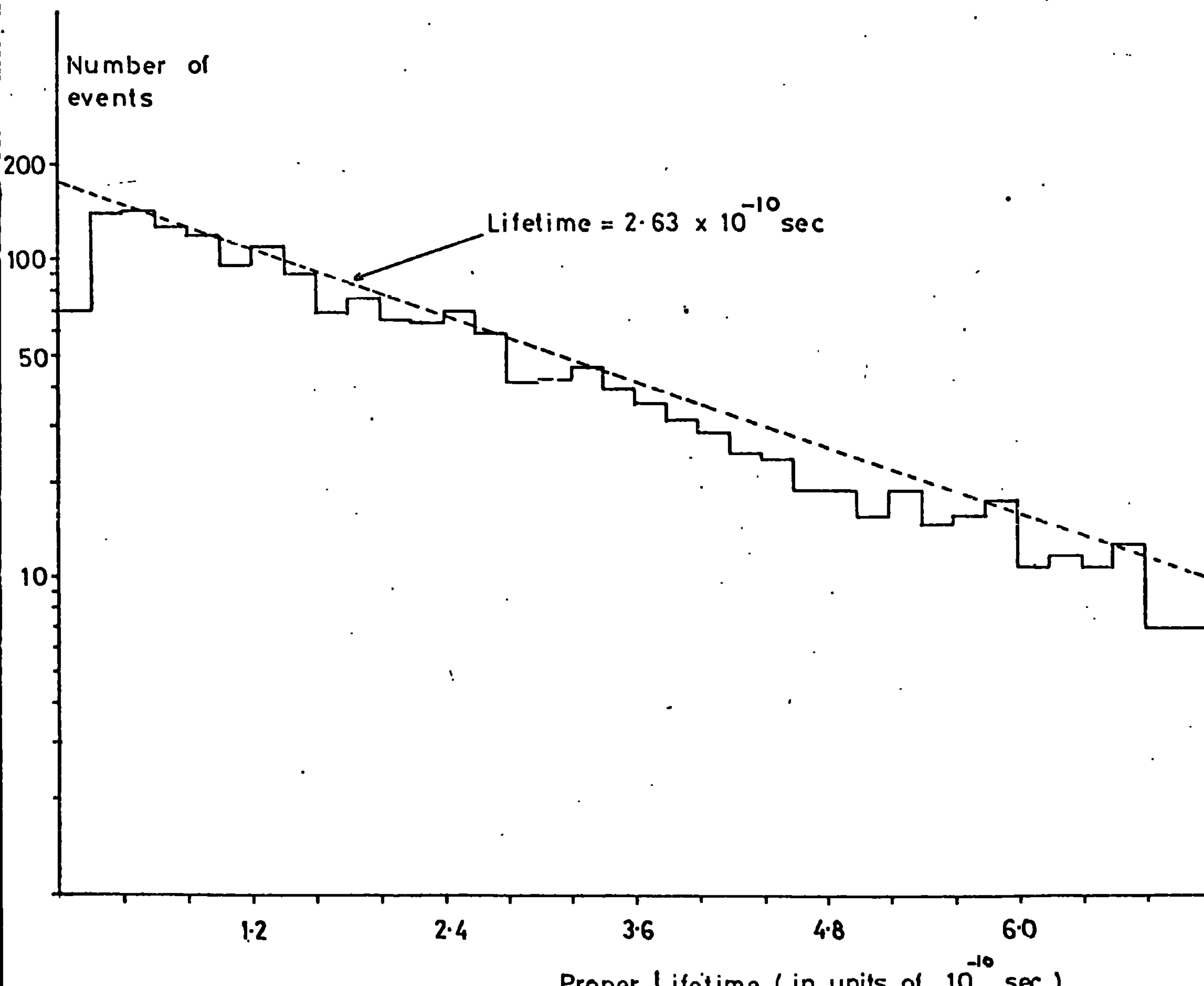

Table 5.10:

Summary Of Correction Factors And Events Selection For Neutral Hyperons

	Number Of Events		Correction Factors	
Decay Branching Ratio			1.557	
Scanning Efficiency			1.042	
Decay Angle Losses			1.161	
Total Number Of Scanned Λ^0 Events	4496			
			1.109*	
Number Of Measurable Events	3953			
			1.034	
Number Of Events Fitting 001 and 002 Hypotheses	3821			
	001	002	001	002
	2884	937		
			1.042	1.067
Hypothesis Selection Of Events	2769	878		
Events Lying Inside Fiducial Volume	1932	645		
			1.013	1.035
Events Remaining After Removal Of Kinematic Fits With Spurious Results	1907	623		
Total Correction Factors For 001 and 002 Hypotheses			2.280	2.386

* 79.7% of the unmeasurable events were unmeasurable for random reasons

this selection. The remaining corrections for scanning efficiency, decay branching ratio and unmeasurable events are also included. The final results for the cross-sections are shown in fig. 5.17 and table 5.11.

5.4 Charge Exchange Channels

The charge exchange channel

$$K^- + p \longrightarrow \overline{K^o} + n$$
$$\overline{K^o} \longrightarrow \pi^+ + \pi^-$$

has a threshold kaon momentum of 90 MeV/c and is topologically similar to the neutral hyperon production channel.

The decay length of the $\overline{K^o}$ meson is typically ~ 1 cm at these low momenta hence there will be no biases in detection due to the shallow chamber, although this channel has the additional problem of a large opening angle between the secondary decay pions (150 - 180°) which makes scanning for these events extremely difficult.

The analysis was carried out in the same way as for the neutral hyperon channel except that no primary momentum selection was made. The lifetime distribution is shown in fig. 5.18 and is clearly consistent with the world value of 0.893×10^{-10} sec although there are losses at short lifetimes which are due to the classification of events with an unseen $\overline{K^o}$ being classified as $\pi^+\pi^-$ events. These losses were corrected for using the weighting factor as defined in 5.3.4. The distribution of production and decay angles are shown in fig. 5.19. Losses in ϕ_d are evident below $\sim 50°$ and are due to the scanning difficulties mentioned earlier, the correction factors are summarised in table 5.12 and the channel cross-sections are shown in table 5.13 and fig. 5.20.

FIG 5·17: Cross-section for Neutral Hyperon Production.

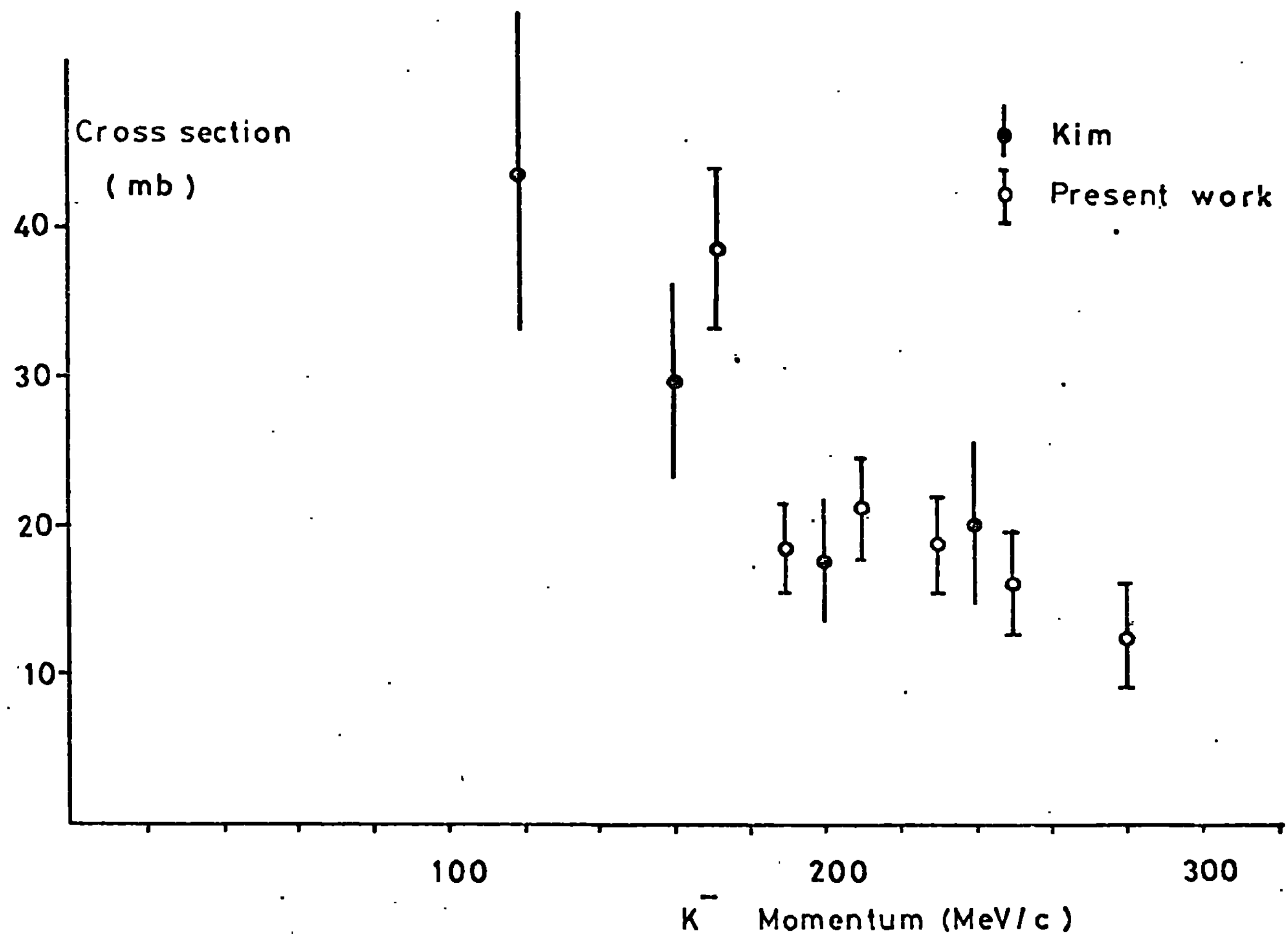

Table 5.11:

Neutral Hyperon Cross-Section

Momentum Interval (MeV/c)	Observed Number of 001 Hypotheses	Observed Number of 002 Hypotheses	Corrected Number Of 001 And 002	Total Neutral Hyperon Cross-Section (mb)
160 - 180	49	12	167.1	39.2 ± 5.6
180 - 200	25	18	122.3	18.8 ± 3.1
200 - 220	32	13	164.2	21.5 ± 3.4
220 - 240	30	8	114.7	19.0 ± 3.3
240 - 260	19	6	84.6	16.3 ± 3.4
260 - 300	12	3	59.6	12.7 ± 3.5

FIG 5·18: Distribution of Proper Lifetimes for ChargeExchange

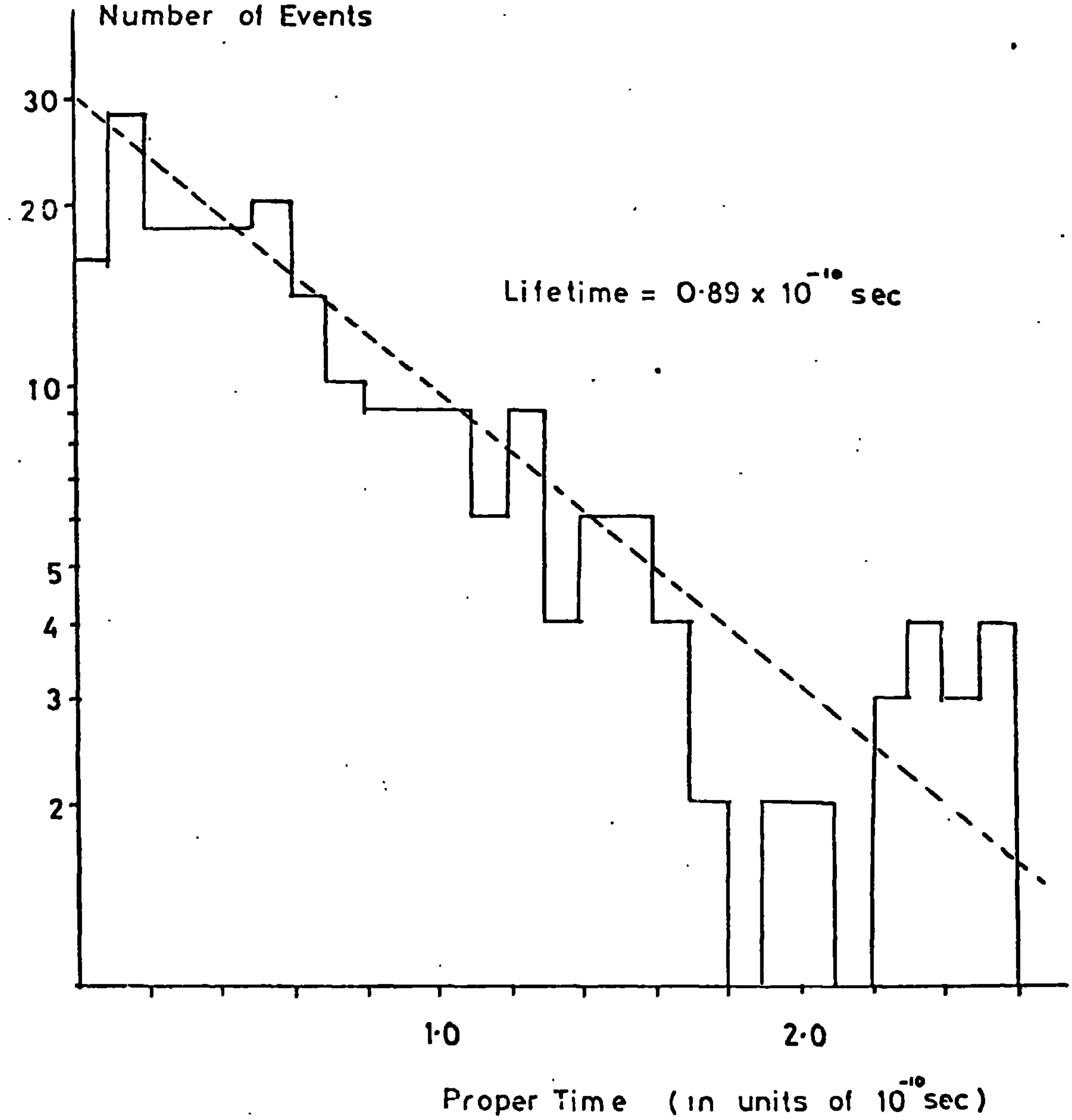

FIG 5·19: Production and Decay Angle Distributions.

Charge Exchange

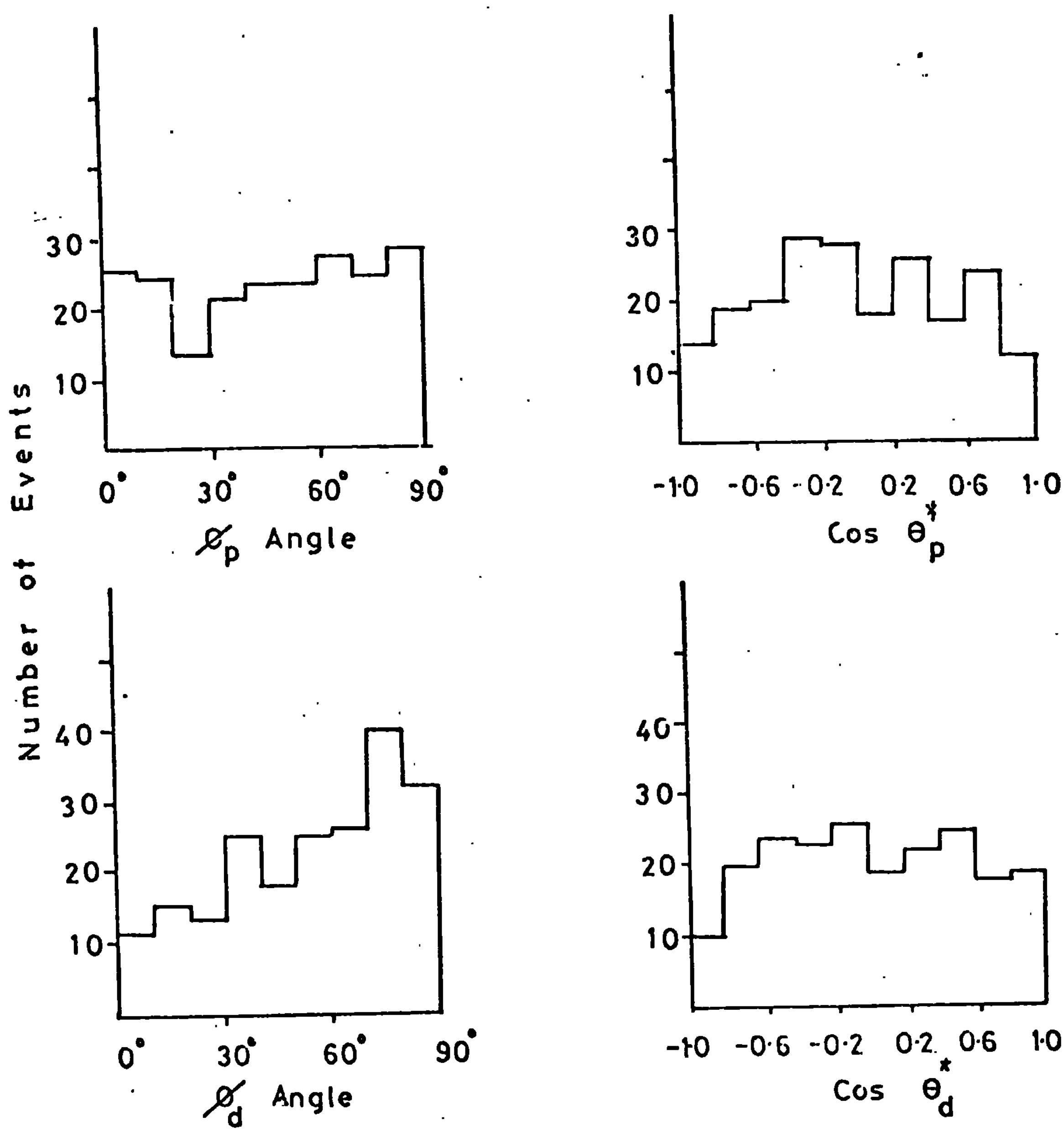

Table 5.12

Summary Of Event Selection And Correction

For The Charge Exchange Channel

	Number Of Events	Correction Factor
Branching Ratio Correction And K^o_L Correction		2.915
Scanning Efficiency		1.071
Decay Angle Losses		1.290
Scanned $\overline{K^o}$ Events	300	
		1.103*
Measurable Events	254	
		1.036
Events Found On D.S.T.	245	
Events Fitting The Multi-Vertex Hypothesis	236	
Events Inside Reduced Fiducial Volume	198	
Overall Correction Factor		4.602

* 57% of the "unmeasurable" events were unmeasurable for random reasons

Table 5.13: $\overline{K^o}n$ Cross-Sections

Momentum Interval (MeV/c)	Observed Number Of Events	Number Of Events After Lifetime Weighting	Corrected Number Of Events	Cross-Section (mb)
100 - 120	11	15.3	70.4	37.2 ± 11.4
120 - 140	12	16.7	76.8	26.5 ± 7.6
140 - 160	20	27.5	126.6	27.0 ± 6.1
160 - 180	27	38.2	175.8	24.2 ± 4.6
180 - 200	30	38.2	175.8	17.2 ± 3.2
200 - 220	31	37.6	173.0	13.3 ± 2.4
220 - 240	28	37.5	172.6	16.7 ± 3.2
240 - 260	23	31.2	143.6	16.2 ± 3.5
260 - 300	12	15.6	7.18	8.9 ± 2.7

FIG 5·20 : Cross section for Charge Exchange

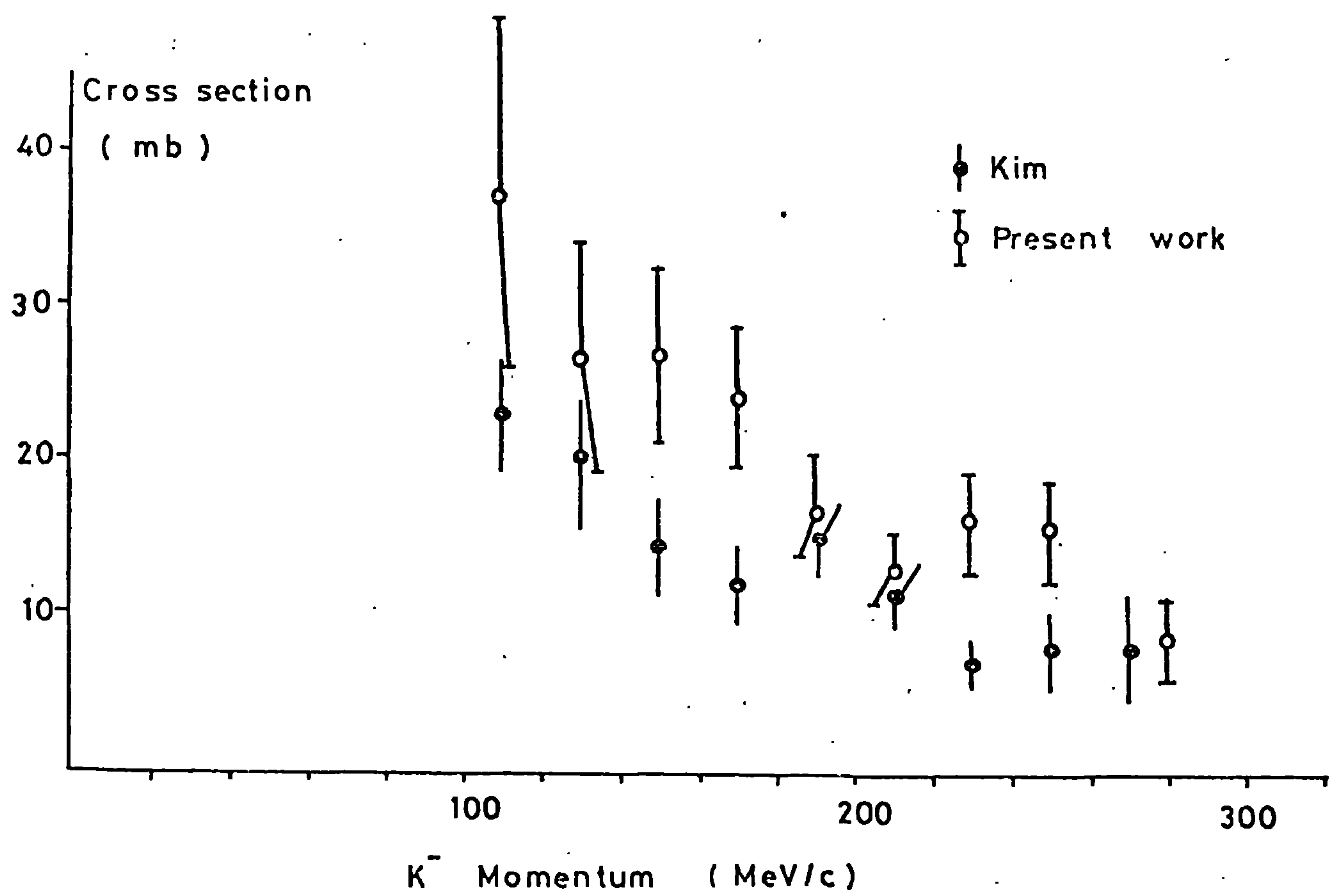

CHAPTER SIX

GAMMA RATIO - DATA AQUISITION

A separate experiment was carried out to determine the ratio, γ, of the charged hyperon production cross-sections at zero kaon momentum. This ratio, which is defined as

$$\gamma = \frac{\sigma(K^- p \longrightarrow \Sigma^- \pi^+)}{\sigma(K^- p \longrightarrow \Sigma^+ \pi^-)}$$

is related to the phase angle between the I = 0 and I = 1 transition amplitudes for Σ hyperon production (§ 1.7.2) and may be used as a low energy parameter in K matrix analyses. In view of the difficulty of obtaining other parameters at zero momentum it is important that the ratio be well determined in order to help in the extrapolation of the low energy $K^- p$ transition amplitudes into the non-physical region near the Λ (1405) bound state. Because of the discrepancy between the γ ratios quoted by Kim (3) ($\gamma = 2.06 \pm 0.06$) and by Tovee et al (4) ($\gamma = 2.34 \pm 0.08$) and also because of the criticisms of Kims results (2) it was felt essential to provide a precise determination of the ratio.

This chapter discusses the general problems associated with scanning for hyperon events and also develops a model which is used as a basis for the two methods which have been used to determine the ratio. The scanning and measuring for this part of the experiment differs slightly from that discussed in chapters two and three and is described later.

Chapter seven contains the data analysis and a detailed discussion of data consistency.

6.1 Detection Of Charged Hyperons In The Chamber

The reaction sequences that are of interest in the determination of the γ ratio are as follows:

$$K^- + p \longrightarrow \Sigma^+ + \pi^-$$
$$\quad \Sigma^+ \longrightarrow p + \pi^0$$

$$K^- + p \longrightarrow \Sigma^+ + \pi^-$$
$$\quad \Sigma^+ \longrightarrow n + \pi^+$$

$$K^- + p \longrightarrow \Sigma^- + \pi^+$$
$$\quad \Sigma^- \longrightarrow n + \pi^-$$

$$K^- + p \longrightarrow \Sigma^- + \pi^+$$
$$\quad \Sigma^- \longrightarrow \text{neutral particles}$$

$$(\text{e.g. } \Sigma^- p \longrightarrow \Lambda^0 n)$$

All events of interest have zero kaon momentum. In general these will display a characteristic collinearity which is used as a detection criterion; however there are two exceptions to this.

Firstly, the short lifetimes of the hyperons give rise to a considerable fraction of the events ($\sim$10%) when the hyperon decays before leaving a visible track, this creates a two prong event comprising either two pions or a pion and a proton.

Secondly, since $\sim$ 1/7 of the events are in-flight interactions, there will be a number of events in which the secondaries are produced in the extreme forward or backward directions and will simulate a collinear event. This amounts to less than 1% of the genuine events.

Furthermore, the close decay of neutral kaons or Λ hyperons simulate and hence contaminate the two pion and pion proton events previously mentioned. Also the range of the decay proton from a Σ^+ hyperon may under certain circumstances be too short to be observed and will cause scanning losses unless care is taken to correct for this.

The methods of analysis and scanning procedure have been developed with a view to taking these problems into account.

6.2 Previous Determinations Of The Gamma Ratio

The results of previous experiments to determine the γ ratio are summarised in table 6.1 overleaf and shows that the two most precise determinations are in disagreement. These determinations use different techniques and are compared in table 6.2.

Table 6.1: Gamma Ratio Determinations

Author		Experiment
Humphrey & Ross (13)	2.15 ± 0.12	Hydrogen Bubble Chamber
Eisele et al (35)	2.2 ± 0.2	Hydrogen Bubble Chamber
Kim (3)	2.06 ± 0.06	Hydrogen Bubble Chamber
Tovee et al (4)	2.34 ± 0.08	Nuclear Emulsion

The motivation for the emulsion experiment was to provide precise measurements of the hyperon events so that measurement errors were small compared to the maximum range of the hyperon. The method used collinear Σ hyperon events where the Σ came to rest in the emulsion. The Σ^+ and Σ^- hyperons were easily separated, their ranges being 702 and 812 μm respectively. Hyperon decays in flight were corrected for using the known decay law.

Bubble chamber experiments whilst using larger statistics than emulsion work suffer from lack of measurement precision for hyperon lengths < 1mm. It is unclear from Kim's results exactly what steps were taken to avoid this problem.

6.3 Present Experiment

The data for this work came entirely from interactions inside the hydrogen target. The particle tracks consisted of closely spaced bubbles which enabled Σ ranges down to ~ 0.5 mm to be resolved.

The data were obtained from sixteen rolls of film which was divided between Durham (five rolls), London (five and a half rolls) and Brussels (five and a half rolls) for separate scanning and measuring. The results discussed here are those for the Durham data only. Before combining the results of the three laboratories it is essential to ensure that the individual experimental biases are understood. The scanning and measuring was standardised to avoid most of these problems; the use

Table 6.2: Comparison Of The Nuclear Emulsion And Bubble Chamber Techniques

Nuclear Emulsion	Hydrogen Bubble Chamber
Spatial Resolution $\sim 1\,\mu m$	Resolution ~ 0.5 mm
Stopping Time For Σ $\sim 10^{-13}$ sec	Stopping Time 10^{-9} sec
Nearly All Σ's Stop Before Decaying	Most Σ's Decay Before Stopping
No Charge Discrimination; But The Unique Ranges Of The Hyperons (702 μm For Σ^{+} And 812 μm For Σ^{-}) Allow Separation	Charge Resolution Using Track Curvature
Difficult And Tedious To Accumulate Large Statistics	Easier To Produce Large Statistics

of different scanning machines with different magnifications and the involvement of different research groups makes a detailed consistency check essential.

6.4 Gamma Ratio Model

There are six main categories into which the hyperon production channels may be classified. These are in table 6.3 and the appearances of the events are shown in fig. 2.7.

The method is based on the assumption that there is a minimum range of the hyperon below which it is impossible to determine the sign of the charge of the hyperon. The problem only arises for events with the pion decay mode, the proton decay mode is unique to the Σ^+ hyperon.

The model uses the following nomenclature:

N^- = total number of Σ^- hyperons produced of lifetime τ^-

N^+ = total number of Σ^+ hyperons produced of lifetime τ^+

t^-_π = time taken to reach the minimum range (cut off distance) for Σ^- hyperons decaying to π^-

t^+_π = time taken to reach the minimum range (cut off distance) for Σ^+ hyperons decaying to π^+

t^+_p = time taken to reach the minimum range (cut off distance) for Σ^+ hyperons decaying to p

t^-_R = time taken for the Σ^- hyperon to come to rest

$$B = \frac{\Gamma(\Sigma^+ \longrightarrow \pi^+ n)}{\Gamma(\Sigma^+ \longrightarrow \pi^+ n) + \Gamma(\Sigma^+ \longrightarrow \pi^0 p)}$$

Using decay laws, the problem may be represented schematically as in fig. 6.1.

The theoretical number of events in each category is given by:

$$\Sigma^-_\pi = N^- \exp(-t^-_\pi/\tau^-) - N^- \exp(-t^-_R/\tau^-)$$

$$\Sigma^-_\sigma = N^- \exp(-t^-_R/\tau^-)$$

Table 6.3: Topological Classifications Of

Charged Σ Hyperon Production Reactions

Group Symbol	Reaction Sequence		
$\Sigma^-\pi$	$K^-p \longrightarrow \Sigma^-\pi^+$	$\Sigma^- \longrightarrow n\pi^-$	clearly visible Σ tracks
$\Sigma^+\pi$	$K^-p \longrightarrow \Sigma^+\pi^-$	$\Sigma^+ \longrightarrow n\pi^+$	clearly visible Σ tracks
Σ^+p	$K^-p \longrightarrow \Sigma^+\pi$	$\Sigma^+ \longrightarrow p\pi^o$	clearly visible Σ tracks
$\Sigma^-\sigma$	$K^-p \longrightarrow \Sigma^-\pi^+$	captured at rest by a proton. No decay seen	
$\pi^+\pi^-$	$K^-p \longrightarrow \Sigma^{\mp}\pi^{\pm}$	$\Sigma^{\mp} \longrightarrow n\pi^{\mp}$	too short to be seen
π^-p	$K^-p \longrightarrow \Sigma^+\pi^-$	$\Sigma^+ \longrightarrow p\pi^o$	Σ^+ too short to be seen

FIG 6·1: Schematic Representation of The Classification of Hyperon Events into Scanning Categories.

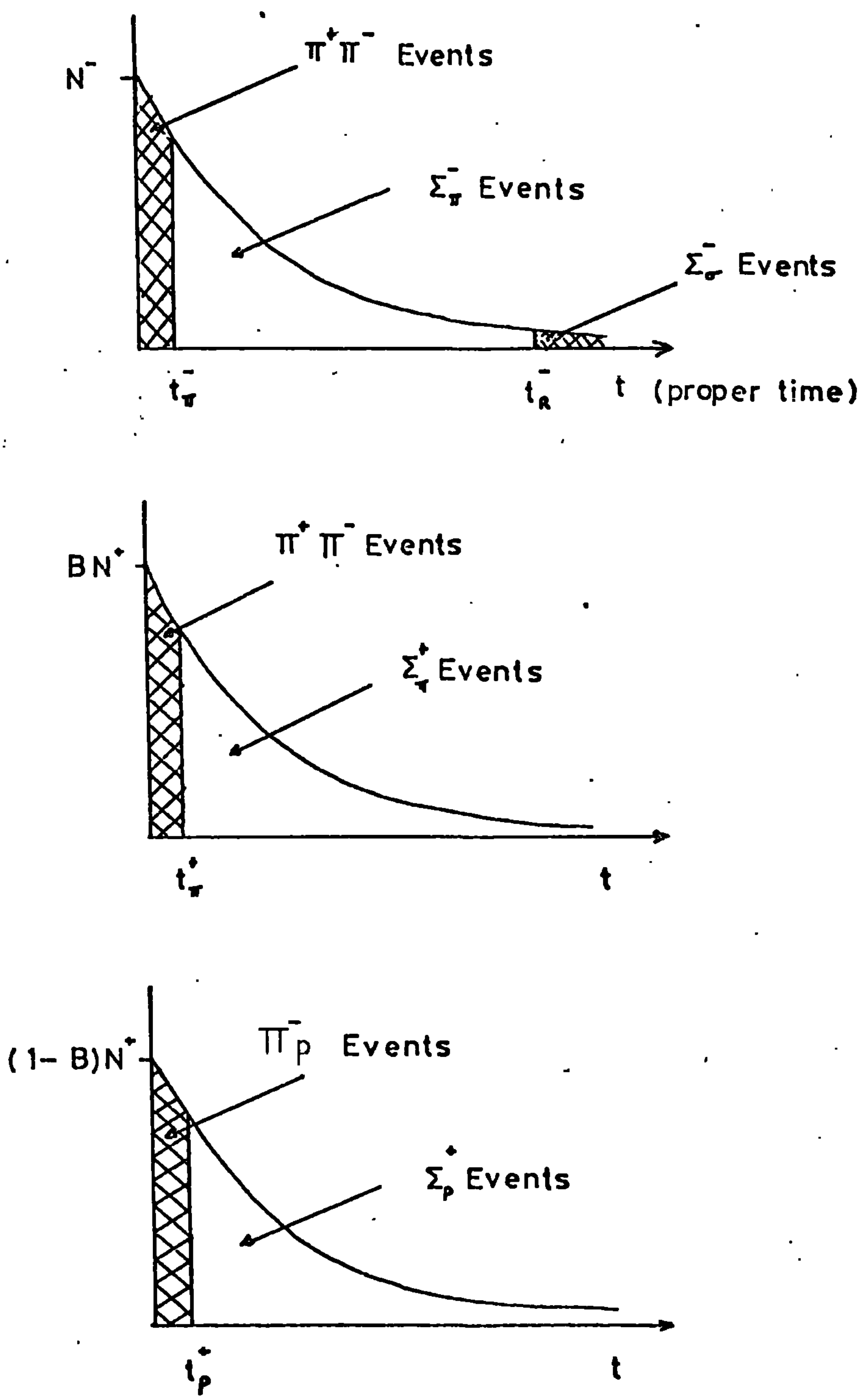

$$\Sigma^+_\pi = BN^+ \exp(-t^+_\pi/\tau^+)$$
$$\Sigma^+_p = (1-B)N^+ \exp(-t^+_p/\tau^+)$$
$$\pi^+\pi^- = N^-(1-\exp(-t^-_\pi/\tau^-)) + BN^+(1-\exp(-t^+_\pi/\tau^+))$$
$$\pi^-p = (1-B)N^+(1-\exp(-t^+_p/\tau^+))$$

The proper times may be converted to laboratory distances using the relation:

$$t = \frac{m\ell}{p(\ell)c}$$

m = particle mass

$p(\ell)$ = particle momentum; length dependent

c = velocity of light

Rewriting the above equations and replacing t by ℓ gives

$$\Sigma^-_\pi + \Sigma^-_\sigma = N^- \exp(-k^- \ell^-_\pi) \qquad 6.1$$
$$\Sigma^+_\pi = BN^+ \exp(-k^+ \ell^+_\pi) \qquad 6.2$$
$$\Sigma^+_p = (1-B)N^+ \exp(-k^+ \ell^+_p) \qquad 6.3$$
$$\pi^+\pi^- = N^-(1-\exp(-k^- \ell^-_\pi)) + BN^+(1-\exp(-k^+ \ell^+_\pi)) \qquad 6.4$$
$$\pi^-p = (1-B)N^+ \exp(1-\exp(-k^+ \ell^+_p)) \qquad 6.5$$

where $k^- = M_\Sigma -(p_\Sigma - (\ell)c\tau^-)^{-1}$

and $k^+ = M_\Sigma +(p_\Sigma+(\ell)c\tau^+)^{-1}$ 6.6

These five equations contain six unknown quantities (N^-, N^+, Σ^+_π, Σ^-_π, Σ^+_p, B) hence one assumption is required to solve the problem. It is the nature of this assumption that distinguishes the two methods used for the γ ratio determination.

6.5 Method I - Branching Ratio Method

The value of B has been determined by other experiments (5) to give an average world value of 0.4835 ± 0.0077. This value of B may be used and the equations 6.1 to 6.5 may be solved to give:

$$N^- = (\Sigma^-_\pi + \Sigma^-_\sigma + \Sigma^+_\pi + \pi^+\pi) - \frac{B}{1-B}(\Sigma^+_p + \pi^-p) \qquad 6.7$$

and $$N^+ = \frac{\Sigma^+ p + \pi^- p}{(1 - B)}$$ (see footnote) 6.8

The remaining quantities $\Sigma^-\pi$, $\Sigma^+\pi$, $\Sigma^+ p$ may be solved for using the world B value.

$$\ell^-_\pi = \frac{1}{k^-} \ln\left(\frac{N^-}{\Sigma^-_\pi + \Sigma^-_\sigma}\right) \qquad 6.9$$

$$\ell^+_\pi = \frac{1}{k^+} \ln\left(\frac{BN^+}{\Sigma^+_\pi}\right) \qquad 6.10$$

$$\ell^+_\pi = \frac{1}{k^+} \ln\left(\frac{(1 - B)N^+}{\Sigma^+_p}\right) \qquad 6.11$$

The values of k^+ and k^- may be found easily by assuming that there is no momentum loss of the Σ hyperon over the short minimum range.

Writing the formulae for N^+ and N^- in this way demonstrates the novelty of this method in that it is only required to determine the numbers ($\Sigma^-_\pi + \Sigma^-_\sigma + \Sigma^+_\pi + \pi\,\pi$) and ($\Sigma^+_p + \pi^- p$) in order to measure the γ ratio. It is only necessary to separate the hyperon events by their decay modes and not by their charges. This can be done easily using ionisation information to distinguish pions from protons. A separation of the $\pi^+ \pi^-$ category into Σ^+ or Σ^- groups is not required. A separation

---

footnote

Equations 6.7 and 6.8 can be derived as follows:

Total number of Σ^+ events which decay via the proton mode = $\Sigma^+_p + \pi^- p$

Then total number of Σ^+ events which decay via the pion mode

$$= \frac{B}{1 - B} (\Sigma^+_p + \pi^- p)$$

Total number of Σ^+ events $= \Sigma^+_p + \pi^- p + \frac{B}{(1 - B)} (\Sigma^+_p + \pi^- p)$

$$= \frac{\Sigma^+_\circ + \pi^- p}{1 - B}$$ same as equation 6.8

Equation 6.7 may be written, in words, as

N^- = (all Σ^- events + all Σ^+_π events) - (all Σ^+_π events).

is undesirable since the composition of the $\pi^+ \pi^-$ category is dependent on the range cut applied (see table 6.4). In a bubble chamber this range cut is comparable with the error of measurement and will produce an uncertainty in the $\pi^+ \pi^-$ separation. A large range cut would avoid this problem but would reduce statistics by ~ 50%.

Table 6.4: Effect Of Range Cuts On $\pi^+ \pi^-$ Separation

Range Cut (cm)	% Of Σ^- Events Classified As $\pi^+ \pi^-$	% Of Σ^+ Events Classified As $\pi^+ \pi^-$	Ratio Σ^-/Σ^+ In $\pi^+ \pi^-$ Category
0.05	7.5	12.8	0.59
0.10	14.4	23.9	0.60
0.15	20.8	33.6	0.62
0.20	26.8	42.1	0.64

6.6 Method II - Minimum Effective Range. (M.E.R.)

Equations 6.1 - 6.6 can be re-arranged to give the following relations:

$$\pi^+\pi^- = (\Sigma^-_{\sigma} + \Sigma^-_{\pi})(e^{k^- \ell^-_{\pi}} - 1) + \Sigma^+_{\pi}(e^{k^+ \ell^+_{\pi}} - 1) \qquad 6.12$$

$$\gamma = \frac{(\Sigma^-_{\sigma} + \Sigma^-_{\pi})\, e^{-k^- \ell^-_{\pi}}}{\pi^- p + \Sigma^+_p + \Sigma^+_{\pi}\, e^{k^+ \ell^+_{\pi}}} \qquad 6.13$$

$$B = \frac{\Sigma^+_{\pi}\, e^{k^+ \ell^+_{\pi}}}{\Sigma^+_{\pi}\, e^{k^+ \ell^+_{\pi}} + \pi^- p + \Sigma^+_p} \qquad 6.14$$

If the assumption that $\ell^+_{\pi} = \ell^-_{\pi}$ is made, it is possible to solve equation for the minimum range (ℓ) using the observed number of $\pi^+ \pi^-$ events. This value of ℓ may be used in 6.13 and 6.14 to yield values for γ and B. The assumption is likely to be reasonable because the Σ^+_{π} and Σ^-_{π} events are topologically identical and there is no reason for one to be less visible than the other. Like method I; this method does not require a division of the $\pi^+ \pi^-$ category into the Σ^+ and Σ^- events.

6.7 Track Ionisation

The essence of the first method for determining the γ ratio is the separation of proton and pion tracks using track ionisations.

The number of bubbles produced by a particle is inversely proportional to the square of its velocity.

$$I = \frac{I_o}{\beta^2} \qquad \text{where } I = \text{ionisation}, \quad I_o = \text{constant}$$

For a particle having an angle of dip λ, a momentum p and a mass m, the ionisation in the x - y plane (normal to the line of sight) may be written as:

$$I_{x,y} = I_o \left(1 + \frac{m}{p}\right)^2 \sec\lambda$$

The relative ionisations of kaons, pions and protons may now be evaluated and are shown in table 6.5.

Table 6.5: Track Ionisations

Particle	Momentum Range MeV/c	Ionisation In Units Of $I_o \sec\lambda$
K	150 ⟶ 250	11.9 ⟶ 5.3
π	100 ⟶ 350	2.9 ⟶ 1.2
p	100 ⟶ 300	89.0 ⟶ 10.0

Ionisations above ~5 or 6 appear as black or unbroken tracks; the eye is able to respond to small changes (~ 0.5) in ionisation below 5 in the T.S.T. chamber, but above this number only large differences are detectable (~ 5 - 10). For tracks which are flat in the chamber there is no difficulty in resolving their ionisations, however the dip angles of the secondary particles vary between $\pm$ 90°. This experiment is interested mainly in the separation of the protons and pions and the ionisations of these would become ambiguous when the most heavily ionising pion simulates a lightly ionising proton. This occurs at a dip angle of about 73°. Assuming an isotropic distribution of pion and proton tracks, the fraction of solid angle where ambiguities may occur is approximately 4%.

All tracks having ionisations > 5 were assumed to be protons, although some ambiguous tracks could be resolved by examination of the continuation into the Ne/H_2 mixture; where pions would occasionally exhibit a characteristic decay, $\pi^+ \longrightarrow \mu^+ \bar{\nu}_\mu$ followed by $\mu^+ \longrightarrow e^+ \nu_e \bar{\nu}_\mu$

6.8 Scanning

This was essentially the same as that discussed in chapter two. The aim was to ascribe physical channels to each event and it was this part of the experiment which gave rise to the scanning codes described in § 2.8. The topologies scanned for were those relevant to charged hyperon production (fig. 2.7) and the scanning categories are summarised in table 6.6. Additional sub divisions were added on the basis of preliminary measurements made during the scanning stage; these are discussed in § 6.9 below.

Table 6.6: Summary Of Scanning Categories

Reaction	Total Number Of Sub-divisions	Sub-divisions
$\Sigma^-\pi$	3	collinear, non collinear, ambiguous
$\Sigma^+\pi$	3	collinear, non collinear, ambiguous
$\Sigma^-\sigma^-$	3	collinear, non collinear, ambiguous
Σ^+p	12	collinear, non collinear, ambiguous
		range of Σ^+ and p tracks, groups 1,2,3,4.
$\pi^+\pi^-$	2	at rest by template, in flight by template (see § 6.9)
π^-p	24	at rest by template, in flight by template (see § 6.9)
		separate into Σ production, Λ production, ambiguous.
		Range of proton track, groups 1,2,3,4

6.9 Measuring

For the two prong $\pi^+ \pi^-$ and $\pi^- p$ events there is no signature of collinearity to specify if the event occured at rest or in flight. In order to remove the in flight events a measurement of some kind must be made.

The difficulties of making a conventional measurement of the beam momentum have already been discussed in detail in § 4.6. The measured value obtained using this approach may take any value below $\sim$ 150 MeV/c making it impossible to specify that a particular event is at rest. Only a statistical separation can be made using this method.

An alternative approach exploits two features of the beam tracks entering the chamber. Firstly, most beam tracks lie within $\sim 10°$ of the x - y plane of the chamber and any curvature measurement on the scanning table will give a direct estimate of the particle momentum; secondly the nature of the range-momentum relation (fig.6.2) in the low momentum region (< 150 MeV/c) gives the stopping kaons a characteristic appearance due to the rapid rate of change of curvature over the last 2 - 3 cm of track length.

These features combine to make the use of a beam profile template a workable method for separating in flight and at rest events individually.

The template was constructed using clearly collinear $\Sigma^-\pi$ events, the final template being an average profile of several beam shapes. Distortions to the beam tracks are caused by small angle elastic scatters; coulomb scattering, a variation of magnification with chamber depth and slight dip angle variations of the beam tracks. The template was checked against further collinear events. The fitting involved sliding the template along the beam track until the best fit was obtained. In general the template vertex and the event vertex were not coincident, however the maximum discrepancy was ~ 3.0 cm corresponding to a residual momentum of $\sim$ 120 MeV/c. This is not a serious problem because the path length

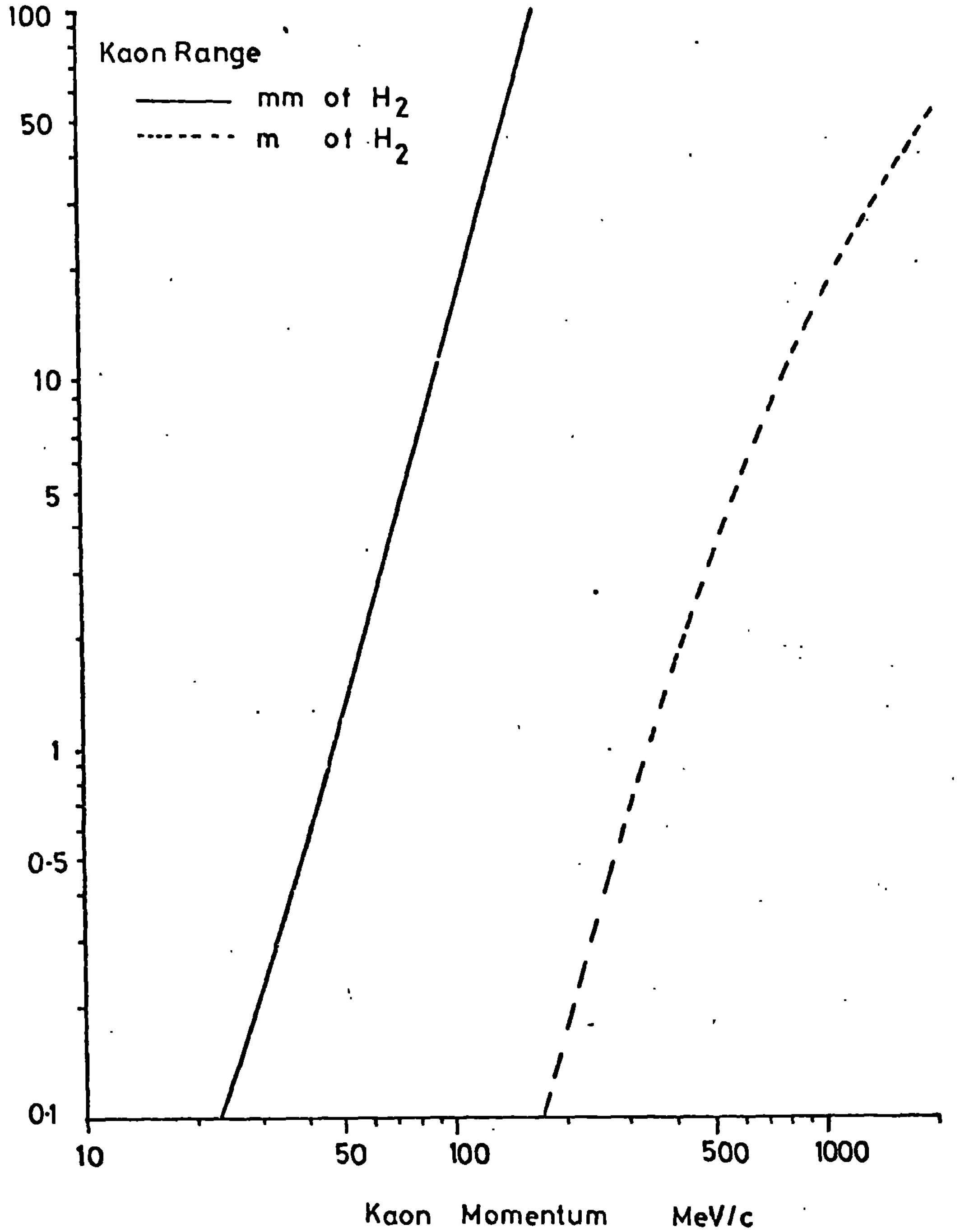

FIG 6·2: Ionisation Energy Loss for Kaons in Liquid Hydrogen.

available for an in-flight interaction is very small compared to the interaction length. Hence events below 120 MeV/c according to the template will be at rest.

A template was also manufactured using the long secondary pion tracks from collinear Σ production events to give a radius corresponding to 180 MeV/c. This was used on the π^-p events only (see below).

A further template was made which comprised of four concentric circles whose radii corresponded to 1,2,3 and 4 mm in chamber space.

These three templates were used during the scanning for the following purposes:

(i) The beam profile template was used to remove from the $\pi^+\pi^-$ and π^-p categories all events which were in flight.

(ii) The 180 MeV/c template was checked against the negative pion in all the π^-p events. Pions having momenta commensurate with 180 MeV/c were classified as $\pi^-p(\Sigma)$ events, whilst those with smaller pion momenta arose from Λ^0 production and were classified as π^-p (Λ) events. Ambiguous events were disignated π^-p (?).

(iii) For each Σ^+p and π^-p event, the distance, r, between the primary vertex and the end point of the dark positive track (proton) was measured using the concentric circles and each π^-p or Σ^+p was sub-divided into four range groups ($r < 1$ mm, $1 \leqslant r \leqslant 2$, $2 \leqslant r \leqslant 3$, $r > 4$ mm). This information is used later to estimate the losses from unseen protons.

It was felt that because the template method was hitherto untried, full measurements of all two prong events should be made in order to carry out a consistency check between the two methods. In particular, the separation of the π^-p events into π^-p (Σ) and π^-p (Λ) events was complicated by the large dip angles of the secondaries which prevented many π^-p events being resolved into Σ or Λ categories.

A small number of collinear and all the non-collinear hyperon events were also fully measured using the system described in chapters two and three.

6.10 Processing

This was carried out using the processing described in chapters two and three. However, initially the judging and remeasuring lists were compiled manually. Judging was carried out with reference to the KINEMATICS data rather than the computer controlled output of the JUDGE programme.

It was decided to process these events in exactly the same way as for the other K^-p data. This involved re-processing the measurements and compiling a complete MASTERLIST for all the scanned events.

As the original processing was less strictly controlled there existed clerical and inconsistency errors in the remeasuring and judging. The third measure was carried out to resolve most of these difficulties, although a few clerical errors ($\sim$ 1%) remain which should not bias the results in any way.

CHAPTER SEVEN

GAMMA RATIO - DATA ANALYSIS

In this chapter the data, their analysis and the value of the γ ratio determined in this experiment are presented. The basic data are given in table 7.1 and are condensed into six major categories in table 7.2. The effect of successive corrections to the data can also be seen in this table and will be explained later. However, prior to that the selection of data for the production of momentum distributions is discussed.

7.1 Selection Of Data For Analysis

The events used in the following analysis are those, having passed both GEOMETRY AND KINEMATICS, which have at least one final kinematic fit. The events not used were those which:

(i) were unmeasurable for some reason

(ii) failed geometrical reconstruction

(iii) failed kinematic fitting

(iv) fitted a hypothesis which was in disagreement with the scanning code.

A system of selection may introduce biases and these must be identified and considered. On the whole the requirement that the event have at least one kinematic fit introduces no serious bias as can be seen in the pass rates for geometrical reconstruction and kinematic fitting for the first and second measures.

Measure 1		Measure 2		Overall
Geom.	Kin.	Geom.	Kin.	Geom. + Kin.
90.5%	83.4%	91.0%	73.6%	91.6%

The similarity between the first and second measures implies that events

Table 7.1: Scanning Results For The Gamma Ratio

Events With A Visible Σ Hyperon Track

Category	Collinear	Non-collinear	Ambiguous
$\Sigma^-\pi$	4271	585	47
$\Sigma^-\sigma^-$	560	84	6
$\Sigma^+\pi$	1035	258	10
Σ^+p (1)	5	6	0
Σ^+p (2)	18	4	0
Σ^+p (3)	28	7	0
Σ^+p (4)	959	205	15

Events With An Invisible Σ Hyperon Track

Category		At Rest By Template	In Flight By Template
π^-p (Σ)	(1)	5	0
(Σ)	(2)	7	0
(Σ)	(3)	5	0
(Σ)	(4)	95	6
π^-p (Λ)	(1)	3	0
(Λ)	(2)	2	0
(Λ)	(3)	0	0
(Λ)	(4)	57	1
π^-p (?)	(1)	2	14
(?)	(2)	7	2
(?)	(3)	2	2
(?)	(4)	92	75
$\pi^+\pi^-$		698	124

Table 7.2: Summary Of Corrections Applied To The Scanning Data

	Number Of Events	Number Of Events After Correction For:				
		Ambiguous Collinearity	Scanning Efficiency	Λ^0 Hyperon Contamination	In-Flight Contamination	Short Proton Losses
$\Sigma^-\pi$ Collinear	4271	4312.2 *	4312.3	4312.3	4242.9 *	4242.9
$\Sigma\bar{\sigma}$– Collinear	560	565.2 *	565.8 *	565.8	560.0 *	560.0
$\Sigma^+\pi$ Collinear	1035	1043.0 *	1043.0	1043.0	1015.0 *	1015.0
$\pi^+\pi^-$ (At Rest)	698	698	699.4 *	699.4	699.4	699.4
π^-p (At Rest)	277	277	278.4 *	209.3 *	209.3	)1242.9 *
Σ^+p Collinear	1010	1023.3 *	1023.3	1023.3	998.6 *	)

* Indicates the numbers which differ from previous column

fail for random reasons rather than for reasons associated with the geometrical nature of the event.

This was confirmed by comparing the pass rates for each scanning category in turn. These were equal (within errors) and indicated that each channel is accepted onto the final D.S.T. with the same probability (see also the fit ambiguity matrix in table 7.3).

7.2 Correction For Ambiguous Collinear And Non-Collinear Events

The numbers being small, this separation was estimated using the ratio of the unambiguous categories to divide the ambiguous events (see table 7.2).

7.3 Correction For Scanning Efficiencies

The detailed calculation of these efficiencies are presented in §5.1.6; the results for the six major categories are shown in table 7.4 and all are extremely high.

Table 7.4: Scanning Efficiencies

(Nomenclature the same as table 5.2)

Category	e_{1+2}
$\Sigma^-\pi$	1.000
$\Sigma^-\sigma^-$	.999
$\Sigma^+\pi$	1.000
Σ^+p	.999
$\pi^+\pi^-$	.998
π^-p	.995

7.4 Template Measurement Of The Primary Kaons For $\pi^+\pi^-$ And π^-p Events

The template measurement was made to separate the "in-flight" events from those occurring "at rest" and this is compared to the separation obtained by using the full measurements made on all the $\pi^+\pi^-$ and π^-p events using the system described in chapters two and three.

Table 7.3: Compatibility Of Scan Code And Fitted Hypotheses

Fitted Hypothesis	Scan Code Category ⟶					
	$\pi^+\pi^-$	π^-p	$\Sigma^-\sigma^-$	$\Sigma^-\pi$	Σ^+p	$\Sigma^+\pi$
$\pi^+\pi^-$	720	42	60	2	3	1
π^-p	11	288	22	2	1	—
$\Sigma^-\sigma^-$	1	2	334	—	—	—
$\Sigma^-\pi$	4 *	2 *	7 *	1501	14 *	11 *
Σ^+p	—	2 *	2 *	10 *	441	17
$\Sigma^+\pi$	3 *	1 *	—	21 *	28	433
Other	8	9	3	5	1	1

Numbers marked with an asterisk are measuring mistakes and are a random sample of each scan code category.

The distributions of beam momentum for the $\pi^+\pi^-$ and π^-p events are shown in fig. 7.1. The peak at zero momentum arises from events whose measured range is greater than that expected from the centre of track momentum (found from the radius of curvature) and their momenta are set to a small value (0.1 MeV/c). The problem of errors of measurement which gives rise to the peak has already been discussed in § 4.6 where equation 4.11 illustrates the severity of the problem for low momentum kaons. The separation of the "in-flight" events from those "at rest" was found empirically by using a sample of collinear $\Sigma^{\pm}$ hyperon events which are known to be at rest. The collinear sample was improved further by excluding forward and backward Σ production events (within 30° of the direction of primary) which contains a small in-flight contamination. The momentum distribution for these events (fig. 7.2) gives a direct measure of the propagations of errors from the track centre to the vertex. The corresponding distribution for in-flight events (i.e. non-collinear) is also shown in fig. 7.2. The sum of these two distributions gives a distribution similar to that for the $\pi^+\pi^-$ events. By knowing the momentum dependence of the ratio of collinear to non collinear events, the separation for the $\pi^+\pi^-$ events may also be deduced assuming the same ratios. This may be formalised as follows.

For events with seen $\Sigma^{\pm}$ hyperons the total number of events (N_T) in a given momentum interval is the sum of the collinear and non-collinear events in the same interval.

This may be written as:

$$N_T = N_C + N_N$$

which may be rewritten in the form

$$N_C = \frac{R}{1 + R} N_T$$

where R is the ratio of the number of collinear events to the number of non-collinear events in a given momentum interval.

FIG 7·1: Distributions of K^- Momenta.

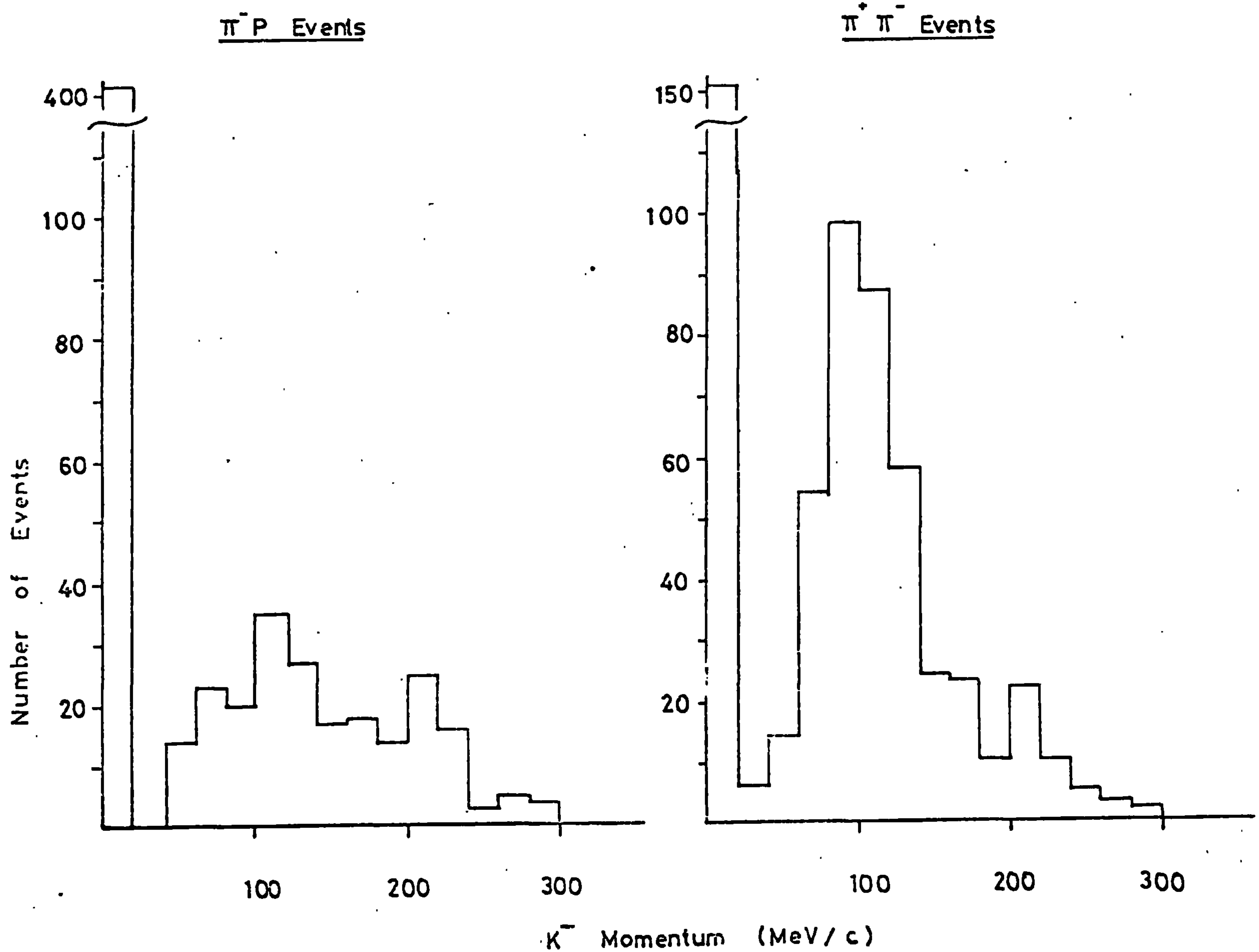

FIG 7·2: Distribution of Primary Momenta.

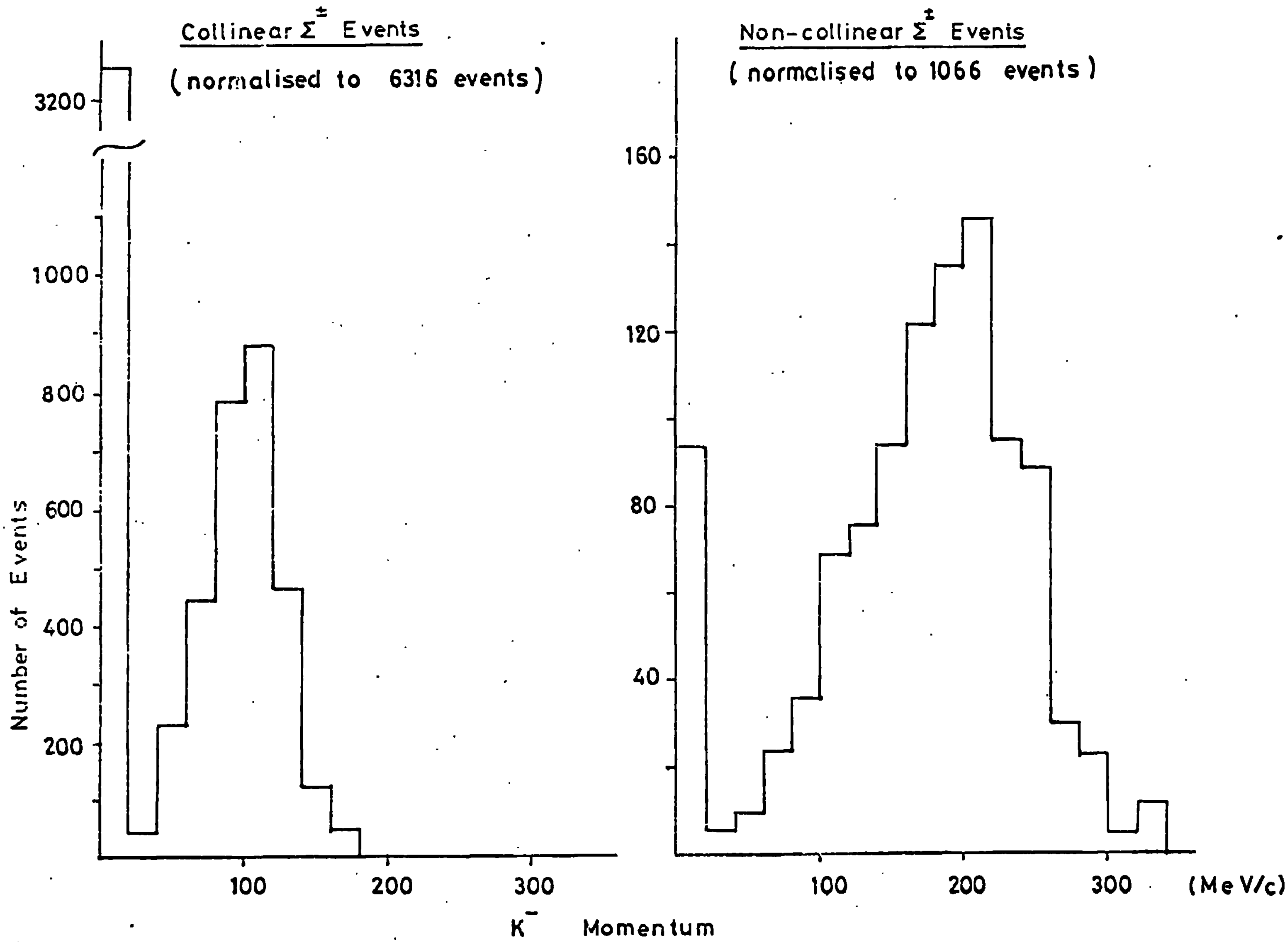

A corresponding relationship can be derived from the at rest $\pi^+ \pi^-$ events, which in obvious notation may be written as

$$n_r = \frac{R_\pi}{1 + R_\pi} n_T$$

Assuming that $R_\pi = R$ then

$$n_r = \frac{N_C}{N_N + N_C} n_T$$

The assumption that $R = R_\pi$ is valid providing that R is calculated using events that have the same cross-section variation with momentum. The R must be calculated using all the Σ hyperon events for the $\pi\,\pi$ separation; but only the Σ^+ hyperon events may be used for the $\pi^- p$ events which is comprised only of Σ^+ hyperons. The results of this analysis are given in table 7.5. The numbers in table 7.5 have been normalised to the total scanned number of events; discrepancies with the numbers quoted in table 7.2. are due to rounding errors and to a few events with momenta > 320. The total numbers of in flight and at rest $\pi^+ \pi^-$ events and π^- p events may now be compared using both methods of separation (table 7.6)

Table 7.6

	Template Method		Statistical Method	
	At Rest	In-Flight	At Rest	In-Flight
$\pi^+ \pi^-$	698	124	707	115
$\pi^- p$	277	100	273	104

These results are in excellent agreement and as the template measurements are able to make the separation on an event by event basis these will be used for the present analysis.

7.5 Separation Of The Σ^0 Hyperon Events From The $\pi^- p$ Sample

This separation was applied only to those events in the at rest

Table 7.5: Separation Of The In-Flight Events From The π^-p and $\pi^+\pi^-$ Categories

Momentum	$\Sigma^\pm$ Coll. N_c	$\Sigma^\pm$ Noncoll N_N	$\pi^+\pi^-$	$\frac{N_c}{N_c + N_N} n_T$	Σ^+ Coll. N_c	Σ^+ Noncoll. N_N	π^-p	$\frac{N_c}{N_c + N_N} n_T$
0 - 20	3255	94	402	390.7	1060	35	151	146.1
20 - 40	46	6	6	5.3	0	1		0
40 - 60	230	10	14	13.4	87	0	14	14.0
60 - 80	445	24	54	51.2	163	2	23	22.7
80 - 100	786	36	98	93.7	255	15	20	18.9
100 - 120	881	69	87	80.7	229	18	35	32.4
120 - 140	446	76	58	49.8	152	29	27	22.7
140 - 160	123	94	24	13.6	59	39	17	10.2
160 - 180	49	121	23	6.6	22	63	18	4.7
180 - 200	5	135	10	0.3	0	59	14	0
200 - 220	10	146	22	1.4	5	82	25	1.4
220 - 240	0	95	10	0	0	52	16	0
240 - 260	4	89	5	0	0	48	3	0
260 - 280	0	30	3	0	4	16	5	1.0
280 - 300	0	22	2	0	0	14	4	0
300 - 320	0	5	2	0	0	8		0
Total	6300	1052	820	706.7	2036	481	372	274.1

sample which posessed fits consistent with the $\pi^- p$ scanning codes. The unique momentum of the pion track from the Σ hyperon reaction is generally higher than that for the Λ^o hyperon reaction, however the errors of measurement (typically ~ 10%) cause an overlap between the two groups. The separation may be improved by plotting the square of the invariant mass, S, of the $\pi^- p$ system against pion momentum (see fig. 7.3). The value of S was found using the relation:

$$S = M_\pi^2 + M_p^2 - 2p_\pi p_p \cos\theta + 2E_\pi E_p$$

where M_π, p_π, E_π, M_p, p_p and E_p are the pion and proton masses, momenta energies and θ is the opening angle between the two particles. The separation using the template measurement of the pion track appears consistent with the separation using the full measurements. Events arising from Λ^o production exhibit an invariant mass scattered around the value of S = 1.24 GeV^2 corresponding to a Λ^o mass of 1.115 GeV; the Σ events occupy the region close to the 180 MeV/c momentum line. The diagonal nature of the cluster $\pi^- p$ (Σ) events arises from the dependence of S^2 on the measured values of p_π and p_p, in particular the value of p_p for these events is independent of the value of p_π and will cause the value of S to vary over a wide range of values.

An alternative method of separating the $\pi^- p$ (Σ) events uses the opening angle of the pion and proton which is generally smaller for the Λ^o hyperon events contained in the sample (see fig. 7.4). The separation is clear except for angles near 180° where the number of ambiguous events is small.

Events of the type:

$$K^- + p \longrightarrow \Sigma^o + \pi^o$$
$$\Sigma^o \longrightarrow \Lambda^o + \gamma$$
$$\Lambda^o \longrightarrow p + \pi^-$$

do not markedly affect the theoretical prediction for Λ^o events; the

FIG 7·3: Invariant Mass Squared vs Pion Momentum

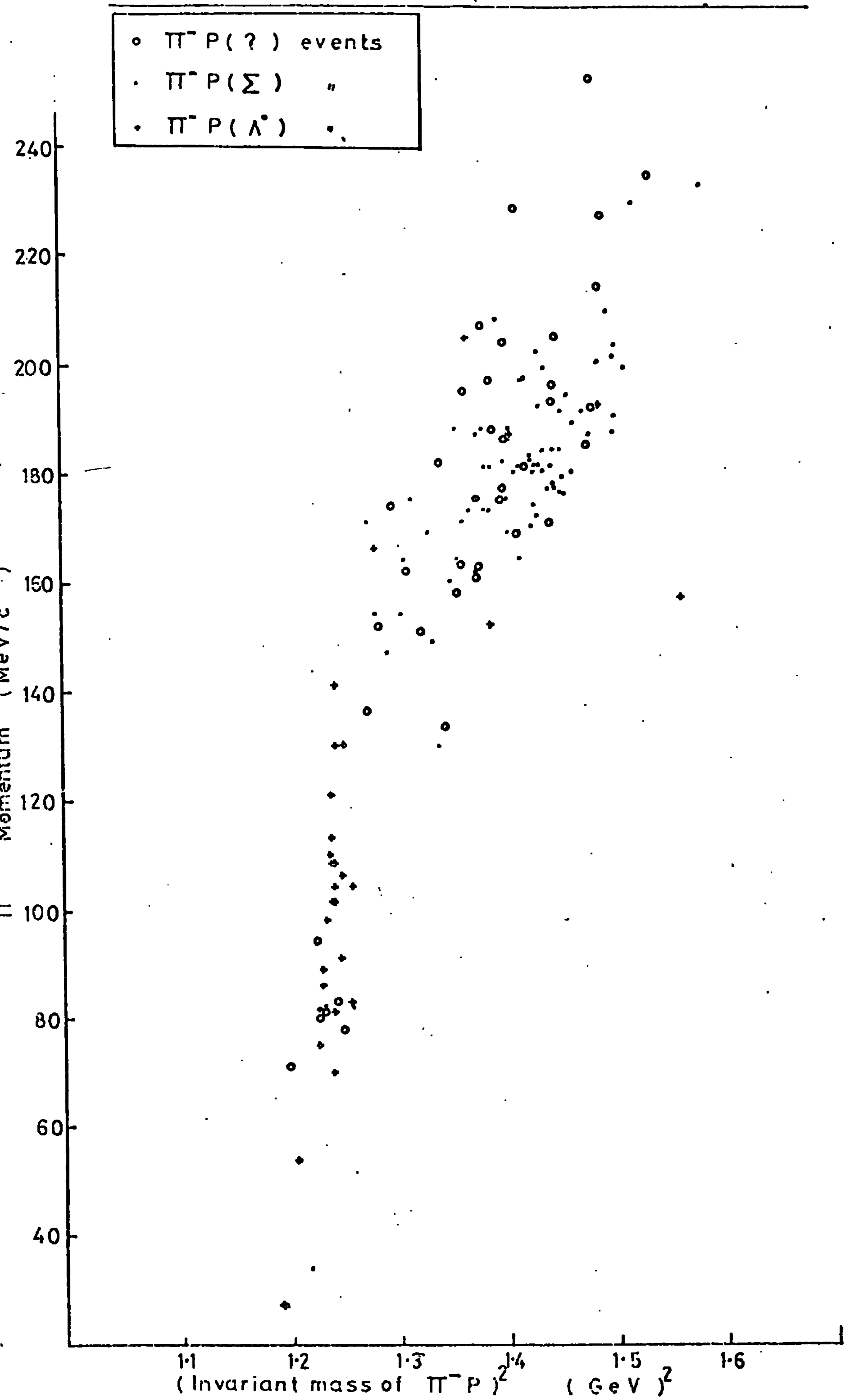

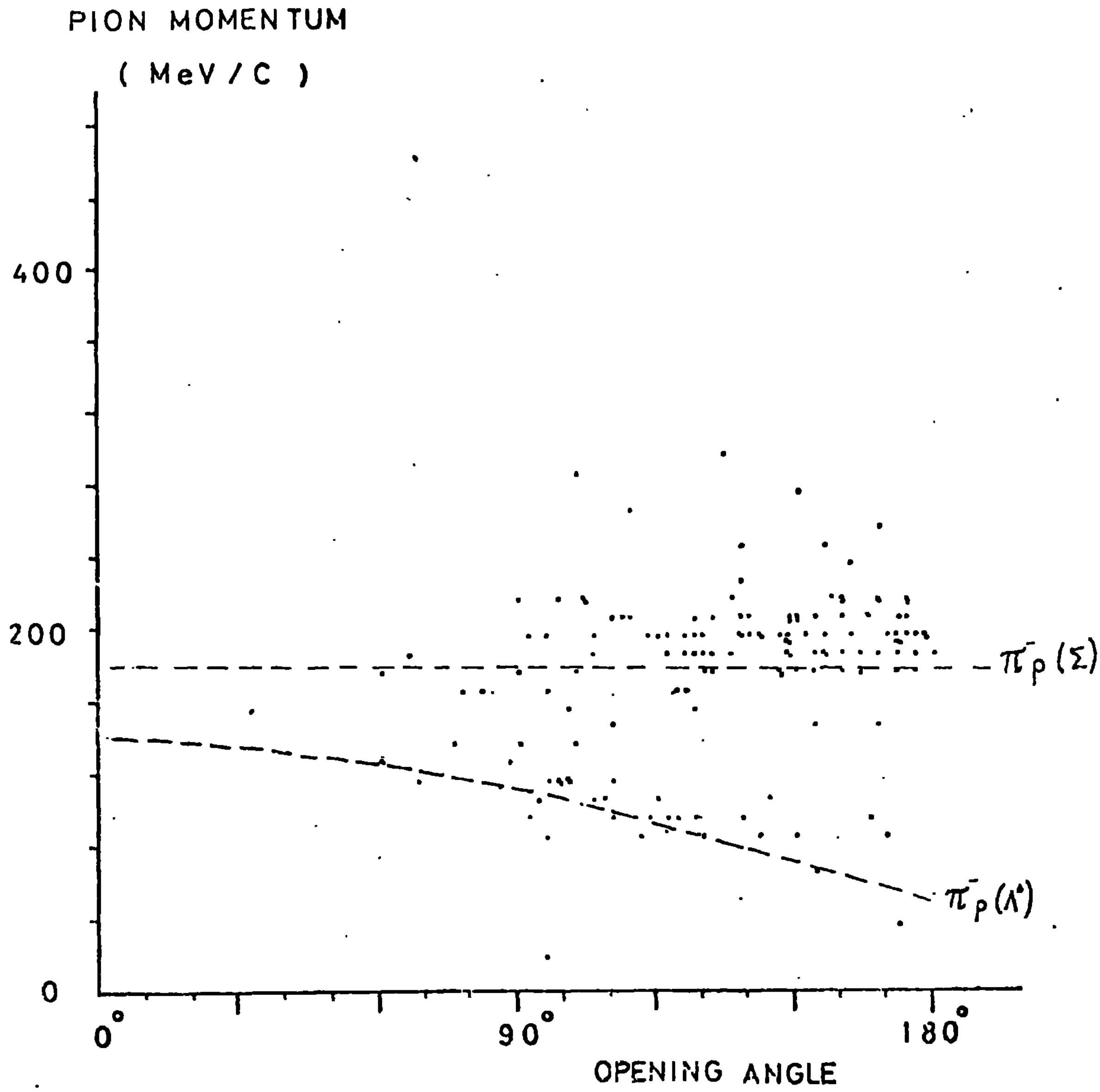

FIG 7·4: Distributions of Opening Angles and Pion Momenta for $\pi^- p$ Events

γ-ray is unable to remove sufficient energy from the system to affect the opening angle significantly.

The final result for the separation was that 24.8% of the π^-p events were found to be due to Σ^0 or Λ^0 hyperon production. The result of this correction is shown in table 7.2

7.6 In-Flight Contamination Of Σ Hyperon Events.

The collinear events with a forward or backward Σ hyperon are not necessarily at rest and it is expected that some of these will be in-flight. A simple inspection of the centre of mass angular distribution (ideally, the cos θ^* distribution is uniform) is insufficient to determine the contamination because any artificial enhancement of the cos θ^* plot in the forward and backward directions due to in-flight contamination is more than offset by the losses in these regions due to unmeasurable events. The contamination, being only a small correction, was estimated in the following manner. The percentage of all hyperon events in the forward and backward 30^o is 13.4 of which only ~ 14% are in-flight (calculated using the collinear, non-collinear ratio). The estimated contamination is then only ~ 1.9%. This was evaluated for the three sigma categories and the results are shown in table 7.2.

7.7 Correction For Σ^+p And π^-p Losses

A sample of at rest π^-p events was chosen by demanding compatibility between the scanning code and fitted hypothesis. This sample was subdivided into π^-p (Σ), π^-p (Λ) and π^-p (?) categories using a template and also into the four groups which depend on the range of the baryon tracks (column 1, table 7.7).

The π^-p (?) group was divided into π^-p (Σ) and π^-p (Λ) categories using the invariant mass plot to assign individual events into each category (column 2). The remaining twenty events in the π^-p (?) group, which had no pion or proton momentum information and did not appear in the invariant mass plot, were divided in the ratio of the already separated events and added into the results in column 2 (see column 3).

Table 7.7: Estimation Of Loss Due To Short Protons

$\pi^- p$ Category	r mm	Column 1	Column 2	Column 3	Column 4	$\Sigma_p^+ + \pi^- p$	Monte Carlo	Number Of Lost Events
$\pi^- p$ (Σ) (By Template)	1	5	5	5	7.6	12.6	31.5	35
	1 - 2	6	9	9.9	15.1	33.1	40.9	
	2 - 3	3	4	4.8	7.3	35.3	43.2	
	4	68	98	110.6	168.3	1127.3	1127.3	
$\pi^- p$ (Λ) (By Template)	1	1	1	1	1.5			
	1 - 2	1	2	2.1	3.1			
	2 - 3	1	1	1.2	1.8			
	4	33	42	47.6	72.4			
$\pi^- p$ (?)	1	-	-	-	-			
	1 - 2	5	1	-	-			
	2 - 3	2	1	-	-			
	4	57	18	-	-			

Column 4 is the number of π^-p events normalised to the total number of at rest π^-p events found on the film. The number of Σ^+p events is added to these in the next column. The Monte Carlo results were normalised to the number of events with $r > 4$ mm as events in this group were unlikely to suffer from serious scanning losses. The loss is most noticeable in the short range group as expected and becomes progressivel[y] less in higher groups. The effect of this final corection is shown in table 7.2 and it allows for the thirty five lost events.

7.8 Final Data

The final data for the Durham sample is given in table 7.2. The data from the London (UCL) and Brussels (UB) groups is given in table 7.8. together with the Durham sample for comparison

Table 7.8: Data For γ Ratio Determination

Number Of Corrected Events In Each Category

	UB	UCL	UDW
$\Sigma^-\pi$	4388	4120	4243
$\Sigma^-\sigma^-$	574	496	560
$\Sigma^+\pi$	982	881	1015
$\Sigma^+p + \pi^-p$	1151	1063	1243
$\pi^+\pi^-$	490	455	699

UDW = Universities of Durham and Warsaw

UB = University of Brussels

UCL = University College, London

7.9 Determination Of The Gamma Ratio (Method I)

Method I (Branching Ratio) requires that the separation of pion and proton tracks be consistent between the laboratories. Each group used different projection systems with different magnifications, although all gave approximately lifesize images of the chamber. In order to check this separation the proportion of events classified in the $\Sigma^+p + \pi^-p$ categories was calculated for each laboratory (table 7.9); the data are consistent and show no systematic biases. Consequently the data from the three laboratories can be combined and substituted into equations 6.7 and 6.8. to give:

$$\gamma = 2.35 \pm 0.07$$

The errors were calculated by rewriting equations 6.7 and 6.8 as

$$\gamma = \frac{N_1}{N_2}(1 - B) - B$$

where $N_1 = \Sigma^-\pi + \Sigma^-\sigma^- + \pi^+\pi^- + \Sigma^+\pi$

$N_2 = \Sigma^+p + \pi p$

N_1 and N_2 were assumed to have poisson errors and the error on the value of B was also included.

The error in the Branching ratio and the poisson error in the $\Sigma^+p + \pi^-p$ category were the main contributions to the overall error of 0.07.

Table 7.9: Fraction Of Proton Type Events

Category	UB	UCL	UDW	Total
$\Sigma^+p + \pi^-p$	1151	1063	1243	3452
Total Number Of Events	7585	7015	7810	22405
$(\Sigma^+p + \pi^-p)$/Total	0.151 ± 0.005	0.152 ± 0.005	0.159 ± 0.005	0.154 ± 0.00

7.10 Determination Of The Gamma Ratio (Method II)

Before combining the results from the three laboratories the assumption of equal minimum effective ranges for the $\Sigma^+\pi$ and $\Sigma^-\pi$ categories must be examined. This may be done in two ways:

(i) Having established the validity of the pion and proton separations, equations 6.9 and 6.10 may be used to calculate the minimum effective ranges ℓ^{-}_{π} and ℓ^{+}_{π}. Putting $k^{-} = 1.56$ and $k^{+} = 2.72$ (assuming no energy loss over the first 0.1 cm of track) the values of ℓ^{+}_{π} and ℓ^{-}_{π} are found to be:

Table 7.10: Minimum Observable Hyperon Length

	UB	UCL	UDW
ℓ^{-}_{π}	0.049 ± 0.010	0.046 ± 0.010	0.069 ± 0.014
ℓ^{+}_{π}	0.034 ± 0.012	0.045 ± 0.016	0.049 ± 0.020

The errors on these quantities are large as the values of $\ell^{\pm}_{\pi}$ are derived from logarithmic expressions. It can be seen that the UDW data and possibly the UB data are inconsistent with the assumption that $\ell^{+}_{\pi} = \ell^{-}_{\pi}$. A more sensitive test is described below.

(ii) It has been established that the pion decay modes are well separated from the total number of events (see table 7·9) and this number may be regarded as well determined for all three laboratories.
Using the gamma ratio model this number may be written as:

$$\Sigma^{-}\pi + \Sigma^{-}\sigma + \Sigma^{+}\pi + \pi^{+}\pi^{+} = N^{-}\exp(-k^{-}\ell^{-}_{\pi}) + BN^{+}\exp(-k^{+}\ell^{+}_{\pi})$$

$$+ N^{-}(1 - \exp(-k^{-}\ell^{-}_{\pi})) + BN^{+}(1 - \exp(-k^{+}\ell^{+}_{\pi}))$$

$$= N^{-} + BN^{+}$$

$$\therefore \quad \frac{(\Sigma^{-}\pi + \Sigma^{-}\sigma) + \Sigma^{+}\pi + \pi^{+}\pi^{-}}{N^{-} + BN^{+}} = 1$$

The $\Sigma^{-}\pi$ and $\Sigma^{-}\sigma$ will be combined into a single category giving

$$f^{-} + f^{+} + f^{\pi} = 1 \qquad 7.5$$

where f^- = the fraction of the pion mode events that are classified as Σ^- and similarly for f^+ and f^π with obvious notation.

Relations of the type given by equation 7.5 may be plotted using triangular coordinates. Using equations 6.1 - 6.5 and putting $\ell^+_\pi = \ell^-_\pi = \ell_\pi$ the fractions are given by,

$$f^- = \frac{N^- e^{-k^-\ell_\pi}}{N^- + BN^+} = \frac{\gamma}{\gamma + B} e^{-k^-\ell_\pi} \qquad 7.6$$

$$f^+ = \frac{BN^+ e^{-k^+\ell_\pi}}{N^- + BN^+} = 1 - \frac{\gamma}{\gamma + B} e^{-k^+\ell_\pi} \qquad 7.7$$

The values of f^- and f^+ depend on ℓ_π and these are likely to be different for each laboratory. The data points from the three laboratories whilst occupying different areas of the trangular plot due to the difference in minimum effective ranges will be joined by a line of constant $\frac{\gamma}{\gamma + B}$ values.

The data for the three laboratories is plotted in fig. 7.5 and the values shown in table 7.11

Table 7.11: Fractions Of $\Sigma^+\pi$, $\Sigma^-\pi$ And $\pi^+\pi^-$ Events

	UB	UCL	UDW
f^-	0.0771 $\pm$ 0.005	0.775 $\pm$ 0.005	0.739 $\pm$ 0.005
f^+	0.153 $\pm$ 0.004	0.148 $\pm$ 0.004	0.155 $\pm$ 0.004
f^π	0.076 $\pm$ 0.003	0.076 $\pm$ 0.003	0.106 $\pm$ 0.003

The value of B was assumed to be 0.4835, equations 7.6 and 7.7 were used to find the values of f^+ and f^- for various values of ℓ_π and γ, these results are shown on the diagram. The UCL and UB points are consistent with each other and indicate a value of $\ell_\pi \sim 0.045$ cm consistent with the

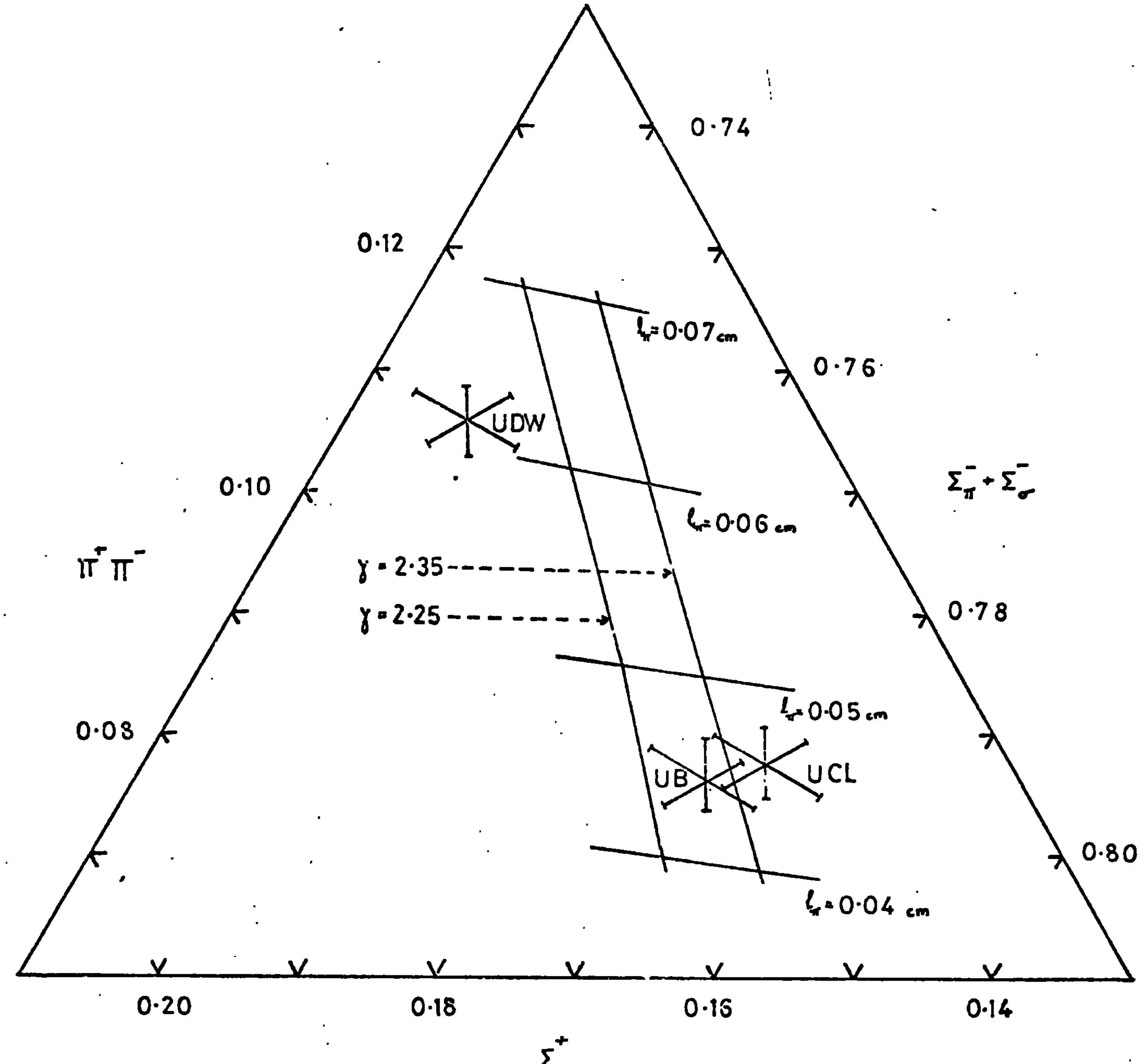

FIG 7·5: Triangular Plot of the Fractions of $\pi^+\pi^-$, Σ^-_π, Σ^+_π Events value obtained in table 7.10. The UDW value corresponds to a larger minimum effective range ($\sim$ 0.062 cm) and to a value of γ which is not consistent with the values obtained by UB and UCL.

It is now clear that the assumption $\ell^{+}_{\pi} = \ell^{-}_{\pi}$ used in equations 6.6 and 6.7 is not valid for the UDW data and these data must be excluded from further analysis by Method II.

The explanation for this discrepancy is that the scanning by Durham - Warsaw was carried out with a view to the Method I determination only. This scanning required that the sign of the Σ hyperon be well determined and in the case of positive hyperons the decay was carefully examined to discriminate between pions and protons . The Σ^- events were not examined in such detail and a detailed separation into $\Sigma^-\pi$ or $\pi^+\pi^-$ was not made as these categories are added in the final analysis. The second method of determination evolved during the experiment and the scanning at UCL and UB was consistent with this approach, the $\Sigma^{\pm}$ hyperons being examined with equal care.

The data from UB and UCL were used in equation 6.12 to determine a value of ℓ_{π} and this value was substituted into 6.13 and 6.14 to yield results for γ and B.

Table 7.12: Dependence Of γ And B

As A Function Of The Number Of $\pi^+\pi^-$ Events

ℓ_{π}	$\pi^+\pi^-$	γ	B
0.02	409	2.363	0.471
0.04	836	2.375	0.484
0.06	1281	2.386	0.498
0.08	1745	2.396	0.512
0.10	2230	2.402	0.526

The number of $\pi^+\pi^-$ events is a sensitive function of γ and B. Using the observed number of $\pi^+\pi^-$ events (945) the final results are:

$$\gamma = 2.38 \pm 0.04$$

$$B = 0.488 \pm 0.008$$

The sources of error on this value for γ are mainly statistical. The particle masses and lifetimes are known to $\lesssim$ 1% accuracy hence the values of k^- and k^+ which appear as exponents are also of a similar accuracy. These exponents being less than unity reduce the overall errors still further.

7.11 Conclusions

The value of γ obtained in this work is in agreement with the value quoted by Tovee et al (4). This being a nuclear emulsion experiment with high measurement precision is considered to give a reliable estimate of the γ ratio; the value of γ was merely quoted by Kim (3) and a detailed description of his analysis for the determination of the ratio was not given.

The value of B obtained from Method II is in excellent agreement with previous results, see table 7.13 below.

Table 7.13: Summary Of The Determinations Of B

Author	Ref.	B	Experiment
Humphrey & Ross	13	0.490 ± 0.024	HBC
Chang	36	0.46 ± 0.02	HBC
Barloutaud et al	37	0.488 ± 0.01	HBC
Tovee et al	4	0.484 ± 0.015	Nucl. Em.
Present Work	25	0.488 ± 0.008	HBC

The decay of the hyperon into a nucleon and pion gives a $\Delta I = \frac{1}{2}$ transition. The decay amplitudes for the hyperon decays are related by the relation:

$$\sqrt{2}\, A(\Sigma^{+} \longrightarrow p\pi^{o}) = A(\Sigma^{-} \longrightarrow n\pi^{-}) - A(\Sigma^{+} \longrightarrow n\pi^{+})$$

which forms the $\Delta I = \frac{1}{2}$ triangle (45). This relationship is left unchanged by the present results.

CHAPTER EIGHT

DISCUSSION OF RESULTS AND K-MATRIX ANALYSIS

With the completion of this experiment there now exist two independent estimates of low energy K^-p cross-sections having comparable statistics; each of these being considerably higher than other experiments in this region (see table 1.1). In this chapter the cross-sections of these two experiments (i.e. the present work, TST, and that of Kim, K) are compared and discussed in the light of the analysis made by Martin (2) which included both high and low energy $K^{\pm}N$ data. This is followed by an analysis in terms of the constant scattering length (CSL) approach and a K-matrix parametrisation of the data which corresponds to the zero effective range approach (ZER).

Finally the experimental problems are summarised and the future of low energy K^-p interactions is discussed.

8.1 Channel Cross-Sections

The channel cross-sections are collected together and shown in fig. 8.1. The momentum values of the TST results and those of Kim have been shifted by 5 MeV/c to the left and right of their measured values to avoid the confusion caused by overlapping data points.

The results of Kim have, throughout this work, been used for comparison purposes as these are generally accepted and have been widely quoted in the absence of any more precise data. Clearly the TST results are in good agreement with the values of Kim for all the hyperon channels. The elastic scattering channels differ by ~ 5% but the most notable difference between the results lies in the $\overline{K^0}n$ channel where the present results are higher by as much as 80%. It has already been mentioned (§ 5.4) that the scanning for these events is extremely difficult owing to the large angle between the decay products of the neutral kaon. This makes it easy for a neutral kaon decay to simulate an unassociated pion track where there

FIG 8.1: Summary of The Channel Cross sections

TST Results (displaced 5 MeV/c to the left)
Kim " (" " " " right)

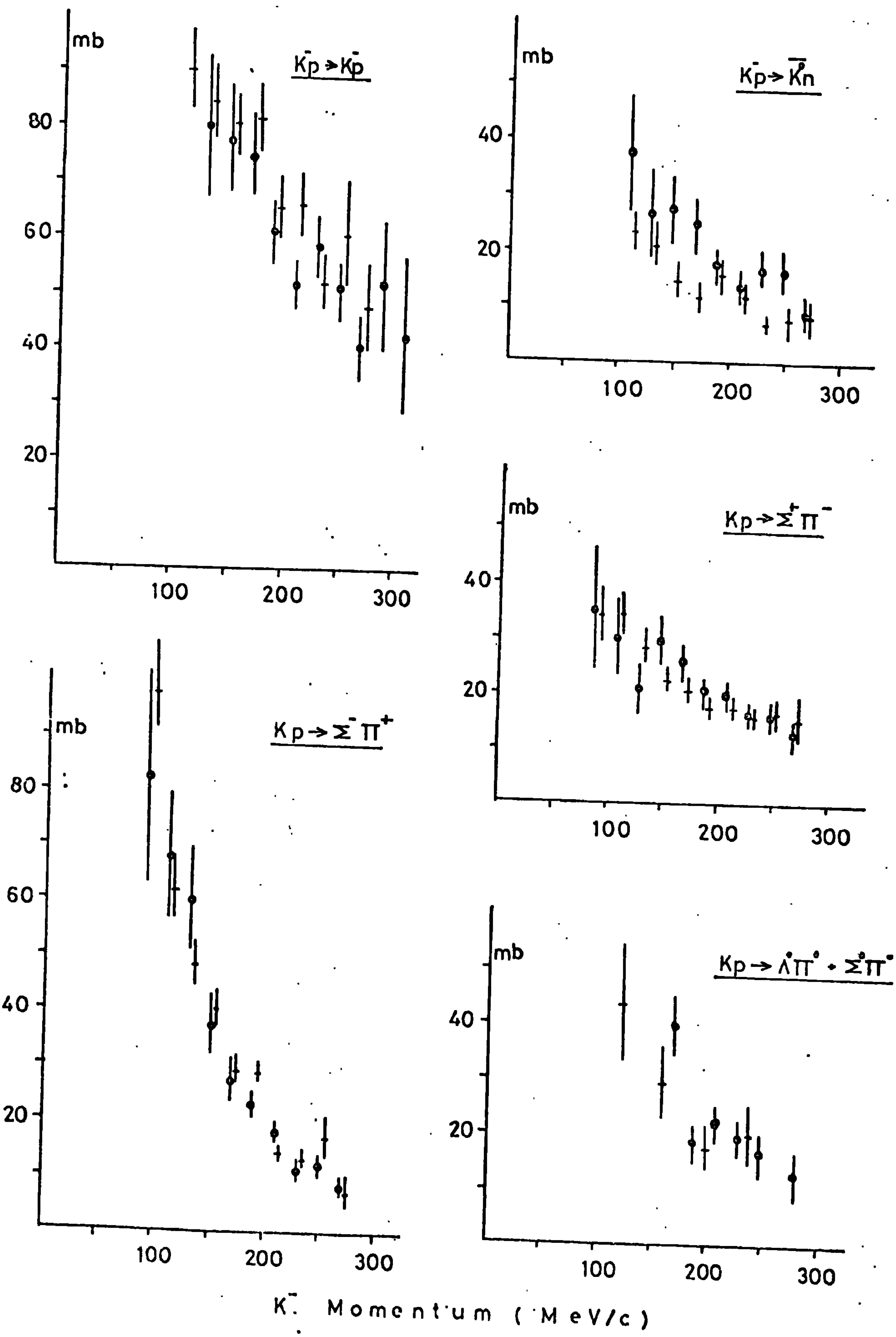

is little or no evidence of a decay kink. In the present experiment the scanning for these events was carried out with extreme care and this is reflected in the high scanning efficiency for these events ($\sim$ 93%). It is, therefore, resonable to expect that this cross-section may be higher than previously determined values. On the whole the data from the two experments are in good agreement and this allows the data to be combined for the subsequent analysis.

The analysis of Martin provides evidence that the $\overline{K^o}$n cross-section should indeed be higher than that found by Kim. This involved fitting simultaneously high and low energy $K^{\pm}N$ cross-sections using dispersion relation constraints and the constraints of unitarity imposed via the K-matrix parametrisation. This approach was prompted by new data on the coulomb-nuclear interference region of the $K^{\pm}p$ elastic scattering. The result of this analysis is a highly constrained fit to the data which should be much more reliable than the separate K^- matrix fit to the K^-p data alone. Fig. 8.2 compares these results with those of the TST and the agreement is good for all channels. In particular the charge exchange channel is seen to agree extremely well with Martin's results and suggests that Kim's data on charge exchange has been underestimated.

It is apparent (fig. 8.2) that these low energy cross-sections are dominated by kinematic factors. The rapidly varying cross-section makes it difficult to judge visually the quality of the fit between the observed data points and the analytical prediction. A cross-section for a two body process a + b $\longrightarrow$ c + d is given by

$$\sigma \propto \frac{q^1}{qs} \int \left| T(\theta) \right|^2 d\Omega$$

where $q(q^1)$ is the centre of mass momentum of the incident (outgoing) channel and s is centre of mass energy squared ($s = \sqrt{q^2 + m_1^2} + \sqrt{q^2 + m_2^2}$).

FIG 8.2: Comparison of The Cross sections With The Results of Martin.

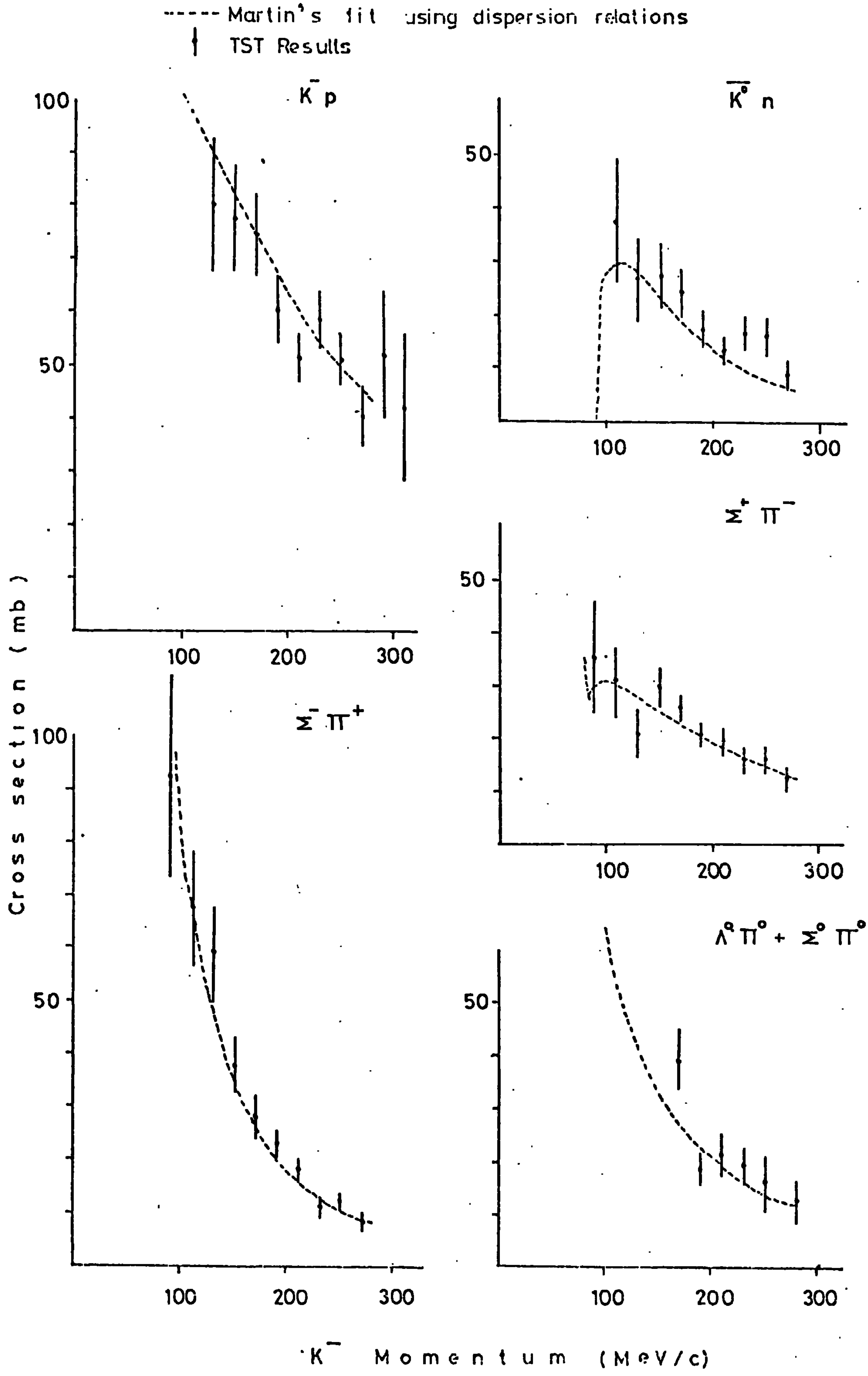

The cross-sections have been divided by the kinematic factor $\frac{q^1}{qs}$ (plotted in fig. 8.3) to leave only the dynamic behaviour (i.e. the variation of the strength of the strong interaction) to manifest itself. These are shown in figs. 8.4 to 8.6 and have been extended to include higher energy data in the region of the Λ (1520) resonance. The TST results appear consistent with the high energy results and form a smooth continuation down to energies of $\sim$1440 MeV.

8.2 Data Analysis

Initially the analysis of the data is carried out using complex scattering lengths A_0 and A_1 ($a_0 + ib_0$, $a_1 + ib_1$) to describe the channel cross-sections. Two other parameters ϵ and ϕ are also required to describe the data and these are the ratios of

$$\epsilon = \frac{\sigma(\bar{K}N \longrightarrow \Lambda^\circ\pi)}{\sigma_1}$$

and
$$\phi = \arg\,(T^0_{K\Sigma} \,/\, T^1_{K\Sigma})$$

as defined in §1.7 (equations 1.10 and 1.11).

The cross-sections are written in terms of these quantities and by fitting to the data the values of these six parameters may be found. This approach is called the Constant Scattering Length (CSL) parametrisation because the scattering lengths A_0 and A_1 are independent of energy.

A more fundamental analysis is considered later in which these six parameters are themselves written in terms of the nine elements of the I = 0 and I = 1 K-matrices. These elements are determined by fitting to the cross-sections in the same way as for the CSL analysis. This approach is the zero effective range (ZER) parametrisation (see §1.7)

8.2.1 Constant Scattering Length Analysis

The cross-sections are written explicitly in terms of the six parameters in §1.7. The fitting was carried out using MINUIT (38) which

FIG 8·3: Kinematic Behaviour of Cross-sections

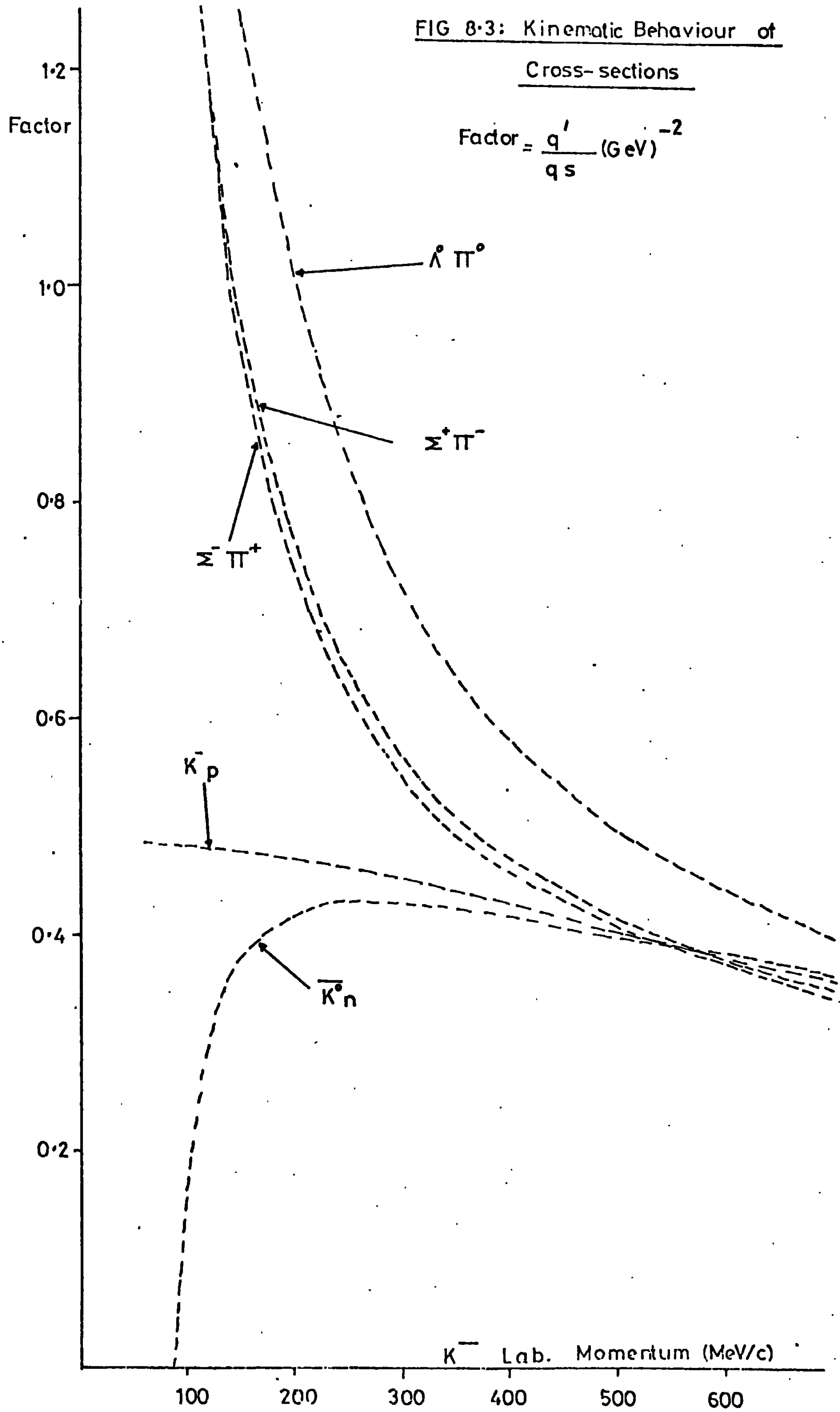

FIG 8·4: Dynamic Behaviour of Charged Hyperon Cross-sections.

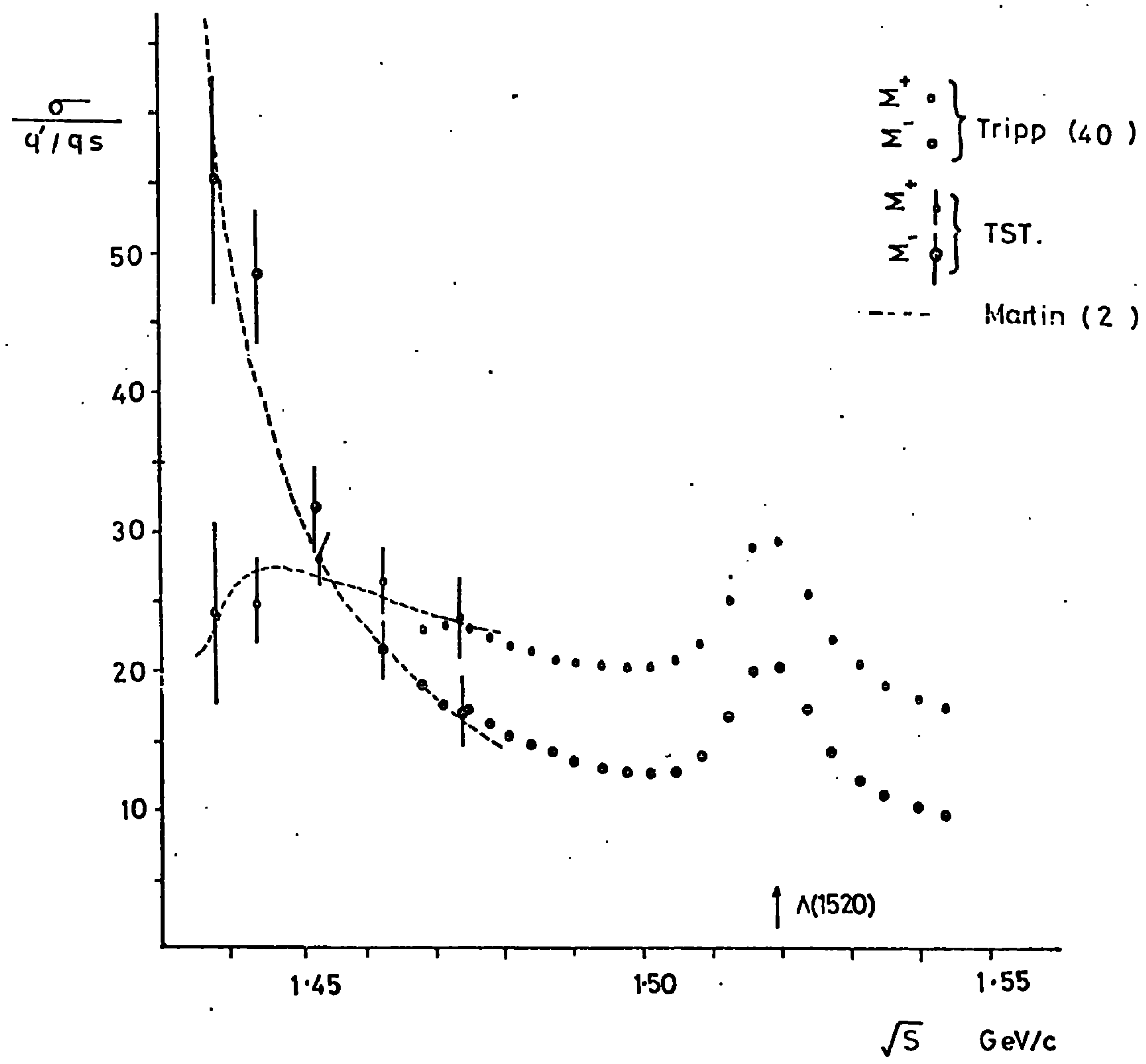

FIG 8.5 Dynamic Behaviour of Elastic Scattering Cross-section.

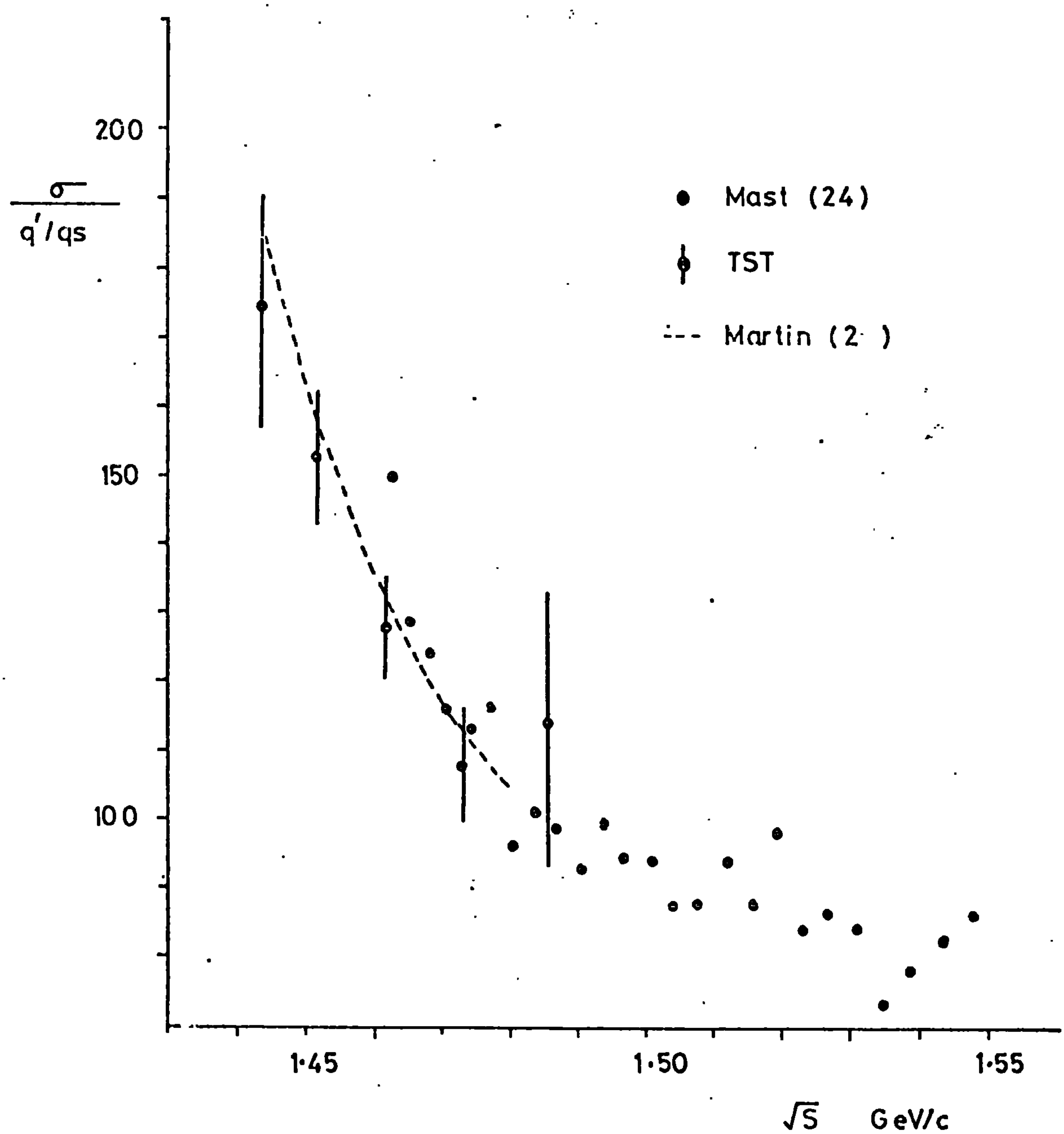

FIG 8·6: Dynamic Behaviour of The Charge Exchange and Neutral Cross-sections

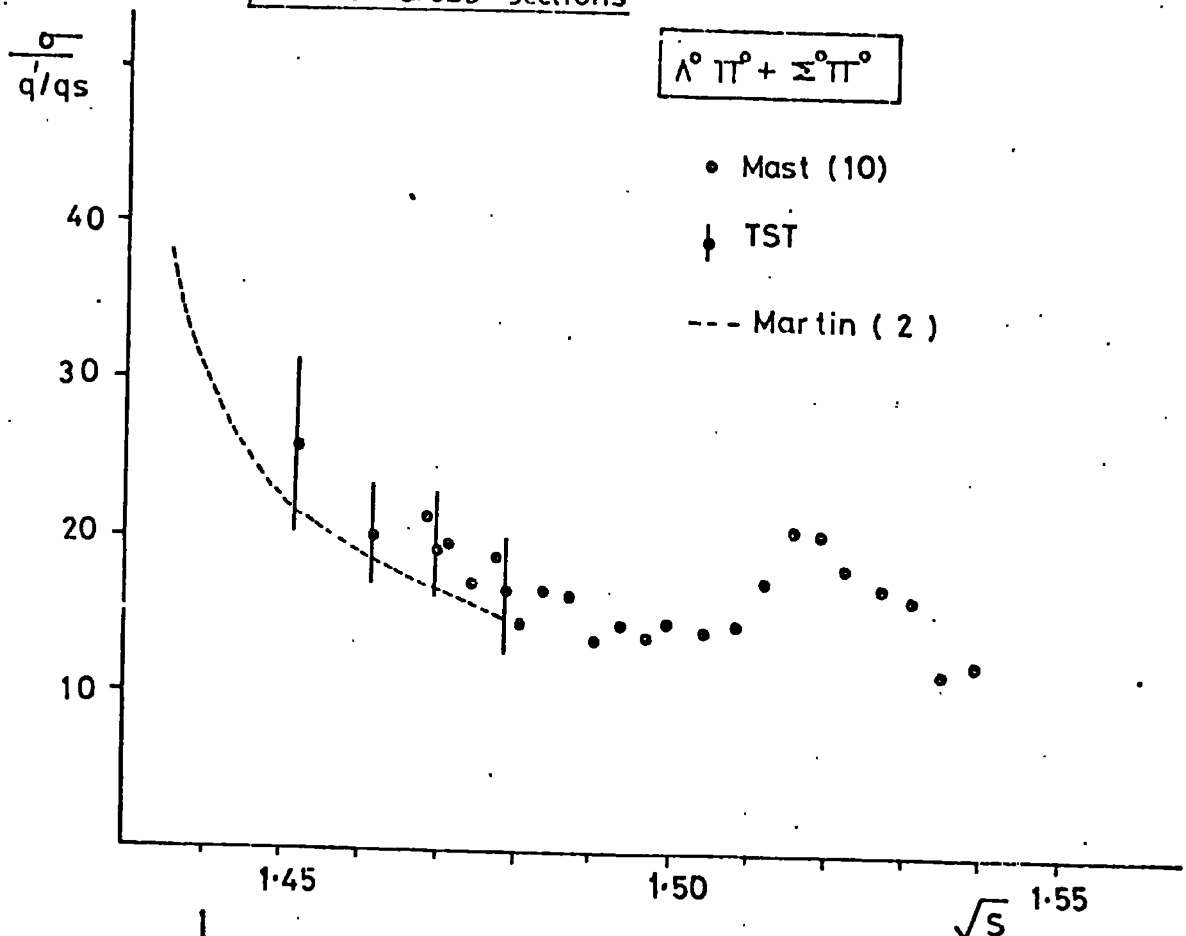

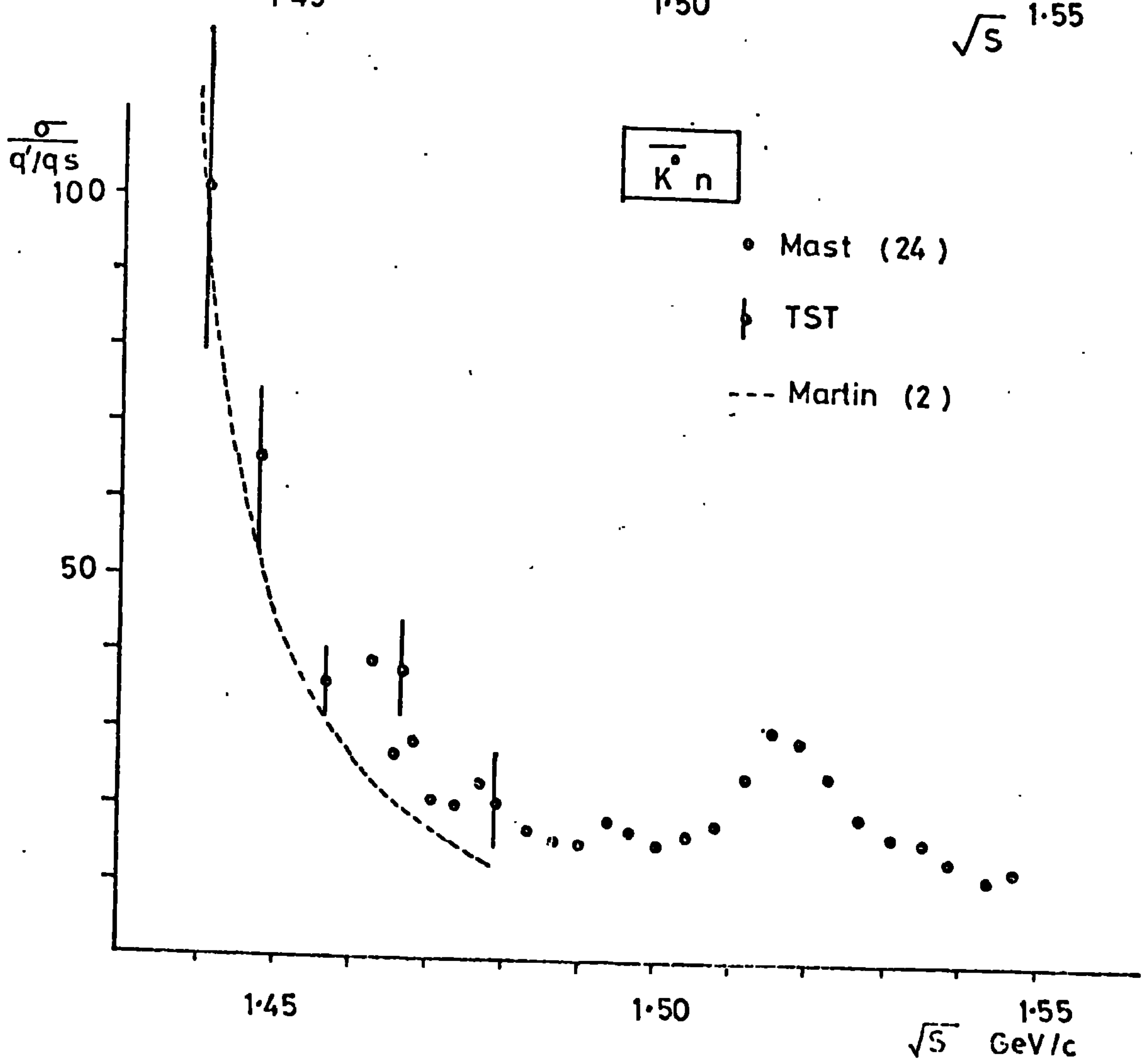

minimised the χ^2 function given by

$$\chi^2 = \sum_{\text{observations}} \frac{(x_{obs} - x_{exp})^2}{\sigma_{exp}^2}$$

where 'obs' and 'exp' refer to the observed and expected quantities respectively. In practice σ_{exp} is replaced by σ_{obs} and is accurate to first order.

The starting values for the parameters were varied in different fits to obtain a good coverage of the χ^2 space. It became clear that the fitting was sensitive to fluctuations in the data. This problem was overcome by redistributing the data into 40 MeV/c momentum intervals which produced fits which were more stable to arbitrary changes in the starting values.

The results of this fitting are shown in tables 8.1 to 8.4. The fit CSL I was obtained using all of the K and TST data and by using as the starting values those results obtained from the CSL fit of Kim. Clearly the main differences lie in the values of a_0 and a_1. During the fitting procedure in which many starting values were used the other four parameters remained approximately constant to within about three standard deviations of their quoted errors.

The CSL II fit was obtained by removing from the combined data the results of the $\overline{K^o}n$ channel obtained by Kim. This channel is the one where the K and TST results differ and this removal increases the value of a_1 and it also causes a general increase in the parameter errors which indicates that the χ^2 function is insensitive to large changes in a_0 and a_1.

8.2.2 K-Matrix Parametrisation

This analysis used the elements of the I = 0 and I = 1 K matrices themselves to describe the data.

Table 8.1: Scattering Length Solutions

	a_0	b_0	a_1	b_1	ε	ϕ	γ	χ^2	n_D
CSL I	-1.44 ± 0.08	0.86 ± 0.05	0.37 ± 0.11	0.85 ± 0.04	0.41 ± 0.03	50.8 ± 1.4	2.23	62.9	40
CSL II	-1.45 ± 0.19	0.90 ± 0.08	0.60 ± 0.22	0.77 ± 0.05	0.39 ± 0.04	46.5 ± 1.6	2.20	46.1	35
K (CSL)	-1.67 ± 0.04	0.71 ± 0.04	-0.07 ± 0.06	0.68 ± 0.03	0.31	53.8			
ZER I	-1.53*	0.72	0.29	0.76	0.38	52.7	2.22	108.0	80
ZER II	-1.58*	0.76	0.47	0.73	0.36	48.7	2.22	88.8	71

n_D is the number of degrees of freedom.

* the fitting programme gives the error matrix for the elements of the K-matrix. These have not been projected through the complex relationship to the scattering lengths. However it is expected that the error will be similar to those of the CSL I and II solutions.

Table 8.2: Correlation Coefficients For CSL Fits

	a_0	b_0	a_1	b_1	ϕ	ε	
a_0	1						
b_0	0.589	1					
a_1	0.841	0.746	1				
b_1	0.477	0.141	0.433	1			CSL I
ϕ	0.090	0.604	0.457	-0.197	1		
ε	0.584	0.420	0.521	0.502	0.102	1	
a_0	1						
b_0	0.876	1					
a_1	0.951	0.897	1				
b_1	0.596	0.405	0.474	1			CSL II
ϕ	0.181	0.420	0.408	-0.307	1		
ε	0.822	0.719	0.741	0.704	0.053	1	

Table 8.3: Number Of Data Points Used In Analyses

Cross-sections	CSL		ZER	
	I	II	I	II
K^-p	10	10	19	19
$\overline{K^o}n$	10	5	19	10
$\Sigma^+\pi^-$	10	10	20	20
$\Sigma^-\pi^+$	10	10	20	20
$\Sigma^o\pi^o$ + $\Lambda^o\pi^o$	5	5	10	10
γ	1	1	1	1
Total	46	41	89	80

Table 8.4: Contributions To The χ^2

	CSL		ZER	
	I	II	I	II
K^-p	6.9	8.1	14.8	15.7
$\overline{K^o}n$	27.5	5.9	33.0	8.5
$\Sigma^+\pi^-$	15.0	14.0	23.1	23.5
$\Sigma^-\pi^+$	10.7	13.6	27.2	29.9
$\Sigma^o\pi^o$ + $\Lambda^o\pi^o$	2.8	5.2	9.9	11.1
γ	0.0	0.1	0.0	0.1
Total	62.9	46.1	108.0	88.8
Data Points	46	41	89	80
Fit Probability %	1.23	16.68	2.14	32.05

These matrices take the form:

$$K^0 = \begin{pmatrix} \alpha_K & \alpha_{K\Sigma} \\ \alpha_{K\Sigma} & \alpha_\Sigma \end{pmatrix} \qquad K^1 = \begin{pmatrix} \beta_K & \beta_{K\Sigma} & \beta_{K\Lambda} \\ \beta_{K\Sigma} & \beta_\Sigma & \beta_{\Sigma\Lambda} \\ \beta_{K\Lambda} & \beta_{\Sigma\Lambda} & \beta_\Lambda \end{pmatrix}$$

and the cross-sections may be expressed directly in terms of these elements (see Appendices B and C). The scattering lengths used in the CSL method are themselves expressed in terms of the α and β elements. The fitting was as before except that the data were not redistributed into 40 MeV/c momentum intervals as the fitting was not sensitive to the starting values of parameters.

The starting values for this analysis were taken from Martin and Ross (36) and remain essentially the same for the present analysis. Starting values were also taken from the results of Chao (39) and these produced results similar to those obtained using the Martin and Ross values. Arbitrary starting values were also used but no improved fit could be found.

The fits were carried out on all the data points (see table 8.3) and it can be seen (table 8.4) that the probabilities of these fits are higher than those of the CSL fits hence an improved description of the data can be found using the K-matrix parametrisation. The results are presented in tables 8.5 and 8.6 and are shown in fig. 8.7.

8.2.3 Scattering Parameters

The scattering parameters a_0, b_0, a_1, b_1, ε and ϕ may be derived from the ZER fit and compared to those of the CSL analysis. Table 8.1 presents the threshold values of these parameters whilst fig 8.8 shows the energy dependence of the four scattering length parameters obtained from the ZER analysis. The variation of ϕ with energy is also presented in fig. 8.9 together with the ratio, γ, and the structure at the $\overline{K^0}n$ threshold is clearly seen in these closely related quantities.

Comparing with Kim, the large and negative value of a_0 is confirmed,

Table 8.5:

Results Of Zero Range K-Matrix Parametrisation

For All TST And K Data (ZER I)		
I = 0	I = 1	
$\alpha_K = -0.22 \pm 0.3$	$\beta_K = 0.34 \pm 0.01$	$\beta_\Sigma = 0.34 \pm 0.01$
$\alpha_{K\Sigma} = -0.12 \pm 0.2$	$\beta_{K\Sigma} = -0.76 \pm 0.2$	$\beta_{\Sigma\Lambda} = -0.15 \pm 0.02$
$\alpha_\Sigma = -0.99 \pm 0.3$	$\beta_{K\Lambda} = -0.45 \pm 0.1$	$\beta_\Lambda = 0.07 \pm 0.04$
For TST + K Data Less $\overline{K^o}n$ Channel From K Data (ZER II)		
I = 0	I = 1	
$\alpha_K = -0.23 \pm 0.05$	$\beta_K = 0.44 \pm 0.08$	$\beta_\Sigma = 0.35 \pm 0.11$
$\alpha_{K\Sigma} = -0.12 \pm 0.11$	$\beta_{K\Sigma} = -0.80 \pm 0.05$	$\beta_{\Sigma\Lambda} = -0.28 \pm 0.07$
$\alpha_\Sigma = -1.0 \pm 0.13$	$\beta_{K\Lambda} = -0.39 \pm 0.09$	$\beta_\Lambda = 0.03 \pm 0.05$

Table 8.6:

Correlation Coefficients For ZER Fit To All The K + TST Data (I)

	α_K	$\alpha_{K\Sigma}$	α_Σ	β_K	$\beta_{K\Sigma}$	$\beta_{K\Lambda}$	β_Σ	$\beta_{\Sigma\Lambda}$	β_Λ
α_K	1								
$\alpha_{K\Sigma}$	-0.358	1							
α_Σ	-0.566	-0.324	1						
β_K	0.215	-0.929	0.075	1					
$\beta_{K\Sigma}$	-0.457	-0.342	-0.385	-0.377	1				
$\beta_{K\Lambda}$	-0.382	0.402	-0.086	-0.597	0.028	1			
β_Σ	-0.026	-0.644	-0.114	-0.179	-0.463	-0.301	1		
$\beta_{\Sigma\Lambda}$	-0.188	0.155	-0.104	-0.342	0.024	-0.093	-0.774	1	
β_Λ	-0.281	-0.708	-0.928	0.176	-0.049	-0.227	-0.174	-0.429	1

FIG 8·7: Results of K-Matrix Parametrisation

ZER I & ZER II are similar except for $\overline{K^0}n$

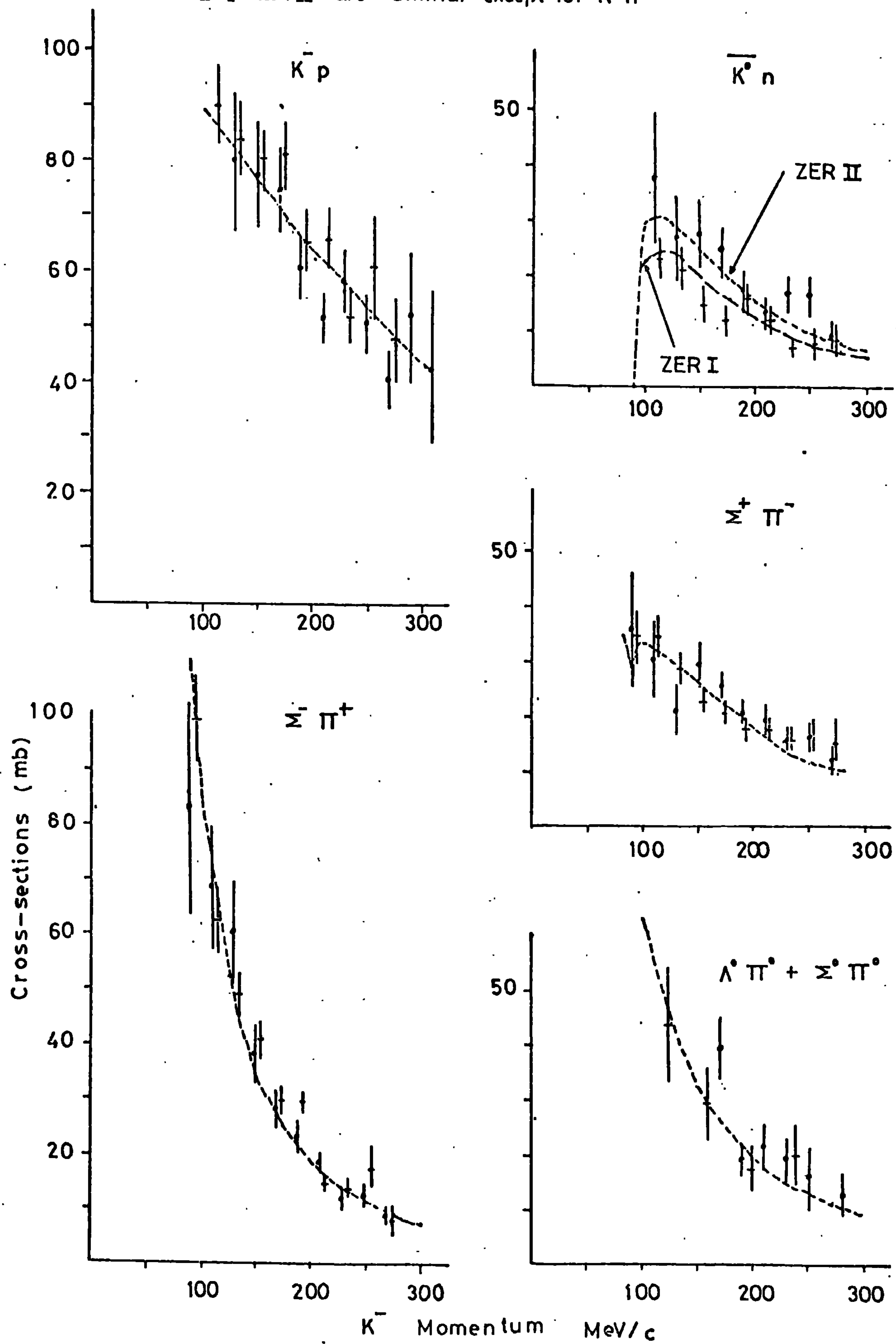

FIG 8·8: Energy Dependence of Scattering Lengths

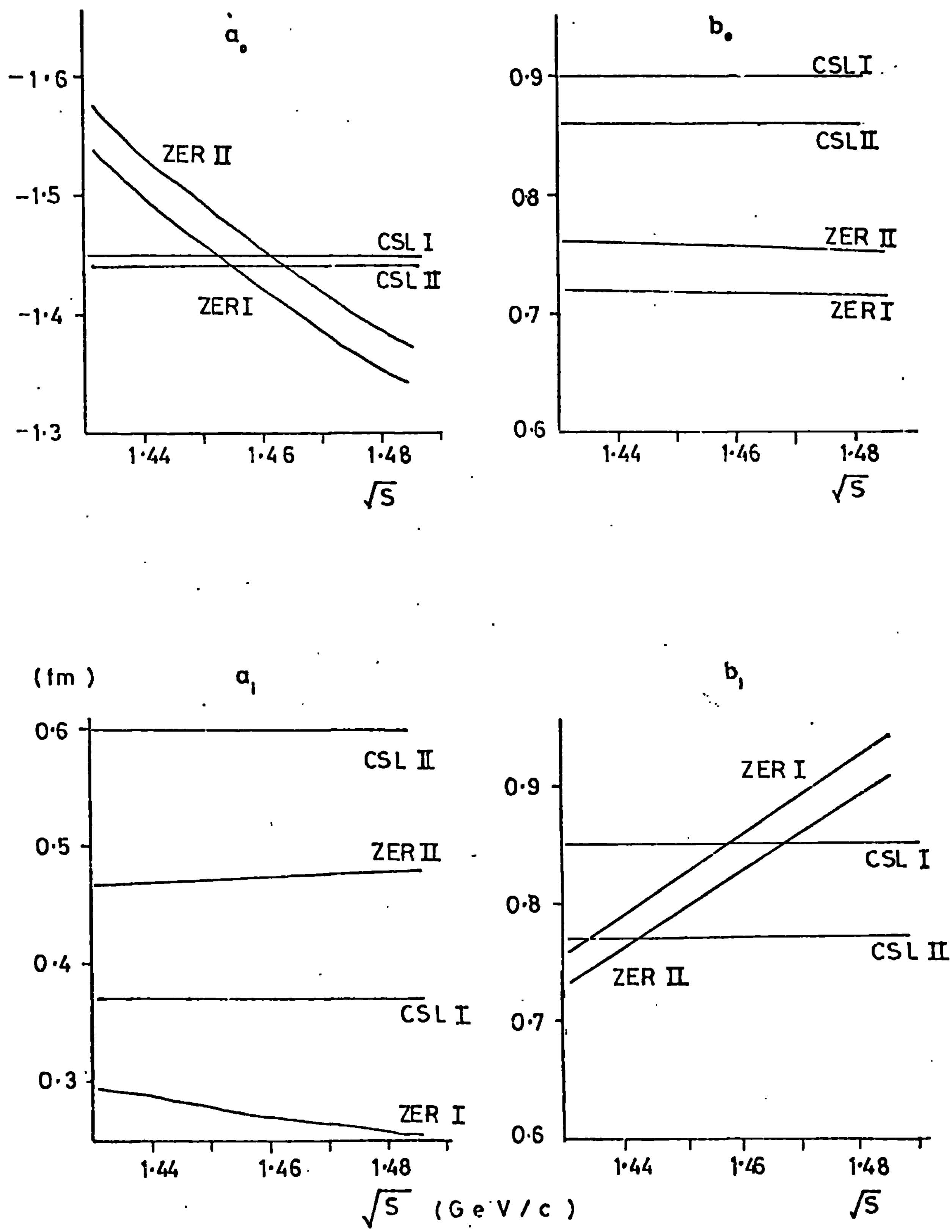

FIG 8·9: Energy Dependence of ϕ and γ

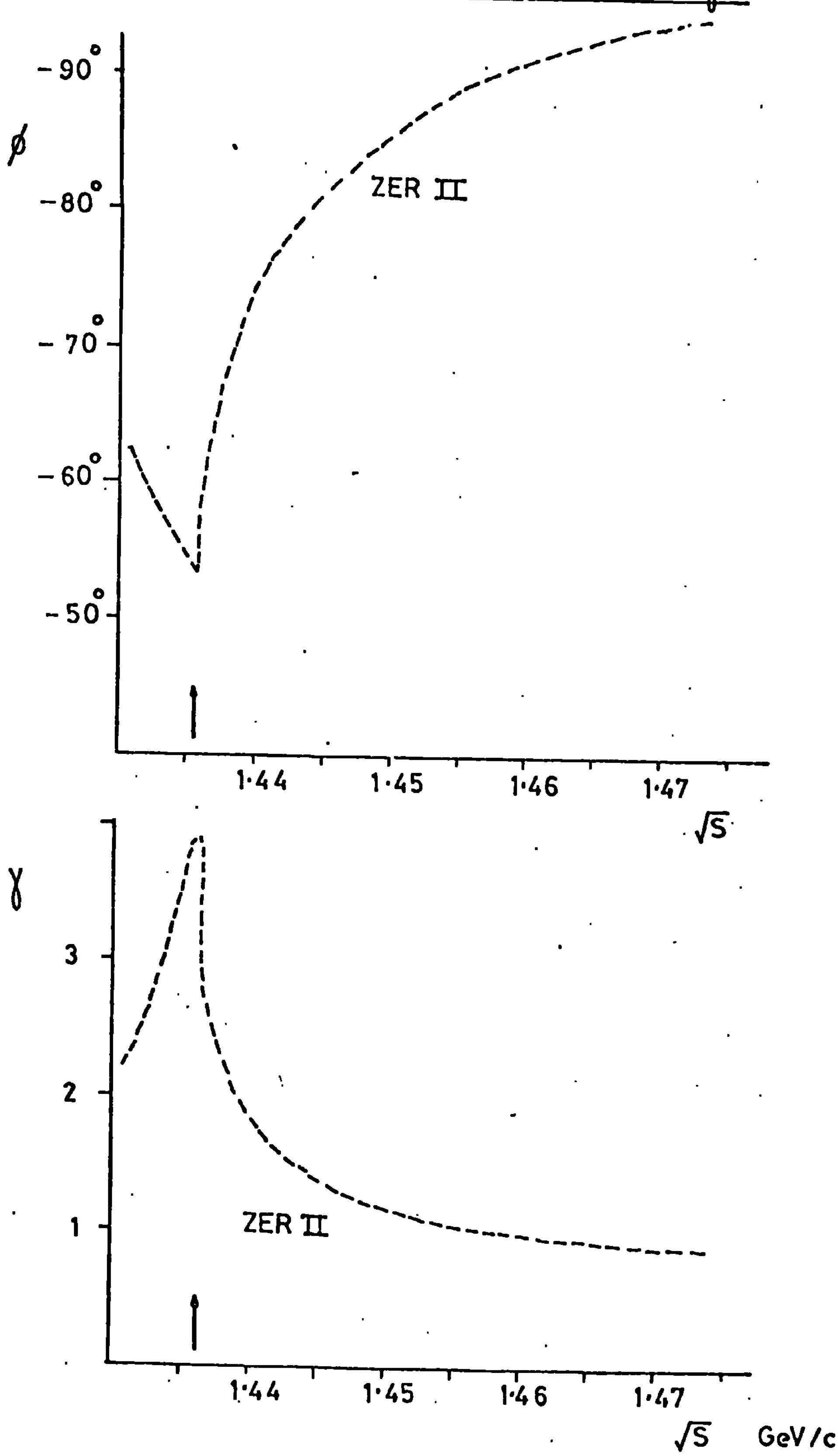

however the value of a_1 is $\sim$ 0.4 rather than zero as found by Kim. The value of a_0 confirms the existence of a bound state below threshold. This is discussed below.

8.3 The Λ (1405) Resonance

The presence of this resonance which lies below threshold manifests itself in the value of the real part of the I = 0 scattering length (a_0) which is large and negative. This implies the existence of a bound state (41). Assuming that the scattering length is energy independent Dalitz derived the mass of this bound state. Using a linear approximation of the Briet Wigner form of the denominator in the elastic scattering amplitude this was found to give for the I = 0 channel

$$E_r = M_p + M_K - \frac{1}{2\mu_K a_0^2}$$

$$\text{and } \Gamma = \frac{2b_0}{\mu_K |a_0|^3}$$

where μ_K is the reduced mass of the K^-p system (323.6 MeV) and M_p and M_K are the proton and kaon masses respectively. Using the values of a_0 and b_0 from the CSL solutions in table 8.1 gives values for E_r and Γ of about 1405 and 70 MeV respectively, see table 8.7 below.

Table 8.7: Mass And Widths Of Bound State Below Threshold

	CSL I	CSL II
Er(MeV)	1403.0	1403.4
Γ (MeV)	69.1	70.8

Clearly these are in good agreement with the established values obtained by Alexander et al (43) and Alston et al (44). There is a discrepancy in the value of the resonance width (35 or 50 MeV) however the precision of the present values a_0 and b_0 is inadequate to distinguish between these values. Typical error on a_0 is $\sim 10\%$ which gives rise to at least a 30% error in the value of Γ.

8.4 Summary Of The Results

It was stated at the beginning of this thesis that the motivation for this experiment arose from several criticisms of the work of Kim which is the only existing work of reasonable statistics at low momentum and at rest. The broad aims of this experiment have been achieved, namely to obtain low energy channel cross-sections in order to check the results of Kim; to determine the ratio, γ, of the rates of production of charged hyperons in order to resolve the discrepancy between the emulsion and bubble chamber results of Tovee and Kim respectively and finally to carry out a K-matrix parametrisation of the data.

The γ ratio was found to be

2.35 ± 0.07 by method I see § 7.8

or 2.38 ± 0.04 by method II see § 7.9

This supports the value of 2.34 quoted by Tovee et al (4) in the emulsion experiment rather than the value of Kim.

The channel cross-sections confirm those already obtained by Kim (see fig. 8.1) with the exception of the $\overline{K^o}n$ channel which is considerabl higher but is consistent with the analysis of Martin.

The K-matrix parameters are also consistent with previous values (3, 14, 30, 46) although a_1 is non zero for all fits and again supports the analysis of Martin. The existence of the bound state below threshold is evident from the large and negative value of a_0, the resonant mass being $\sim$ 1405 MeV of width $\sim$ 70 MeV.

8.5 Conclusion

During the course of the K-matrix analysis it became evident that even the most precise data in the low energy K^-p region are inadequate to obtain a high precision determination of the parameters of the Λ (1405). Some of the K-matrix elements are highly correlated and although these do not appear to affect the values of A_0 and A_1 by large amounts, it does make it extremely difficult to interpret the usual error matrix produced by fits of this kind. This results in large uncertainties in the parameter errors which naturally affects the determination of the mass and width of the Λ (1405), hence only the existence and the mass of the resonance may be determined with confidence, its width is less precise.

The current world data are described adequately by a zero effective range theory and in other analyses (30) it is found unnecessary to include effective range terms (i.e. include the energy dependence of the K-matrix elements themselves). The analysis of Martin, which by its nature was more highly constrained than a K-matrix analysis alone, did require the introduction of effective range terms for the I = 0 matrix elements. The existing low momentum data are unable to confirm the need for energy dependent analyses and only a high precision experiment with an order of magnitude increase in statistics will clarify the situation. The region of particular interest is the $\overline{K^o}n$ threshold which does produce structure in the cross-sections of other channels by virtue of the unitarity constraint This structure is particularly noticeable in the behaviour of the γ ratio and a precise determination of this ratio would constrain the K-matrix analysis considerably as this structure is highly sensitive to the values of the matrix elements.

A new experiment would need very careful design. The present TST experiment suffered from several problems some of which are peculiar to the T.S.T. chamber itself and could be avoided by the use of a conventiona chamber and some which are inherent to the bubble chamber technique. Those common to the TST are :

(i) that the shallow nature of the chamber introduced extra difficulties in the data analysis. The data were carefully examined to investigate the effect of biases caused by this. It also increased the number of unmeasurable events by reducing the potential length of the secondary particles.

(ii) that the density of the liquid hydrogen inside the target could only be determined with a precision of ~ 2%.

(iii) that the complexity of the TST system introduced a complex transformation between the measurements and the three dimensional reconstruction.

The main problem which is common to all bubble chambers is that of measuring the momentum of low energy kaons. This has already been discussed in detail in chapter four, however it is worth mentioning that in order to obtain precise measurements of the momentum at the interation vertex an extremely accurate momentum must be measured at some point along the track. For example, in order to obtain a vertex momentum of ~ 100 MeV/c with an accuracy of 5% then the measurement made at the track centre at, say, 20 cm from the vertex will be (via the range-momentum relation) a value of 210 MeV/c and this must be known to the nearest 5 MeV/c (i.e. better than 2½%). The situation becomes considerably more acute if momenta down to 50 MeV/c are required to 5% accuracy, these will require centre of track measurements accurate to better than 1%.

Clearly this precision is impossible to obtain by making track curvature measurements, Even if long beam tracks are used coulomb scattering will introduce errors in excess of the 1% level. The only means of obtaining a high precision vertex momentum is to use a beam with a well defined entrance momentum and instead of passing this through a degrader (which then necessitates a radius of curvature measurement) pass it directly into the chamber. This will require the entrance momentum to be ~ 320 MeV/c if the beams are to come to rest before passing through a one metre long chamber. A precise measurement can then be made on the length of the beam track and an accurate momentum can be determined using the range energy relation. If the track length can be found to an accuracy of 1 mm this will give a precision of $\pm$ 5 MeV/c at 60 MeV/c. This approach would require a low momentum selection system to be placed close to the chamber entrance port together with a set of bending magnets to compensate for the fringe field of the chamber which would have a noticeable effect on the low momentum beam direction. The secondary particle tracks could be measured in the conventional manner in order to obtain kinematic fits to the events for the studies of geometrical losses and angular distributions.

Care would have to be taken to ensure that all the events were measured, even if only the beam momentum was determined as this would then allow these partially unmeasured events to be included in the momentum distributions.

To summarise, the requirements of the experiment to obtain cross-sections down to ~ 50 MeV/c with an overall accuracy of ~ 2% would be:

(i) A well established bubble chamber whose optical constants have been thoroughly evaluated.

(ii) A large chamber ~ 1.0 x 0.50 x 0.50 metres with good visibility and small ionisation bubbles (these are usually artificially enhanced by the diffraction airy disk).

(iii) A well defined entrance momentum for the beam (~ ½% for 320 MeV/c).

(iv) An analysis procedure which allowed only the barest minimum of events to remain with unmeasured beam momenta. The most important problem to be solved is the allocation of events to particular momentum intervals.

(v) A careful scanning procedure, which classifies each event precisely according to its appearance (see scan code in table 2.5

(vi) A large amount of data resulting in at least 100,000 events of which ~ 50,000 will be elastic scattering. This would give ~ 2,000 events in 10 MeV/c momentum intervals and lead to statistical errors of ~ 2½%.

A return to the study of low energy K^-p interactions represents a great challenge and would stretch the techniques of bubble chamber work to their limits. However it must be stressed that this low energy region will only succumb to the most meticulous and careful analysis and any other approach would result in no improvement on the existing situation.

APPENDIX A

Relationship Between The K-Matrix And T-Matrix

This relationship may be found using equivalent boundary conditions which are strictly only valid for S wave channels related by zero range interactions; the resulting formulae are however valid generally.

For an S wave incident in channel i the wave function is

$$r\phi^K_{ij} = \delta_{ji} \frac{\sin k_j r}{k_j} + K_{ji} \cos k_j r \qquad \text{(A1)}$$

at r = 0 then:

$$\left\{ r\phi^K_{ij} \right\}_{r=0} = K_{ji}$$

$$= \sum_m K_{jm} \delta_{mi} \qquad \text{(A2)}$$

The first derivative at r = 0 is:

$$\left\{ \frac{d}{dr} r\phi^K_{ij} \right\}_{r=0} = \delta_{ji} \qquad \text{(A3)}$$

Combining equations (A2) and (A3) leads to the result:

$$\left\{ r\phi^K_{ij} \right\}_{r=0} = \sum_m K_{jm} \left\{ \frac{d}{dr} r\phi^K_{im} \right\}_{r=0} \qquad \text{(A4)}$$

Since the ϕ^K_{im} form a complete set the boundary condition (A2) holds for any wave function ϕ_m. On substitution of the wave function ($r\phi^T_{ij}$ in equation 1.1) appropriate to the T-matrix formalism into equation (A4) the result is obtained:

$$T_{ji} = \sum_m K_{jm} (\delta_{mi} + ik_m T_{mi}) \qquad \text{(A5)}$$

In matrix notation this becomes

$$T = K(1 + ikT) \qquad \text{(A6)}$$

and on rearranging to obtain T explicity

$$T = (1 - ikK)^{-1}K \qquad \text{(A7)}$$

which is the same as the equation 1.5.

APPENDIX B

The Calculation Of The T-Matrix Elements

Using equation (A4) and replacing $r\phi_{ij}$ by ψ for convenience, the two channel case is represented by

$$\begin{pmatrix} \psi_1 \\ \psi_2 \end{pmatrix}_{r=0} = \begin{pmatrix} \alpha & \beta \\ \beta^{+} & \gamma \end{pmatrix} \begin{pmatrix} d\psi_1 / dr \\ d\psi_2 / dr \end{pmatrix}_{r=0} \qquad \text{(B1)}$$

This gives two equations thus:

$$\left(\psi_1\right)_{r=0} = \alpha\left(\frac{d\psi_1}{dr}\right)_{r=0} + \beta\left(\frac{d\psi_2}{dr}\right)_{r=0} \qquad \text{(B2)}$$

$$\left(\psi_2\right)_{r=0} = \beta^{\dagger}\left(\frac{d\psi_1}{dr}\right)_{r=0} + \gamma\left(\frac{d\psi_2}{dr}\right)_{r=0} \qquad \text{(B3)}$$

The two channel wave functions are found from equation 1.1 and substituted into (B2) and (B3) to give:

$$\left(\psi_1\right)_{r=0} = \alpha\left(\frac{d\psi_1}{dr}\right)_{r=0} + i\beta k_2\left(\psi_2\right)_{r=0} \qquad \text{(B4)}$$

and

$$\left(\psi_2\right)_{r=0} = \beta^{\dagger}\left(\frac{d\psi_1}{dr}\right)_{r=0} + i\gamma k_2\left(\psi_2\right)_{r=0} \qquad \text{(B5)}$$

Equation (B5) may be rearranged to find $\left(\psi_2\right)_{r=0}$ and this is then substituted into (B4) to yield

$$\left(\psi_1\right)_{r=0} = (\alpha + i\beta k_2 (1 - i\gamma k_2)^{-1}\beta^{+})\left(\frac{d\psi_1}{dr}\right)_{r=0} \qquad \text{(B6)}$$

Equation (B6) and the rearranged version of (B5) may be written as

$$\left(\psi_1\right)_{r=0} = A\left(\frac{d\psi_1}{dr}\right)_{r=0} \tag{B7}$$

and

$$\left(\psi_2\right)_{r=0} = M\left(\frac{d\psi_1}{dr}\right)_{r=0} \tag{B8}$$

where

$$A = \alpha + i\beta k_2(1 - i\gamma k_2)^{-1}\beta^{+} \tag{B9}$$

and

$$M = (1 - i\gamma k_2)^{-1}\beta^{+} \tag{B10}$$

knowing that

$$\left(\frac{d\psi_1}{dr}\right)_{r=0} = 1 + ik_1T_{11} \qquad \text{from equation 1.1}$$

and that $\left(\psi_2\right)_{r=0} = T_{21}$

Then

$$T_{11} = \frac{A}{1 - ik_1A} \tag{B11}$$

and

$$T_{21} = \frac{M}{1 - ik_1A} \tag{B12}$$

These are shown for both isospin states in equations 1.9.

The meaning of A is found by recalling that

$$T_{11} = \frac{\sin\delta\, e^{i\delta}}{k_1}$$

and substitute into B11

$$k_1 \cot\delta = \frac{1}{A} \tag{B13}$$

which is the usual zero range approximation and A is the scattering length.

In terms of the elements of the K-matrix A is given by

$$A = \alpha - \frac{\beta^2 k_2^2 \gamma}{1 + k_2^2 \gamma^2} + \frac{i\beta^2 k_2}{1 + k_2^2 \gamma^2} \tag{B14}$$

The values of A and M for the two isospin states can be found explicitly in terms of the K-matrix elements.

For the I = 0 case, the K-matrix elements are simply scalars and equations (B9) and (B10) give the relationships directly.

$$A_0 = \alpha_K + \frac{i\alpha_{K\Sigma}^2 k_\Sigma}{1 - i\alpha_\Sigma k_\Sigma} \tag{B15}$$

and

$$M_0 = \frac{\alpha_{K\Sigma}}{1 - i\alpha_\Sigma k_\Sigma} \tag{B16}$$

For I = 1, the situation is more complex, and the α, β and γ of equations (B9) and (B10) are matrices in themselves.

$$\alpha \equiv (\beta_K) \qquad \beta \equiv (\beta_{K\Sigma}, \beta_{K\Lambda}) \qquad \gamma \equiv \begin{pmatrix} \beta_\Sigma & \beta_{\Sigma\Lambda} \\ \beta_{\Sigma\Lambda} & \beta_\Lambda \end{pmatrix}$$

and

$$k_1 = (k_K) \qquad k_2 = \begin{pmatrix} k_\Sigma & 0 \\ 0 & k_\Lambda \end{pmatrix}$$

Substitution into (B9) gives

$$A_1 = \beta_K + i(\beta_{K\Sigma}, \beta_{K\Lambda}) \begin{pmatrix} k_\Sigma & 0 \\ 0 & k_\Lambda \end{pmatrix} \left[\begin{pmatrix} 1 & 0 \\ 0 & 1 \end{pmatrix} - i \begin{pmatrix} \beta_\Sigma & \beta_{\Sigma\Lambda} \\ \beta_{\Sigma\Lambda} & \beta_\Lambda \end{pmatrix} \begin{pmatrix} k_\Sigma & 0 \\ 0 & k_\Lambda \end{pmatrix} \right]^{-1} \begin{pmatrix} \beta_{K\Sigma} \\ \beta_{K\Lambda} \end{pmatrix} \tag{B17}$$

Evaluating the inverse matrix, gives

$$\begin{pmatrix} 1 - ik_\Sigma \beta_\Sigma & -ik_\Lambda \beta_\Lambda \\ -ik_\Sigma \beta_{\Sigma\Lambda} & 1 - ik_\Lambda \beta_\Lambda \end{pmatrix}^{-1} = X^{-1}$$

now $$X^{-1} = \frac{1}{\det|X|} \quad \text{(adjoint of X)} \tag{B18}$$

Then $$\det|X| = (1 - ik_\Sigma\beta_\Sigma)(1 - ik_\Lambda\beta_\Lambda) + k_\Lambda k_\Sigma \beta_{\Sigma\Lambda}^2 = W_1 \tag{B19}$$

and (adjoint of X) = $\begin{pmatrix} 1 - ik_\Lambda\beta_\Lambda & ik_\Lambda\beta_{\Sigma\Lambda} \\ ik_\Sigma\beta_{\Sigma\Lambda} & 1 - ik_\Sigma\beta_\Sigma \end{pmatrix}$

Substituting (B18) and (B19) into (B17) gives the equation

$$A_1 = \beta_K + \frac{i}{W_1}(\beta_{K\Sigma}, \beta_{K\Lambda})\begin{pmatrix} k_\Sigma & 0 \\ 0 & k_\Lambda \end{pmatrix}\begin{pmatrix} 1 - ik_\Lambda\beta_\Lambda & ik_\Lambda\beta_{\Sigma\Lambda} \\ ik_\Sigma\beta_{\Sigma\Lambda} & 1 - ik_\Sigma\beta_\Sigma \end{pmatrix}^{-1}\begin{pmatrix} \beta_{K\Sigma} \\ \beta_{K\Lambda} \end{pmatrix}$$

This can be multiplied out and simplified to yield:

$$A_1 = \beta_K + \frac{1}{W_1}(\beta_{K\Sigma}W_2 + \beta_{K\Lambda}W_3) \tag{B20}$$

where $W_2 = k_\Sigma k_\Lambda(\beta_{K\Sigma}\beta_\Lambda - \beta_{\Sigma\Lambda}\beta_{K\Lambda}) + ik_\Sigma\beta_{K\Sigma}$

and $W_3 = k_\Sigma k_\Lambda(\beta_{K\Lambda}\beta_\Sigma - \beta_{\Sigma\Lambda}\beta_{K\Sigma}) + ik_\Lambda\beta_{K\Lambda}$

The value of M_1 is found in the same way by substituting the appropriate matrices into equation (B10). M_1 does not reduce to a 1 x 1 matrix, but reflects the fact that there are two inelastic isospin one channels, and reduces to a 2 x 1 matrix as shown

$$M_1 = \frac{1}{W_1}\begin{pmatrix} \beta_{K\Sigma}(1 - ik_\Lambda\beta_\Lambda) + ik_\Lambda\beta_{\Sigma\Lambda}\beta_{K\Lambda} \\ \beta_{K\Lambda}(1 - ik_\Sigma\beta_\Sigma) + ik_\Sigma\beta_{\Sigma\Lambda}\beta_{K\Sigma} \end{pmatrix}$$

The usual notation puts $M_1 = (\beta_{K\Sigma}(1 - ik_\Lambda\beta_\Lambda) + ik_\Lambda\beta_{\Sigma\Lambda}\beta_{K\Lambda})/W_1$ (B21)

and $N_1 = (\beta_{K\Lambda}(1 - ik_\Sigma\beta_\Sigma) + ik_\Sigma\beta_{\Sigma\Lambda}\beta_{K\Sigma})/W_1$ (B22)

The values of A_0, A_1, M_0, M_1 and N_1 used in equation 1.9 have now been expressed explicitly in terms of the K-matrix elements in equations (B15), (B16), (B20), (B21) and (B22).

APPENDIX C

Calculation Of Channel Cross-Sections

Equations 1.3 and 1.13 give the elastic scattering cross-section:

$$\sigma(K^-p) = \pi \left| T_K^1 + T_K^0 \right|^2$$

$$= \pi \left| \frac{A_1}{1 - ik_K A_1} + \frac{A_0}{1 - ik_K A_0} \right|^2$$

$$= \pi \left| \frac{A_1 + A_0 - 2ik_K A_0 A_1}{(1 - ik_K A_1)(1 - ik_K A_0)} \right|^2$$

Similarly for the charge exchange

$$\sigma(\overline{K^0}n) = \pi \left| \frac{A_1 - A_0}{(i - ik_K A_0)(1 - ik_K A_1)} \right|^2$$

The remaining cross-sections are expressed more easily in terms of σ_1 and σ_0 where

$$\sigma_1 = \frac{4\pi k_\Sigma |M_1|^2}{k_K |1 - ik_K A_1|^2} + \frac{4\pi k_\Lambda |N_1|^2}{k_K |1 - ik_K A_0|^2}$$

$$\sigma_0 = \frac{4\pi k_\Sigma |M_0|^2}{k_K |1 - ik_K A_0|^2} \qquad \text{(C1)}$$

σ_0 and σ_1 are the total hyperon cross-sections for each isospin state M_1 and N_1 may be eliminated using σ_1 and ϵ defined in equation 1.10

$$\sigma_1 \epsilon = \frac{4\pi k_\Lambda |N_1|^2}{k_K |1 - ik_K A_1|^2}$$

$$\sigma_1 (1 - \epsilon) = \frac{4\pi k_\Sigma |M_1|^2}{k_K |1 - ik_K A_1|^2} \qquad \text{(C2)}$$

The charged hyperon cross-section may now be evaluated (e.g. $^{-}\pi^{+}$) from equations 1.13

$$\sigma(\Sigma^-\pi^+) = \frac{4\pi k_\Sigma}{k_K}\left[\frac{1}{4}\left|T^1_{K\Sigma}\right|^2 + \frac{1}{6}\left|T^0_{K\Sigma}\right|^2 - \frac{1}{2\sqrt{6}}\left(T^{1*}_{K\Sigma}T^0_{K\Sigma} + T^1_{K\Sigma}T^{0*}_{K\Sigma}\right)\right]$$

$$= \frac{\pi k_\Sigma |M_1|^2}{k_K\left|1 - ik_K A_1\right|^2} + \frac{1}{6}\frac{4\pi k_\Sigma |M_0|^2}{k_K\left|1 - ik_K A_0\right|^2} - \frac{1}{\sqrt{6}}\sqrt{\left|T^1_{K\Sigma}\right|^2\left|T^0_{K\Sigma}\right|^2}\arg\left(\frac{T^1_{K\Sigma}}{T^0_{K\Sigma}}\right)$$

$$= \frac{1}{6}\sigma_0 + \frac{1}{4}\sigma_1(1 - \varepsilon) - \frac{1}{\sqrt{6}}(\sigma_0\sigma_1(1 - \varepsilon))^{\frac{1}{2}}\cos\phi$$

similarly for the $\Sigma^+\pi^-$ channel

$$\sigma(\Sigma^+\pi^-) = \frac{1}{6}\sigma_0 + \frac{1}{4}\sigma_1(1 - \varepsilon) + \frac{1}{\sqrt{6}}(\sigma_0\sigma_1(1 - \varepsilon))^{\frac{1}{2}}\cos\phi$$

The neutral hyperon cross-sections follow immediately from equation 1.3, 1.13, (C1) and (C2), to give

$$\sigma(\Sigma^0\pi^0) = \frac{1}{6}\sigma_0$$

and $\sigma(\Lambda^0\pi^0) = \frac{1}{2}\varepsilon\,\sigma_1$

REFERENCES

(1) Compilation of Cross-Sections for K^- Induced Reactions	CERN HERA REPORT 70-6		(1970)
(2) Martin, A.D.	Phys. Lett. 65B	346	(1976)
(3) Kim, J.K.	Phys. Rev. Lett. 14	29	(1965)
(4) Tovee, D.N., Davis, D.H., et al	Nucl. Phys. B33	493	(1971)
(5) Particle Data Group	Review of Particle Properties		(1978)
(6) Miller, D.H.	Duke	229	(1970)
(7) Kim, J.K.	Phys. Rev. Lett 27	356	(1971)
(8) Bowen, T., et al	Phys. Rev. D2	2599	(1970)
(9) Carroll, A.S., et al	Phys. Rev. Lett. 37	806	(1976)
(10) Mast, T.S., Alston-Garnjost, M., et al	Phys. Rev. D11	3078	(1975)
(11) Fleming, G.	Ph. D. Thesis, Univ. of Durham		(1976)
(12) Fallahi, T.	Ph. D. Thesis, Univ. of Durham		(1978)
(13) Humphrey, W.E., Ross, R.R.	Phys. Rev. 127	1305	(1962)
(14) Sakitt, M., Day, T.B., et al	Phys. Rev. 139	B719	(1965)
(15) Ascoli, G., Hill, R.D., Yoon, T.S.	Nuo. Cim. 9	813	(1958)
(16) Nordin, P.	Phys. Rev. 123	2168	(1961)
(17) Watson, M.B., Ferro-Luzzi, M., Tripp, R.D.	Phys. Rev. 131	2248	(1963)
(18) Abrams, G.S., Sechi-Zorn, B.	Phys. Rev. 139	B454	(1965)
(19) Csejthey-Barth, M., Lagnaux, J.P., et al	Phys. Lett. 16	89	(1965)
(20) Schlosser, K., Buschbeck-Czapp, B., et al	Phys. Lett. 17	334	(1965)

(21) Kittel, W., Otter, G., Wacek, I.	Phys. Lett. 21	349 (1966)
(22) Thomas, G.P., Jain, P.L.	Nucl. Phys. B13	385 (1969)
(23) Berley , D., Yamin, S.P., et al	Phys. Rev. D1	1996 (1970)
(24) Mast, T.S., Alston-Garnjost, M., et al	Phys. Rev. D14	13 (1976)
(25) Nowak, R.J., Armstrong, J., et al	Nucl. Phys. B139	61 (1978)
(26) Dalitz, R.H., Tuan, S.F.	Ann. Phys. 10	307 (1960)
(27) Jackson, J.D., Ravenhall, D.G., Wyld, H.W.	Nuo. Cim. 9	834 (1952)
Jackson, J.D., Ravenhall, D.G., Wylde, H.W.	Phys. Rev. Lett. 2	355 (1959)
(28) Shaw, G.L., Ross, M.H.	Phys. Rev. 126	806 (1962)
Shaw, G.L., Ross, M.H.	Phys. Rev. 126	814 (1962)
(29) Baillon, P., Bricman, C., et al	Nucl. Phys. B105	365 (1976)
(30) Martin, A.D., Ross, G.G.	Nucl. Phys. B16	479 (1970)
(31) Hamam, Y.	Ph. D. Thesis, Univ. of Durham	(1972)
(32) Burren, J.W., Sparrow, J.	Geometrical Reconstruction Of Bubble Chamber Tracks NIRL/R/14	
(33) Wilson, A.G.	A Kinematical Fitting Programme For the Analysis of Bubble Chamber Events	NIRL/M/38
(34) Leutz, H., Schmeisser, F., Wenninger, H.	CERN 74-20	(1974)
(35) Eisele, F., Engelmann, R., et al	Z. Physik 221	1 (1969)
(36) Chang., C.Y.	Phys. Rev. 151	1081 (1966)
(37) Barloutaud,R., De Bellephon,A	Nucl. Phys. B14	153 (1969)
(38) James, F., Roos, M.	MINUIT: CERN PROGRAM LIBRARY D506	D516 (1977)
(39) Chao, Y.A., Kraemer, R.W., et al	Nucl. Phys. B56	46 (1973)

(40) Tripp, R.D.	Private Communication	
(41) Dalitz, R.H., Tuan, S.F.	Phys. Rev. Lett. 2	425 (1959)
(42) Dalitz, R.H.	Rev. Mod. Phys. 33	471 (1961)
Dalitz, R.H.	Phys. Rev. Lett. 6	239 (1961)
(43) Alexander, G., Kalberfleisch, G.R., et al	Phys. Rev. Lett. 8	447 (1962)
(44) Alston, M.H., Alvarez, L.W., et al	Proc. Int. Conf. on H.E.N.P. Geneva	311 (1962)
(45) Lipman, N.H., Uto, H., et al	Phys. Lett. 43B	89 (1973)
(46) Kittel, W., Otter, G.	Phys. Lett. 22	115 (1966)

ACKNOWLEDGEMENTS

I would like to thank Professors A.W. Wolfendale and B.H. Bransden who, as sequential heads of the physics department in Durham, made available the facilities of the department throughout this work.

I wish particularly to thank Dr. J.V. Major who as my supervisor has been of considerable help throughout and a constant source of advice, particularly so during my absence from Durham in the latter stages of this work.

Thanks also go to Dr. D. Evans for many stimulating discussions and to A.P. Lotts and R. Nelson for their invaluable help in the data processing and for their advice on matters computational.

The help of the other group members is not forgotten, neither is the work of the scanning and measuring staff at the University of Durham.

The help of Professor J.A. Zakrzewski and J. Ciborowski and their colleagues in scanning the film is also much appreciated.

I acknowledge the financial support given to me by the Science Research Council during the three years of this work.

Thanks are due to my typist Kaye Holyoak who has put in many hours of excellent work and last, but by no means least to Barbara for her moral support throughout this period of study.